Dipl.-Ing. Karl Freiberger

Measurement Methods for Estimating the Error Vector Magnitude in OFDM Transceivers

Doctoral Thesis

in partial fulfillment of the requirements for the degree of
Doctor of Technical Sciences

submitted to

Graz University of Technology, Austria
Doctoral School of Information and Communication Engineering

Advisor and First Assessor/Examiner:
FH-Prof. Priv.-Doz. DI Dr. Christian Vogel
FH–JOANNEUM – University of Applied Sciences, Graz, Austria

Second Assessor/Examiner:
Prof. Dr. Nuno Borges Carvalho
Institute of Telecommunications, University of Aveiro, Portugal

Third Assessor/Examiner:
Univ.-Prof. DI Dr. Gernot Kubin
Signal Processing and Speech Communication Laboratory, Graz University of Technology

Graz, November 2017

STATUTORY DECLARATION

I declare that I have authored this thesis independently, that I have not used other than the declared sources/resources, and that I have explicitly marked all material which has been quoted either literally or by content from the used sources.

EIDESSTATTLICHE ERKLÄRUNG

Ich erkläre an Eides statt, dass ich die vorliegende Arbeit selbstständig verfasst, andere als die angegebenen Quellen/Hilfsmittel nicht benutzt, und die den benutzten Quellen wörtlich und inhaltlich entnommene Stellen als solche kenntlich gemacht habe.

date	signature

Abstract

The error vector magnitude (EVM) is a standard metric to quantify the performance of digital communication systems and related building blocks. Regular EVM measurements require expensive equipment featuring inphase and quadrature (IQ) demodulation, wideband analog-to-digital converters (ADCs), and dedicated receiver algorithms to demodulate the data symbols. With modern high data rate communication standards that require high bandwidths and low amounts of error, it is difficult to avoid bias due to errors in the measurement chain. This thesis develops and discusses measurement methods that address the above-described issues with EVM measurements.

The first method is an extension of the regular EVM, yielding two results from a single measurement. One result equals the regular EVM result, whereas the other excludes potential errors due to mismatches of the I- and Q- paths of direct conversion transmitters and receivers (IQ imbalance). This can be helpful for troubleshooting, or when measuring a radio frequency (RF) device under test (DUT), where EVM contributions due to IQ imbalance constitute measurement errors.

The second method, SLIC-EVM, is an alternative to the EVM that is simpler to adapt to new standards, since it does not require demodulation of the data symbols. SLIC-EVM is based on fitting a linear approximation to the DUT and estimating the power spectral density (PSD) of the modeling error. The measurement methods developed later in this thesis can be motivated by an application of the EVM in the context of digital predistortion (DPD) of a power amplifier: Multi-objective optimization of the EVM and the spectral mask distance leads to Pareto-optimal DPD coefficients. In contrast to conventional methods, the proposed DPD optimization allows for a very low bandwidth in the feedback path. This advantage is, however, foiled by the EVM measurement that requires high-rate ADCs. The noise power ratio (NPR) is a classical metric that can be measured without high-rate ADCs.

The third measurement method, called the error power ratio (EPR), shows that the EVM can be estimated based on the principle of the NPR for typical analog transceiver impairments like additive noise, phase noise, nonlinearity, and IQ imbalance. Besides measurement results of a wireless LAN power amplifier, Monte-Carlo simulations indicate that the EPR predicts the EVM well for various impairment scenarios. There is however an important constraint. The frequency response of the system and the error must be well-behaved, as derived and specified mathematically.

The final method, the swept EPR (SWEEPR), overcomes this constraint and allows for estimation of highly frequency-dependent EVMs. An EPR test signal features constant stopband locations, within which the error is measured. The key idea of SWEEPR is to use a linearly-swept stopband center, covering the entire bandwidth of the signal. A swept-tuned spectrum analyzer, which is available in most RF labs, is the perfect device for SWEEPR analysis. By synchronizing the analyzer sweep to the stopband sweep, it is possible to measure the power within the stopband, and, by delaying the sweep, outside of the stopband. The ratio of the stopband PSD to the inband PSD

estimates the EVM, which is shown analytically and verified with measurements.

Summing up, this thesis presents alternatives to standard EVM measurements that excel with their simplicity, accuracy, and generality. The derived theory and results represent a big leap to the current state of the art of EVM estimation and signal- to-noise and distortion ratio measurement based on best linear approximation and PSD measurement. Furthermore, this thesis reveals limitations of traditional NPR measurements that are ultimately overcome with the proposed SWEEPR method.

Kurzfassung

Die „Error Vector Magnitude“ (EVM) ist ein gängiges Maß zur Bestimmung der Leistungsfähigkeit digitaler Kommunikationssysteme und der dazugehörigen elektronischen Bausteine. EVM-Messungen erfordern üblicherweise teure Messgeräte und spezielle Algorithmen um die Datensymbole zu demodulieren. Bei hohen Bandbreiten ist es schwierig kleinste Fehler zu messen, da Fehler in der Messkette zunehmen und nicht vom wahren Fehler getrennt werden können.

Diese Doktorarbeit entwickelt und diskutiert neuartige Messverfahren zur Schätzung der EVM. Die erste Methode ist eine Erweiterung der regulären EVM-Messung. Eine einzelne Messung mit der neuen Methode liefert zwei Resultate: Das erste Ergebnis entspricht dem regulären EVM und beinhaltet etwaige Fehler durch Abweichungen der beiden Quadraturpfade eines Direktmisch-Sendeempfängers (IQ-Imbalance). Das zweite Ergebnis schließt hingegen IQ-Imbalance aus. Dies kann z.B. bei der Messung eines Radiofrequenz-Verstärkers hilfreich sein, wo IQ-Imbalance nicht Teil des Testobjektes ist, sondern einen Messfehler darstellt.

Die zweite Methode, SLIC-EVM, ist eine Alternative zu EVM, die einfacher auf neue Signalstandards zu übertragen ist, da sie ohne Demodulation der Datensymbole auskommt. Danach wird eine Anwendung der EVM gezeigt, die auch als Motivation für die zwei nachfolgenden Messverfahren gesehen werden kann. Durch direkte Mehrziel-Optimierung der EVM und der Distanz zur spektralen Maske können Pareto-optimale digitale Vorverzerrer-Koffizienten identifiziert werden. Im Gegensatz zu üblichen Identifizierungsverfahren erlaubt das vorgestellte Prinzip der stochastischen Optimierung eine sehr niedrige Abtastrate der Analog-Digitalwandler (ADCs) im Rückwärtspfad. Dieser Vorteil würde jedoch durch die EVM Messung, die eine hohe Abtastrate benötigt, konterkariert. Das „Noise-Power Ratio“ (NPR) ist ein Maß das ohne Breitband-ADCs gemessen werden kann.

Die dritte Methode zeigt, dass die EVM für wichtige Fehlertypen wie Phasenrauschen, Nichtlinearitäten, und IQ-Imbalance auf Basis des NPR gemessen werden kann. Da hierzu die klassische NPR Messung etwas abgewandelt wird, führen wir den Begriff „Error Power Ratio“ (EPR) ein. Neben Messergebnissen eines WLAN Verstärkers zeigen Monte-Carlo Simulationen, dass die Abweichung des EPR vom EVM vernachlässigbar klein ist. Die Vorraussetzung hierfür ist jedoch, dass der Frequenzgang des Systems und des Fehlers nicht zu stark ausgeprägt sind.

Das letzte vorgestellte Messverfahren, genannt „Swept EPR“ (SWEEPR), löst dieses Problem. Ein EPR Testsignal weist Stopbänder mit einer zeitlich konstanten Mittenfrequenz auf. Bei SWEEPR hingegen wird das Stopband kontinuierlich durchgestimmt, sodass die gesamte Bandbreite des Signals abgedeckt wird. Für die Messung ist der weitverbreitete Spektrumanalysator nach dem Heterodynprinzip ideal geeignet. Durch Abstimmen der Analyse-Mischfrequenz auf die Testsignal Stopbandfrequenz, kann innerhalb des Stopbandes, oder bei entsprechendem Zeitversatz, außerhalb des Stopbandes gemessen werden. Das Verhältnis der beiden Messungen schätzt die EVM, was

theoretisch gezeigt und experimentell belegt wird.

Die in dieser Doktorarbeit vorgestellten Alternativen zur Standard-EVM Messung zeichnen sich durch ihre Einfachheit, Genauigkeit und allgemeingültige Verwendbarkeit aus. Neben der Vorstellung teilweise neuartiger Methoden, stellen die theoretischen Ableitungen sowie die zahlreichen Mess- und Simulationsresulte einen gewichtigen Beitrag zum gegenwärtigen Stand der Forschung und Technik im Bereich der messbasierten EVM-Schätzung dar. Weiters offenbart diese Arbeit die Probleme von traditionellen NPR-Messungen mit frequenzabhängigen Systemen und EVM-Verläufen. Diese Probleme werden durch die neuartige SWEEPR-Messmethode gelöst.

Acknowledgments

I would like to express my gratitude and thank all people that made this thesis possible by supporting me during my time as a doctoral student.

First of all, I thank Christian Vogel for being a world-class advisor. By hiring me for the telecommunications research center Vienna (FTW), Christian enabled my shift of focus from audio-signal processing to transceivers, digital predistortion and RF measurement, culminating in this thesis. Christian, you always found the perfect balance between being incentive and amicable. I am deeply grateful for your guidance and steady support. Thank you!

Many thanks go to Gernot Kubin for discussions and advice, for assessing this thesis, and for making his lab a great workplace, not least because of the excellent coffee. Furthermore, I would like to thank Nuno Borges Carvalho for assessing this thesis, and for being very flexible with my late delivery.

Much credit for over four successful and pleasant years of work belongs to my workmate Harald Enzinger. Harald, I cannot appreciate enough your invaluable help, exemplary way of working, willingness to discuss countless questions, and, most importantly, your likeable character. Thank you!

I acknowledge the funding of my work by the Austrian Research Promotion Agency FFG within the competence headquarter projects 835187 and 4718971. Special thanks go to the project partner Intel, Villach, formerly known as Lantiq Austria, in particular to Alexander Kahl, Steffen Trautmann, and David Schwingshackl, for their support and for directing me towards research questions with practical relevance. Steffen deserves an extra "thank you" for handling my paper and invention submissions and obtaining approvals for publication. Furthermore, I thank Denis Matveev and Markus Korak for assistance with measurements in the lab. Another round of thanks goes to my former colleagues at FTW, in particular to Martin Wolkerstorfer for help with optimization.

I would like to thank all members of the Signal Processing and Speech Communication Laboratory for their helpfulness, the relaxed and pleasant atmosphere, and the many interesting discussions we had during lunch or coffee breaks. Particularly mentioned should be Klaus Witrisal for scientific advice, my office neighbor Johannes Stahl for everything that comes with sitting opposite, and Josef Kulmer for having extra work with teaching when I was absent. Further thanks go to Michael Gadringer and Dominik Amschl from TUG's microwave group for lending me their vector signal analyzer.

Last but not least, my heartfelt thanks go to my family for their unconditional support. In particular, I thank my daughter Flora's grandparents Zita, Alfred, Virág, and László for being there for her when I was busy or abroad. I thank Flora for being my daily sunshine and hope that her soon-to-be-born brother will be as healthy and cheerful as her. The last and most heartfelt thanks go to Réka. She supported me each and every day to an extend that is definitely not to be taken for granted. Réka, thank you for everything!

Contents

List of Figures

List of Tables

List of Abbreviations and Symbols

Abbreviations

ACPR	Adjacent Channel Power Ratio
ADC	Analog-to-Digital Converter
AM	Amplitude Modulation
AM-AM	Amplitude Deviation at the DUT Output due to AM of the DUT Input Signal
AM-PM	Phase Deviation at the DUT Output due to AM of the DUT Input Signal
AWG	Arbitrary Waveform Generator
AWGN	Additive White Gaussian Noise
BLA	Best Linear Approximator
CCDF	Complementary Cumulative Distribution Function
CPE	Common Phase Error
CSCN	Circularly-Symmetric Complex Normal
DAC	Digital-to-Analog Converter
dBm	Decibel Related to 1 Milliwatt
DC	Direct Current
DE	Differential Evolution
DFT	Discrete Fourier Transform
DLA	Direct Learning Architecture
DPD	Digital Predistortion
DSO	Digital Sampling Oscilloscope
DSP	Digital Signal Processor
DUT	Device Under Test
EPR	Error Power Ratio
EVM	Error Vector Magnitude

EVP	Error Vector Power
FFT	Fast Fourier Transform
FIR	Finite Impulse Response
FSQ	Rhode & Schwarz FSQ Signal Analyzer
ICI	Inter-Carrier Interference
IF	Intermediate Frequency
ILA	Indirect Learning Architecture
IM3	Third-Order Intermodulation Distortion
IP3	Third-Order Intercept Point
IQ	In-Phase and Quadrature-Phase
ISI	Inter-Symbol Interference
LO	Local Oscillator
LS	Least Squares
LTE	Long-Term Evolution
LTI	Linear Time Invariant
M-QAM	M-ary Quadrature Modulation
MMSE	Minimum Mean Squared Error
MOO	Multi-Objective Optimization
MSE	Mean Squared Error
NMSE	Normalized Mean Squared Error
NPR	Noise Power Ratio
OFDM	Orthogonal Frequency-Division Multiplexing
PA	Power Amplifier
PAPR	Peak-to-Average Power Ratio
PDF	Probability Density Function
PM	Phase Modulation
PSA	Power Spectrum Analyzer
PSD	Power Spectral Density

QPSK	Quadrature Phase-Shift Keying (4-QAM)
RBW	Resolution Bandwidth
RF	Radio Frequency
RMS	Root Mean Square
RX	Receive(r)
SLIC	Subtraction of Linearly Correlated Components
SNDR	Signal-to-Noise and Distortion Ratio
SNR	Signal-to-Noise Ratio
ST	Swept-Tuned
SWEEPR	Swept Error Power Ratio
TD	Time Domain
TRX	Transceive(r)
TX	Transmit(ter)
VNA	Vector Network Analyzer
VSA	Vector Signal Analyzer
VSG	Vector Signal Generator
WLAN	Wireless Local Area Network

Letters and Symbols

j	Imaginary unit $j^2 = -1$
e	Error signal
s	Source signal
v	Noise signal
x	DUT input signal
y	DUT output signal
ω	Angular frequency (rad/s)
τ	Time shift (s)
B	Bandwidth (Hz)
f	Frequency (Hz)

T	Duration (s)
t	Time (s)
k	Discrete frequency index (bin): $k \in \mathbb{Z} : \{-K/2 \leq k < K/2\}$
l	Frame index
n	Discrete time index
$\lceil \cdot \rceil$	Ceiling operator, round towards next higher integer
$\lfloor \cdot \rfloor$	Floor operator, round towards next lowest integer

Specifiers

$x(t)$	Either RF or baseband signal
$x[n]$	Square brackets denote a discrete domain $n \in \mathbb{Z}$
$\tilde{x}(t)$	Baseband signal
$x_{\mathrm{RF}}(t)$	RF signal
f_a	Start frequency
f_b	Stop frequency
f_c	Center frequency
f_s	Sampling rate

Signals and Transforms

$r_x(\tau)$	Autocorrelation function of $x(t)$
$r_{xy}(\tau)$	Cross-correlation function of $x(t)$ and $y(t)$
$S_x(\omega)$	Power spectral density of $x(t)$
$S_{xy}(j\omega)$	Cross-spectral density of $x(t)$ and $y(t)$
$X(j\omega)$	Fourier transform of $x(t)$
$X[k, l]$	Short-time discrete Fourier transform of $x[n]$
$\delta[n]$	Kronecker delta (impulse sequence) $\delta[n] = 0 \; \forall n \neq 0$, $\delta[0] = 1$
$u[n]$	Unit step sequence $u[n] = 1 \; \forall n \geq 0$, $u[n] = 0 \; \forall n < 0$

1 Introduction

This chapter provides an introduction to the work presented in this thesis. Section 1.1 outlines the topic tackled in this thesis and points out why it is relevant. An overview of related work in Section 1.2 leads to a formulation of open questions and research challenges in Section 1.2.2. Finally, Section 1.3 outlines the scope of this thesis and presents contributions along with a list of papers.

1.1 Inband Error Measurement of Digitally Modulated Signals

This thesis focuses on measurements of the inband error of digitally modulated signals. A good part of the following introductory section is devoted to explaining what is meant by the term *inband error* and what makes its measurement important and difficult.

We start by briefly reviewing high data rate digital communication systems in Section 1.1.1, discussing the fundamental fact that to increase the data rate, the inband signal-to-noise ratio (SNR) and/or the bandwidth must be increased. Here, the term *inband* refers to the fact that only noise within the transmitted signal bandwidth limits the achievable data rate.

Section 1.1.2 discusses potential sources of error based on a block diagram of a transceiver. Since the term *noise* is often regarded synonymous with disturbances that are statistically independent from the signal, we will use the more general term *error* to subsume all unwanted disturbances affecting the effective SNR. This distinction between noise and error is important, because the statistical dependence of errors on the signal is a critical issue that complicates the measurement.

Measurement of inband error is certainly not a new topic. Popular communication standards like wireless LAN (WLAN) [62] or LTE [122] specify how to measure the inband error by means of the error vector magnitude (EVM). We briefly introduce the concept of EVM in Section 1.1.3, and highlight its advantages and disadvantages. Several alternative methods have been proposed that overcome specific disadvantages of EVM. A review of the state-of-the art of these methods in Section 1.2 leads to a formulation of open research questions, motivating the work presented in this thesis.

1.1.1 High Datarates Require High Bandwidth and SNR

In recent years, a rapidly increasing amount of data is exchanged wirelessly. Applications driving this trend are for instance digital video streaming and cloud-based data services. In the near future, the internet of things, robots and smart devices, will gather and exchange more and more data and, therefore, will very likely push the demand for high data throughput even further. The achievable throughput is fundamentally limited by the channel capacity, an information-theoretic upper bound on the rate of information (in bits/second) that can be reliably transmitted over a communication channel [133]. Considering a bandwidth B in hertz, the Shannon-Hartley theorem states that the channel capacity C of an additive white Gaussian noise (AGWN) channel is

$$C = B \log_2(1 + \mathrm{SNR}) \tag{1.1}$$

where the signal-to-noise ratio (SNR) is the ratio of the signal power P_S to the noise power P_N, i.e., $\mathrm{SNR} = P_S/P_N$. Hence, to increase the amount of data that can be exchanged, both the SNR and the bandwidth can be increased. This fundamental relation is reflected in modern communication standards, e.g., for wireless local area networks (WLAN-11ac/ad/ax), digital video broadcast (DVB-T2), and mobile networks (4G/LTE and 5G). Compared to their predecessors, refined standards typically define modes that employ

1. Higher bandwidth
2. (Better) spatial selectivity, e.g., by beamforming or MIMO processing
3. Denser modulation, e.g., 1024-QAM instead of 256-QAM

Using higher bandwidth linearly increases the capacity according to (1.1). Beamforming can help to improve the SNR, because energy is transmitted to (or received from) the desired direction whereas other directions are suppressed. Similarly, if the wireless multipath channels from the transmit to the receive antennas are mutually uncorrelated, data can be split in several streams and their mutual interference can be cancelled. Such multiple-input-multiple-output (MIMO) processing allows to effectively use more than one channel in parallel [122, p.73]. The third point, using denser modulation, *requires* higher SNR. This is evident considering the following:

Digital communication systems send and receive data encoded into symbols. The set of different symbols is called the alphabet. In case of M-ary quadrature amplitude modulation (M-QAM), the alphabet consists of M different complex values. Denser modulation, i.e., a larger alphabet, allows to encode more bits per symbol, e.g., 8 bits for 256-QAM instead of 4 bits for 16-QAM. However, denser modulation requires a larger SNR to correctly assign noisy symbols to the correct transmitted symbol locations, because the symbol locations move closer together while the variance in the observed symbols remains constant. This is illustrated in Fig. 1.1. If transmitted symbols are incorrectly assigned, bit errors may occur. The bit error rate (BER) is the number

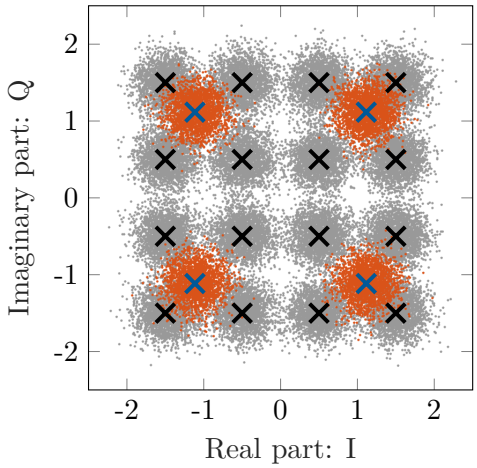

Figure 1.1: Constellation diagram for 16-QAM and QPSK (4-QAM) modulation. The crosses represent the true data symbols (ideally transmitted), whereas the cluttered dots indicate the received symbols in case of AWGN at an SNR of 28 dB. 16-QAM modulation requires a higher SNR to reliably assign the received symbols to the transmitted location.

of bit errors divided by the total number of transmitted bits. Since the information is transmitted within a frequency band $\mathcal{B}$ of finite bandwidth B, only noise within $\mathcal{B}$ increases the BER. Hence, the SNR above restricts to the *inband* SNR, i.e., the noise power is integrated only over the band $\mathcal{B}$.

To conclude, modern and future high-datarate systems require high inband SNR at high bandwidths. To achieve this, high-performance transmitter and receiver systems must be designed, which involves verification of the system's performance by means of measurements. The error vector magnitude (EVM) is the primary figure of merit to measure the inband performance at the system level. This thesis explores and evaluates new measurement methods to overcome specific drawbacks of regular EVM measurements.

1.1.2 Inband Error Caused by Transceiver Non-Idealities

Besides a noisy wireless channel, non-idealities of the transmitter and receiver impair the signal quality. Before we elaborate on the error introduced by these impairments, we briefly discuss a direct conversion (homodyne, zero-IF) transmitter and receiver (transceiver) based on the block diagram in Fig. 1.2. This structure is well-suited for high-level integration and is therefore widely-used in modern, integrated circuit designs [135].

The first block in the transmitter in Fig. 1.2 is a digital baseband processor that generates the signal (SIG GEN). Then, digital baseband pre-enhancement algorithms can be applied to reduce the detrimental effect of analog circuit impairments. For instance,

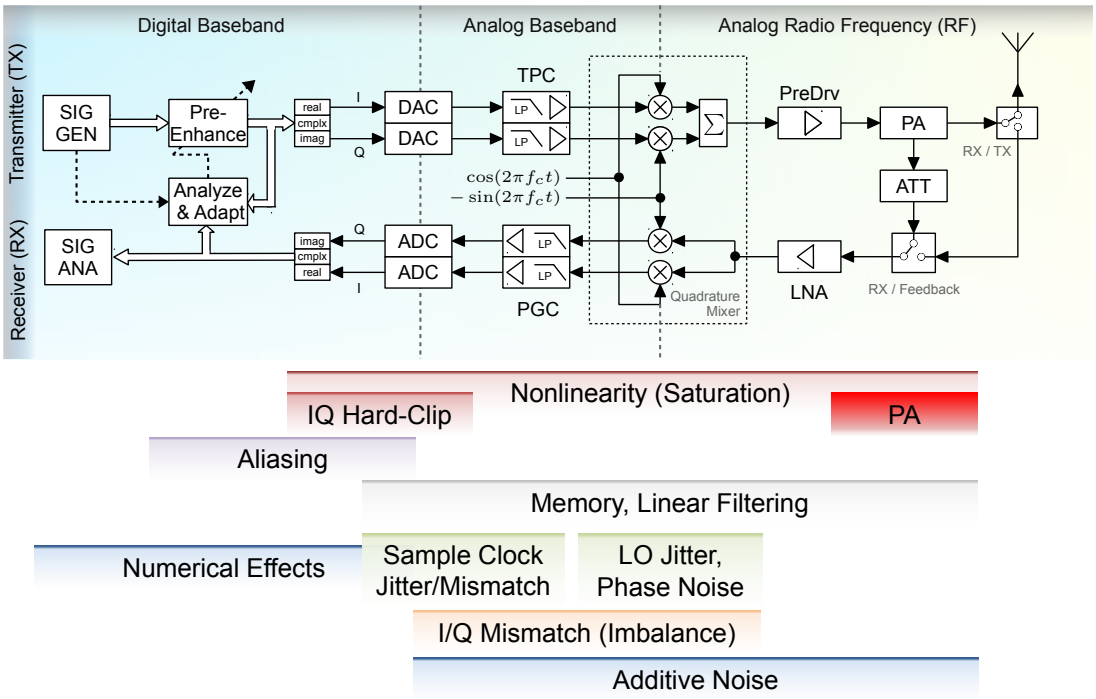

Figure 1.2: Zero-IF transceiver with typical impairments.

digital predistortion (DPD) and crest factor reduction (CFR) are two widely-used methods to improve the linearity-efficiency tradeoff inherent to power amplifiers (PAs) [29]. Digital-to-analog converters (DACs) convert the in-phase (I) and the quadrature (Q) component of the complex baseband signal from the digital to the analog domain. Low-pass filters may be employed to suppress unwanted images at the outputs of the DACs. In a homodyne transmitter, the quadrature mixer translates the baseband signal directly to the radio frequency (RF), e.g., $f_c = 2.4$ GHz or $f_c = 5.6$ GHz for WLAN. A programmable gain amplifier may be used to pre-drive (PreDrv) the input to the PA that usually features a fixed gain.

A single-die RF integrated circuit (RFIC) transceiver is typically a half-duplex system because the isolation of present semiconductors is not good enough to allow transmission and reception at same time [50, p. 142]. Therefore, the connection from TX and RX to the antenna is drawn with a switch in Fig. 1.2. Another switch indicates that it may be possible to feed back the PA output signal to the receiver instead of the antenna signal. This feedback is important for adaption of the DPD but may also be used for built-in self test of the transceiver. The structure of the receiver is essentially the inverse of the transmitter. First, a low noise amplifier (LNA) raises the RX signal to an appropriate level required for quadrature mixing. I- and Q-path low pass filters are required to remove images that occur in the mixing process. Programmable gain control (PGC) amplifiers set the level for the analog-to-digital converters (ADCs).

Typical transceiver impairments are shown related to the place of their emergence in Fig. 1.2. At higher output power levels, the nonlinearity of the PA is typically the dominant impairment in a transceiver. At lower levels, however, other impairments like additive noise, phase noise, or IQ imbalance may prevail. Frequency-dependent IQ imbalance occurs due to mismatches of the frequency responses of the analog I- and Q path. Frequency-independent IQ imbalance is caused by gain and phase mismatch of the I- and Q local oscillator (LO) in quadrature mixing. Random deviations of the LO oscillator frequency from its desired center f_c lead to phase noise. Section 2.2 discusses these impairments and their mathematical modeling in more detail.

While we understand additive noise to be independent from the signal, all other impairments listed in Fig. 1.2 introduce an error that is statistically dependent on the signal S. Denoting the impaired signal by Y, we have $Y = S + E(S)$, instead of $Y = S + N$ for the case of AWGN N. The dependence of the error E on the signal S makes inband error measurement much more difficult than measuring the SNR in case of additive noise. While additive noise can be measured when the signal is turned off, dependent errors usually vanish if the signal is turned off. More generally, the actual communication signal must be used for measurement to provoke the same error as during regular operation. In practice, it is often enough if the statistics of the test signal used for measurement resemble the statistics of the communication signal to predict the average behavior of the error, e.g., the power P_E of the inband error.

With the more general term inband error we also cover the special case of additive noise. A characteristic of the term *noise* is, that it implies randomness, whereas the inband error may also contain deterministic parts. Deterministic errors can be compensated for, e.g., by using a DPD in case of nonlinearity, or widely-linear equalizers to reduce the effect of IQ mismatch in a receiver [5]. However, also the effective error due to phase noise that is random in nature, can be reduced. The reason is that the error is dependent on the transmitted signal. By giving away part of the spectrum to pilot sequences known at the receiver, the common phase error, i.e., the slowly varying part of the phase noise, can removed by means of phase tracking.

In general, the inband error depends on the signal. Statistical dependence does, however, not necessarily go along with correlation. In fact, an equalizer removing the correlated part of the "error" is included in most wireless receivers. Error is written in quotes here because we may omit counting effects to the error that are removed by a standard receiver. In fact, such a definition of the inband error is very useful. If we define the error as $E = S - \hat{S}(Y)$, instead of $E = S - Y$, where $\hat{S}(Y)$ is the estimate of S obtained via correcting the received signal Y, the signal-to-inband error ratio

$$\mathrm{SNR}_E = P_S/P_E \tag{1.2}$$

allows to predict the BER during regular operation using a standard receiver. We also refer to SNR_E as the *effective inband SNR*. An important thing to note in this context is that not only a linear filter but also a static nonlinearity leads to a correlated "error", as explained by the Bussgang theorem [16] discussed in Section 2.2.3.

Besides causing inband error, nonlinearities also broaden the spectrum, which is often referred to as spectral regrowth [41]. Measurement of this out-of-band distortion is more straightforward than measurement of inband distortion, because the out-of-band distortion is separated from the signal (inband) in the frequency-domain. The difficulty specific to inband error measurement is the separation of the error from the erroneous signal, because the inband error and the signal share the same location in the time-frequency plane.

An obvious way to extract the error is to compute the difference between the transmitted and received data symbols, i.e., the (true) signal and the erroneous signal, respectively. This is the idea behind the error vector magnitude (EVM), as outlined in the following section.

1.1.3 Inband Error Measurement Methods

In the following, we briefly introduce two established inband error measurement methods that we refer to throughout this thesis, namely the error vector magnitude (EVM) and the noise power ratio (NPR).

Error Vector Magnitude (EVM)

The standard system-level metric for measuring the inband error is the error vector magnitude (EVM). In the EVM, the error is defined as the deviation of the estimated symbols $\{\hat{X}_l\}$ from the true data symbols $\{X_l\}$, as illustrated in Fig. 1.3a. The estimate $\{\hat{X}_l\}$ is obtained from the received (erroneous) symbols $\{\hat{Y}_l\}$ according to the standard, e.g., by applying equalization and de-rotation in WLAN. The EVM is the square root of the error vector power (EVP), which is defined as the the mean squared error (MSE) normalized by the mean squared signal power.

$$\mathrm{EVP} = \frac{\sum_l |X_l - \hat{X}_l|^2}{\sum_l |X_l|^2} = \frac{P_E}{P_S} = \frac{1}{\mathrm{SNR}_E} \tag{1.3}$$

Since the EVP is the inverse of SNR_E, the EVM in dB differs from the SNR_E in dB only by the sign. This direct relation to the effective inband SNR during regular operation, and thus to the achievable bit error rates [1], is a major reason for the popularity of EVM. Note that this simple relation to SNR_E only holds for data-aided EVM analysis, i.e., the true symbol locations (the test signal) is known in the analysis, which is assumed throughout this thesis. With non-data-aided analysis, the true symbol locations are obtained from quantizing the observed symbols towards the closest true symbol locations. Thus, the EVM is underestimated at high (bad) values [85], as soon as there are quantized symbols that do not equal the true transmitted symbols.

Although the principle of the EVM as outlined above is straightforward, measurement of the EVM is not a trivial task. The reason is that comparing measured with ideal

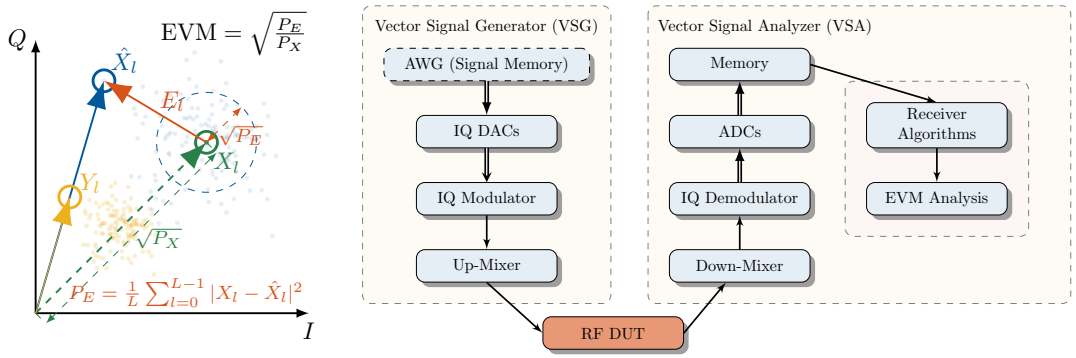

(a) Error Vector Definition

(b) EVM Measurement Setup

Figure 1.3: Principle of EVM measurements. (a) The equalizer scales the received symbols $Y_l = HX_l + E_l$ (yellow) by a factor of $1/H \in \mathbb{C}$ to obtain the symbol estimates X_l (blue). The EVM is the root mean square of the error $E_l = X_l - \hat{X}_l$, normalized by the RMS of the true reference symbols X_l. (b) A typical setup to measure the EVM of an RF DUT requires transmitter and receiver capabilities, which introduce errors, e.g., IQ mismatch, that may bias the measured EVM of the RF DUT. The required receiver algorithms and the EVM analysis routines are provided by dedicated software.

data symbols requires dedicated receiver algorithms when analyzing transmitters or RF devices like a power amplifier (PA). Implementing a receiver can be time-consuming because it requires in-depth knowledge of the particular standard. Commercial EVM analyzers are expensive and may not even be available at the time when developing next generation devices for upcoming communication standards. Furthermore, accurate synchronization between the ideal and the received time-domain signals is required, to avoid bias due to clock and frequency mismatches and drift.

An advantage of the EVM is that the same signal enhancement methods that are employed in receivers, e.g., equalization of linear channels and de-rotation of common phase errors, can be used for EVM analysis. Both equalization and de-rotation must be used for EVM measurements according to the 802.11ac WLAN standard [2].

Looking at the constellation can help when troubleshooting and searching for the prevailing source of error [69]. However, it is not possible to simply switch off the effect of one impairment, e.g., IQ mismatch, and get a quantitative EVM result without that impairment. Every source of error contributes to the result, also imperfect synchronization and receiver algorithms. This can be a critical issue when trying to measure an EVM of -50 dB and below. Another major limitation for the achievable EVM measurement floor is the required highly linear and low-noise measurement chain (including the ADCs of the receiver) over the whole signal bandwidth.

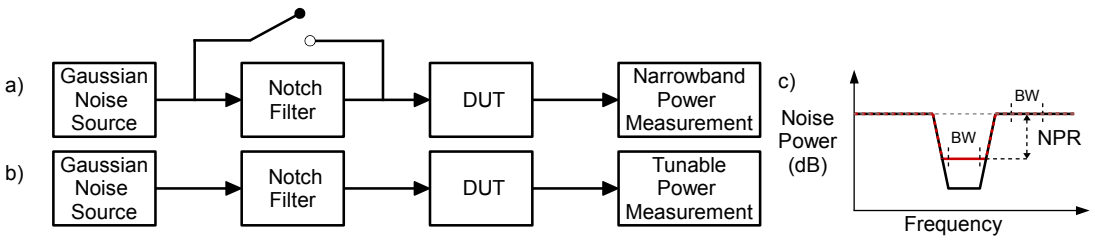

Figure 1.4: Principle of Noise Power Ratio Measurements

Noise Power Ratio (NPR)

The principle of traditional NPR measurements [68] is depicted in Fig. 1.4. A notch filter or band-stop filter is used to suppress a certain band of a Gaussian noise signal. The device under test (DUT) fills the notch with error power, e.g., due to intermodulation products caused by a nonlinearity. The NPR is defined as a signal plus noise to noise power ratio. The signal can be measured a) by bypassing the notch filter, or b) by measurement outside of the notch, whereas the noise power is measured inside the notch in both cases.

NPR measurements have some clear advantages over EVM measurements. As explained above, the EVM requires highly accurate wideband ADCs, IQ demodulation and dedicated receiver functionality. EVM measurements are hence expensive and limited at high bandwidths. The NPR overcomes these drawbacks because it only requires relative power measurements over specified frequency bands. Such measurements can be made with a swept-tuned spectrum analyzer, which is standard gear available in most RF labs. As outlined in Section 2.1.3, swept-tuned analyzers allow for a low noise floor even at very high signal bandwidths.

If the only source of error is additive white Gaussian noise (AWGN), the NPR is an unbiased estimate of the signal plus noise to noise ratio. Therefore, the NPR approaches the inverse of the EVP in (1.3) for the AWGN case. In other words, we have NPR $\approx$ $-$EVM (dB) for for high values of SNR. However, there are some well-justified scientific objections to using the NPR instead of the EVM for cases other than AWGN. Clearly, a test signal featuring a notch is different from a communication signal, which may be problematic as discussed above. Furthermore, the error is only observed within the stopband, which is only a fraction of the entire inband. There is research indicating that the NPR can significantly underestimate [47] or overestimate [108] the inband error due to a nonlinearity in certain cases. Section 4 of this thesis clarifies these objections and shows that is possible to estimate the EVM based on the principle of the NPR not only for AWGN but also for phase noise, IQ mismatch and nonlinearity.

1.2 Related Work and Motivation

The following Section 1.2 presents a literature overview of work related to this thesis. The goal is to outline the state of the art of inband error measurement and EVM estimation. Work relevant to specific topics and issues will be discussed later, directly in the respective context. Section 1.2.2 outlines research challenges which motivate this thesis' research question, formulated in Section 1.2.3.

1.2.1 Overview of Related Work

Many measurement methods exist for quantifying the signal distortion due to a nonlinear device. A good overview of classic measurements and metrics can be found in [18]. In the following review, we start with a brief introduction to these methods, but quickly advance to more recent state-of-the art methods for EVM estimation.

Using a single tone excitation with frequency f_0, the output of a nonlinear DUT may feature harmonic components at kf_0, $k \in \{1, 2, 3, \ldots\}$. The total harmonic distortion is defined as the ratio of the overall power at the higher harmonics to the power at the fundamental frequency. In transmitters, the higher harmonics are typically suppressed by proper RF design. However, the intermodulation distortion (IMD) that occurs in response to at least two tones cannot be suppressed in the same way, because it occurs in the same frequency-region as the excitation signal. For instance, a dual tone excitation at frequencies f_1 and f_2 leads to third-order intermodulation (IM3) products located at $2f_1 - f_2$ and $2f_2 - f_1$. If the two tones have similar frequency, e.g., $f_1 = 10$ kHz and $f_2 = 11$ kHz, the IM3 will be located close-by at 9 kHz and 12 kHz. The intermodulation ratio (IMR) is defined as the ratio between the fundamental power and the IMD output power. The output power where the extrapolated 1-dB/dB slope line of the DUT output fundamental power intersects the extrapolated 3-dB/dB slope line of the (third-order) IMD power is the third-order intercept point (IP3). The IP3 is popular due to its simplicity and is valuable for coarsely estimating the amount of nonlinear distortion. However, using the IP3 to predict the EVM is not advisable if the DUT features a more complex nonlinear behavior than a memoryless nonlinearity of third order.

Another classic concept to characterize nonlinear DUTs is the measurement of the AM-AM and AM-PM. These describe the baseband amplitude modulation (AM) and phase modulation (PM) in response to a modulation of the DUT baseband input amplitude [26], respectively. The AM-AM defines a memoryless model of the DUT. Adding the AM-PM extends the memoryless model to a so-called quasi-memoryless model [14, 31]. The prefix *quasi-* stems from the fact, that in order to have a non-zero AM-PM in baseband, the passband system must feature memory [110]. The standard approach for AM-AM and AM-PM measurements is to use a vector network analyzer (VNA) to measure the amplitude scalings and phase shifts in response to a single frequency excitation with discretely swept amplitudes. However, there are numerous

alternative methods for measuring AM-AM and AM-PM [131]. As outlined above a quasi-memoryless nonlinear model of the DUT can be extracted from measured AM-AM and AM-PM characteristics.

There are three ways to obtain an EVM estimate from a model of the DUT:

1. Analytic relation: The EVM is directly computed based on the model parameters, which requires that an analytic relation between EVM and the model parameters can be established.

2. Regression or machine learning: A direct mathematical relation between measured data and the desired quanitity (EVM) is established based on training data.

3. Simulation: The model is used in a simulation, and the standard EVM is analyzed based on the simulated DUT output.

During test, the first two options typically requires less computational power, since no EVM analyzer and baseband simulation are required. If a direct relation between EVM and the model can be established, as it is the case for AM-AM and AM-PM characteristics [95], it is therefore the preferred approach. Gharaibeh [46] fits a quasi-memoryless polynomial of order 5 from AM-AM AM-PM measurements. Orthogonalization of the model allows to separate the linear component from the uncorrelated higher order components. Although this is also possible for nonlinear behavioral models with memory, e.g., the Wiener model and Volterra filters [47], it does not seem practical. For accurate measurement of the parameters of these models, a synchronized baseband measurement setup is required. If such a system is available, it is probably easier to directly compute the regular EVM instead of estimating it based on an orthogonalized model.

All model-based methods share the same drawback: If the model is not powerful enough to model the DUT sufficiently well, the estimated EVM will be wrong. Particularly problematic is that the influence of the model mismatch on the EVM estimation error is typically not readily apparent and hard to estimate quantitatively. For higher bandwidth systems, where memory effects come into play, quasi-memoryless models as obtained from AM-AM and AM-PM measurements are typically not sufficient [74]. Frequency-dependent AM-AM and AM-PM can be measured using a dual tone signal, allowing to construct a memory polynomial model [74] of the DUT [134]. Still, the memory polynomial is just a simplified model of the true DUT behavior, leading to an unknown bias if used for EVM estimation as described above.

Model-based techniques are also used in the *alternate EVM testing* methods proposed by Abhijit Chatterjee's group at Georgia Tech [53, 98, 140]. They estimate the EVM based on nonlinear solvers [9, 54, 97, 132], and can be classified into the above-described regression category. Their main objective is to obtain binary decisions for detecting faulty devices during production with minimum test cost. This means that quick testing is crucial. Therefore, they use optimized multitone test signals [9, 54, 97, 132]. Another group working on EVM estimation for testing is Sule Ozev's group at Arizona State University [65, 94, 157]. In [158], they propose a built-in EVM measurement with

reduced DFT precision that allows for a pass/fail decision with low hardware overhead. In [2, 93, 96], they employ the analytic modeling approach. To be able to do so, they use quite simple models, e.g., a static third-order nonlinearity model. In [99], the DUT is a transmitter assumed to work in the linear region. Only phase noise and IQ mismatch model parameters are measured with a single-tone excitation. The EVM is computed from the measured model parameters via analytic relations. Webster *et al.* [152] describe built-in self tests of the DACs, the oscillator, and the gain and linearity of a WLAN transceiver system-on-chip. The correlation between the measured built-in self test parameters and the EVM allows for pass/fail testing.

Angrisani *et al.* proposed measurement methods for estimating the effect of IQ mismatch on the error vector of WCDMA and single-carrier QAM modulation [3], and for evaluating IQ-mismatch induced error in OFDM transmitters [4]. A frequency-independent IQ mismatch model is assumed and gain and phase mismatch parameters are estimated based algebraic relations [3] or least squares [4]. The algorithms are only tested with IQ mismatch added according to the used model. The influence of the presence of other transmitter impairments is not addressed. In a recent paper, Li *et al.* also use a frequency-independent IQ mismatch model, and additionally consider the influence of a linear channel when estimating IQ mismatch model parameters.

The class of DUTs where the EVM can be estimated accurately with a model-based technique is restricted to DUTs that are well fitted by the model. In typical testing applications this might not be a big issue, because the expected DUT behavior is typically well known and a working archetype of the DUT exists. In the design and prototype phase, however, this is not the case. Methods better suited for this application are discussed in the following.

The EVM can also be estimated based on a linear model of the DUT. The key difference to the model-based methods discussed above is the lack of a model assumption on the mechanism that causes the error we want to measure. Rather, the error is obtained by subtracting the linear model output from the DUT output. This corresponds to the behavior of a receiver, that also removes linearly correlated parts. There are numerous publications from Vrije Universiteit Brussel on the best linear approximation (BLA) to a nonlinear system, e.g., [119, 126, 127, 149]. Still, only recently they proposed to use BLA explicitely for EVM estimation [120]. A direct comparison of results obtained with their method and the standard EVM is however missing in [120] and in all earlier BLA papers. Furthermore their focus is only on nonlinear DUTs, the effect of phase noise and IQ mismatch is not mentioned.

The excitation signals for BLA are typically random-phase multitones approaching Gaussian amplitude statistics. The procedure proposed in [120, 149] is to make several measurements, e.g., 16 in [120], each with a different realization of the random multitone signal. While the linear (correlated) part of the DUT response Y_{BLA} is always the same, the stochastic nonlinear part and the independent additive noise are different for each realization. Consequently, the (inband) variance estimated over the different realizations is an estimate of the inband error power $P_{E_{\mathrm{ib}}}$. By synchronous

averaging over several measurements with identical excitation, the effect of additive noise can be separated from the error due to distortion. Such averaging has been applied to measurements of PA model fidelity [143] and for EVM measurements with a sampling scope [36]. In principle, any inband error measurement technique allows for synchronous averaging. Separating additive noise from signal-dependent contributions such as nonlinear distortion is therefore not a unique "ability of the (BLA) framework" [120]. In [42], properties of the NPR are discussed based on the BLA framework. BLA measurements using large signal network analyzers are presented in [119].

Lavrador, Carvalho and Pedro [80] use BLA based on cross-correlation to obtain the signal to noise and distortion (SINAD) ratio (SNDR) in the frequency-domain and define a noise and distortion figure as the ratio of the DUT input to the output SINAD. However, measurement results are missing in [80] and the connection to the EVM is not established. Pedro and Carvalho also proposed an inband distortion measurement method performing a coarse linear approximation [107, 108] based on analog feedforward cancellation. The same approach has been used later by Gharaibeh [45]. In contrast to BLA, where frequency-dependent gain and phase factors are modeled, only a scalar gain and phase factor is adjusted in analog feedforward cancellation. However, modern communication standard receivers remove the correlated parts up to a certain equalizer filter length [110]. The analog feedforward cancellation will therefore, in general, overestimate the EVM employing the standard equalizer. An advantage of feedforward cancellation in the analog domain is that demodulation and wideband ADCs are not required for signal analysis. Rather, the remaining RF error signal can be analyzed with a swept-tuned spectrum analyzer. In [154], Wilkerson, Gard, and Steer present a sophisticated automated feedforward cancellation measurement setup composed of highly linear amplifiers, RF sources, isolators, combiners, vector modulators, a vector signal analyzer, and four DACs. Their goal is to have enough dynamic range to assess passive intermodulation distortion. For a dual tone test signal the dynamic range is well below 100 dB. For a WCMA signal with 5 MHz bandwidth, however, only 45 dB are achieved.

Most of the above-described measurement methods do not take reflections into account, or implicitly assume matched conditions. For linear two-port networks, the relation between incident and reflect waves are quantified with the S-parameters. These are commonly measured with a vector network analyzer (VNA). To describe the amplitude and relative phase of harmonics of incident and reflected waves, nonlinear vector network analyzer (NVNA) and large signal vector analyzer (LSNA) measurements [88] are used. NVNAs and LSNAs are very expensive devices and require sophisticated calibration. Estimation of the EVM with an NVNA based on an irregularly-spaced multitone test signal is proposed in [79]. Since only the power of third- and fifth-order intermodulation products is measured to obtain the error in [79], the influence of noise and higher nonlinear orders on the EVM is implicitly neglected.

1.2.2 Research Challenges And Goals

This thesis presents new measurement methods to estimate the EVM, dealing with the following research challenges. These challenges can also be interpreted as goals of this thesis. They address weak points of the standard EVM and the alternative methods discussed in the previous section.

High Sensitivity at High Bandwidths: The bandwidth of modern, high-datarate communication signals has increased significantly in recent years. For instance, in WLAN, the maximum allocable bandwidth per channel increased from 20 MHz for the 802.11a and 802.11g standard in 1999, to 160 MHz for 802.11ac released in 2013. Due to the crowded spectrum in the GHz range, there is an increased interest in millimeter wave carrier frequencies. At extremely high frequencies (30-300GHz) there is space for bandwidths in the GHz-range. This implicates severe measurement challenges [114]. In general, the critical issue is that it is hard to design a measurement system with low noise and distortion at high bandwidths, e.g., -55 dB EVM at 160 MHz bandwidth. To allow 256-QAM transmission at a 5/6 code rate, the overall EVM must not exceed -32 dB according to the 802.11ac WLAN standard [62]. The design specifications for individual components of a transceiver can be significantly tougher than the targeted overall EVM, e.g., -45 dB. To have a bias less than $10\log_{10}(1.1) \approx 0.41$ dB, the measurement system must feature a noise floor at least 10 dB lower than the true EVM to be measured, i.e., high sensitivity is required. Having 10 dB margin is often used as a rule of thumb, e.g., in [72, p. 4].

Avoid Synchronization and Demodulation: Measurement of EVM is based on synchronized demodulation. Insufficient synchronization leads to a higher effective measurement floor which may bias the EVM result. Demodulation of the data symbols requires in-depth knowledge of the signal standard. Synchronization and demodulation of data symbols are key tasks of a receiver. Therefore, a key challenge with EVM is that a receiver with better performance than the DUT, e.g. a transmit DAC, must be available. This thesis presents methods to estimate the EVM that do not require synchronization and/or demodulation. Measuring EVM without demodulation makes it easy to adapt to new communication standards. Moreover, avoiding the need for synchronization eliminates a typical reason for a limited measurement floor.

Model-free Measurement: Model-based alternatives to EVM require the DUT to comply with an assumed or pre-trained mathematical model. If the DUT behaves differently than the assumed model, poor EVM estimates may be the consequence. In this thesis, we use models only to understand and simulate the properties of the presented EVM estimation methods. The proposed methods are however model-free, i.e., the analysis algorithms do not incorporate assumed DUT models.

Test Signal Similar to Communication Signal: The error introduced by typical transceiver impairments depends on the signal statistics. The only exception is addi-

tive noise. To estimate the performance during regular operation, the test signal statistics must be similar to the communication signal statistics. What *similar* means exactly depends on the DUT and is best judged by the estimation result. Certainly, a dual tone signal is too different from the communication signal for most DUTs. For the SLIC-EVM method proposed in Section 3.2, an unaltered communication signal can be used for testing. For measurements based on NPR (EPR, SWEEPR), however, the PSD (a second order statistic) must be altered to include a stopband. Still, we are able to estimate the EVM for a large class of DUTs with NPR-inspired measurements, as shown in Sections 4 and 5.

Simplicity and Use of Standard Gear: A key challenge and restriction imposed in this thesis is to keep things simple and devise methods that work with established gear that is available in most RF labs. For signal generation we will use a vector signal generator with arbitrary waveform generation (AGW) option. Instead of proposing new analysis front-ends or using less prevalent ones like NVNAs or LSNAs, we either use a swept-tuned analyzer or a VSA to capture the baseband signal. As a consequence, we do not track reflections and matching problems that can be detected with (nonlinear) vector network analyzer measurements. Rather, this thesis focuses on system-level performance measurements as indicated by standard EVM measurements. The potential influence of the connections and connecting cables is hence intrinsically tied to the DUT performance results. However, since NPR measurements can also be performed with VNAs [144], many of the ideas presented in this thesis may be valuable for VNA measurement setups as well, that allow for detection and compensation of matching problems.

Frequency Dependence of the EVM: Increasing the signal bandwidth makes it more likely that the inband error varies significantly over frequency. Typical EVM analyzers allow to display the EVM over frequency (subcarrier). In contrast to the traditional NPR, all methods proposed in this thesis are able to observe frequency-dependent error. However, with a single measurement of the EPR, the error can only be observed at a few selected subcarriers. The goal of the SWEEPR method presented in Section 5 is to overcome this limitation. A single SWEEPR measurement displays the error over all subcarrier frequencies.

1.2.3 Research Questions

The challenges and goals outlined above lead to the following research questions tackled in this thesis.

Is it possible to estimate the subcarrier-dependent error vector magnitude for typical transceiver impairments without assumed device under test models and without demodulation of the communication signal? Can this also be achieved without synchronization, with a standard power spectrum analyzer?

1.3 Scope, Contributions, and Outline

1.3.1 Scope

This thesis presents several inband error measurement methods that overcome specific disadvantages of error vector magnitude (EVM) measurements. The goal is to resemble the EVM result, but to do better in cases where EVM is biased by sources of error that we are not interested in, e.g. residual IQ mismatch and noise of the measurement setup. Further goals are simplicity, straightforward extensibility to new standards, and low cost. The presented methods are particularly suited for measuring the system-level performance of RF or mixed-signal devices in the laboratory, without the need for expensive EVM analyzers dedicated to the investigated signal standard. Furthermore, they could be useful in self-calibration of transceivers.

Although we focus on WLAN-OFDM signals, the presented methods should be applicable to other multicarrier modulation schemes as well. The only restriction is that methods based on the noise power ratio require (complex) Gaussian distributed signals. This thesis is focused on measurement of the error caused by non-ideal (components of) digital communication transceivers. However, the presented approaches may also be interesting for measuring the performance of nonlinear components operated without digital modulation, e.g., audio DACs and amplifiers.

The methods presented in this thesis are system level performance measurement methods that employ signal and spectrum analyzers. Like with standard EVM measurements, errors due to matching problems are seen as an implicit part of the DUT system and contained in the result. However, the methods and ideas presented in this thesis may be valuable for vector network measurement setups as well, which allow for detection and compensation of matching problems [144].

A way to increase the energy-efficiency of a PA is to turn the supply down whenever possible, and turn it up just before transmission. Due to transient behavior and thermal effects, the PA may respond differently in the steady-state when the data is transmitted, than it responds immediately after the power-up, during the preamble at the start of a package. This can lead to biased equalizer estimates, resulting in *dynamic EVM* values that are worse than static EVM values [159]. There are PA front-end-modules that already include thermal transient equalization to enhance the dynamic EVM [124]. No standard guideline how to measure dynamic EVM exists, and the results are dependent on the actual standard and equalizer implementation. Therefore, we limit our scope to estimation of the *static EVM*.

1.3.2 Contributions

The following list highlights some contributions of this thesis, grouped by topic or proposed method in the order of their appearance in this thesis.

EVM without IQ mismatch The EVM includes the effect of IQ mismatch. Section 3.1 presents a method that delivers not only an ordinary EVM result including potential IQ mismatch, but also an EVM result that is free from the effect of IQ mismatch. This can be helpful when troubleshooting transceivers and related components because the potential bias due to imperfect IQ calibration is visible and the result free from IQ mismatch is readily available. There are two main differences to standard data-dependent EVM measurements: First, symmetric null-subcarriers are inserted when generating the test signal, and second, the EVM analysis of the nulled and the modulated subcarriers is made separately.

Planned publication:

[A1] K. Freiberger, H. Enzinger, and C. Vogel, "A method to exclude IQ mismatch from multicarrier EVM measurements", *IEEE Transactions on Microwave Theory and Techniques*, pp. 1–6, 2017, planned submission.

SLIC-EVM: Section 3.2 presents an alternative to the EVM that also requires synchronized baseband samples, but has the advantage of being independent of the modulation scheme, because the signal is not fully demodulated. To obtain the error signal, the proposed SLIC-EVM method subtracts linearly correlated components (SLIC) from the DUT output signal. These components are obtained by fitting a linear FIR filter of the EVM equalizer length to model the DUT input-to-output behavior. The ratio between the error PSD and the FIR filter output resembles the frequency-dependent EVM in case of nonlinearity and IQ mismatch and phase noise. Furthermore, SLIC-EVM can be extended to mimic the effect of phase tracking in regular EVM analysis.

Related publication:

[A2] K. Freiberger, H. Enzinger, and C. Vogel, "SLIC EVM – Error vector magnitude without demodulation", in *89th ARFTG Microwave Measurement Conference*, Honolulu, HI, USA, Jun. 2017, pp. 1–4.

Direct Optimization of EVM and Spectrum Mask by Digital Predistortion: An application of the presented measurement methods is to use the EVM (estimate) as an objective when optimizing the systems performance, e.g., by means of digital predistortion (DPD). Section 3.3 presents a constrained, multi-objective optimization approach to DPD identification.

Related publication:

[A3] K. Freiberger, M. Wolkerstorfer, H. Enzinger, and C. Vogel, "Digital predistorter identification based on constrained multi-objective optimization of WLAN standard performance metrics", in *IEEE International Symposium on Circuits and Systems (ISCAS)*, Lisbon, Portugal, 2015, pp. 862–865.

Error Power Ratio (EPR): Section 4 reviews the noise power ratio (NPR) method and analyzes the effect of transmitter impairments on it. The presented analysis and

results reveal that measurements based on the principle of NPR can replace the EVM in many practically relevant cases. To distinguish our NPR-inspired EVM estimation method from the traditional NPR, we use the term error power ratio for the proposed method. Besides measurement results comparing the EPR with the EVM, Monte-Carlo simulation results confirm that the EPR resembles the EVM in various cases of combined IQ mismatch, phase noise, power amplifier nonlinearity impairments. We discuss sources of uncertainty and stress that a main limitation of the EPR is that the error should be smooth over frequency, because EPR measurements sample the error only at a certain number of stopbands.

Related publications:

[A4] K. Freiberger, H. Enzinger, and C. Vogel, "A noise power ratio measurement method for accurate estimation of the error vector magnitude", *IEEE Transactions on Microwave Theory and Techniques*, vol. 65, no. 5, pp. 1632–1645, 2017.

[A5] K. Freiberger, H. Enzinger, and C. Vogel, "The error power ratio estimates EVM for a wide class of impairments: Monte carlo simulations", in *Integrated Nonlinear Microwave and Millimetre-wave Circuits Workshop (INMMiC)*, Graz, Austria, 2017, pp. 1–3.

Swept Error Power Ratio (SWEEPR): The major limitation of the EPR is that a single measurement can only observe the error at the specified stopbands, and not over the entire inband. Section 5 presents an innovative method that overcomes this problem. The test signal is the communication signal of interest, filtered with a time-varying filter to obtain a time-dependent (linearly-swept) stopband location. Synchronizing a superheterodyne spectrum analyzer sweep to the stopband sweep allows for simple measurement of frequency-dependent errors with a measurement floor that is more or less independent of the analysis bandwidth.

Related publications:

[A6] K. Freiberger, H. Enzinger, and C. Vogel, "SWEEPR – The swept error power ratio for measuring the EVM with a spectrum analyzer", *IEEE Microwave and Wireless Components Letters*, pp. 1–3, Oct. 2017, submitted.

[A7] K. Freiberger, *Error Measurement Method Using a Time-Variant Stopband Test Signal*, US provisional patent application 62/476405, Intel Corporation, 2200 Mission College Boulevard, Santa Clara, California, 95054 USA, Mar. 2017.

Besides the work presented in this thesis, I also worked on digital pre-enhancement methods for WLAN transmitters during my time as a PhD student at TU Graz. This is reflected in several co-authored papers on nonlinear digital baseband modeling and predistortion [27–33]. These papers are consolidated in the PhD thesis of my colleague Harald Enzinger [26].

Author's Contributions

To clarify questions of copyright and to comply with my doctoral school's ethics, I, Karl Freiberger, declare my own contributions to each chapter of this thesis.

My advisor Christian Vogel contributed with helpful suggestions to the final wording and structure of this thesis, throughout all chapters.

As the title "Preliminaries" suggests, Chapter 2 mainly consists of a restatement of well-established concepts. My personal contributions are the selection of content, as well as its wording and presentation, including generation of all shown figures and related simulations. Some content and phrasing is taken from [A4], © 2017 IEEE. My contributions to [A4] are further outlined below.

Chapter 3 contains three different contributions. Section 3.1 contains recent, previously unpublished work. A publication [A1] is planned, as soon as we have conducted respective measurements. I have developed the idea and the contents exclusively by myself. Apart from an extended introduction, Section 3.2 presents and reproduces the content of [A2], © 2017 IEEE. I have developed the idea and most of the contents exclusively by myself, with suggestions and corrections by my co-authors from [A2]. Harald Enzinger also contributed to conducting the measurements. Section 3.3 presents and reproduces the content of [A3], © 2017 IEEE. I slightly modified and extended that content to better fit into this thesis. The wording of the text, as well as the preparation and analysis of the results are mainly my own contribution, while the idea and first proof of concept originated from Martin Wolkerstorfer. Harald Enzinger implemented large parts of the simulation framework used to integrate the optimization code that Martin Wolkerstorfer provided.

For Chapter 4, I modified and extended the content from [A4] and [A5], © 2017 IEEE, to better fit into this thesis. The original ideas and concepts, derivations, the wording of the text, as well as the preparation and analysis of the results in this chapter are almost exclusively my own contribution. Harald Enzinger coded large parts of the framework used to obtain the presented simulation and measurement results. Furthermore, he suggested the proposed stopband filter implementation. Besides contributions to the structure and wording of [A4], Christian Vogel first noticed the importance of the stopband integration bandwidth on the NPR. I am obliged to the editors of [A4], John Martens and Dominique Schreurs, for fruitful suggestions and several minor corrections.

Chapter 5 contains content I have developed almost exclusively by myself. I am the sole inventor of a patent application [A7] to protect some of the core ideas presented in this chapter. Besides the content submitted as a letter [A6], this chapter includes additional content, in particular in Section 5.3.

I have prepared the introduction in Chapter 1 and the conclusions in Chapter 6 exclusively for this thesis. However, some phrases from [A4] and [A2] may be contained.

1.3.3 Outline

This thesis is structured in 6 chapters. The first chapter contains the above introduction, concluded with this outline.

The second chapter presents preliminaries, i.e., established concepts needed in the subsequent chapters. More precisely, we investigate power spectral density measurement, transceiver impairment models, and the mathematical description of EVM for OFDM systems.

Chapter 3 incorporates three different original contributions: The first is an *extension* to the standard EVM allowing to exclude the effect of IQ mismatch from the EVM result. The second is SLIC-EVM, an *alternative* way to compute the EVM without demodulation. The third section presents an *application* of EVM or respective estimates, namely a digital predistortion identification scheme that directly optimizes the EVM and the spectrum mask given a power constraint.

In Chapter 4, the ability of the NPR to estimate the EVM is investigated in detail. This leads to a few modifications of the traditional NPR, motivating the new term error power ratio (EPR). Measurement results of a power amplifier and extensive Monte Carlo simulations show the viability of EPR to estimate the EVM if the frequency dependence of the EVM is gentle.

In Chapter 5, the EPR's limitation in case of heavily frequency dependent EVM is overcome by introducing the idea of sweeping the stopband center frequency continuously through the entire inband. The resulting measurement method is termed SWEEPR – the swept error power ratio. Besides the test signal generation, analysis, and methods to reduce the estimator variance, Chapter 5 presents simulation and measurement results corroborating the practicability of SWEEPR measurements to estimate subcarrier-dependent EVM.

Finally, Chapter 6 summarizes and concludes this thesis.

2
Preliminaries

This chapter[1] introduces and reviews established concepts required to understand the methods developed later in this thesis. After introducing the general notation used throughout this thesis, Section 2.1 reviews power spectral density estimation. To analyze and simulate the properties of the proposed measurement methods in case of typical transceiver impairments, mathematical models of these impairments are helpful. Section 2.2 presents such models. Finally, Section 2.3 reviews the EVM for OFDM signals, with particular focus on the 802.11ac WLAN standard.

2.1 Power Spectral Density

The power spectral density (PSD) is the basis for several transceiver performance metrics and measurements, including the EVM estimation methods proposed in this thesis. After introducing the mathematical notation used in the remainder of this section and throughout this thesis, Section 2.1.3 presents how PSD estimates can be computed and measured. We will focus on two approaches: First, we review Welch's PSD estimation method that is based on Fourier transform of time domain (TD) signal blocks. Second, we discuss measurements with a swept-tuned (ST) spectrum analyzer.

2.1.1 Notation

Let $x(t) : t \in \mathbb{R} \to \mathbb{C}$ denote a signal that may be either complex-valued or real-valued. Signals with a discrete domain are denoted with square brackets, e.g., $x[n] : n \in \mathbb{Z} \to \mathbb{C}$. In this thesis, $t \in \mathbb{R}$ represents the continuous time in seconds, whereas $n \in \mathbb{Z}$ is the discrete time index, i.e., $x[n] = x(nT_s)$, with the sampling period T_s. The sampling rate in hertz is given as $f_s = 1/T_s$.

By modulating a complex-valued baseband signal $\tilde{x}(t)$ to an angular carrier frequency $\omega_0 = 2\pi f_0$ we obtain a corresponding radio (RF) frequency signal

$$x_{\mathrm{RF}}(t) = \Re\{\tilde{x}(t)e^{j\omega_0 t}\} \tag{2.1}$$

[1] Some text and content presented in this chapter is reproduced from [A4], and [A2], © 2017 IEEE.

where $j^2 = -1$. The real and imaginary part of $\tilde{x}(t)$ are denoted by $\Re\{\tilde{x}(t)\} = \tilde{x}_I(t)$, and $\Im\{\tilde{x}(t)\} = \tilde{x}_Q(t)$, respectively. In cases where the distinction between baseband and RF is not of relevance, we simply use the notation $x(t)$. Bold symbols denote vectors e.g., $\boldsymbol{\omega} = [\omega_1, \ldots, \omega_N]^T$, where ^{T} denotes transposition. The notation $(\cdot)^H$ means Hermitian transposition, i.e., the vector is transposed and complex-conjugated. Complex conjugation is defined as $(x_i + jx_q)^* = x_i - jx_q$.

The cumulative density function (CDF) of a real-valued random variable (RV) X is the probability that X is less than or equal to x, i.e., $F_X(x) = P\{X \leq x\}$. The complementary CDF (CCDF) is given as $\overline{F}_X(x) = 1 - F_X(x) = P\{X > x\}$. Assuming an absolutely continuous CDF[2], the expected value of X is

$$\mathbb{E}\{X\} = \int_{-\infty}^{\infty} x f_X(x)\,\mathrm{d}x \tag{2.2}$$

where $f_X(x)$ is the probability density function (PDF)

$$f_X(x) = \frac{d}{\mathrm{d}x} F_X(x)\,. \tag{2.3}$$

X and Y are called uncorrelated if $\mathbb{E}\{X^*Y\} = \mathbb{E}\{X^*\}\,\mathbb{E}\{Y\}$. They are called orthogonal if $\mathbb{E}\{X^*Y\} = 0$. A random process $\{X_t\}$ is wide-sense stationary (WSS) if both its expected value and autocovariance do not depend on t [105]. Then, the expected value is

$$\mu_X = \mathbb{E}\{X_t\} \;\forall t \tag{2.4}$$

and the autocovariance is defined as

$$c_X(\tau) = \mathbb{E}\{(X_t - \mu_X)^*(X_{t+\tau} - \mu_X)\} \;\forall t\,. \tag{2.5}$$

A process $\{X_t\}$ is ergodic if estimates of the moments based on a realization $\{x(t)\}$ of the process $\{X_t\}$ converge in the squared mean to the respective ensemble moments. For ergodicity in the wide sense (WSS-ergodic), this requirement is relaxed to the first and second moment, i.e., the mean and the covariance. The mean of a WSS-ergodic process is

$$\mu_x = \mathrm{E}\{x(t)\} = \lim_{T\to\infty} \frac{1}{T} \int_{-T/2}^{T/2} x(t)\mathrm{d}t\,. \tag{2.6}$$

The crosscorrelation of two WSS-ergodic processes with realizations $\{x(t)\}$ and $\{y(t)\}$ is defined as

$$r_{xy}(\tau) = \mathrm{E}\{x^*(t)y(t+\tau)\} = \lim_{T\to\infty} \frac{1}{T} \int_{-T/2}^{T/2} x^*(t)y(t+\tau)\,\mathrm{d}t\,. \tag{2.7}$$

[2]The PDF exists only if the CDF is absolutely continuous, i.e., differentiable almost everywhere. Even if the PDF does not exist, the expected value may exist, since it can be defined as a Lebesque integral with respect to a probability measure.

The autocorrelation $r_x(\tau) = \mathrm{E}\{x^*(t)x(t+\tau)\}$ is defined analogously by replacing y with x in (2.7). If not stated otherwise, we assume all stochastic processes to be ergodic in the wide sense, so the ensemble moments of first and second order can be replaced by their sample counterparts. Above, we distinguished between upper case random variables X, a process $\{X_t\}$, its realization, i.e., the collection of all samples $\{x(t)\}$, and a single sample $x(t)$. In the remainder of this thesis we may use a more relaxed notation, if the clarity and brevity of the presentation benefit from it. For instance, we may simply write $\mathbb{E}(x^*y)$ instead of $\mathbb{E}(x^*(t)y(t))$ or $\mathbb{E}\{X_t^*Y_t\}$ to describe the crosscorrelation (at lag 0) of two realizations $\{x(t)\}$ and $\{y(t)\}$ of stochastic processes $\{X_t\}$ and $\{Y_t\}$.

We call two random signals $x(t)$ and $y(t)$ *dependent* if they are generated from random processes that are dependent. We say that two random signals $x(t)$ and $y(t)$ are uncorrelated if their covariance is zero, i.e., the cross-correlation must fulfill $r_{xy}(\tau) = \mu_x\mu_y \ \forall\tau$. Otherwise they are correlated. Orthogonality means $r_{ex}(\tau) = 0 \ \forall\tau$. In the literature related to this thesis, the terms "correlated" and "uncorrelated" are commonly used instead of "non-orthogonal" and "orthogonal" [42, 46, 80, 108]. If we neglect the mean, orthogonality and uncorrelatedness are equivalent. Neglecting the mean can be justified since the mean of communication signals is typically not used to carry information.

2.1.2 PSD Definition

The power spectral density (PSD) of a WSS-ergodic random signal $x(t)$ is [105]

$$S_x(\omega) = \int_{-\infty}^{\infty} r_x(\tau)e^{-j\omega\tau}d\tau\,. \tag{2.8}$$

We define the PSD in (2.8) as the Fourier transform of the auto-correlation function $r_x(\tau)$. However, as explained by the Wiener-Khinchin Theorem [141], the PSD may exist even if the Fourier transform does not exist, i.e., if the integral (2.8) does not converge. Similar to the PSD, the cross (power) spectral density of two WSS-ergodic random signals is the Fourier transform

$$S_{xy}(j\omega) \quad = \quad \int_{-\infty}^{\infty} r_{xy}(\tau)e^{-j\omega\tau}d\tau \tag{2.9}$$

of the cross-correlation in (2.7). The PSD is always real-valued, because the auto-correlation is Hermitian, i.e., $r_x(-\tau) = {r_x}^*(\tau)$, whereas $S_{xy}(j\omega)$ is complex-valued, in general.

The average power[3] of $x(t)$ within a frequency band described as a set of frequencies $\mathcal{K} \subset \mathbb{R}$ can be obtained by averaging the PSD of $x(t)$ over that band, i.e.,

$$\bar{S}_x(\mathcal{K}) = \frac{1}{\lambda(\mathcal{K})}\int_{\omega\in\mathcal{K}} S_x(\omega)\ \mathrm{d}\omega \tag{2.10}$$

where $\lambda(\mathcal{K})$ is the Lebesque measure of the set $\mathcal{K}$, i.e., the overall bandwidth of the integration. The set-based definition in (2.10) allows for concise notation of the average PSD of several non-adjacent subbands.

[3]To obtain a unit of power, we have to multiply the average PSD $\bar{S}_x(\mathcal{K})$ with the bandwidth $\lambda(\mathcal{K})$.

2.1.3 PSD Estimation

Since the PSD is defined upon a statistical expectation, it must be estimated in practice, when only a finite amount of time samples are available. Two methods for PSD estimation are outlined in the following. The first one, Welch's method, is a nonparametric method that is appropriate when we have access to a reasonable amount of time-domain samples of the random signal. Nonparametric methods make no assumptions on the generation of the observed samples other than wide-sense stationarity [25]. By contrast, parametric methods assume a model of the random process, leading to a small number of parameters to estimate. Hence, parametric methods have an advantage if the PSD must be estimated from a small number of observed samples [67], which is not the case in our application.

The second approach we use for PSD estimation is the classic measurement using a swept-tuned spectrum analyzer [73]. It is conceptually similar to Welch's method. The major difference is that instead of the discrete Fourier transform (DFT), analog frequency mixing and filtering is used. Consequently, swept spectrum measurements avoid the additional conversion from RF to digital baseband that is required for Welch's method. Avoiding the conversion excludes a potential source of bias to the PSD estimate. Furthermore, the PSD noise floor of swept measurements is independent from the bandwidth of the analysis. Therefore, swept-tuned measurements are particularly interesting for measurements that require high bandwidth and high SNR, which we identified as a key challenge for EVM measurements in Section 1.2.2.

There is, however, also a range of applications where Welch's method is advantageous for us: It is convenient for simulations, direct comparisons with EVM based on the same measured baseband data, or if DSP algorithms have to be applied prior to PSD estimation, as with the SLIC EVM method proposed in Section 3.2.

Welch's Method

Welch's method [153] for spectral density estimation is based on averaging periodograms. The periodogram is the squared magnitude of the Fourier transform of the windowed time-domain signal. Typically, Welch's method uses modified periodograms, which means that a window function other than rectangular is used. Welch's method divides the observed signal into a number of L potentially overlapping blocks, computes the periodogram for each block, and averages those periodograms.

In contrast to a single periodogram, Welch's method obtains an asymptotically consistent spectrum estimator [67]. We use Welch's method for PSD estimation based on a discrete time observation $x[n]$ of a random signal. The Welch PSD estimate can be written as

$$S_x[k] = \frac{1}{L} \sum_{l=0}^{L-1} X^*[k,l] X[k,l] \tag{2.11}$$

where $X[k,l]$ denotes the short time discrete Fourier transform of $x[n]$, defined as

$$X[k,l] = \sum_{n=0}^{N_a-1} w[n]x[n - lN_{\text{hop}}]e^{-j\frac{2\pi}{N_a}nk}. \tag{2.12}$$

Blocks of time samples are indexed by l, $k \in \mathcal{K} \subset \mathbb{Z}$ is the frequency index, N_a is the DFT length, $w[n]$ is a window function with support $0 \leq n < N_a$, and N_{hop} is the hop size that determines the overlap of the windows in time.

In practice, we must estimate the PSD from a finite-length observation of N_x baseband samples. Consequently, there is a trade-off between the DFT length resulting in a certain frequency resolution and the amount of averaging and hence the variance of the estimator [12, 13]. We define the frequency resolution as the spacing between two adjacent frequency points, i.e., $f_{\text{res}} = f_s/N_a$, where f_s is the sample rate. The resolution in the sense of the minimum frequency distance where two adjacent tones can be resolved as distinct is at least $2f_{\text{res}}$ and depends on the window function $w[n]$. A comprehensive overview of window functions for spectral analysis is given in [39].

Swept-Tuned Spectrum Analyzer Measurements

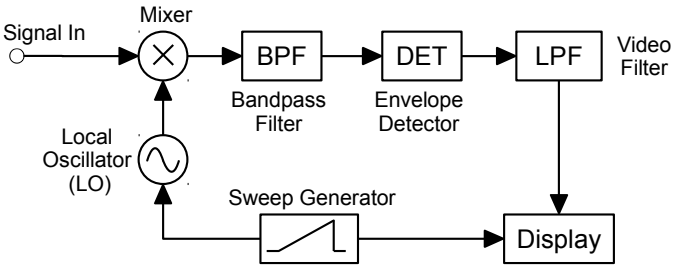

Figure 2.1: Principle of a swept-tuned analyzer.

Swept-tuned spectrum analyzers are classic laboratory equipment available in most RF labs. These analyzers are able to display signal power in dB over frequency by performing PSD estimation based on the superheterodyne receiver principle [73].

As indicated in Fig. 2.1, swept-tuned analyzers can tune into different analysis frequencies by changing the local oscillator (LO) frequency of the mixer. It is possible to tune to a fixed frequency in the *zero span* mode, or sweep the frequency linearly, by specifying the start frequency $f_{\text{sw,a}}$, stop frequency $f_{\text{sw,b}} \geq f_{\text{sw,a}}$ and a sweep time T_{sw} of the sweep generator. The start and the stop frequency can also be expressed in

terms of the sweep span f_{span} and the center frequency $f_{\text{sw,c}}$ as follows:

$$f_{\text{span}} = f_{\text{sw,b}} - f_{\text{sw,a}} \tag{2.13}$$

$$f_{\text{sw,c}} = \frac{f_{\text{sw,a}} + f_{\text{sw,b}}}{2} \tag{2.14}$$

$$f_{\text{sw,a}} = f_{\text{sw,c}} - \frac{f_{\text{span}}}{2} \tag{2.15}$$

$$f_{\text{sw,b}} = f_{\text{sw,c}} + \frac{f_{\text{span}}}{2}. \tag{2.16}$$

For a free-run sweep, at time t, the signal frequency mixed to IF, is

$$f_{\text{sw}}(t + T_0) = f_{\text{sw,a}} + f_{\text{span}} \operatorname{mod}(t, T_{\text{sw}})/T_{\text{sw}} \tag{2.17}$$

where $f_{\text{sw,a}} = f_{\text{sw}}(T_0)$ and $\operatorname{mod}(t, T) = t - \lfloor \frac{t}{T} \rfloor$ is the modulo function, which leads to a repeating sweep with period T_{sw} in (2.17).

After downmixing to the IF, the signal is filtered with a band-pass filter centered at the IF. This bandpass determines the resolution bandwidth (RBW) of the spectral analysis, because only components that pass through the filter enter the following envelope detector. Typical instruments offer several detector modes, including peak, sample and RMS detection. To minimize bias, an RMS detector should be used not only when measuring absolute power [11], but also when making power ratio measurements [142]. The output of the detector is further smoothed by a lowpass filter, the so-called video bandwidth filter.

Analyzers typically offer the following trigger modes to define when to start the sweep.

- *Trigger once* launches a single sweep. This mode is useful for automated measurements.
- *Free run* triggers a new sweep, as soon as the previous one ends. This is the standard mode when working hands-on with the instrument.
- *External trigger* starts a new sweep whenever there is a rising edge detected at the external input. Typically, there is also a trigger polarity switch and a trigger delay parameter. With the polarity switch, we can choose between triggering on positive or negative edges, whereas the delay allows to start the sweep the specified delay time after an edge is detected. The external trigger and trigger delay (or polarity switching) are key enablers for SWEEPR analysis with a swept-tuned analyzer, as outlined in Section 5.

By sweeping the whole bandwidth of the signal with a narrow RBW, it is possible to get PSD estimates similar to Welch's method. However, such a measurement can take a significant amount of time, e.g., 10 seconds, since the sweep time T_{sw} must be high if we sweep with a narrow RBW over a wide span f_{span}. The problem is that if we sweep too fast, the RBW filter output is not settled, since its rise time is inversely

proportional to its bandwidth. The shortest permissible sweep time is [82, p. 34] [73, p. 18]

$$T_{\mathrm{sw}} = C\frac{f_{\mathrm{span}}}{\mathrm{RBW}^2} \tag{2.18}$$

where $C \geq C_{\min}$ is a dimensionless constant. For Gaussian RBW filters, typical values are $2 < C_{\min} < 3$ [73]. The derivation of (2.18) is as follows: Since the time required to observe the whole span is T_{sw}, the time we have to observe a bandwidth RBW is $T_{\mathrm{RBW}} = \mathrm{RBW} \cdot T_{\mathrm{sw}}/f_{\mathrm{span}}$. The rise time of a filter is $C_{\min}/\,\mathrm{RBW}$. If we equate that rise time to T_{RBW} and solve for the sweep time T_{sw}, we obtain (2.18). Using a value $C \geq C_{\min}$ results in a higher sweep time and hence slower measurements, but typically yields more precise results.

2.1.4 Generating Random Signals with Given PSD

To simulate the effect of transmitter impairments like phase noise or additive flicker noise, we must be able to generate a realization of a noise process with a given PSD $S_v(f)$. This can be achieved with an inverse Fourier transform of a noise spectrum [135, p. 50]

$$V(f) = \sqrt{\frac{S_v(f)}{2}}e^{j\varphi(f)}\,. \tag{2.19}$$

The randomness comes from the phase, which is typically chosen to be uniformly distributed, i.e., $\varphi(f) \sim \mathcal{U}(0, 2\pi)$. To generate a real-valued signal $v(t)$, we must ensure that the spectrum is Hermitian, i.e., $V(f) = V^*(-f)$ [103].

2.2 Transceiver Impairment Models

This section discusses non-idealities of transmitters and receivers, with a focus on additive noise, phase noise, IQ mismatch and power amplifier nonlinearities. The presented mathematical models of these impairments help us to analyze and design EVM estimation methods. A good reference on analog transceiver impairment modeling is the book by L. Smaini [135].

Models can be established in the passband or in an equivalent complex baseband formulation. Passband models describe the system behavior given an RF input and an RF output signal, whereas baseband models additionally include an ideal up- and down-conversion from baseband to RF and RF to baseband [31].

Depending on what results in a more concise description, we either use passband or baseband models. We use the passband representation to outline the basic behavior of nonlinearities, whereas IQ mismatch and phase noise baseband models are described in the analog baseband. For simulations, digital baseband models are best suited.

2.2.1 Additive Noise

The signal model for additive noise is

$$y(t) = x(t) + v(t) \tag{2.20}$$

where $x(t)$ denotes the signal and $v(t)$ the noise. The auto-correlation and the PSD of the noisy signal $y(t)$ in (2.20) are

$$r_y(\tau) = r_x(\tau) + r_{xv}(\tau) + r_{vx}(\tau) + r_v(\tau) \tag{2.21}$$
$$S_y(\omega) = S_x(\omega) + S_{xv}(j\omega) + S_{vx}(j\omega) + S_v(\omega)\,. \tag{2.22}$$

If the noise $v(t)$ is orthogonal to $x(t)$, the cross terms vanish, and we obtain

$$r_y(\tau) = r_x(\tau) + r_y(\tau) \tag{2.23}$$
$$S_y(\omega) = S_x(\omega) + S_v(\omega)\,. \tag{2.24}$$

Different types of noise can be distinguished depending on the origin of the noise, the shape of the PSD, and the PDF. Johnson-Nyquist noise is also known as thermal noise, because it is due to thermal movement of the charge carriers inside an electric conductor. Thermal noise is approximately white Gaussian, i.e., its PSD is constant and the PDF is Gaussian. A fundamentally different kind of white noise is "quantization noise", because it is not independent from the signal. Although quantization is a nonlinear effect, the error due to quantization may be modeled as additive, uniformly-distributed, white noise uncorrelated with the unquantized signal. This additive noise model is adequate in our application, because our communication signal features a continuous PDF [86].

Flicker noise is another common noise-type in electronic devices. The PSD of flicker noise is inversely proportional to frequency ($1/f$-noise or pink noise). Besides appearing as additive noise, thermal and flicker noise occurring in oscillators leads to phase noise.

2.2.2 Phase Noise

Phase noise occurs due to jitter, i.e., random fluctuation, of the local oscillator (LO) frequency of an analog mixer. Ideally, the LO produces only a single frequency f_c, i.e, the PSD is a Dirac distribution. Due to the practically inevitable jitter, however, the LO frequency is varying, which leads to a "skirt" around the desired frequency, as illustrated in Fig. 2.2.

The LO is typically controlled by a phased looked loop (PLL). A double sideband PLL phase noise model is [135]

$$L(f) = \frac{B_{\mathrm{PLL}}^2 L_0}{B_{\mathrm{PLL}}^2 + f^2}\left(1 + \frac{f_{\mathrm{corner}}}{f} + L_{\mathrm{floor}}\right) \tag{2.25}$$

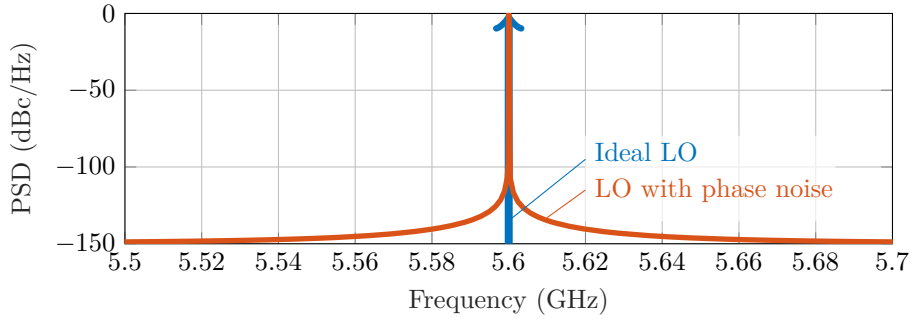

Figure 2.2: PSD of a 5.6 GHz local oscillator (LO). Phase noise leads to a "skirt" around the desired LO frequency. The phase noise is modeled based on the profile depicted in Fig. 2.3.

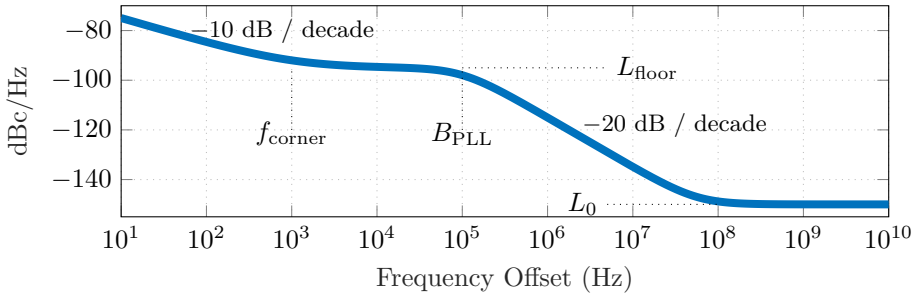

Figure 2.3: Phase noise profile model $L(f)$ according to (2.25), with $f_{\text{corner}} = 1$ kHz, $B_{\text{PLL}} = 100$ kHz, $L_0 = -150$ dB, and $L_{\text{floor}} = -95$ dB.

where $f > 0$ denotes the frequency offset from the carrier, B_{PLL} is the PLL -3 dB bandwidth and L_0 is the inband phase noise level in rad^2/Hz, f_{corner} is the flicker corner frequency, and L_{floor} the noise floor.

A baseband model for phase noise is given as [7, 135]

$$\tilde{y}(t) = \tilde{x}(t)e^{j\phi(t)} \approx \tilde{x}(t) + j\tilde{x}(t)\phi(t) \tag{2.26}$$

where $\phi(t)$ is the phase noise with PSD $S_\phi(\omega)$. The first-order Taylor series approximation in (2.26) is valid if $\phi(t) << 1$, which is a reasonable assumption for LOs in modern transceivers [135]. The PSD of $\tilde{y}(t)$ is hence

$$S_y(\omega) \approx S_x(\omega) + (S_x * S_\phi)(\omega) \, . \tag{2.27}$$

In (2.27), there is an additive error $S_{e,PN}(\omega) = (S_x * S_\phi)(\omega)$, i.e., the convolution of the signal and the phase noise PSD. This means that in contrast to (2.24), the additive error due to phase noise is statistically dependent on the signal $\tilde{x}(t)$.

Depending on the bandwidth of $S_\phi(\omega)$ compared to the OFDM subcarrier spacing Δ_f, two cases can be distinguished:

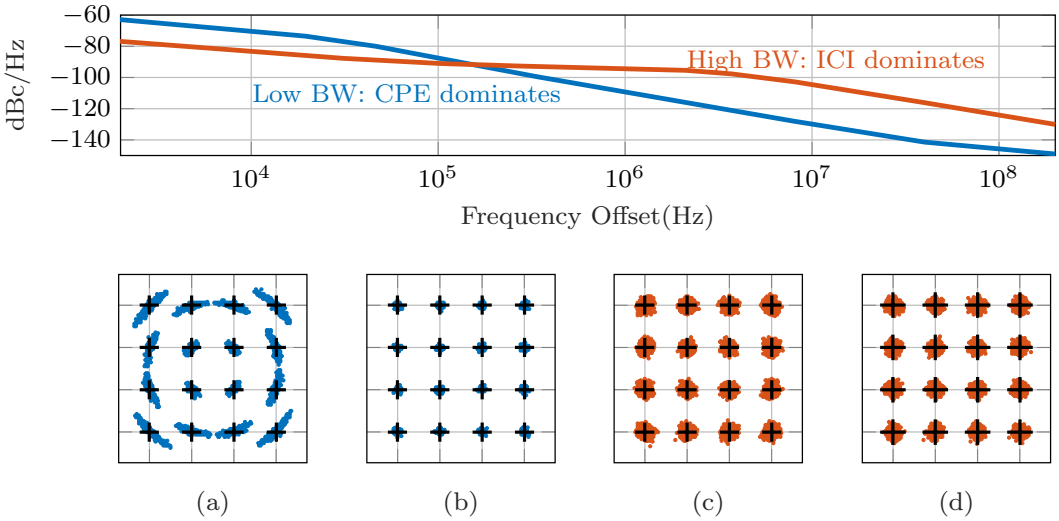

Figure 2.4: Constellations for an OFDM signal with 16-QAM subcarrier modulation for two different simulated phase noise profiles (top). The CPE dominating in (a) can be removed with de-rotation (b). Phase noise with high power at offset frequencies $f > \Delta_f/2$ leads to ICI (c), resulting in noisy-looking constellation. De-rotation (d) does not help in this case.

1. Inter-carrier interference (ICI) prevails if $\mathrm{BW_{PLL}} > \Delta_f/2$.

2. Common phase error (CPE) is dominant if $\mathrm{BW_{PLL}} < \Delta_f/2$.

In the time domain, the low-bandwidth phase noise leading to CPE corresponds to frequency variations that are slower than the OFDM symbol duration. These slow changes can be tracked by transmitting a pilot-sequence at a few subcarriers that is known at the receiver. Phase tracking is mandatory for EVM measurements according to the 802.11ac WLAN standard [62]. Since the whole symbol is rotated by the same common phase, phase tracking is also known as de-rotation.

In the frequency domain, the signal is convolved with the phase noise. Thus, phase noise components with higher bandwidth than $\Delta_f/2$ smear energy from one carrier to its neighbors, leading to ICI. For the CPE-dominated case, the phase of the constellation points varies randomly around the true point leading to the characteristic constellation shape exemplified in Fig. 2.4 (a), whereas for the case where ICI dominates, the constellation looks similar to additive noise. While the CPE can be mitigated by de-rotation as described above, it is very hard to remove ICI in a receiver [135]. This is illustrated in Fig. 2.4 (b) and (d), respectively.

2.2.3 Power Amplifier Nonlinearity

A key impairment in transmitters is the nonlinearity of the power amplifier (PA). The PA is typically the dominating contributor to the inband error, because the most energy-efficient operation is close to saturation, where the PA heavily distorts the signal. The importance of this tradeoff between linearity and efficiency [30] is reflected by the vast amount of work in the field of crest factor reduction and digital predistortion [51]. A detailed discussion on PA modeling can be found in [109, 130]. This section presents a short survey on concepts needed to understand the remainder of this thesis. After an introduction, we investigate the nature of the error introduced by a PA.

PA models can be categorized into three groups: white-box, grey-box, and black-box, depending on whether full, some, or no information on the internal structure of the PA is used in the model. White-, grey-, and black-box models are also known as physical, semi-physical, and behavioral models, respectively [111]. For our discussion, we restrict to behavioral models, because they are the most general. Furthermore, simple behavioral models like a third-order polynomial allow for an analytic description of the inband error. Many behavioral PA models feature static nonlinear functions connected by delay elements [109]. The delays are required to model memory-effects, which becomes increasingly important with increasing bandwidth.

An important class of behavioral models is based on the Volterra series [125] that is an universal approximator to causal, time-invariant nonlinearities with fading memory [15]. Since the number of parameters of a full Volterra series model grows exponentially with nonlinear order, pruned versions like memory polynomial (MP) [75] or generalized memory polynomial (GMP) [89] are more commonly used in practice. Another popular approach to obtain a reduced amount of parameters is to use two- or three-box models [44], e.g.,

- the Wiener model, where a linear filter precedes a static nonlinearity,
- the Hammerstein model, where a linear filter follows a static nonlinearity, or
- the Wiener-Hammerstein model, where the static nonlinearity is sandwiched between two linear filters.

While Volterra series, MP and GMP use polynomial basis functions to approximate the nonlinearity, also lookup tables and splines are popular for that purpose. Another way to model a static nonlinear block is based on an analytical description of the input-output behavior, as in Saleh's [123] or Rapp's [113] model.

Bussgang's Theorem and Best Linear Approximation

Bussgang stated and proved the following theorem in [16]: "*For two Gaussian signals, the crosscorrelation function taken after one of them has undergone nonlinear amplitude distortion is identical, except for a factor of proportionality, to the crosscorrelation*

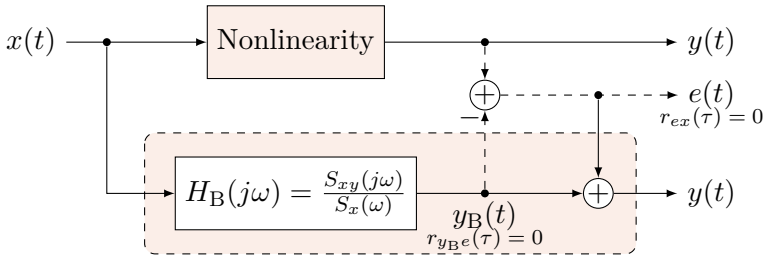

Figure 2.5: A nonlinear sytem can be replaced by a best linear approximation (BLA) $H_{\mathrm{B}}(j\omega)$ and an additive error source $e[n]$. The BLA depends on both the nonlinearity and the input signal. The error is orthogonal to the input signal $x(n)$ and to the BLA signal $y_{\mathrm{B}}(t)$.

function taken before the distortion". Using the notation introduced in Section 2.1.2, Bussgang's theorem reads

$$r_{xy}(\tau) = \alpha\, r_x(\tau) \tag{2.28}$$

where $x(t)$ and $y(t)$ denote the input and output of the static nonlinearity, respectively. Bussgang's theorem has been generalized to non-Gaussian but separable [102] signals, such as sinusoidal [128] and nonzero-mean nonstationary complex Gaussian [22] input signals and to systems with memory [34]. A closely related concept is the best linear approximation (BLA) to a nonlinear system [83, 112]. A good introduction is given in [128, Chap. 1].

For given input signal statistics[4] , e.g., $x(t) \sim \mathcal{N}(0, \sigma_x)$, a large class of nonlinearities[5] can be substituted by an LTI system $H_{\mathrm{B}}(j\omega)$ that is a best linear approximation (BLA) to the nonlinearity and an additive error signal that is orthogonal to the input signal. This is illustrated in Fig. 2.5.

According to the BLA framework, the output $y(t)$ of a nonlinearity with additive noise $v(t)$ at its output can be written as [42]

$$y(t) = \underbrace{y_0(t) + y_c(t)}_{y_{\mathrm{B}}(t)} + \underbrace{y_s(t) + v(t)}_{e(t)} \tag{2.29}$$

where:

- $y_0(t) = (h_0 * x)(t)$ is the output of the underlying LTI system with impulse response $h_0(t)$, which may be identified with a small-signal measurement to keep the DUT in the linear region.
- $y_{\mathrm{B}}(t) = (h_{\mathrm{B}} * x)(t)$ is the BLA of $y(t)$. The system $h_{\mathrm{B}}(t)$ is also called the related linear dynamic system [42] and depends both on the nonlinear system and on the input signal.

[4] within the Riemann equivalence class of asymptotically normally distributed input signals, which includes and random multisines and OFDM signals [128].

[5] including Volterra series [80], hard saturation and deadzone nonlinearities, but excluding chaotic systems and hysteretic systems [128, p.18].

- $y_c(t) = y_\mathrm{B}(t) - y_0(t)$ is the contribution correlated with the input $x(t)$ excluding the underlying LTI response.
- $e(t) = y_s(t) + v(t)$ contains the remaining distortion $y_s(t)$ and the noise $v(t)$. It can be obtained by removing the correlated part from the output signal, i.e. $e(t) = y(t) - y_\mathrm{B}(t)$.

The BLA of the nonlinear system is obtained by minimizing the mean squared error (MSE) $\mathbb{E}\left\{|y(t) - (h_\mathrm{B} * x)(t)|^2\right\}$. In the frequency domain, this yields [80]

$$H_\mathrm{B}(j\omega) = \frac{S_{xy}(j\omega)}{S_x(\omega)} \,. \tag{2.30}$$

Channel estimatation in receivers is usually performed in a similar way. An equalizer c_eq is obtained by inverting the channel estimate. If the input signal $x(t)$ is WSS and the nonlinear DUT is time-invariant during the time interval used of channel estimation and equalization, the equalized DUT output signal is

$$\begin{aligned} y_r(t) &= (c_\mathrm{eq} * (y_0 + y_c + e))(t) && \text{(2.31a)} \\ &= x(t) + (c_\mathrm{eq} * e)(t). && \text{(2.31b)} \end{aligned}$$

where (2.31b) assumes $c_\mathrm{eq}(t) * h_\mathrm{B}(t) = 1$. The correlated co-channel distortion component is equalized together with the linear frequency response. Only an equalized version of the uncorrelated noise and distortion remains in addition to the true signal $x(t)$. In [108], the goal was to measure the error including the correlated distortion. For our EVM estimation methods, however, an error definition that excludes correlated distortion seems more reasonable, since modern wireless receivers include equalizers that invert a linear channel estimate.

Memoryless Nonlinearity

In the following, we illustrate the above discussion on BLA and the error introduced by nonlinear systems with a simple example. Consider the third-order polynomial passband system

$$y_\mathrm{RF}^{(\mathrm{NL3})}(t) = c_1 x_\mathrm{RF}(t) + c_3 x_\mathrm{RF}^3(t) \,. \tag{2.32}$$

Assuming a Gaussian input signal $x_\mathrm{RF}(t)$, the autocorrelation function of (2.32) is given as [42]

$$r_y^{(\mathrm{NL3})}(\tau) = (c_1 + 3c_3 r_x(0))^2 r_x(\tau) + 6c_3^2 r_x^3(\tau) \,. \tag{2.33}$$

Relation (2.33) can be derived using the theorem for the average of products of Gaussian variables presented in [125, p. 217]. The PSD of the output signal is obtained by taking the Fourier transform of (2.33), which results in

$$\begin{aligned} S_y^{(\mathrm{NL3})}(\omega) &= (c_1 + 3c_3\sigma_x^2)^2 S_x(\omega) + 6c_3^2 S_{x,3*}(\omega) && \text{(2.34a)} \\ &= c_1^2 S_x(\omega) + 6c_1 c_3 \sigma_x^2 S_x(\omega) + 9c_3^2\sigma_x^4 S_x(\omega) + 6c_3^2 S_{x,3*}(\omega) && \text{(2.34b)} \end{aligned}$$

with the abbreviations

$$S_{x,3*}(\omega) = (S_x * S_x * S_x)(\omega) \tag{2.35}$$

and, presuming a zero mean distribution of $x(t)$,

$$\sigma_x^2 = R_x(0) \tag{2.36}$$

for the variance of the input signal. The convolution in (2.35) follows from the frequency convolution theorem [104, p. 27], i.e., a multiplication in the time domain transforms to a convolution in the frequency domain.

For an LTI system with additive uncorrelated noise at its output, the PSD of the noisy output signal is [105]

$$S_y(\omega) = |H(j\omega)|^2 \, S_x(\omega) + S_v(\omega) \tag{2.37}$$

where $H(j\omega)$ is the frequency response of the LTI system and $S_v(\omega)$ is the PSD of the noise. By defining

$$H_{\mathrm{B}}(\omega) = c_1 + 3c_3\sigma_x^2 \tag{2.38}$$

$$S_e(\omega) = 6c_3^2 S_{x,3*}(\omega) \tag{2.39}$$

it is possible to write (2.34a) in the same way as the noisy LTI system in (2.37), i.e.,

$$S_y^{(\mathrm{NL3})}(\omega) = |H_{\mathrm{B}}(j\omega)|^2 \, S_x(\omega) + S_e(\omega)\,. \tag{2.40}$$

Before discussing the differences of the noisy LTI model and (2.40), we highlight their similarity: In both (2.37) and (2.40), the first term contains that part of the output signal that is correlated with the input, whereas the second term contains the remaining uncorrelated part. While for (2.37) this is evident since $S_v(\omega)$ was defined to be uncorrelated noise, it may be less intuitive for (2.40).

The best linear approximate to (2.32) in a mean square sense is $H_{\mathrm{B}}\, x_{\mathrm{RF}}(t)$, with

$$H_{\mathrm{B}} = \arg\min_{H} \left\{ \mathbb{E}\left(|y - Hx|^2 \right) \right\} = \frac{\mathbb{E}\,(x^* y)}{\mathbb{E}\,(x^* x)} \tag{2.41a}$$

$$= \frac{\mathbb{E}\left(x\left(c_1 x + c_3 x^3\right)\right)}{\mathbb{E}\,(|x|^2)} = \frac{c_1 \mathbb{E}\,(x^2) + c_3 \mathbb{E}\,(x^4)}{\mathbb{E}\,(|x|^2)} \tag{2.41b}$$

$$= \frac{c_1\sigma_x^2 + c_3 3\sigma_x^4}{\sigma_x^2} = c_1 + 3c_3\sigma_x^2 \tag{2.41c}$$

where (2.42) follows from the general definition in (2.41) using our third-order signal model in (2.32), using $x = x_{\mathrm{RF}}(t)$ and $y = y_{\mathrm{RF}}^{(\mathrm{NL3})}(t)$ for brevity. The result in (2.42) is obtained by assuming a zero-mean Gaussian input $x \sim \mathcal{N}(0, \sigma_x)$ for which $\mathbb{E}\,(x^4) = 3c_3\sigma_x^4$ [105, (5-75)]. The remaining term $e = y - H_{\mathrm{B}}x$ is uncorrelated to $x \sim \mathcal{N}(0, \sigma_x)$ because they are orthogonal, i.e.,

$$\mathbb{E}\,(x^*(y - H_{\mathrm{B}}x)) = \mathbb{E}\,(x^* y) - \mathbb{E}\left(x^* \frac{\mathbb{E}\,(x^* y)}{\mathbb{E}\,(x^* x)} x \right) = 0\,. \tag{2.42}$$

$H_{\mathrm{B}}(\omega)$ in (2.39) is independent of frequency because we have a memoryless nonlinearity. The crucial difference between $H(j\omega)$ in (2.37) and $H_{\mathrm{B}}(\omega)$ in (2.39) is that the latter depends on the power of the input signal σ_x^2. Furthermore, for (2.34a), we assumed a certain class of input signals, namely Gaussians. Certainly, a system that behaves differently for different input signals is not linear.

This paragraph focused on the error by a very simple memoryless system providing a good intuition on the error introduced by a nonlinearity. However, as outlined in the more general discussion on page 32, the theory of BLA holds for a large class of nonlinearities, e.g., Volterra series [80]. A nonlinearity with memory leads to a frequency-dependent BLA $H_{\mathrm{B}}(\omega)$ that depends on the input signal PSD $S_x(\omega)$, and not only on σ_x^2 as in the memoryless case.

2.2.4 IQ Imbalance

A baseband model for IQ mismatch is [5]

$$\tilde{y}(t) = (\tilde{x} * \alpha)(t) + (\tilde{x}^* * \beta)(t) \,, \tag{2.43}$$

i.e., $\tilde{x}(t) = \tilde{x}_I(t) + j\tilde{x}_Q(t)$ and its conjugate $\tilde{x}^*(t)$ are convolved with impulse responses (IRs) given as

$$\alpha(t) = 1/2 \left(\tilde{h}_I(t) + g e^{j\varphi} \tilde{h}_Q(t) \right) \tag{2.44a}$$

$$\beta(t) = 1/2 \left(\tilde{h}_I(t) - g e^{j\varphi} \tilde{h}_Q(t) \right) . \tag{2.44b}$$

Here, g is the mixer amplitude imbalance factor, φ the phase imbalance, and $\tilde{h}_I(t)$ and $\tilde{h}_Q(t)$ the IRs of the the in-phase and quadrature path of the D/A converter, respectively. The power spectral density (PSD) of (2.43) is

$$S_y(\omega) = |A(j\omega)|^2 \, S_x(\omega) + |B(j\omega)|^2 \, S_x(-\omega) \,, \tag{2.45}$$

where $A(j\omega)$ and $B(j\omega)$ are the Fourier transforms of $\alpha(t)$ and $\beta(t)$, respectively. If $|B(j\omega)| > 0$, there is IQ mismatch, and an excitation at ω_0 causes interference at the mirrored frequency $-\omega_0$. With $g = 1$, $\varphi = 0$, and $\tilde{h}_I(t) = \tilde{h}_Q(t)$, we have $|B(j\omega)| = 0$ and there is no mirror interference. In the Fourier domain, we have

$$Y(j\omega) = A(j\omega)X(j\omega) + B(j\omega)X^*(-j\omega) \tag{2.46}$$

If we use an equalizer that inverts a linear MMSE channel estimate (the BLA), we have

$$Y_r(j\omega) = C_{\mathrm{eq}}(j\omega)Y(j\omega) \approx X(j\omega) + \underbrace{\frac{B(j\omega)}{A(j\omega)} X^*(-j\omega)}_{E(j\omega)} \tag{2.47}$$

By defining the image suppression ratio

$$G_{\mathrm{ISR}}(\omega) = \left| \frac{B(j\omega)}{A(j\omega)} \right|^2 \tag{2.48}$$

the PSD of the received (equalized) signal can be written as

$$S_{y_r}(\omega) = S_x(\omega) + \underbrace{G_{\mathrm{ISR}}(\omega) S_x(-\omega)}_{S_e(\omega)} \tag{2.49}$$

The frequency-dependent inband error[6] as quantified by the EVM is

$$\frac{1}{\mathrm{SNR}_E(\omega)} = \frac{S_e(\omega)}{S_x(\omega)} = \frac{G_{\mathrm{ISR}}(\omega) S_x(-\omega)}{S_x(\omega)} \tag{2.50}$$

If the source signal is constant within the inband $\mathcal{W}_p$, we have $S_x(\omega) = S_x(-\omega)\ \forall \omega \in \mathcal{W}_p$, and hence, the EVM due to IQ mismatch only depends on $G_{\mathrm{ISR}}(\omega)$ and is independent of the source signal x.

In exemplary simulations, e.g., Fig. 2.6, we use a simple discrete time IQ mismatch model specified by

$$\tilde{h}_I[n] = 0.98\delta[n] + 0.02\delta[n-1] \tag{2.51a}$$
$$\tilde{h}_Q[n] = 0.94\delta[n] + 0.06\delta[n-1] \tag{2.51b}$$
$$g e^{j\varphi} = 1.01 \cdot \exp\left(\pi j 2\pi / 360\right) \tag{2.51c}$$

where $\delta[n]$ is the delta impulse sequence, i.e., we use two-tap FIR filters to model frequency-dependent mismatch of the DAC's I- and Q-path, a gain imbalance factor $g = 1.01$ and π degree phase imbalance.

[6] We stick to the general term error to signal ratio SNR_E introduced in the introduction. However, the more common term signal to inference ratio (SIR) is also appropriate, since the error due to IQ mismatch is deterministic.

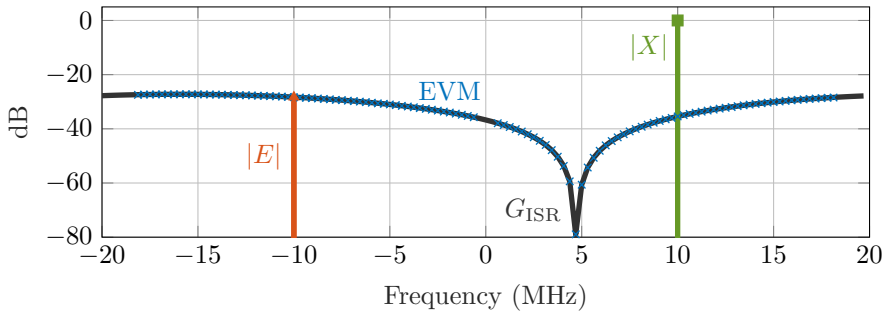

Figure 2.6: IQ mismatch simulation at $f_s = 40$ MHz sample rate using the model in (2.51). A single tone X at 10 MHz results in an image component E at -10 MHz. The power of the image is defined by the image suppression ratio $G_{\mathrm{ISR}}(\omega)$. Depicted is $G_{\mathrm{ISR}}(f_k)$ computed as the ratio of the DFTs of $\beta[n]$ and $\alpha[n]$ according to (2.51) and (2.44). The EVM is estimated based on a simulation with a 20-MHz OFDM signal. Since the inband is flat, the EVM coincides with G_{ISR}.

2.3 Error Vector Magnitude for OFDM Systems

We already introduced the principle of the EVM in 1.1.3. This section provides a slightly more formal definition tailored to the WLAN OFDM signals this thesis focuses on.

2.3.1 Orthogonal Frequency-Division Multiplexing

OFDM is a multicarrier modulation scheme used in communication standards like WLAN [62] and LTE [122]. Reasons for the popularity of OFDM are are its spectral efficiency due to the overlap of orthogonal subcarriers, its robustness to narrowband interference and fading, and its straightforward implementation based on the fast Fourier transform (FFT). As long as the channel impulse response is shorter than the cyclic prefix, intersymbol interference due to a linear channel can be avoided, because a linear filter can be equalized by multiplying the received signal with the inverse of a channel estimate in the frequency domain. If the impulse response is longer than the cyclic prefix, the channel estimate will be biased due to cyclic convolution artifacts involved with the multiplication or division in the FFT domain [103].

The main drawbacks of OFDM are its sensitivity to frequency and phase offsets and timing errors [135, p.14], and the high crest factor, also known as peak to average power ratio (PAPR). The PAPR is high due to the summation over many orthogonal complex exponentials. Since the data spread onto the subcarriers can be modeled as independent random variables, a baseband OFDM signal approaches a complex Gaussian distribution, due to the central limit theorem. The subcarrier modulation and coding scheme (MCS), e.g., whether QPSK or 16-QAM is used, does not affect the distribution.

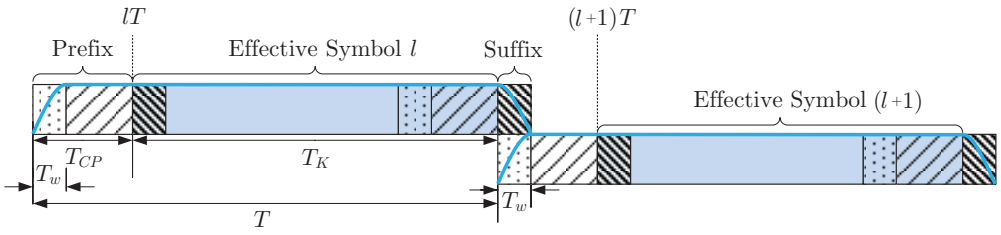

Figure 2.7: Two consecutive OFDM symbols with a windowed overlap in the time domain.

Mathematically, a baseband OFDM signal $s(t)\colon \mathbb{R} \to \mathbb{C}$ can be written as

$$\tilde{s}(t) = \sum_{l \in \mathcal{L}} \tilde{s}_l(t - lT) \tag{2.52}$$

where $T = T_g + T_K$ is the symbol duration consisting of guard (cyclic prefix) time T_g and effective symbol time T_K [155]. The symbol index set $\mathcal{L}$ is a connected set of integers. Unless otherwise stated, we assume $\mathcal{L} = \{0, \ldots, N_L - 1\}$. The lth OFDM symbol is given as

$$\tilde{s}_l(t) = w(t) \sum_{k \in \mathcal{K}} S[l,k] e^{j\frac{2\pi k}{T_K}t} \tag{2.53}$$

where $w(t)$ is a window function with finite support $-T_g \leq t < T_K + T_w$ fulfilling $\sum_{l \in \mathbb{Z}} w(t - lT) = 1$ [155]. The overlap $T_w : 0 \leq T_w \leq T_g$ between consecutive OFDM symbols allows for spectral shaping, i.e., instead of a hard transition between consecutive symbols there is a smooth fade, as illustrated in Fig. 2.7.

The window function $w(t)$ and the associated overlap time T_w are not standardized. A reasonable choice is $T_w = 100$ ns and a flat-top raised cosine window $w(t)$ given as

$$w(t) = \begin{cases} \frac{1}{2}\left(1 - \cos\left(\pi(t + T_g)/T_w\right)\right), & \text{if } t \in \mathcal{T}_1 \\ 1, & \text{if } t \in \mathcal{T}_2 \\ \frac{1}{2}\left(1 + \cos\left(\pi(t - T_K)/T_w\right)\right), & \text{if } t \in \mathcal{T}_3 \end{cases} \tag{2.54}$$

with

$$\mathcal{T}_1 = \{t \in \mathbb{R} : -T_g \leq t < -T_g + T_w\} \tag{2.55}$$

$$\mathcal{T}_2 = \{t \in \mathbb{R} : -T_g + T_w \leq t < T_K\} \tag{2.56}$$

$$\mathcal{T}_3 = \{t \in \mathbb{R} : T_K \leq t < T_K + T_w\}\ . \tag{2.57}$$

$S[l,k]$ in (2.53) is a complex-valued {data, pilot, null} constellation symbol modulated on the kth subcarrier of the lth OFDM symbol. The set of subcarriers $\mathcal{K} =$

BW (MHz)	N_K	Used Subcarriers $\mathcal{S} = \mathcal{D} \cup \mathcal{P}$	N_D	Pilot Subcarriers $\mathcal{I}$	N_I	N_U
20	64	$\pm\{1, \ldots, 28\}$	52	$\pm\{7, 21\}$	4	8
40	128	$\pm\{2, \ldots, 58\}$	108	$\pm\{53, 25, 11\}$	6	14
80	256	$\pm\{2, \ldots, 122\}$	234	$\pm\{103, 75, 39, 11\}$	8	14
160	512	$\pm\{6, \ldots, 126, 130, \ldots, 250\}$	468	$\pm\{25, 53, 89, 117, 139, 167, 203, 231\}$	16	28

Table 2.1: IEEE 802.11ac subcarrier set-up [62]

$\{-N_K/2, -N_K/2 + 1 \ldots, N_K/2 - 1\}$ may be divided into disjoint subsets for data carrying, pilot, and unused (null) tones $\mathcal{D}$, $\mathcal{I}$, and $\mathcal{U}$, respectively. The associated cardinalities are N_D, N_I and N_U, respectively, with $N_K = N_D + N_I + N_U$. Table 2.1 lists the respective values for the 801.11ac WLAN standard [62]. The subcarrier spacing in WLAN is $\Delta_f = 312.5$ kHz, leading to $T_K = 1/\Delta_f = 3.2$ µs. The guard interval $T_g = T_K C_g$ with the standard guard length factor of $C_g = 1/4$, we have $T_G = 0.8$ µs. Consequently, a WLAN OFDM symbol is $T = T_K + T_G 4$ µs long.

The data symbols $\{S[l,k] : k \in \mathcal{D}\}$ are complex values selected from the alphabet. For instance, with M-QAM as the subcarrier modulation format, each data symbol is represented by one of the M possible constellation points in the I-Q plane. This was already discussed in the introduction and illustrated in Fig. 1.1. In practice, the OFDM modulation in (2.53) is implemented via an inverse fast Fourier transform (IFFT) and the rear part of the effective symbol is copied to the front to obtain the cyclic prefix.

2.3.2 Error Vector Magnitude

The demodulated DUT output constellation symbols are given as

$$Y[l,k] = \frac{1}{T_K} \int_{t=lT}^{lT+T_K} y_s(t) e^{-j\frac{2\pi k}{T_K}(t-lT)} \, \mathrm{d}t \,, \tag{2.58}$$

where $y_s(t)$ indicates that the DUT output $y(t)$ must be synchronized to $s(t)$. For instance, a potential (fractional) time-delay must be compensated, e.g., with the method discussed in [26, 27]. By inserting $s(t)$ instead of $y_s(t)$ in (2.58), we certainly obtain the source data symbols $S[l,k]$, as shown in Appendix A.2. In practice, the FFT is used to compute $Y[l,k]$ from $y_s[n]$.

Error Definition

The constellation symbol error is defined

$$E[l,k] = Y_c[l,k] - X[l,k] \,, \tag{2.59}$$

where $Y_c[l,k]$ is a corrected version of $Y[l,k]$, and $X[l,k]$ is the error-free reference. In data-aided EVM analysis, the symbols $X[l,k]$ are the known, true source symbols, i.e., $X[l,k] = S[l,k]$. The required processing to obtain $Y_c[l,k]$ from $Y[l,k]$ corresponds to the signal enhancement facilities of a receiver: To remove linear filtering effects, a frequency-dependent equalization factor $C_{\mathrm{EQ}}[k] \in \mathbb{C}$ is introduced. Potential degradation due to a common phase error (CPE) is combated using a symbol-dependent phase de-rotation factor $C_{\mathrm{CPE}}[l] \in \mathbb{C}$. With that, the observed constellation symbol enhanced by equalization and phase tracking is given as

$$Y_c[l,k] = C_{\mathrm{EQ}}[k]\, C_{\mathrm{CPE}}[l]\, Y[l,k]\ . \tag{2.60}$$

EVM measurements according to the WLAN standard must use an equalizer obtained by inverting a channel estimate, which is commonly referred to as zero-forcing. As outlined in Appendix A.1, a linear channel estimate that is optimal in the least squares sense is

$$\begin{aligned} \hat{H}[k] &= \underset{H[k]}{\arg\min} \sum_{l \in \mathcal{L}_{\mathrm{train}}} |Y[l,k] - H[k]X[l,k]|^2 \\ &= \frac{\sum_{l \in \mathcal{L}_{\mathrm{train}}} X^*[l,k]Y[l,k]}{\sum_{l \in \mathcal{L}_{\mathrm{train}}} X^*[l,k]X[l,k]} \qquad (2.61) \\ &= \frac{\boldsymbol{X}_k^{\mathrm{H}} \boldsymbol{Y}_k}{\boldsymbol{X}_k^{\mathrm{H}} \boldsymbol{X}_k}\,. \qquad (2.62) \end{aligned}$$

Equation (2.62) introduces a compact inner product notation using $(L_{\mathrm{train}} \times 1)$ vectors to describe the summations over a set $\mathcal{L}_{\mathrm{train}}$ of a number of L_{train} OFDM symbols. In data-aided EVM estimation, all transmitted OFDM symbols are known and can be used for training, and hence $\mathcal{L}_{\mathrm{train}} = \mathcal{L}$. The zero-forcing equalizer based on inverting (2.62), is given as

$$C_{\mathrm{EQ,ZF}}[k] = \frac{\boldsymbol{X}_k^{\mathrm{H}} \boldsymbol{X}_k}{\boldsymbol{X}_k^{\mathrm{H}} \boldsymbol{Y}_k}\,. \tag{2.63}$$

Minimizing a mean squared error $\boldsymbol{E}_k^{\mathrm{H}} \boldsymbol{E}_k$, where $\boldsymbol{E}_k = \boldsymbol{X}_k - C_{\mathrm{EQ}}[k]\boldsymbol{Y}_k$, results in an equalizer

$$C_{\mathrm{EQ,MMSE}}[k] = \frac{\boldsymbol{Y}_k^{\mathrm{H}} \boldsymbol{X}_k}{\boldsymbol{Y}_k^{\mathrm{H}} \boldsymbol{Y}_k}\,. \tag{2.64}$$

Similarly, de-rotation coefficients to correct the common phase error (CPE) can be computed as

$$\begin{aligned} C_{\mathrm{CPE}}[l] &= \underset{C[l]}{\arg\min} \sum_{k \in \mathcal{K}_{\mathrm{train}}} |X[l,k] - C[l]Y_{\mathrm{c,EQ}}[l,k]|^2 \qquad (2.65) \\ &= \frac{\sum_{k \in \mathcal{K}_{\mathrm{train}}} Y^*_{c,\mathrm{EQ}}[l,k]X[l,k]}{\sum_{k \in \mathcal{K}_{\mathrm{train}}} Y^*_{c,\mathrm{EQ}}[l,k]Y_{c,\mathrm{EQ}}[l,k]} \qquad (2.66) \end{aligned}$$

with $Y_{c,\mathrm{EQ}} = C_{\mathrm{EQ}}[k]\, Y[l,k]$, meaning that equalization and de-rotation is performed sequentially, in contrast to finding the joint global optimum which would be much more involved. Furthermore, we implicitly assume an already compensated time-delay and frequency offset, which allows for simple least-squares optimization of the compensation parameters, whereas the joint determination of optimal compensation parameter values is a non-convex problem [64]. In WLAN 802.11ac, $C_{\mathrm{CPE}}[l]$ is estimated only from the pilot subcarriers in Tab. 2.1, i.e., $\mathcal{K}_{\mathrm{train}} = \mathcal{I}$. In a data-dependent measurement scenario, however, we are free to use all modulated subcarriers, i.e., $\mathcal{K}_{\mathrm{train}} = \mathcal{S}$, to improve the precision of the estimate.

To allow for synchronization and channel estimation in regular information transmission, a preamble known at the receiver is transmitted at the beginning of every frame. Since the so-called "training field" for channel estimation is short, e.g., only a two or three symbols in WLAN [62], an equalizer estimated only from the preamble is not very precise. Practical experience suggests that using an equalizer trained from only the preamble leads to EVM results up to 3 dB higher than the true EVM obtained with the data-dependent approach. Besides this imprecise "preamble only" equalizer, commercial WLAN EVM analyzers also offer a "preamble+data"[7] equalizer [70, 151] that is able to obtain the same result as the data-dependent approach and estimate the SNR correctly. This is illustrated in Fig. 2.8. In contrast to a true data-aided scenario, the transmitted symbols are not required for EVM analysis with the "preamble+data" equalizer. Rather, a two-step procedure is used. A first equalizer is estimated based on the preamble yielding a coarse estimate. Using this first equalizer, the constellation data is quantized to obtain the reference constellation. The true reference constellation can be fully recovered, if the EVM with the preamble-only EQ is good enough to avoid symbol errors. Having the true reference constellation, the equalizer can be trained again on the entire data field. Due to increased amount of averaging over time (OFDM symbols), the obtained "preamble+data" equalizer is more precise than the first, "preamble-only" equalizer. In case of a low EVM where no symbol errors occur, the "preamble+data" scenario yields the same results as the data-dependent approach that requires the known transmitted symbols. As soon as symbol errors occurs, however, the "preamble+data" approach underestimates the data-dependent EVM, due to the same reasons as described in [85].

EVM Definition

The mean constellation power over a set of subcarriers $\mathcal{C}$ with cardinality $|\mathcal{C}|$ is

$$P_{S_\mathcal{C}} \;=\; \frac{1}{|\mathcal{C}|} \sum_{k \in \mathcal{C}} P_S[k] \;, \tag{2.67}$$

[7] or "preamble+pilots+data"

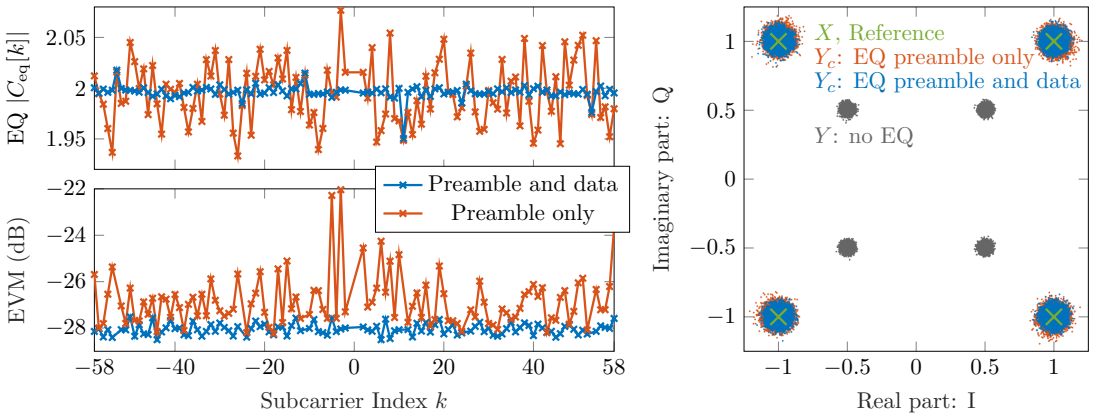

Figure 2.8: Simulation of EVM comparing two different equalizers (EQs). The source signal $\tilde{s}[n]$ is a 40-MHZ 802.11ac signal with 320 symbols and QPSK subcarrier modulation. A channel $H = 0.5$ with AWGN at an SNR of 28 dB leads to scaled, noisy constellation symbols $Y[l, k]$ shown in grey in the scatter plot on the right. Using only the preamble for channel estimation results in an EQ with high variance around the true value of 2 compared to the case where the data is also used for estimating the EQ. The average EVM over the data subcarriers is −26.67 dB for the preamble-only EQ, and −28.05 dB for data+preamble EQ.

where the tone-dependent power $P_S[k]$ is obtained by averaging over all L symbols, i.e.,

$$P_S[k] \quad = \quad \frac{1}{L} \sum_{l \in \mathcal{L}} |S[l, k]|^2 = \frac{1}{L} \boldsymbol{S}_k^{\mathrm{H}} \boldsymbol{S}_k \,. \tag{2.68}$$

The error vector power (EVP) is defined as the mean error power over all data tones $\mathcal{D}$ normalized by the respective reference constellation power.

$$\mathrm{EVP} \quad = \quad \frac{P_{E_\mathcal{D}}}{P_{X_\mathcal{D}}} \tag{2.69}$$

$$\mathrm{EVM} \quad = \quad \sqrt{\mathrm{EVP}} \tag{2.70}$$

If every constellation point occurs with the same probability, $P_{X_\mathcal{D}}$ is an estimate of the average constellation power, which is a constant for a given modulation format. In practice, for $N_l \geq 100$, $P_{X_\mathcal{D}}$ is more or less identical to the average constellation power. In any case, we use the exact value of $P_{X_\mathcal{D}}$ for computing the EVM. We see that EVP is defined as a power ratio. The difficulties and flaws of EVM come into play because for the error power $P_{E_\mathcal{D}}$, the demodulated symbols $Y_c[l, k]$ are needed as can be seen from (2.59). Consequently, accurate synchronization and equalization is required.

To inspect the distribution of the EVM over the subcarriers k, we define

$$\mathrm{EVM}[k] = \sqrt{\frac{P_E[k]}{P_{X_\mathcal{D}}}} \,. \tag{2.71}$$

The overall EVP in (2.69) is obtained by averaging the square of (2.71) over $k \in \mathcal{D}$.

3

EVM – Extension, Alternative, and Application

This chapter presents three different contributions related to the EVM.

- Section 3.1 investigates a new approach to exclude IQ mismatch from EVM measurements that requires only a minor extension of the OFDM signal generation and analysis routines. Section 3.1 contains recent, previously unpublished work. A publication [A1] is planned.
- Section 3.2 presents an alternative way of computing the EVM, without demodulation of the data symbols. Apart from an extended introduction, Section 3.2 reproduces the content of [A2], © 2017 IEEE, slightly modified to better fit into this thesis.
- Section 3.3 presents an application of the EVM: We optimize the EVM of a signal impaired by power amplifier nonlinearity in a direct way using a stochastic optimizer that identifies digital predistorter coefficients. Section 3.3 presents and reproduces content from [A2], © 2017 IEEE, slightly modified and extended to better fit into this thesis.

In this chapter we only deal with digital baseband signals. Therefore, to avoid double superscripts and improve the readability of the equations, we drop the superscript tilde that we introduced to tag baseband signals, i.e., in this chapter we write $x[n]$ instead of $\tilde{x}[n]$.

3.1 Excluding IQ Mismatch from EVM

This section presents a measurement method that delivers two different subcarrier-dependent EVM characteristics from a single measurement run. The first EVM characteristic resembles the standard EVM, i.e., it includes the effect of potential IQ mismatch. The second characteristics, on the other hand, is free from the effect of IQ mismatch. The method can be valuable in many practical measurement situations,

e.g., when the EVM performance is biased by residual IQ imbalance of the measurement chain, when trying to track down the source of limited EVM performance, or as a benchmark when assessing the performance of an IQ calibration scheme.

3.1.1 Problem Description

The standard EVM includes the error caused by various transceiver imperfections, e.g., additive noise, nonlinearity, phase noise, and IQ mismatch. On the one hand, this is a welcome property, leading to a strong correlation of the EVM with the overall system performance in terms of the bit error rate (BER) [52]. On the other hand, however, the mixing of errors caused by different types of impairments might be a drawback, since it is not possible to separate the contributions from different sources of error. This mixing is hence not desirable when looking for the reason of limited EVM performance. When measuring the EVM of an RF DUT, e.g., a power amplifier, the EVM contribution due to imperfect IQ modulation represents an unwanted bias to the true EVM of the DUT. Therefore, it is desirable to have the possibility to exclude potential IQ mismatch. Without requiring a calibration procedure, the method proposed in this section obtains both an EVM result excluding and including IQ mismatch from a single measurement run. Before introducing the proposed approach, we first review related IQ mismatch calibration and measurement methods.

As shown in Section 2.2.4, IQ mismatch leads to an error at frequencies mirrored to the excited frequencies, where the mirror axis is the carrier frequency of the IQ modulator. If there is no mirror-excitation at a subcarrier $-k_m$, there is no IQ mismatch at k_m. Moreover, if we have no excitation at two frequencies forming a symmetric pair around the carrier, there is no IQ mismatch present at both frequencies. This property can be used to exclude IQ mismatch from inband error measurements. In particular, it can be applied to the error power ratio (EPR) presented in Section 4. In a related paper on the EPR [A4], we claimed "this is not possible with EVM". Indeed, it is not possible with the regular EVM, but requires the extensions to the signal generation and analysis proposed in this section. Using the EVM instead of the EPR is advantageous in the case when it cannot be ruled out that the error exhibits a strong frequency-dependency, a case where the EPR may be biased [A2].

IQ mismatch compensation and related measurement methods have been extensively studied in literature. However, many publications limit to frequency-independent IQ mismatch [3, 81, 148]. The objective of the measurement methods proposed in [3, 81] is to estimate IQ imbalance model parameters, e.g., gain and phase mismatch.

We have a different objective: We want to measure the EVM of RF devices and be *certain* that we do not have bias due to frequency-dependent IQ mismatch. We do not want to rely on the assumption that the transmitter and receiver required for EVM measurement of an RF device are calibrated so well that their EVM is below -50 dB over the entire bandwidth, e.g., 160 MHz in WLAN 11ac. Our objective is also different from the objective driving most publications on frequency-dependent IQ compensation

[5, 148]. They target at improving data-transmission, whereas our approach is only suitable for measurement purposes. Besides compensating the IQ mismatch, Anttila *et al.* also proposed the combination with nonlinear pre-distortion [6], whereas our goal is to not tamper with the nonlinear DUT behavior.

To mitigate the effect of IQ mismatch by means of pre- or post-compensation requires fitting a compensator model, e.g., a widely[1] linear FIR filter [5]. This requires assuming a certain filter length, and requires computational effort for fitting. The proposed method does not rely on a compensation scheme to *reduce* the IQ mismatch, but rather *precludes* it by an appropriate design of the test signal. In contrast to methods based on simple test signals like single- or dual-tones, we alter the test signal statistics only very little, which is important when characterizing nonlinear devices [106]. Besides the EVM characteristic excluding IQ mismatch, we also obtain the EVM including IQ mismatch. Both EVMs are obtained as a function of the data subcarriers, allowing to inspect the frequency-dependence of the error with and without IQ mismatch. To this end, we only require a minor modification of the standard EVM test signal generation and analysis routines. The measurement setup is the same as with standard EVM measurements.

3.1.2 Method

In this section, we show analytically that the proposed method is able to exclude transmitter and receiver IQ mismatch. We start our discussion with a review of the standard EVM. The obtained standard EVM results for the case without IQ mismatch and with IQ mismatch are the target we compare our method to.

Standard EVM for the Case of no IQ mismatch

In the following, we discuss the EVM for a linear channel with uncorrelated additive noise at its output. As presented in Section 2.2, this is a quite general scenario, since the error due to phase noise and intermodulation distortion can also be modeled as additive noise that is uncorrelated (but not statistically independent) to the excitation signal. Although we focus on OFDM, the following derivation only assumes a multicarrier signal allowing for a time-frequency-representation with a symbol (time) index l and a frequency index k. Hence, our results also apply to other multicarrier-modulation formats like filter bank multicarrier [37].

We do the following analysis independently for each frequency bin k and use bold-face to denote $L \times 1$ vectors and use inner products to sum over L symbols. With $\boldsymbol{V}_k$ denoting the additive noise, the DUT output signal model is

$$\boldsymbol{Y}_k = H_k \boldsymbol{X}_k + \boldsymbol{V}_k. \tag{3.1}$$

[1] The output of a widely linear filter does not only depend linearly on its input signal but also linearly on the conjugate of the input signal [129].

The definition of EVM can be written as

$$\mathrm{EVM}_k = \sqrt{\frac{\frac{1}{L}\boldsymbol{E}_{\boldsymbol{x}k}{}^{\mathrm{H}}\boldsymbol{E}_{\boldsymbol{x}k}}{R_k}} \tag{3.2}$$

$$R_k = \frac{1}{L}\boldsymbol{X}_k{}^{\mathrm{H}}\boldsymbol{X}_k \tag{3.3}$$

$$\boldsymbol{E}_{\boldsymbol{x}k} = \boldsymbol{X}_k - \hat{\boldsymbol{X}}_k \tag{3.4}$$

$$\hat{\boldsymbol{X}}_k = C_k\boldsymbol{Y}_k \tag{3.5}$$

where the estimate $\hat{\boldsymbol{X}}_k$ of the transmitted symbols is corrected by a linear equalizer in the frequency domain. We use an equalizer C_k obtained as the inverse of an MMSE channel estimate $\hat{H}_k$, given in (2.63). For the system model in (3.1), the MMSE estimate is unbiased, i.e., $\mathbb{E}\left\{\hat{H}_k\right\} = H_k$. Assuming $C_k = 1/H_k$ and inserting (3.1) in (3.5), we obtain

$$\mathrm{EVM}_k = \frac{\sqrt{\boldsymbol{V}_k^{\mathrm{H}}\boldsymbol{V}_k}}{\sqrt{LR_k}\,|H_k|} = \sqrt{\frac{\boldsymbol{V}_k^{\mathrm{H}}\boldsymbol{V}_k}{\boldsymbol{X}_k{}^{\mathrm{H}}\boldsymbol{X}_k\,|H_k|^2}}\,. \tag{3.6}$$

The EVM in (3.6)[2] weighs the $\boldsymbol{V}_k$ with the equalizer $C_k = 1/H_k$. Thus, the EVM does not equal the signal (X_k) to noise (V_k) ratio, but rather the filtered-signal (X_kH_k) to noise ratio.

Standard EVM for the Case of Transceiver IQ Mismatch

As discussed in Section 2.2.4, frequency-dependent transmitter and receiver IQ mismatch can be modeled as

$$\boldsymbol{X}_k^{(\mathrm{t})} = \alpha_k^{(\mathrm{t})}\boldsymbol{X}_k + \beta_k^{(\mathrm{t})}\boldsymbol{X}_{-k}^{*} \tag{3.7}$$

$$\boldsymbol{Y}_k^{(\mathrm{r})} = \alpha_k^{(\mathrm{r})}\boldsymbol{Y}_k + \beta_k^{(\mathrm{r})}\boldsymbol{Y}_{-k}^{*} \tag{3.8}$$

with

$$\alpha_k^{(\mathrm{t})} = 1/2\left(H_k^{(I,\mathrm{t})} + \gamma_{\mathrm{t}}H_k^{(Q,\mathrm{t})}\right) \tag{3.9a}$$

$$\beta_k^{(\mathrm{t})} = 1/2\left(H_k^{(I,\mathrm{t})} - \gamma_{\mathrm{t}}H_k^{(Q,\mathrm{t})}\right) \tag{3.9b}$$

where $\gamma_{\mathrm{t}} = g_{\mathrm{t}}e^{j\varphi_{\mathrm{t}}}$ represents the gain and phase mismatch and $H_k^{(I,\mathrm{t})}$ and $H_k^{(Q,\mathrm{t})}$ denote the frequency response of the inphase and quadrature path of the transmitter analog front end, respectively. The relations for the receiver are obtained by replacing (t) with (r) in (3.9).

Replacing $\boldsymbol{X}_k$ with $\boldsymbol{X}_k^{(\mathrm{t})}$ in (3.1) to consider the transmitter IQ mismatch in our noisy channel model results in

$$\boldsymbol{Y}_k^{(\mathrm{t})} = H_k\alpha_k^{(\mathrm{t})}\boldsymbol{X}_k + H_k\beta_k^{(\mathrm{t})}\boldsymbol{X}_{-k}^{*} + \boldsymbol{V}_k. \tag{3.10}$$

[2] A similar relation in the time-domain is given in (2.31b)

Using $\boldsymbol{Y}_k^{(\mathrm{t})}$ instead of $\boldsymbol{Y}_k$ in (3.8) gives the DUT model including transmitter and receiver IQ mismatch:

$$\begin{aligned}\boldsymbol{Y}_k^{(\mathrm{trx})} &= \alpha_k^{(\mathrm{r})}\left(H_k\alpha_k^{(\mathrm{t})}\boldsymbol{X}_k + H_k\beta_k^{(\mathrm{t})}\boldsymbol{X}_{-k}^* + \boldsymbol{V}_k\right)\\ &\quad + \beta_k^{(\mathrm{r})}\left(H_{-k}^*\alpha^{*(\mathrm{t})}_{-k}\boldsymbol{X}_{-k}^* + H_{-k}^*\beta^{*(\mathrm{t})}_{-k}\boldsymbol{X}_k + \boldsymbol{V}_{-k}^*\right)\\ &= \left(\alpha_k^{(\mathrm{r})}H_k\alpha_k^{(\mathrm{t})} + \beta_k^{(\mathrm{r})}H_{-k}^*\beta^{*(\mathrm{t})}_{-k}\right)\boldsymbol{X}_k\\ &\quad + \left(\alpha_k^{(\mathrm{r})}H_k\beta_k^{(\mathrm{t})} + \beta_k^{(\mathrm{r})}H_{-k}^*\alpha^{*(\mathrm{t})}_{-k}\right)\boldsymbol{X}_{-k}^*\\ &\quad + \alpha_k^{(\mathrm{r})}\boldsymbol{V}_k + \beta_k^{(\mathrm{r})}\boldsymbol{V}_{-k}^*\,.\end{aligned}$$

With the definitions

$$A_k = \alpha_k^{(\mathrm{r})}H_k\alpha_k^{(\mathrm{t})} + \beta_k^{(\mathrm{r})}H_{-k}^*\beta^{*(\mathrm{t})}_{-k} \tag{3.11}$$

$$B_k = \alpha_k^{(\mathrm{r})}H_k\beta_k^{(\mathrm{t})} + \beta_k^{(\mathrm{r})}H_{-k}^*\alpha^{*(\mathrm{t})}_{-k} \tag{3.12}$$

$$\boldsymbol{E}_k^{(\mathrm{trx})} = B_k\boldsymbol{X}_{-k}^* + \alpha_k^{(\mathrm{r})}\boldsymbol{V}_k + \beta_k^{(\mathrm{r})}\boldsymbol{V}_{-k}^* \tag{3.13}$$

we obtain the following compact relation:

$$\boldsymbol{Y}_k^{(\mathrm{trx})} = A_k\boldsymbol{X}_k + \boldsymbol{E}_k^{(\mathrm{trx})}\,. \tag{3.14}$$

Similar to H_k and $\boldsymbol{V}_k$ in (3.1), there is a linear filter A_k and an additive disturbance $\boldsymbol{E}_k^{(\mathrm{trx})}$ that is uncorrelated with the signal X_k. Similar to (3.6), the EVM is therefore

$$\mathrm{EVM}_k^{(\mathrm{trx})} = \frac{\sqrt{\boldsymbol{E}_k^{(\mathrm{trx})\mathrm{H}}\boldsymbol{E}_k^{(\mathrm{trx})}}}{\sqrt{LR_k}\,|A_k|}\,. \tag{3.15}$$

This result is of the same form as (3.6). However, instead of $\boldsymbol{V}_k$ we have an error $\boldsymbol{E}_k^{(\mathrm{trx})}$ that includes the IQ mismatch, and a different linear channel A_k that includes the filter-effect of the TX and RX path, as given in (3.11).

Proposed EVM for the Case of Transceiver IQ Mismatch

In the following, we present the proposed method and show that it is able to estimate both the result without IQ mismatch in (3.6) and the result including IQ mismatch in (3.15).

Our measurement method requires a test signal where we null some subcarriers $-k_m(l)$ and evaluated the EVM at $k_m(l)$, i.e. at the mirrored subcarrier. The dependence of k_m on l indicates that the position of the nulled subcarriers is changed from symbol to symbol. Similar to the EPR with symmetrically nulled stopbands, we also null symmetric pairs, i.e., $k_m(l)$ and $-k_m(l)$. While this is necessary with the EPR, the EVM would also allow to only null one side, $-k_m(l)$, and evaluate the EVM at the other side $k_m(l)$. However, the symmetric nulling has the advantage of being free from bias due to imperfect equalization, since the transmitted data symbol is zero.

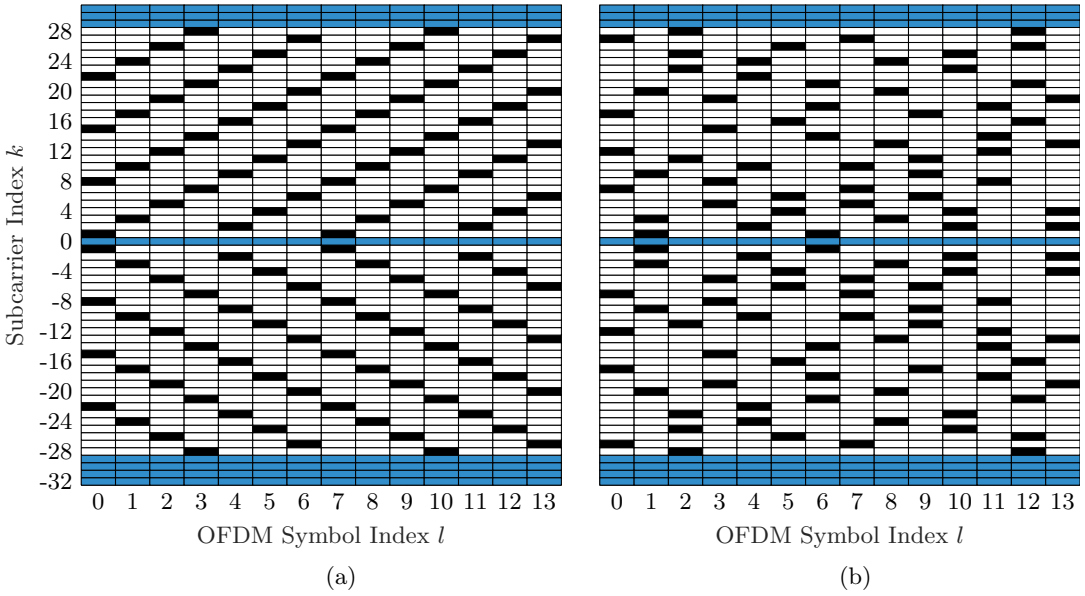

Figure 3.1: First 14 symbols of a 20-MHz OFDM test signals featuring nulled subcarrier symbols. Moduled data symbols $X[l, k]$ are shown in white color, whereas the nulled data (and pilot) subcarriers are shown in black color. Blue color indicates the unmodulated subcarriers according to the standard, as shown in Tab. 2.1. In (a), the location of the nulled time-frequency bins in black is changed linearly from symbol to symbol, whereas in (b), it is randomized.

Two different ways how to change the nulled positions from symbol to symbol are shown in Fig. 3.1. In all our experiments, both approaches seemed to work equally well. Since it is more straightforward, it is preferable to linearly sweep the nulled subcarrier positions, as shown in Fig. 3.1 (a). The main idea of the proposed method is to analyze the EVM of the nulled (black) time-frequency bins separately from the modulated (white) ones. At the DUT output, the nulled bins will contain uncorrelated errors without IQ-mismatch, whereas the modulated bins include IQ mismatch, as derived in the following.

We split the vector $\boldsymbol{X}_k$ of length L containing all symbols $l \in \{0, \ldots, L-1\}$ into two vectors: A vector $\boldsymbol{X}_k^{(p)}$ of length $L_p(k)$ containing those time frequency-bins where the data is present, and a vector $\boldsymbol{X}_k^{(m)}$ of length $L_m(k)$ where the data is symmetrically nulled, i.e., $\boldsymbol{X}_k^{(m)} = \boldsymbol{X}^{*(m)}_{-k} = \boldsymbol{0}_{L_m(k)}$, with $L_m(k)+L_p(k) = L$. The lengths may depend on the subcarrier. However, for clarity and without loss of generality, we assume the number of null-occurrences to be the same for each subcarrier, i.e., $L_m(k) = L_m$.

To analyze the received signal, we use the information about the location of the nulled bins $k_m(l)$ to divide the received signal in two parts, $\boldsymbol{Y}_k^{(m)}$ and $\boldsymbol{Y}_k^{(p)}$, respectively. If the EVM is reasonably good, e.g., < -10 dB, the nulled bins $k_m(l)$ can also be detected based on the low power of $|Y_{k_m(l)}|$.

We analyze the EVM of $Y_{k_p(l)}$ and $Y_{k_m(l)}$ separately. First, by averaging the EVM only over the bins $k_p(l)$ with mirror excitation *present* at $-k_p(l)$, we include potential IQ mismatch, and hence

$$\mathrm{EVM}_k^{(\mathrm{trx},p)} \approx \mathrm{EVM}_k^{(\mathrm{trx})} \,. \tag{3.16}$$

The approximation is only there because we average over L_p instead of L symbols. Assuming typical values of $L_p = 275$ and $L = 320$, the difference is negligible.

Second, by analyzing the symbols $\boldsymbol{Y}_k^{(\mathrm{trx},m)}$ with *missing* mirror excitation $\boldsymbol{X}_{-k}^{(m)} = 0$, the EVM excludes transceiver IQ mismatch. We derive this in the following. Because $\boldsymbol{X}^{*(m)}_{-k} = \boldsymbol{0}_{L_m}$, averaging only over the nulled excitation time-frequency-bins of (3.13) results in

$$\boldsymbol{E}_k^{(\mathrm{trx},m)} = \alpha_k^{(\mathrm{r})} \boldsymbol{V}_k^{(m)} + \beta_k^{(\mathrm{r})} \boldsymbol{V}^{(m)*}_{-k} \,. \tag{3.17}$$

Summing over the L_m individual squared errors gives

$$\begin{aligned} \boldsymbol{E}^{(\mathrm{trx},m)\mathrm{H}}_k \boldsymbol{E}_k^{(\mathrm{trx},m)} &= \left|\alpha_k^{(\mathrm{r})}\right|^2 \boldsymbol{V}^{(m)\mathrm{H}}_k \boldsymbol{V}_k^{(m)} \\ &\quad + \alpha^{(\mathrm{r})*}_k \beta_k^{(\mathrm{r})} \boldsymbol{V}^{(m)\mathrm{H}}_k \boldsymbol{V}^{(m)*}_{-k} \\ &\quad + \alpha_k^{(\mathrm{r})} \beta^{(\mathrm{r})*}_k \boldsymbol{V}^{(m)\mathrm{T}}_{-k} \boldsymbol{V}_k^{(m)} \\ &\quad + \left|\beta_k^{(\mathrm{r})}\right|^2 \boldsymbol{V}^{(m)\mathrm{T}}_{-k} \boldsymbol{V}^{(m)*}_{-k} \end{aligned} \tag{3.19}$$

$$\approx \left|\alpha_k^{(\mathrm{r})}\right|^2 \boldsymbol{V}^{(m)\mathrm{H}}_k \boldsymbol{V}_k^{(m)} \,. \tag{3.20}$$

The approximation is valid in almost all practical situations, because of two reasons. First, the EVM due to receiver IQ mismatch is typically less than -10 dB, and hence $\left|\beta_k^{(\mathrm{r})}\right| \ll \left|\alpha_k^{(\mathrm{r})}\right|$. Second, ${\boldsymbol{V}^{(m)}}_{-k}^{\mathrm{H}} \boldsymbol{V}^{(m)*}_{-k}$ and ${\boldsymbol{V}^{(m)}}_{-k}^{\mathrm{T}} \boldsymbol{V}_k^{(m)}$ are small compared to ${\boldsymbol{V}^{(m)}}_k^{\mathrm{H}} \boldsymbol{V}_k^{(m)}$, because the noise and its mirrored conjugated version are orthogonal, i.e., $\mathbb{E}\left\{V_k V_{-k}\right\} = \mathbb{E}\left\{V_k^* V_{-k}^*\right\} = 0$. In analogy to (3.15), the resulting EVM is

$$\mathrm{EVM}_k^{(\mathrm{trx},m)} = \frac{\sqrt{{\boldsymbol{V}^{(m)}}_k^{\mathrm{H}} \boldsymbol{V}_k^{(m)}}\left|\alpha_k^{(r)}\right|}{\sqrt{L_m R_k}\,|A_k|}\,. \tag{3.21}$$

To compare (3.21) with the standard EVM for the case of no IQ mismatch in (3.6), we use the approximation

$$\sqrt{\frac{1}{L_m}{\boldsymbol{V}^{(m)}}_k^{\mathrm{H}} \boldsymbol{V}_k^{(m)}} \approx \sqrt{\frac{1}{L}\boldsymbol{V}_k^{\mathrm{H}} \boldsymbol{V}_k} \tag{3.22}$$

which is valid since both expressions estimate the same noise power by averaging over a different amount of symbols. Furthermore, $A_k \approx \alpha_k^{(\mathrm{r})} H_k \alpha_k^{(\mathrm{t})}$, follows from the argument of limited IQ mismatch that we already used for (3.20). Using these two approximations, the relation between the standard EVM without IQ mismatch in (3.6) and the proposed EVM averaged over the nulled excitation bins for the case of combined transmitter and receiver mismatch is

$$\mathrm{EVM}_k^{(\mathrm{trx},m)} \approx \frac{1}{|\alpha|_k^{(t)}} \cdot \mathrm{EVM}_k\,. \tag{3.23}$$

This result corroborates our idea that is is possible to estimate the true EVM of the DUT EVM_k from a measurement $\mathrm{EVM}_k^{(\mathrm{trx},m)}$ with frequency-dependent transmitter and/or receiver IQ mismatch. The apparent difference, i.e., the factor $1/|\alpha|_k^{(t)}$ in (3.23), is perfectly reasonable considering our DUT model featuring additive noise V that is independent of the signal and the TX IQ mismatch filter. Since the SNR is increased if the signal power is increased, a scale factor $|\alpha|^{(t)}$ applied to the signal prior to the constant additive noise must show up in the EVM. Since the SNR gets higher if $|\alpha|_k^{(t)} > 1$, the EVM in (3.23) is lowered by that factor.

3.1.3 Results

In the following, we show simulation results that verify the analytic results in (3.23) and (3.16). Our EVM analyzer is implemented in Matlab and supports the standard EVM as well as the proposed method with nulled subcarriers. Our source signal is a WLAN OFDM signal with QPSK subcarrier modulation. The results look the same for denser modulation schemes, since the proposed method required no assumptions on the modulation scheme. To simulate transmitter and receiver IQ mismatch we implement (3.7) and (3.8) in the discrete time-domain.

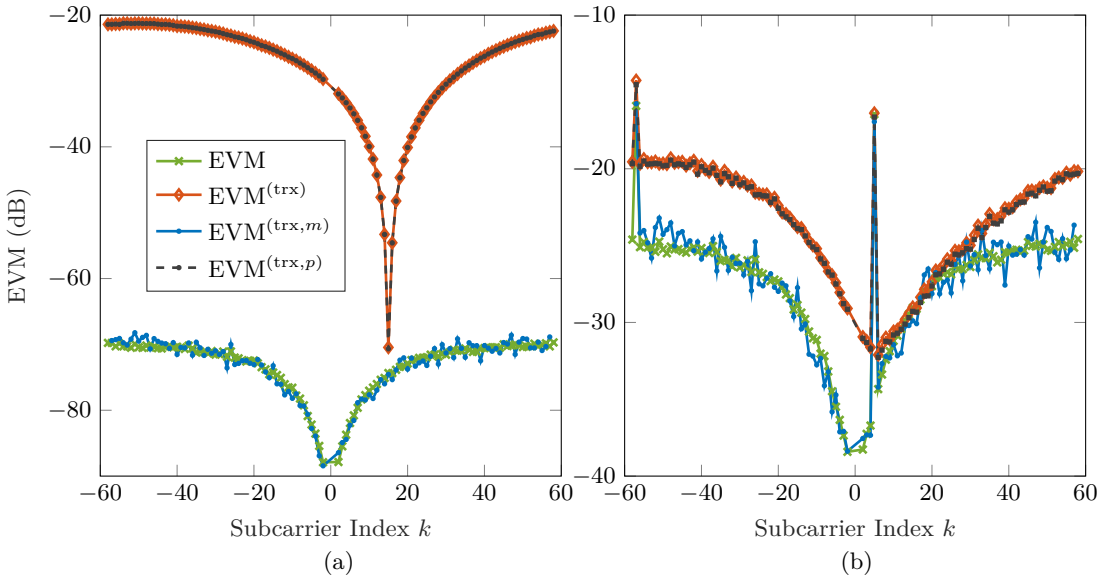

Figure 3.2: Additive error simulation. Although there is heavily frequency-dependent TX and RX IQ mismatch, our method $\mathrm{EVM}^{(\mathrm{trx},m)}$ is able to estimate the true EVM of the DUT, even in the following extreme cases: In (a), the true EVM is far beyond the EVM with IQ mismatch, whereas in (b) the true DUT EVM level is increased and highly frequency-dependent, since there are two additional subcarriers with an intentionally increased EVM. In both cases, the second result $\mathrm{EVM}^{(\mathrm{trx},p)}$ matches the result with IQ mismatch.

Additive Noise

In Fig. 3.2, we compare the following EVM characteristics for the model from (2.51) at a sample rate rate of 40 MHz.

1. Standard EVM: simulation of the DUT only, without IQ mismatch (IQmm).
2. Standard $\mathrm{EVM}^{(\mathrm{trx})}$: simulation of the chain TX-IQmm, DUT, RX-IQmm
3. Proposed $\mathrm{EVM}^{(\mathrm{trx},m)}$: simulation setup like $\mathrm{EVM}^{(\mathrm{trx})}$, but with a 320 symbol test signal with 8 concurrent nulled symbols as shown in Fig. 3.1(a).
4. Proposed $\mathrm{EVM}^{(\mathrm{trx},p)}$: same simulation as $\mathrm{EVM}^{(\mathrm{trx},p)}$.

We use the same model for TX and RX IQ mismatch. The error is filtered Gaussian noise (a), and filtered Gaussian noise with additional single-tone interferers (b). The simulation results confirm the results derived above: By evaluating the EVM at the nulled bins $\mathrm{EVM}^{(\mathrm{trx},m)}$ we estimate the EVM without IQ mismatch, whereas the EVM $\mathrm{EVM}^{(\mathrm{trx},p)}$ evaluated at the present bins is the same as the standard EVM with TRX IQ mismatch. Although the error in Fig. 3.2 due to the IQ mismatch is heavily frequency-dependent, the frequency-response of the transmit and receive filters is negligible.

In Fig. 3.3, we show the case of heavily frequency-dependent LTI filters in the TX and RX path. While such extreme filter responses are not likely to be encountered with practical transceivers and measurement devices, they help us to visualize and understand some properties of our method derived above. We simulate additive colored noise for several different IQ mismatch scenarios. In Fig. 3.3(a) we simulate frequency-independent RX IQ mismatch with $\gamma_{\mathrm{r}} = 1.005e^{j0.001}$, $\boldsymbol{h}^{(Q,\mathrm{r})} = \boldsymbol{h}^{(I,\mathrm{r})} = 1$, whereas in (b) we simulate frequency-dependent IQ mismatch. At a sample rate of 20 MHz, we use the following FIR models for frequency-dependent TX and RX IQ mismatch:

$$\boldsymbol{h}^{(I,\mathrm{t})} = [0.99, -0.705]/2 \tag{3.24a}$$
$$\boldsymbol{h}^{(Q,\mathrm{t})} = [0.97, -0.695]/2 \tag{3.24b}$$
$$\boldsymbol{h}^{(I,\mathrm{r})} = [0.97, -0.890, 0.805]/3 \tag{3.24c}$$
$$\boldsymbol{h}^{(Q,\mathrm{r})} = [0.99, -0.910, 0.795]/3 \tag{3.24d}$$
$$\boldsymbol{\alpha}^{(\mathrm{t})} = (\boldsymbol{h}^{(I,\mathrm{t})} + \boldsymbol{h}^{(Q,\mathrm{t})}/2 \tag{3.24e}$$
$$\boldsymbol{\alpha}^{(\mathrm{r})} = (\boldsymbol{h}^{(I,\mathrm{r})} + \boldsymbol{h}^{(Q,\mathrm{r})})/2 \tag{3.24f}$$

where the division is performed element-wise. Besides simulating TX and RX mismatch with the models given in (3.24), we simulate the case where we have no IQ mismatch, but the same transmit (TX filter) or transmit and receive (TRX filter) frequency response. The "TX filter" scenario is implemented by setting

$$\boldsymbol{h}^{(I,\mathrm{t})} = \boldsymbol{h}^{(Q,\mathrm{t})} = \boldsymbol{\alpha}^{(\mathrm{t})} \tag{3.25}$$

and the "TRX filter" setting is obtained by additionally setting

$$\boldsymbol{h}^{(I,\mathrm{r})} = \boldsymbol{h}^{(Q,\mathrm{r})} = \boldsymbol{\alpha}^{(\mathrm{r})}\,. \tag{3.26}$$

The results in Fig. 3.3 are perfectly in line with the theoretic results, e.g., (3.23) and (3.16).

Phase Noise

To simulate phase noise, we use the model depicted in Fig. 2.3. We already know from Section 2.2.2 that with de-rotation we can remove common phase error and yield better EVM results. Fig. 3.4 shows the results without (a) and with (b) de-rotation applied in the EVM analysis. $\mathrm{EVM}^{(\mathrm{trx},m)}$ obtained with symmetrically-nulled data-symbols always estimates the EVM with de-rotation even if we use no de-rotation in the analysis. This is clear since a null symbol is not affected by common phase error (CPE), i.e., $0 = 0e^{j\phi}$. The property of always returning the result with de-rotation can be a valuable feature when verifying the performance of de-rotation algorithms. Furthermore, standards like IEEE 802.11ac for WLAN require the use of de-rotation [62]. If it is, however, desired to obtain the phase noise result with CPE included, an asymmetrically nulled test signal must be used. The EVM without IQ mismatch is then measured at the frequency bin mirrored to the nulled bin.

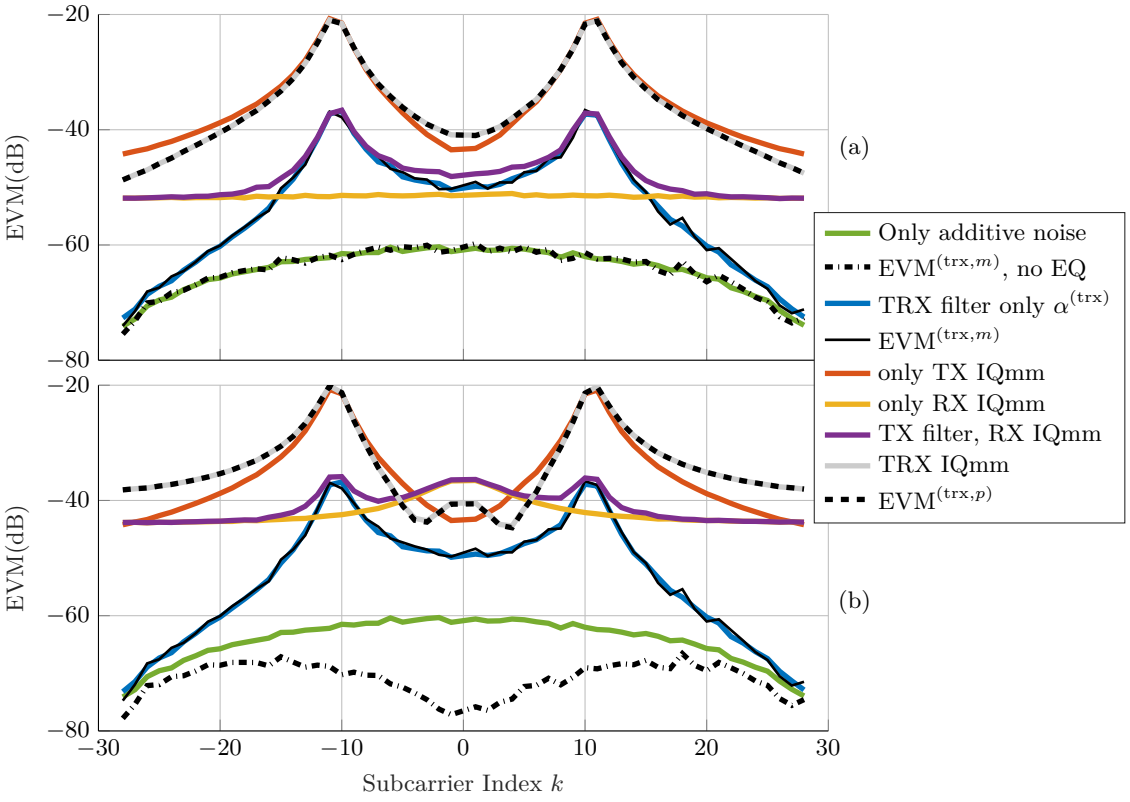

Figure 3.3: EVM for additive noise with frequency-independent receiver IQ mismatch (a), and frequency-dependent receiver IQ mismatch (b). The standard EVM is shown in different colors for different simulated TX/RX IQ mismatch scenarios. The results obtained with the proposed method for the case of TRX IQ mismatch is shown in black. As shown in (3.16), $\mathrm{EVM}^{(\mathrm{trx},p)}$ equals the standard EVM, whereas (3.23) shows that $\mathrm{EVM}^{(\mathrm{trx},m)}$ estimates the EVM including the TX filter effect. If we do not use an equalizer when computing $\mathrm{EVM}^{(\mathrm{trx},m)}$, the EVM in (3.21) is multiplied with $|A_k|$. Consequently, the TX frequency response ${\alpha_k}^{(\mathrm{t})}$ is excluded but the RX frequency response ${\alpha_k}^{(\mathrm{r})}$ is included in the EVM. Therefore, in (a), we obtain the noise-only EVM because ${\alpha_k}^{(\mathrm{r})} = 1$, whereas the bottom curve in (b) displays the effect of an RX frequency-response ${\alpha_k}^{(\mathrm{r})} \neq 1$.

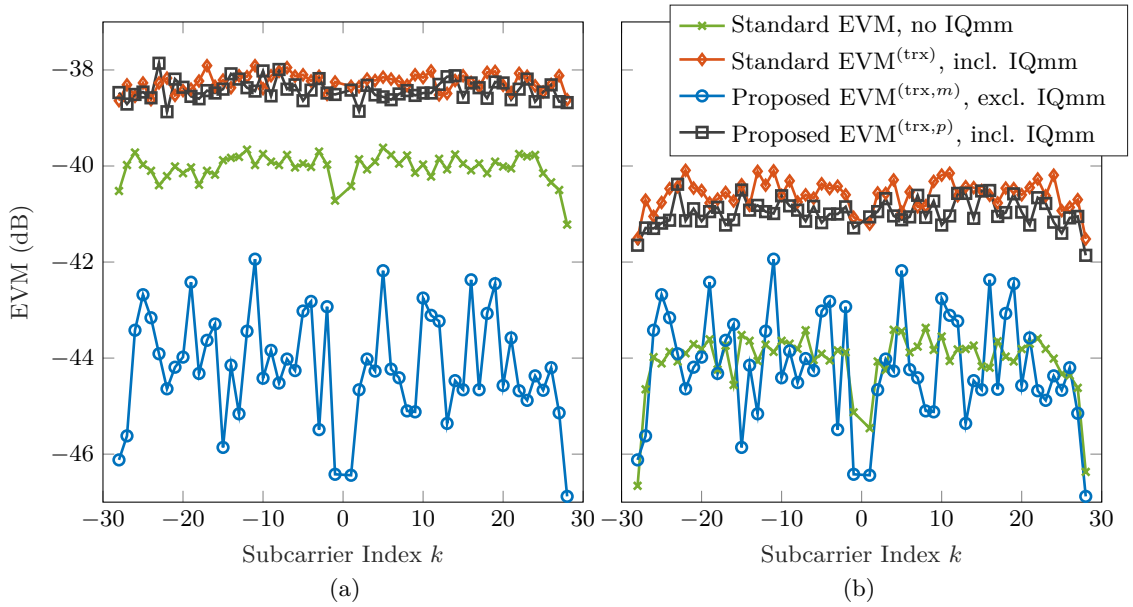

Figure 3.4: Phase noise simulation result without de-rotation (a), and with de-rotation (b) applied in the EVM analysis. The standard EVM is shown for the case of phase noise only, i.e., without IQ mismatch (IQmm), and for the case where there is additional TRX IQmm. The two results obtained with the proposed EVM method using nulled subcarriers are shown only for the case of additional TRX IQ mismatch. The first result $\text{EVM}^{(\text{trx},p)}$ resembles the standard EVM with IQmm, whereas the second $\text{EVM}^{(\text{trx},m)}$ excludes IQmm and resembles the case of standard EVM when no IQmm is present. Our method, i.e. $\text{EVM}^{(\text{trx},m)}$, returns the DUT EVM result with de-rotation, even if we do not apply de-rotation in the corresponding EVM analysis. This is clear because null-symbols do not change by rotating the phase, i.e. $0 = 0e^{j\phi}$. The true phase noise EVM (averaged over the data subcarriers, with de-rotation) is, EVM $= -44$ dB. Our estimate is $\text{EVM}^{(\text{trx},m)} = -44.02$ dB.

Nonlinearity

To model nonlinearity we use the Wiener power-amplifier (PA) model from [35] that was also used in [A4, 161, 21]. This model consists of an FIR filter with coefficients $[0.7692, 0.1538, 0.0769]$ followed by a quasi-memoryless [31] nonlinear Saleh model [123] given as

$$y[n] = \frac{1.1x[n]}{1 + 0.3\left|x[n]\right|^2} \exp\left(\frac{j0.8\left|x[n]\right|^2}{1 + 3\left|x[n]\right|^2}\right). \tag{3.27}$$

Our source signal is a 40-MHz WLAN signal at a sample rate of 200 MHz. The oversampling is required to avoid aliasing caused by the nonlinearity. We use 4th-order digital butterworth filter with detuned cutoff-frequency, i.e., 25 MHz and 25.1 MHz for the I- and Q- path filters of the TX and RX path and add frequency-independent mismatch with $\gamma = 1.001e^{-j0.0005}$. The results are shown in Fig. (3.5). Although the filters are flat in the inband, the inband error due to IQ mismatch features a highly frequency-dependent V-shape, similar to what we have also seen encountered in measurements, as shown in Fig. 3.10. By introducing more stopbands (concurrent nulled bins) or longer signals the precision of the measurement can be increased. To increase the accuracy when measuring nonlinear DUTs, it is better to use only few stopbands in order to not alter the excitation signal statistics.

Discussion

The method proposed in this section delivers two results. $\mathrm{EVM}^{(\mathrm{trx},m)}$, evaluated at the mirror-components of nulled bins is free from IQ mismatch, whereas $\mathrm{EVM}^{(\mathrm{trx},p)}$ evaluated at bins where the mirrored-bin is modulated resembles the standard EVM and includes IQ mismatch. We have derived this analytically and verified it with simulations.

The shape of the IQ mismatch does not matter, as long as there is no intersymbol interference (ISI) due to the IQ mismatch, i.e., a symbol is affected by the IQ mismatch of the previous symbol. In such a case, we could null two consecutive symbols at the same subcarrier bin k and only evaluate the second one. In OFDM, ISI occurs if the impulse responses bandlimited to the inband is longer than the effective guard interval. It is not likely to encounter this case in typical transceivers or measurement devices. To rule out whether ISI causes limited EVM performance, the EVM estimation method proposed in the next section can be of help, since it allows to easily change the equalizer length and compensate linear channels longer than the OFDM guard interval.

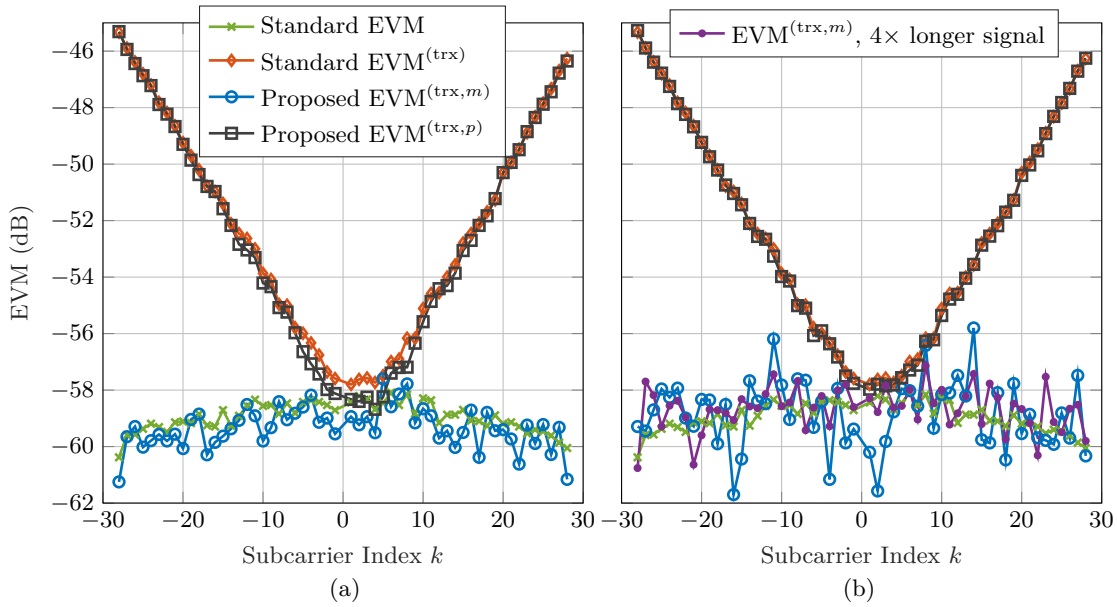

Figure 3.5: PA nonlinearity simulation with frequency-dependent IQ mismatch. (a) Using the test signal shown in Fig. 3.1, the proposed method underestimates the overall standard EVM by 0.6 dB and the true EVM without IQ mismatch by 0.1 dB. This bias can be explained by considering that the regular OFDM test signal used for the standard EVM has been changed by nulling $N_M = 8$ subcarriers per symbol. In (b), only $N_M = 2$ subcarriers are nulled concurrently, which is the minimum number due to the symmetry constraint. Since the test signal is more similar to the regular OFDM signal used for the standard EVM, there is less (virtually no) bias. However, we have an increased variance since we average over less symbols when computing $\mathrm{EVM}^{(\mathrm{trx},m)}$. By using a four times longer signal, the same variance as in (a) can be obtained.

3.2 SLIC-EVM – Error Vector Magnitude without Demodulation

This section presents the alternative method for EVM analysis we proposed in [A2]. The key advantage over the standard EVM is that the proposed method is simpler to adapt to new communication standards, because it does not require demodulation of the data symbols. Such a demodulation requires in-depth knowledge of the communication standard. The presented method, however, only requires basic information like the subcarrier spacing and the equalizer length.

3.2.1 Problem Description

The EVM compares measured with ideal data symbols, requiring dedicated receiver algorithms when analyzing transmitters or RF devices like a power amplifier (PA). This dedicated receiver algorithms makes the adaption of an existing EVM measurement setup to a new standard an expensive task, either in development time or purchase cost. On the one hand, implementing a receiver is a non-trivial task and requires in-depth knowledge of the particular standard. Commercial EVM analyzers, on the other hand, are expensive and may not even be available at the time when developing next generation devices for upcoming communication standards.

There are other approaches to inband error measurement that do not require demodulation. One of these is the noise power ratio, which is discussed in detail in Chapter 4. Another approach is based on analog signal cancellation [108]. To obtain the error signal, a coarse best linear approximation (BLA) of the DUT's linear response is subtracted from the DUT output in the analog domain. To this end, a gain and phase adjustment network and an analog coupler are used. This approach typically overestimates the EVM, because receivers typically feature a channel equalizer (EQ) that can correct the effect of linear filtering. The analog adjustment proposed in [108], however, merely corrects for a scalar complex gain factor. Furthermore, the influence of common phase error on the EVM can[3] be mitigated by applying phase-tracking, i.e., (OFDM) symbol-wise de-rotation. As already indicated above, the analog signal cancellation method removes a (best) linear approximator (BLA) restricted to a single complex filter coefficient from the DUT output. This gain can also be obtained in the digital baseband by means of cross-correlation as proposed recently in [138]. Estimation of the BLA of a nonlinear DUT can also be achieved with a vector network analyzer measuring the phases and the gains of the DUT response to a random-phase multisine [149]. However, although the stochastic nonlinear contribution of the DUT is measured, a comparison to EVM is missing in [149]. Recently, the BLA framework has been used to measure EVM of nonlinearites [120]. Similar to [138], [120] does not show results

[3] Both EQ and de-rotation are mandatory for EVM measurements according to the 802.11ac WLAN standard.

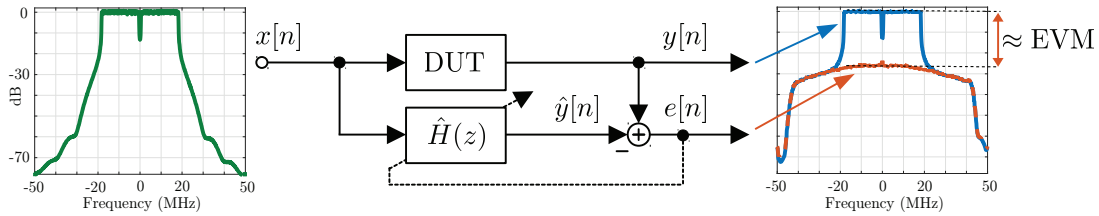

Figure 3.6: Principle of SLIC-EVM. A linear filter $\hat{H}(z)$ cancels the linear response of the device under test (DUT). The remaining signal $e[n]$ contains the inband error introduced by the DUT. Averaging the ratio between error PSD and the DUT output PSD over the inband gives an estimate for the EVM.

comparing the estimated EVM side-by-side with the standard (true) EVM. Phase noise and IQ mismatch are not considered.

The method presented in this section estimates the EVM via feedforward cancellation in the digital baseband. The principle of the proposed method is depicted in Fig. 3.6. While [108] only adjusts gain and phase, we optimize a finite impulse response (FIR) filter to minimize the mean square of the error signal. This way, signal components that are linearly correlated with the input signal are removed from the DUT output signal. What remains is the uncorrelated error, containing all signal components that can not be modeled by FIR filtering of the DUT input. In contrast to the approach of Gharaibeh [47], who obtains the uncorrelated error by orthogonalization of a behavioral model of the DUT, we work on the signal level, without assuming a certain model of the DUT. In other words, the error signal is obtained by subtracting linearly correlated (SLIC) parts (up to a certain maximum lag length) of the DUT output signal from the DUT output signal. We choose the FIR filter length to be equal to the length of the channel estimate in EVM analysis (the cyclic prefix length in OFDM). Consequently, we do not necessarily remove the entire correlated part but only that part, that is also equalized in an EVM analyzer.

Besides addressing equalization, we present a straightforward method to replicate the effect of de-rotation in EVM. Like regular data-aided EVM [85], our analysis routine requires synchronized baseband DUT input and output signals. Consequently, our method shares some disadvantages with the regular EVM: Insufficient synchronization biases the result and hiqh-quality wideband analog-to-digital converters are required [A4]. Benefits shared with the EVM are that the standard communication signal can be used for testing and that the error is observed over the whole inband. The main advantage of SLIC-EVM over regular EVM is that SLIC-EVM allows to use the same, straightforward analyzer code for different signal standards.

3.2.2 Method

To estimate the EVM we need length-N vectors of DUT input samples $\boldsymbol{x}[n]$ and output samples and $\boldsymbol{y}[n]$.

$$\boldsymbol{x}[n] = \Big(x[n], x[n-1], \ldots, x[n-N+1]\Big)^{\mathrm{T}} \tag{3.28}$$

$$\boldsymbol{y}[n] = \Big(y[n], y[n-1], \ldots, y[n-N+1]\Big)^{\mathrm{T}} \tag{3.29}$$

For brevity, we drop the dependence of the above signal vectors on the discrete time index n, whenever possible.

Since the required measurement setup is exactly the same as for EVM analysis, the results can be easily compared. However, potential errors due to digital-to-analog conversion, RF up- and downmixing, and analog-to-digital conversion may bias the true error introduced by the actual DUT.

Our method can be divided into two steps: First, the computation of an error signal $e[n]$ considering equalization and de-rotation, and second, the computation of the EVM estimate as an error to signal ratio in the power spectral density domain.

Computation of the Error Signal

Before estimating the filter that models the linear part of the DUT, the signals $x[n]$ and $y[n]$ must be synchronized, to ensure a causal input-output relation with minimum delay. In addition to compensating the delay indicated by the maximum of the cross correlation between the signal vectors $\boldsymbol{x}$ and $\boldsymbol{y}$ as described in [27], some samples additional delay of $\boldsymbol{y}$ may be required to ensure causality and get the best results.

A vector of output samples of an LTI FIR filter can be written as

$$\hat{\boldsymbol{y}} = \boldsymbol{X}\hat{\boldsymbol{h}} \tag{3.30}$$

where $\hat{\boldsymbol{h}}$ is an $N_h \times 1$ vector of complex-valued filter coefficients and $\boldsymbol{X}$ is the $N \times N_h$ convolution matrix

$$\boldsymbol{X} = \Big(\boldsymbol{x}[n], \boldsymbol{x}[n-1], \ldots, \boldsymbol{x}[n-N_h+1]\Big). \tag{3.31}$$

As indicated in Fig. 3.6, we want to fit the filter-coefficients in the least squares sense to the output of the DUT, i.e., minimize a cost function $J(\boldsymbol{h}) = \boldsymbol{e}^{\mathrm{H}}\boldsymbol{e}$, where the error is defined as $\boldsymbol{e} = \boldsymbol{y} - \hat{\boldsymbol{y}}$. The optimal filter coefficients are

$$\hat{\boldsymbol{h}} = \boldsymbol{X}^{\dagger}\boldsymbol{y} \tag{3.32}$$

where $\boldsymbol{X}^{\dagger} = \Big(\boldsymbol{X}^{\mathrm{H}}\boldsymbol{X}\Big)^{-1}\boldsymbol{X}^{\mathrm{H}}$ is the pseudo-inverse of $\boldsymbol{X}$, as derived in Appendix A.1.

An LTI filter can emulate the equalizer in EVM analysis, but is not able to accommodate for phase tracking. To address phase tracking in SLIC-EVM, i.e., to de-rotate a common phase error (CPE), we do the following: We divide $\hat{\boldsymbol{y}}$ and $\boldsymbol{y}$ into a number of $L_b = \lfloor N/N_b \rfloor$ non-overlapping blocks of length N_b, denoted as $\hat{\boldsymbol{y}}_l$ and $\boldsymbol{y}_l$, respectively. The block length should equal the OFDM symbol duration including the guard interval (cyclic prefix), i.e., $N_b = (1+C_g)f_s/\Delta_f$ where f_s denotes the baseband sample rate, C_g is the guard factor and Δ_f is the OFDM subcarrier spacing, as explained in Section 2.3. For each block indexed by l, a single complex coefficient $C_{\mathrm{DeRot}}[l]$ is estimated such that $\boldsymbol{y}_l - C_{\mathrm{DeRot}}[l]\hat{\boldsymbol{y}}_l$ is minimized in the least squares sense. To obtain the corrected version $\hat{\boldsymbol{y}}^{(2)}$ with applied de-rotation, the correction factor is applied to each block and the blocks are concatenated, i.e.,

$$\hat{\boldsymbol{y}}^{(2)} = \sum_{l=0}^{L_b-1} C_{\mathrm{DeRot}}(l)\hat{\boldsymbol{y}}_l * \delta[n - lN_b]\,. \tag{3.33}$$

Here, shifting the individual blocks back to the original location is denoted by means of convolutions with shifted versions of the unit impulse sequences $\delta[n]$. The error signal vector with applied de-rotation is given as $\boldsymbol{e} = \boldsymbol{y} - \hat{\boldsymbol{y}}^{(2)}$.

PSD Analysis and Computation of the EVM Estimate

We define our EVM estimate as the ratio of the PSD of the error signal to the PSD of the linear estimate of the DUT:

$$\widehat{\mathrm{EVM}}[k] = \sqrt{\frac{S_e[k]}{S_{\hat{y}[k]}}} \tag{3.34}$$

We use Welch's method [153] to compute PSD estimates as described in Section 2.1.3.

$$S_y[k] = \frac{1}{L}\sum_{l=0}^{L-1} Y^*[k,l]Y[k,l] \tag{3.35}$$

$$Y[k,l] = \sum_{n=0}^{N_a-1} w[n]y[n - lN_{\mathrm{hop}}]e^{-j\frac{2\pi}{N_a}nk} \tag{3.36}$$

where blocks of time samples are indexed by l, $k \in \mathcal{K} \subset \mathbb{Z}$ is the frequency index, and $w[n]$ is a window function with support $0 \leq n \leq N_a - 1$. For comparison with EVM it is desirable to have a PSD frequency resolution equal to the OFDM subcarrier spacing Δ_f. With that, a scalar figure of merit is obtained by averaging the subcarrier-dependent result over the set of modulated OFDM subcarriers $\mathcal{D}$ with cardinality $|\mathcal{D}|$, as shown in Tab. 2.1.

$$\widehat{\mathrm{EVM}} = \sqrt{\frac{1}{|\mathcal{D}|}\sum_{k\in\mathcal{D}} \widehat{\mathrm{EVM}}^2[k]} \tag{3.37}$$

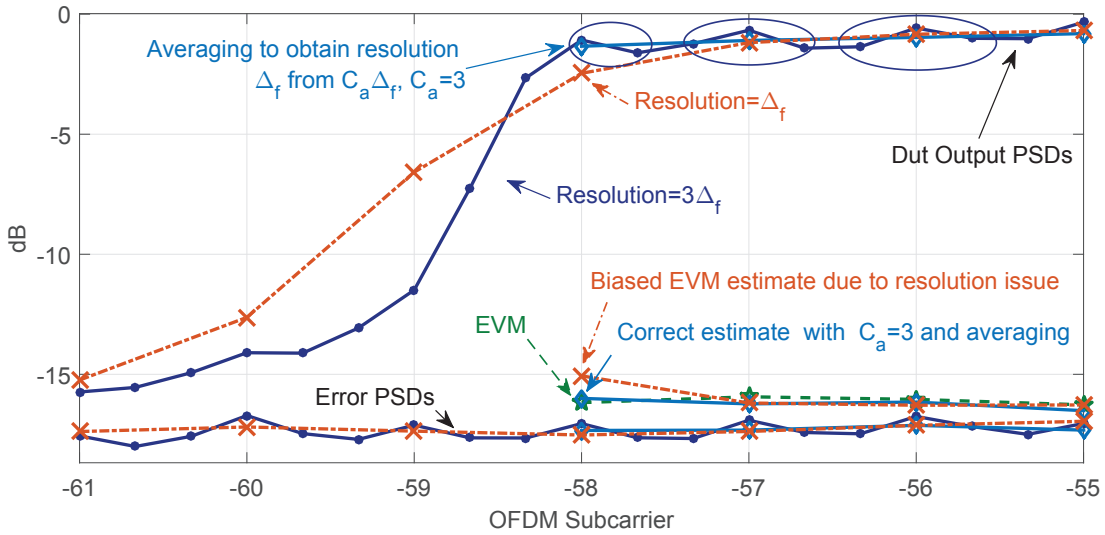

Figure 3.7: PSD resolution issue. To obtain results at the same bins as with EVM, we need a resolution Δ_f. However, at the outermost bins, e.g., bin $k = -58$ for 40MHz WLAN, the steep band-edge cannot be resolved with low resolution. Thus, we first use a $C_a = 3$-times higher resolution and then reduce it by averaging only over modulated bins.

A frequency resolution of Δ_f can be obtained by setting $N_a = f_s/\Delta_f$ in (3.36). However, it is advisable to first use a C_a-times increased frequency resolution $N_a = C_a f_s/\Delta_f$, and then decrease the resolution by averaging over C_a bins, with exception of the outer- and innermost bins $\mathcal{D}_O = \{\pm k_{min}, \pm k_{max}\}$. At these bins, the power should only be averaged over the actual subcarrier and its $(C_a - 1)/2$ modulated neighbors $\mathcal{D} \setminus \mathcal{D}_O$, due to the following. If power from out-of-band frequencies $|f| > k_{max}\Delta_f$ or the unmodulated band around DC $|f| < k_{min}\Delta_f$ is included, $S_y(\mathcal{D}_O)$ is likely to be underestimated. However, the error PSD in the numerator stays roughly the same, because there is typically not a big change in error power when going from a modulated bin to the next unmodulated bin in case of uncorrelated errors like intermodulation distortion. Because a constant is divided by an underestimated value in (3.34), we would overestimate the EVM at the bins $\mathcal{D}_O$. By excluding the influence of frequencies $|f| > k_{max}\Delta_f$ and $|f| < k_{min}\Delta_f$, this systematic deviation can be avoided. Fig. 3.7 visualizes this matter.

Theoretical Equivalence of EVM and SLIC-EVM

In the following, we investigate why (3.34) estimates the EVM based on discussing a linear channel with uncorrelated additive noise at the output. We already know from Section 2.2 that this model is quite general, since the error due to intermodulation distortion or phase noise can also be modeled as uncorrelated (but not statistically

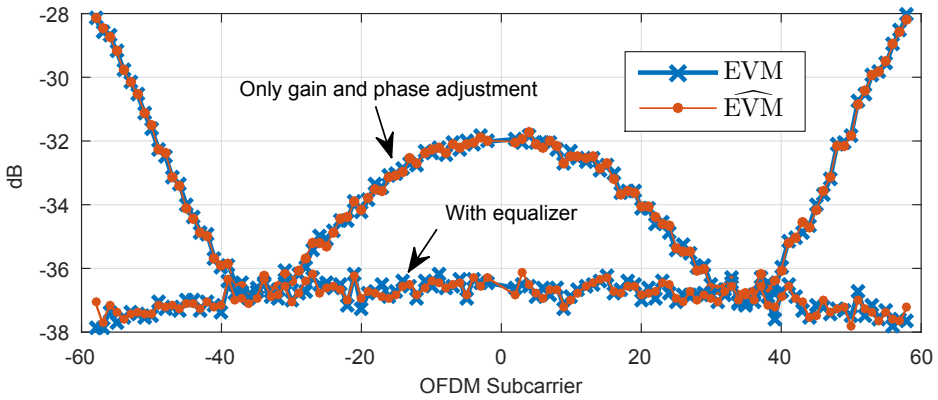

Figure 3.8: Wiener PA model simulation results. SLIC-EVM accurately estimates the subcarrier-dependent EVM. With EQ, the overall EVM and estimated EVM averaged over the data subcarriers are −36.89 dB and −36.88 dB, respectively.

independent) additive noise. As already highlighted in Section 2.2.3, the correlated co-channel distortion can be removed by the equalizer.

The equivalence of EVM and SLIC-EVM can be derived concisely by analyzing each subcarrier k independently. Below, we use bold-face to denote $L \times 1$ vectors, and inner products to sum (average) over L symbols for EVM and L PSD-blocks for SLIC-EVM, respectively. With $\boldsymbol{V}_k$ denoting the additive noise, the DUT output signal model is

$$\boldsymbol{Y}_k = H_k \boldsymbol{X}_k + \boldsymbol{V}_k. \tag{3.38}$$

Assuming an equalizer that inverts the linear channel H_k, the EVM is

$$\text{EVM}[k] = \sqrt{\frac{\boldsymbol{V}_k^{\text{H}} \boldsymbol{V}_k}{(H_k \boldsymbol{X}_k)^{\text{H}} H_k \boldsymbol{X}_k}}. \tag{3.39}$$

The definition of SLIC-EVM in (3.34) can be written as

$$\widehat{\text{EVM}}[k] = \sqrt{\frac{\boldsymbol{E}_k{}^{\text{H}} \boldsymbol{E}_k}{\hat{\boldsymbol{Y}}_k{}^{\text{H}} \hat{\boldsymbol{Y}}_k}} \tag{3.40}$$

$$\boldsymbol{E}_k = \boldsymbol{Y}_k - \hat{\boldsymbol{Y}}_k \tag{3.41}$$

$$\hat{\boldsymbol{Y}}_k = \hat{H}_k \boldsymbol{X}_k\,. \tag{3.42}$$

Assuming $\hat{H}_k = H_k$ in (3.42) and using the signal model in (3.38) we have $\boldsymbol{E}_k = \boldsymbol{V}_k$. Inserting into (3.40) reveals that $\widehat{\text{EVM}}$ equals the EVM in (3.39).

3.2.3 Results

The test signal used for all results presented in this section is an 802.11ac WLAN signal with 40-MHz bandwidth and 320 data symbols. Fig. 3.8 shows simulation results using

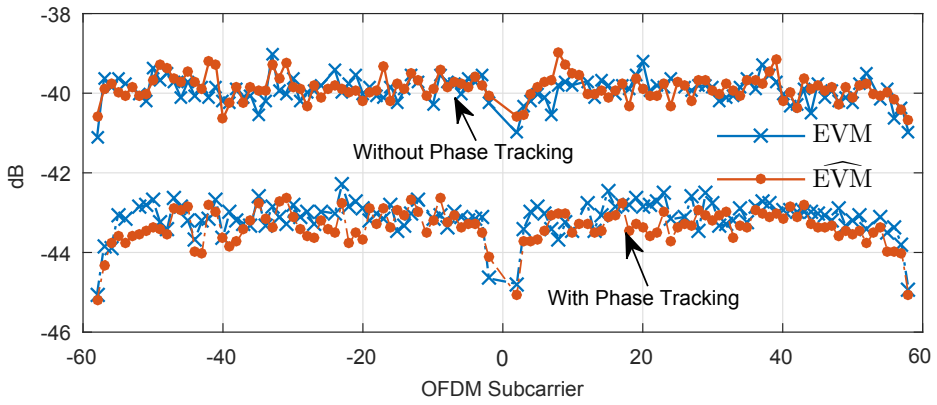

Figure 3.9: Phase noise simulation results. SLIC-EVM estimates the standard EVM very well both in case with and without phase tracking (de-rotation). The average EVM and SLIC-EVM values are -39.92 dB, and -39.86 dB without phase-tracking; and -43.11 dB, and -43.35 dB, with phase tracking, respectively.

the Wiener PA model we also used in [A4] (a 3-Tap FIR filter followed by the Saleh PA model in (19) in [A4]), illustrating the importance of using an equalizer. To demonstrate the effect of de-rotation on EVM and SLIC-EVM, we use the phase noise model from Fig. 2.3. As shown in Fig. 3.9, SLIC-EVM is able to estimate the standard EVM both with and without phase tracking.

Our measurement setup consist of a PC with MATLAB for signal generation and analysis, an Agilent PSG for waveform generation and mixing to 5.6 GHz, an RFMD 5522 WLAN PA as a nonlinear DUT followed by a 30 dB attenuator, and a R&S FSW vector signal analyzer (VSA) for downmixing the attenuator's output and capturing the digital baseband signal. We generated and sampled the signals at $f_s = 100$ MHz, the maximum sample rate of the PSG. Since we do not have the VSA demodulation option for 11ac WLAN, we use our own code for EVM analysis. The equivalence of results obtained using our EVM analyzer with those measured with a commercial EVM analyzer, is verified in Section 4.4.

In Fig. 3.10, we present frequency-dependent results for three impairment cases: dominated by nonlinearity, dominated by IQ-mismatch, and at our measurement floor. At low levels, the PA has almost linear behavior, resulting in an EVM dominated by the IQ mismatch of the PSG. To achieve a lower measurement floor we employ frequency-dependent IQ calibration using a widely-linear IQ mismatch pre-compensation filter [5] with 10 filter taps. The results of a power sweep are shown in Fig. 3.11, with and without the above-described IQ mismatch calibration. The SLIC-EVM results deviate less than 0.2 dB from regular EVM for the entire range of error levels from -50 dB to -15 dB.

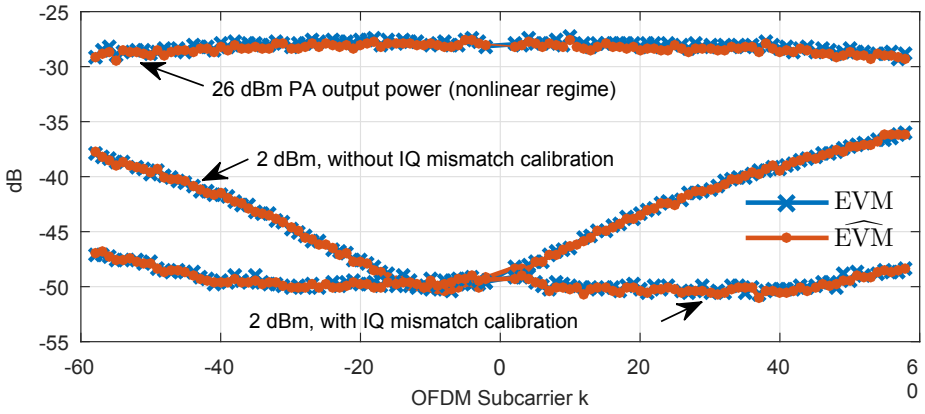

Figure 3.10: Measurement of the RFPA5522. At low power (2 dBm), the EVM is dominated by generator IQ mismatch, which we pre-compensate by applying a widely linear 10 Tap FIR filter (IQ mismatch calibration). At high levels, the nonlinearity of the PA prevails.

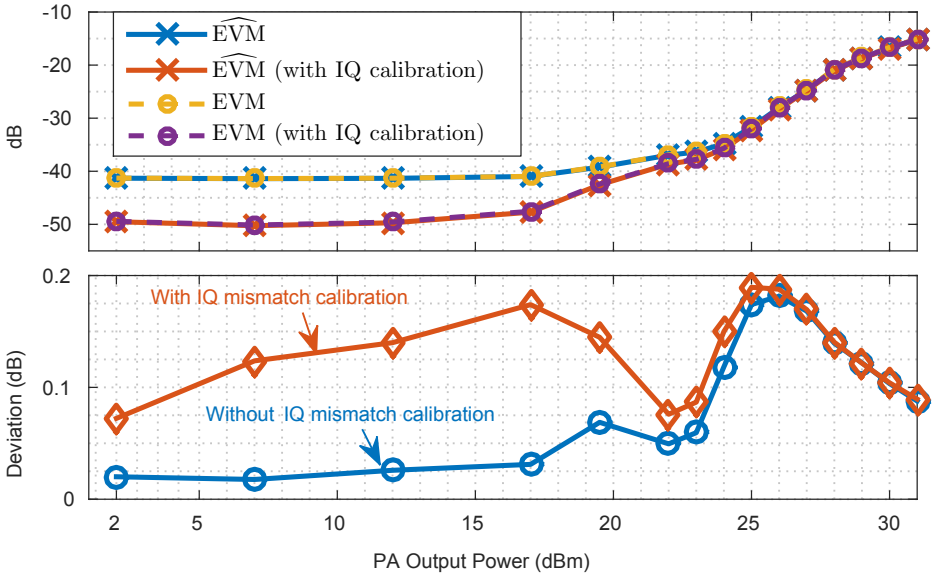

Figure 3.11: Measurement of the RFPA5522 with swept PA input power. The deviation $\text{EVM(dB)} - \widehat{\text{EVM}}\text{(dB)}$ is less than 0.2 dB over the entire range of power levels.

3.3 Direct Optimization of EVM via Digital Predistortion

This section presents the multi-objective predistorter optimization approach proposed in [A3]. Besides introducing the multi-objective optimization paradigm to DPD identification, [A3] was also the first to consider constrained optimization for DPD identification. While conventional DPD identification requires feedback ADCs with high bandwidth, the proposed scalar feedback allows for a much lower bandwidth. This motivates the measurement method in the following Chapter 4, as discussed at the end of the present section.

3.3.1 Problem Description

Modern wireless standards pose challenging demands on the transmitter to achieve the required quality of service at high throughput. Typically, both the in-band and out-of-band behavior of the transmitted signal are subject to standard-specific requirements. In WLAN, maximum allowed error vector magnitude (EVM) values are specified to restrict the in-band error. To restrict the out-of-band spectral broadening, the power spectral density (PSD) of the transmitted signal must stay below a given spectral mask.

To achieve high power efficiency, the power amplifier (PA) of a transmitter must be operated close to its saturation level [24]. This, however, increases nonlinear distortion which leads to an increase of in-band error and spectral broadening. To fulfill the standard, the PA must hence be backed-off, leading to decreased transmitter power output and decreased efficiency.

The trade-off between efficiency and linearity can be tackled by means of digital predistortion (DPD) [91]. The idea behind DPD is to linearize the PA by applying an inverse characteristic on the digital baseband signal before the RF-part of the transmitter. Besides the choice of the DPD filter structure, the identification of parameter values for a given DPD structure has a big impact on the linearization performance and has attracted much research interest [1, 58, 60, 78, 139, 161]. DPD identification is an optimization task and hence the outcome depends heavily on the objectives, i.e., what costs are minimized.

Most DPD identification schemes, e.g., [1, 24, 161], focus on matching the DPD input and the PA output signal in the time-domain by minimizing a mean squared error (MSE) criterion. Ideally, if the DPD succeeds in driving the MSE to zero, perfect linearization is achieved and the DPD is also optimal with respect to the in-band and out-of-band performance metrics defined in the standard. However, due to under-modeling, measurement noise, or the use of a convex optimizer for a non-convex problem, perfect linearization is typically not possible. The best[4] result can be expected if the standard

[4]Here, "best" is defined with respect to the standard metrics. This definition is practically meaningful because system designers also use these metrics to judge the transmitter performance.

metrics are directly optimized. This can be achieved by means of meta-heuristics [84] that are known for their global optimization capabilities. Such algorithms have already been shown to be effective for DPD of real-world PAs [1, 78, 139].

In [139], a memory polynomial DPD is identified based on a genetic algorithm minimizing an out-of-band emission objective allowing for a lower rate in the feedback path. However, the reported linearization performance is not better than with conventional wide-band feedback. Laki and Kikkert [78] also minimize an out-of-band error metric, the weighted adjacent channel power. There, the weighting introduced to trade off in-band and out-of-band distortion brings a heuristic factor into the objective function. Hence, an optimal trade-off in terms of in-band and out-of band distortion cannot be expected. In [1], particle swarm optimization is used to jointly estimate parameter values and DPD structure parameters. However, a time-domain least-squares error cost function is used.

All identification methods discussed above are unconstrained. To know if the solution fulfills the standard, the DPD must be tested separately, after the actual identification. If the constraints are not met, one can only repeat the identification with different settings based on trial-and-error.

In the following, we investigate the effectiveness of direct, multi-objective optimization (MOO) of in-band error and spectral broadening metrics for DPD identification. We set up a known MOO algorithm [76] for DPD optimization of a WLAN system and present simulation results that support the proposed approach. The proposed approach [A3] is the first to address constrained optimization for DPD identification. It allows for checking the compliance with the communication standard at the time of the DPD identification.

3.3.2 Method

Multi-objective optimization (MOO) seeks for Pareto-optimal solutions instead of a single optimum. Pareto-optimal solutions are non-dominated, which means that none of the objectives can be improved without worsening at least one other objective [76]. Instead of weighting the objectives prior to optimization, MOO returns a set of solutions revealing insight into trade-offs between the objectives [156]. As illustrated in Fig. 3.12, we use MOO to directly optimize transmitter performance metrics.

Transmitter Performance Metrics

In WLAN, the required in-band performance is specified by the EVM. The maximum allowed EVM at the data-carrying subcarriers is limited depending on the modulation

[5] DAC, ADC, up- and down-conversion are neglected in this illustration because we use a baseband PA-model to demonstrate the effectiveness of our approach.

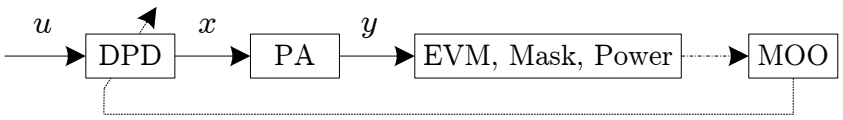

Figure 3.12: Proposed direct, multi-objective optimization (MOO) of transmitter performance metrics. For the WLAN application considered in this paper, we use the error vector magnitude (EVM), spectral mask margin and the PA[5] output power as objectives and constraints.

Table 3.1: Allowed EVM according to the IEEE 802.11ac standard [62, Tab. 22-24]

MCS	Modulation	Coding Rate	EVM (dB)
1	BPSK	1/2	-5
2	QPSK	1/2	-10
3	QPSK	3/4	-13
4	16-QAM	1/2	-16
5	16-QAM	3/4	-19
6	64-QAM	1/2	-22
7	64-QAM	3/4	-25
8	64-QAM	3/4	-27
9	64-QAM	3/4	-30
10	256-QAM	5/6	-32

scheme and coding rate, e.g., $\mathrm{EVM}_{\max} = -25\mathrm{dB}$ for 64-QAM and coding rate 3/4 [62].

The WLAN standard requires the power spectral density (PSD) of the transmitted signal to stay below a given spectral mask. To have a real-valued metric instead of only a pass/fail criterion for assessing the out-of-band spectral broadening, we use the maximum out-of-band difference of the transmitted signal PSD and the mask (in dB), refer to it as spectral mask margin, and denote it as Mask$(\cdot)$. Consequently, the WLAN standard requirement translates to a mask margin less than zero.

A metric that should not be neglected when assessing the DPD performance is the power of the PA output signal, since by lowering the power, the linearization performance can easily be improved, which does however counteract the goal of having low input power back-off[6]. To make fair comparisons, the PA output power should hence not be decreased by inserting the DPD system. Further, widely-used metrics to asses transmitter linearity are the time-domain normalized mean squared error (NMSE) between the source signal $u[n]$ and PA output $y[n]$ [161] and the adjacent channel power ratio (ACPR) of the PA output [92].

[6]For a given maximum PA output power, there is a direct inverse relation between the output back-off and the PA output power [161].

Multi-objective optimization for DPD

The output $x[n]$ of a DPD model H_{DPD} to an input signal $u[n]$ given a vector of real DPD model parameters $\boldsymbol{\theta} = \begin{bmatrix}\theta_0, \ldots, \theta_{N-1}\end{bmatrix}^T \in \mathbb{R}^N$ is denoted as

$$x[n;\boldsymbol{\theta}] = H_{\mathrm{DPD}}\{\boldsymbol{u}_M[n], \boldsymbol{\theta}\} \tag{3.43}$$

where n denotes discrete time and $\boldsymbol{u}_M[n] = \begin{bmatrix}u[n], \ldots, u[n-M]\end{bmatrix}^T$ indicates that H_{DPD} is a model with M samples memory. The baseband equivalent of the PA output is denoted $y[n]$. If it is of relevance, the dependence of the PA output on the DPD parameter vector is made evident by writing $y[n;\boldsymbol{\theta}]$. We tackle DPD identification as a general, multi-objective optimization problem:

$$\begin{aligned} \underset{\boldsymbol{\theta}}{\text{minimize}} \quad & \begin{bmatrix}f_1(\boldsymbol{\theta}), \ldots, f_{N_{obj}}(\boldsymbol{\theta})\end{bmatrix} \\ \text{subject to} \quad & g_i(\boldsymbol{\theta}) \leq b_i,\ i = 1, \ldots, N_{\mathrm{cstr}}. \end{aligned} \tag{3.44}$$

For our WLAN application, we use the EVM and spectral mask margin as objectives:

$$f_1(\boldsymbol{\theta}) = \mathrm{EVM}(y[n;\boldsymbol{\theta}]) \tag{3.45}$$

$$f_2(\boldsymbol{\theta}) = \mathrm{Mask}(y[n;\boldsymbol{\theta}]) \tag{3.46}$$

As constraint functions $g_i(\boldsymbol{\theta}), i = 1, \ldots, N$, we use box constraints, i.e., $|\theta_i| \leq \theta_{\max}$. Additionally, we constrain the power to be larger than the power obtained with the initial solution $\boldsymbol{\theta}_0$, i.e., the constraint $g_{N_{\mathrm{cstr}}}(\boldsymbol{\theta})$, is given as

$$-\operatorname{Power}(y[n;\boldsymbol{\theta}]) \leq -\operatorname{Power}(y[n;\boldsymbol{\theta}_0])\ . \tag{3.47}$$

To tackle the MOO problem in (3.44), we employ the GDE3 algorithm [76], which generalizes differential evolution for global optimization with an arbitrary number of objectives and constraints. To obtain the initial population, we take an initial guess $\boldsymbol{\theta}_0$ for the coefficients and generate the other $N_{\mathrm{pop}} - 1$ solutions by random perturbation. The initial guess $\boldsymbol{\theta}_0$ may be obtained from any other DPD identification method.

3.3.3 Results

Setup

In [60] it is shown that without measurement noise, the indirect learning architecture (ILA) outperforms direct learning and hence we use the ILA in the noise-free case as a baseline for comparison and as an initial solution $\boldsymbol{\theta}_0$ for our method. We use a WLAN signal with 40 MHz bandwidth, 64-QAM subcarrier modulation, $0.8\,\mu$s cyclic prefix and 10 ns windowed overlap between consecutive symbols as our source signal $u[n]$. The signal generator performs oversampling by a factor 5, yielding 200 MHz

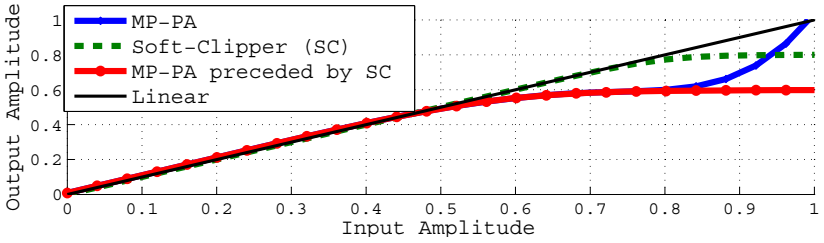

Figure 3.13: PA-model output to a ramp-function on the input. To prevent the MP-PA model from [24] from expanding input amplitudes > 0.8, the MP-PA is preceded by a soft-clipping function in our PA model.

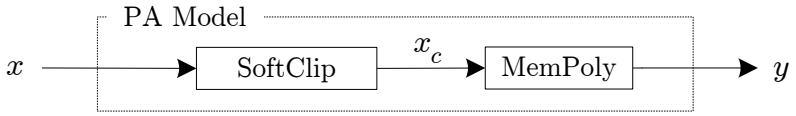

Figure 3.14: The PA model used in our simulations.

samplerate. For DPD identification, we use 32 OFDM symbols, i.e., 25624 complex-valued samples at 200 MHz samplerate. In the GDE3 optimization algorithm, we use a population size $N_{\text{pop}} = 30$, DE stepsize $F = 0.4$, crossover-probability CR $= 0.8$, and $\theta_{\max} = 1000$. We use a fixed number of 100 iterations, but other stopping criteria could also be devised, e.g., stop as soon as a feasible solution fulfilling the standard is found.

As a PA-model in our simulations, we use the memory polynomial (MP) PA model from example 2 in [24], hereafter referred to as the MP-PA. As shown in Fig. 3.13 the MP-PA exhibits a physically unrealistic expansion behavior for input amplitudes larger than 0.8. Such an expansion is typical for polynomial PA models outside the fitting range. Most likely, the MP-PA was fitted from data with amplitudes smaller than 0.8. Therefore, our PA-model includes a soft-clipper [113] preceding the MP-PA, as shown in Fig. 3.14. The soft-clipper is given as

$$x_c[n] = \frac{g_0\,|x[n]|}{\left(1 + \left(\frac{g_0|x[n]|}{x_{\text{c,max}}}\right)^{2p}\right)^{\frac{1}{2p}}} e^{j\angle x[n]}\,, \tag{3.48}$$

with $x_{\text{c,max}} = 0.8$, $p = 10$, and $g_0 = 1$. A MP with input $u[n] \in \mathbb{C}$, output $x[n] \in \mathbb{C}$ and coefficients $c_{p,m} \in \mathbb{C}$ is given as

$$x[n] = \sum_{p\in\mathbf{P}} \sum_{m=0}^{M} c_{p,m}\, u[n-m]\, |u[n-m]|^{p-1}\,. \tag{3.49}$$

As a DPD model, we also use a MP with $M = 2$ samples memory and $\mathbf{P} = \{1, 3, 5\}$, i.e., we consider odd orders up to the 5th order. For reference, the MP-PA coefficient values from [24], and the DPD-coefficients obtained by the ILA and our MOO approach are

Setting	Power	EVM	Mask	NMSE	ACPR
No Dpd	+1.91	**−24.01**	−1.11	−21.78	−28.60
ILA-DPD	+1.94	−29.85	**+3.81**	−26.08	−31.02
MOO-DPD	+1.95	−30.16	−3.64	−26.95	−31.37

Table 3.2: Simulation Results in Decibel

listed in Table I in [A3]. The real optimization parameter vector in (3.44) is obtained by stacking the real and imaginary parts of all $c_{p,m}$, the ordering is of no relevance. As we do not optimize the linear coefficient $c_{1,0}$, we have 16 real optimization parameters in total.

Simulation Results

We made $N_{\text{eval}} = 25$ evaluation trials, each with 320 random OFDM symbols and specify the mean over the individual performance metrics discussed in Section 3.3.2 in dB, e.g., EVM $= \frac{1}{N_{eval}} \sum_{i=1}^{N_{eval}} \text{EVM}_i$. The results are shown in Table 3.2, violations of the communication standard are indicated in boldface. The required EVM of -25 dB cannot be achieved without DPD, while the mask constraint (Mask $< 0\,$dB) is just met. With ILA-based identification, the DPD reduces the NMSE, EVM and ACPR, but the mask margin is deteriorated. Using the same DPD-model, our MOO approach finds coefficients that achieve the desired result: The mask margin is significantly improved, the standard constraints (mask margin $<$ 0dB, EVM < -25dB) are fulfilled, and the power is slightly increased, compared to using no DPD or the ILA-DPD.

At low output power[7] (high back-off), the ILA works well in reducing both the EVM and mask margin. However, at high back-off the EVM and mask margin are anyways far beyond the maximum allowed values, even without the DPD. Hence, it is more interesting to investigate a higher power (low back-off) case, where without DPD, the constraints imposed by the WLAN standard are not met, as shown in Table 3.2. The strong expansion characteristic of the ILA-DPD in the high-power setting drives the PA even deeper into saturation leading to a deteriorated mask margin, see Table 3.2 and the right plot in Fig. 3.15. This effect has been described as "DPD avalange effect" in [92]. Iterating the ILA-identification as in [60] makes the problem even worse. Using a DPD identified at a lower power at the high-power setting does also not help.

As shown in Fig. 3.16, our MOO approach reveals a trade-off between the EVM and mask margin. This effect gets pronounced when the PA is operated close to its saturation point. The initial solution (ILA-DPD) is far away from the Pareto-front in Fig. 3.16, representing the best trade-off between the EVM and mask objective as obtained by the MOO population. Our MOO approach offers the freedom to select any solution

[7] The power of $y[n]$ was changed by changing the power of $u[n]$, the PA-model was left untouched. The output back-off at the high power setting is approximately 6.7 dB.

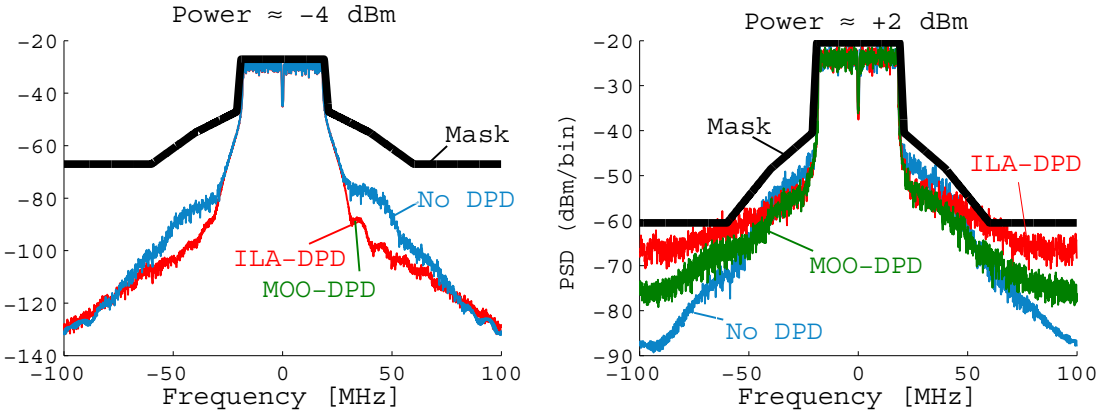

Figure 3.15: PA-model output PSD and spectral mask. For the low power setting on the left, the ILA improves spectral broadening and cannot be improved further by optimization. For the high-power setting on the right, things are different: When using the ILA-solution, the spectral mask (black) is violated (red), whereas our MOO-DPD improves the out-of-band behavior as well as the EVM, see Table II.

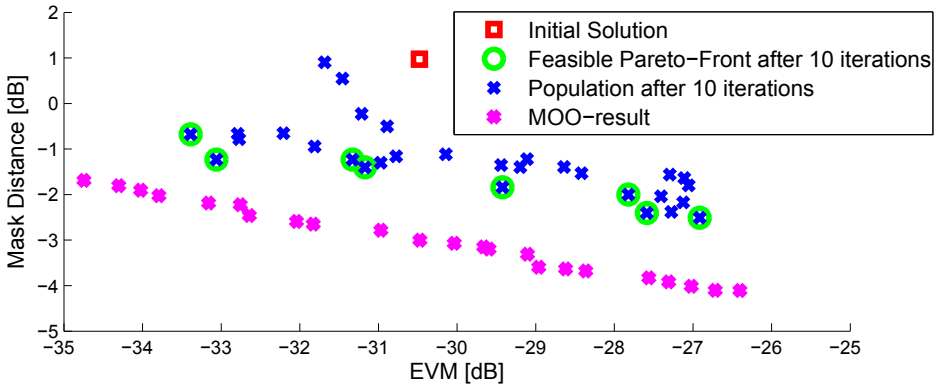

Figure 3.16: Population of solutions and Pareto-front. Each point illustrates the objective function values for one solution within the population. After 100 trials a smooth trade-off curve of feasible solutions has formed revealing that mask margin and EVM are conflicting objectives. The initial solution (ILA-DPD) can be improved significantly (lower values of EVM and Mask are better).

on the Pareto-front. For the results reported in Table 3.2, we chose a solution with an EVM slightly better than that achieved by the ILA-DPD[8].

[8]The values depicted in Fig. 3.16 cannot be directly compared to those in Table 3.2 because Fig. 3.16 is based on a single training signal, whereas Table 3.2 is based on several random test signals.

Discussion

The presented identification approach identifies "good" DPD coefficients for a given DPD model structure. We have stressed out that it is reasonable to define "good" with respect to the transmitter performance metrics defined in the particular communication standard, e.g., EVM and spectral mask in WLAN. Traditional DPD identification methods are based on single-objective optimization. These methods are, in general, not able to provide an optimal trade-off between the EVM and spectral mask margin, potentially leading to standard violations. The proposed multi-objective method, on the other hand, returns a set of solutions providing insight and access to a good trade-off between the objectives.

The presented identification approach is very general and can be easily adapted to other DPD structures, communication standards, objectives, and constraints. Instead of having to separately test the DPD to check if the communication standard is met, our method allows for direct incorporation of the constraints imposed by the standard. Because it is not limited to DPD models that are linear in the parameters, our method is particularly well-suited for assessing new DPD model structures and may also serve as a reference for assessing the performance of other identification algorithms. It is guaranteed[9] that our method delivers a solution that is equal or better than the solution obtained by any other method, because our method can be initialized with the coefficients obtained by any other method.

The practical application of stochastic optimization to DPD is not without difficulties. First, the global optimization of a larger number of DPD parameters may not converge due to the "curse of dimensionality" [84]. To decrease the dimensionality of the problem, several smaller problems may be scheduled by forming groups of coefficients and optimizing them consecutively. Though suboptimal, this can lead to good results in practice [77, 78]. Further difficulties emerge when trying to apply the stochastic optimization approach to a hardware in-the-loop, i.e., when measuring the performance metrics at the output of a real PA. One reason why this thesis does not cover this topic is that using our measurement setup, the download and acquisition of a new solution (predistorted signal) and its response (PA output), is very slow, e.g., nearly 10 seconds. Furthermore, there are some major research challenges: Testing very bad solutions on the hardware must be avoided to avoid wasting time and to not damage the hardware. To this end, a PA model could be used and only solutions that perform reasonably well with that model are tested on the hardware. Finally, the optimizer must be robust to noise in the objective function(s), because due to noise and drift the measured result may not be the same even if the same solution is tested twice.

An important advantage of the proposed method is that the sample rate and the bandwidth of the feedback required for DPD identification can be much lower than with traditional methods that require the PA output signal in the digital baseband. The

[9] Presuming noise-free objective functions and a time-invariant system.

problem of reducing the feedback rate in DPD identification has experienced an increased research attention in recent years [55, 59, 150, 160]. Although the popular undersampling approach allows to reduce the sampling rate, the bandwidth of the sampling process is still coupled to the bandwidth of the signal. With our stochastic optimization, to test N trials[10] and obtain the optimization result within a second, we just need N EVM results, N Mask distance values, and N power values, i.e., theoretically, we only need a feedback rate of only $3N$ Hz in that case. Unfortunately, there is a major flaw with this: The EVM measurement requires high-rate ADCs. However, if we replaced the EVM measurement with an NPR measurement, this problem would vanish. We would just need to quantize the results of power measurements in the notch of the NPR signal, the channel power, and the power in the out-of-band[11]. Replacing the EVM with power ratio measurements inspired by the NPR is the topic of the next two chapters.

3.4 Conclusions

This chapter contained three different original contributions:

Section 3.1 presented a method to exclude IQ mismatch from regular EVM measurements. We used a special test signal obtained by nulling data subcarriers $k_0(l)$ and $-k_0(l)$ of a standard OFDM signal. Due to the symmetry around the carrier, there is no IQ mismatch at those nulled subcarriers. By evaluating the EVM separately for the nulled subcarriers and the remaining modulated subcarriers, we obtained two EVM results from a single measurement: A "regular" EVM result including IQ mismatch and a result without IQ mismatch. This can be helpful when troubleshooting transmitters or receivers, or when measuring RF DUTs. In the latter case, IQ mismatch is not part of the DUT but constitutes an error of the measurement chain. Thus, IQ mismatch should be excluded from the EVM result of an RF DUT. The proposed method achieves this without additional, potentially imperfect calibration.

Section 3.2 presented SLIC-EVM for analyzing the EVM without demodulating the data symbols. We were able to replicate the effect of equalization and de-rotation in regular EVM analysis by knowing only the main parameters of the communication standard, i.e., the symbol length, equalizer length, and the location of the data subcarriers. SLIC-EVM results agree very well with the regular EVM in case of phase noise, IQ mismatch, and PA nonlinearity, as shown in simulations and measurements. Although we focused on WLAN OFDM systems, we can be very confident that SLIC-EVM also works for other standards, because we made no assumptions on the excitation signal (like Gaussianity). Furthermore, the linear filter estimated in SLIC-EVM can be easily adjusted to the length of the channel estimate, which may be different for different standards.

[10] N is the size of the population times the number of iterations, e.g. $N = 50 \cdot 200$.
[11] Instead of the spectral mask distance, we may optimize the adjacent channel power ratio.

Section 3.3 presented a novel stochastic, multi-objective optimization (MOO) approach to DPD identification. In contrast to traditional minimization of a mean squared error in the time-domain, we directly optimized the transmitter performance metrics relevant for the given communication signal standard. Therefore, the method allows to check for standard compliance at the time of DPD identification. The Pareto-front obtained from MOO revealed a trade-off between the inband performance in terms of the EVM, and the out-of-band performance in terms of the spectrum mask margin. We have compared the proposed method with the widely-used indirect learning architecture (ILA) by means of simulations. While the ILA leads to violations of the spectral mask when using the PA at low power back-off, the proposed method does not suffer from this problem and achieves superior performance using the same DPD structure. Finally, we highlighted that by replacing the EVM with the NPR, the proposed optimization principle allows for a very low ADC rate.

4

EPR – Error Power Ratio

This chapter is largely based on the material presented in [A4] and [A5], © 2017 IEEE. We analyzes the capability of the noise power ratio (NPR) to estimate the EVM. More precisely, we investigate the following hypothesis [A4]:

The principle behind NPR allows to accurately estimate the EVM in OFDM systems in case of typical RF transmitter impairments like phase noise, IQ imbalance, and power amplifier nonlinearity.

The main contributions of this chapter are to present:

- The effect of IQ mismatch and phase noise on the NPR.
- An analysis and guidance how to setup NPR (EPR) measurements to estimate the EVM in OFDM systems with phase noise, IQ mismatch and power amplifier nonlinearity.
- The usage of multiple stopbands for resolving smooth frequency-dependent errors with a single measurement.
- A straightforward procedure to obtain an NPR test signal preserving the statistics of the OFDM signal.
- Measurement results comparing NPR (EPR) with EVM over a wide range of inband error levels, using a commercial hardware WLAN EVM analyzer as a reference.
- Monte-Carlo simulation results verifying the equivalence of EVM and EPR for a wide range of simulated IQ mismatch, phase noise and nonlinearity impairment scenarios.
- A discrete time Wiener Hammerstein model with feedback allowing for the simulation of a wide range of PA nonlinearity scenarios by tuning only a few, intuitive parameters.

4.1 Introduction

Section 1.1.3 already introduced the NPR and motivated why investigating the hypothesis stated on page 75 is worthwhile. To recap: The NPR test signal (DUT input) is band-limited Gaussian noise filtered with a bandstop- or notch-filter. An error power estimate is obtained by measuring the power of the DUT output within the stopband. This can be done with a swept-tuned spectrum analyzer as presented in Section 2.1.3, i.e., no IQ demodulation and synchronization is required, which is a major advantage of the NPR over the EVM.

The roots of NPR measurements date back to a paper from 1939 [57] describing early frequency division multiplexing telephone systems [68]. As indicated by respective sections in textbooks on nonlinear distortion measurement [47, 108] and on RF design [8, 49], the NPR has become an established measurement method. Furthermore, there are application notes on NPR measurements by major measurement companies [43, 66, 68, 71]. The NPR is popular for quantifying distortion and noise in applications like power amplifier design [145], cellular systems and satellite networks [147], and testing of ADCs [10, 61, 63]. The EVM is even more popular and is the standard measurement for quantifying the inband error of modern transceivers for WLAN [62], DVB [23, 146], and mobile communication networks like GSM/EDGE [56], UMTS [99], and LTE [122].

For the trivial case of AWGN there is a direct relation between NPR and EVM, as already outlined in Section 1.1.3. However, if the DUT includes nonlinearity, phase noise or modulator imperfections, the inband error depends on the test signal exciting the DUT. Since the NPR test signal must include at least one inband notch, it cannot be identical to the EVM test signal. Therefore, it is not obvious that measurements of NPR can be used to replace EVM, in cases when the inband error depends on the test signal. Rather, prior research seems to suggest quite the opposite [47, 108], as discussed below.

A thorough search through the literature revealed there is no publication on the influence of IQ imbalance and phase noise on the NPR, and only a single paper that explicitly addresses the relation of EVM and NPR [137]. In [137], Sombrin relates the EVM and NPR via the SNR, but does not cover important issues like the bandwidth and location of the stopband(s) of the NPR test signal, or the frequency-dependence of the error. Interestingly, [137] lists the equivalent gain method [19] as a measurement method for the NPR. As discussed in Section 3.2, the equivalent gain method [19] allows to estimate the EVM *without* equalization and without de-rotation. However, the NPR estimates the EVM *with* equalization and de-rotation, as shown later in this chapter.

Sombrin [137] also brings up the peculiar idea of estimating the NPR by means of an EVM measurement, which is further elaborated in [87]. That paper reports good agreement of the NPR and the NPR estimated from EVM. However, it remains unclear why it is an advantage to use a "commercial high resolution and narrow-band IQ demodulator" to first measure the EVM, instead of measuring the NPR directly with

a spectrum analyzer. Another interesting issue in [87] is the definition of the EVM using the maximum of the constellation instead of the average constellation power in the denominator. With maximum normalization, the EVM depends on the modulation format, i.e., it will be different for 16-QAM and QPSK. The EVM defined this way is not a direct estimate of the SNR, but needs a correction factor. Unfortunately, the normalization by the maximum is also contained in standards for testing active cable telecommunications equipment [136] and measurement guidelines for digital video broadcasting (DVB) systems [23]. The more reasonable definition with average constellation power normalization is termed modulation error ratio (MER) in [23, 87, 136].

While there is not much literature explicitly relating the NPR to the EVM, there are a few papers addressing the (in)ability of the NPR to quantify the inband error due to a nonlinearity. Pedro and Carvalho [108] argue that the NPR *underestimates* the inband error up to 7 dB, because they view correlated co-channel[1] distortion as a relevant source of error. However, Geens *et al.* [42] reach the conclusion that the approach in [108] is only valid if the input to the nonlinear system varies a lot in amplitude. In most practical cases however, the power of the and NPR is a good figure of merit for the inband error [42]. In [110], Pedro *et al.* note that for systems where an equalizer gets rid of dynamic linear effects, and hence the correlated co-channel distortion, the NPR is a good choice to assess the inband error.

Gharaibeh [47] shows that the NPR *overestimates* the inband error of a (quasi-) memoryless nonlinearity by up to 10 dB if the excitation signal differs significantly from a circularly-symmetric complex normal (CSCN) distribution, where the in-phase (I) and quadrature (Q) component are independent and identically distributed (i.i.d) Gaussian [129]. However, the NPR is shown to be a good estimate of inband distortion, if the signal approaches a CSCN distribution. In OFDM systems, equalizers are ubiquitous and the signal is CSCN distributed. Consequently, [42, 47, 108] do not contradict our hypothesis on page 75.

Traditional NPR measurements use an analog noise source and an analog filter to generate the test signal [121]. More recently, digital test signal generation has been proposed [115], allowing for better repeatability and lower test times [68]. A multitone signal is generated via inverse fast Fourier transform (IFFT) of a large number (1k–10k) of tones with random phases. Equal magnitudes are used in [115], apart from "5 to 10% of the tones" in the center of the bandwidth that are set to zero to form the stopband. As outlined above, it is desirable to have a test signal matching the statistics of the communication signal of interest. Therefore, the higher order cross PSDs of a multitone can be optimized [109], which is however computationally demanding [17]. For matching the distribution of each individual sample of an OFDM signal, such an optimization is not necessary, because summing a large number of random phase tones yields independent CSCN distributed samples. However, OFDM uses a cyclic prefix and oversampling may be applied via zero-padding before the IFFT [155]. Consequently,

[1] The word "co-channel" is used instead of "inband" in some relevant papers, e.g., [108].

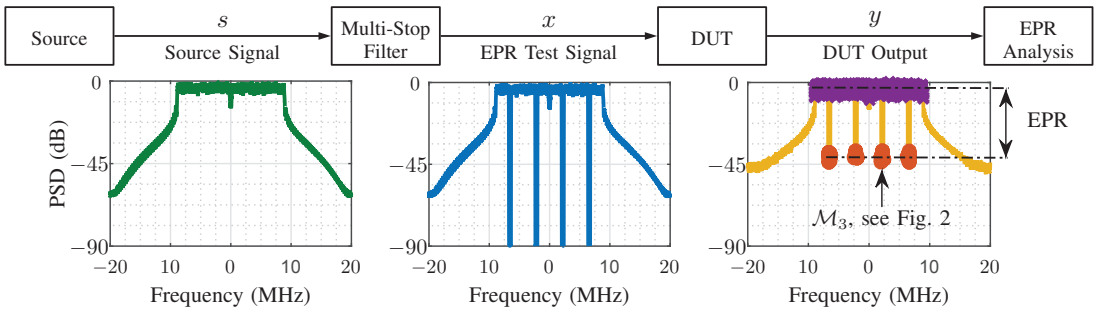

Figure 4.1: Principle of the error power ratio (EPR). The source signal s is the communication signal of interest. Depicted is a WLAN signal with 20 MHz bandwidth. We obtain the test signal x by digitally filtering s to attenuate parts of the inband, achieving steep stopband notches. The device under test (DUT) introduces errors, which rise the power in the stopbands of the DUT output y. The EPR is the ratio between average power in the stopbands and average power in the inband of y.

the samples are not independent. Rather, there is correlation, manifesting in a PSD different to the PSD obtained from a signal with random phases as discussed above.

The shape of the PSD is important when assessing the out-of band behavior, e.g., spectral mask [62] or adjacent channel leakage ratio (ACLR) [122]. It is desirable to have an NPR signal matching the out-of-band PSD of the OFDM signal, because this allows for measuring the inband error (NPR) and the out-of-band performance with the same test signal. With established NPR test signals [115] this is not advisable, because they are strictly bandlimited.

To use a new measurement method with confidence, it is not enough to show that it works for a particular DUT. It might be plain luck that the method behaves as expected. To address this issue, we will have a look at simulation results obtained from numerous simulations with randomly varied impairment model parameter values. These Monte-Carlo simulations allow to get a feeling for the uncertainty and bias, that we can expect when we measure a new, unknown DUT[2].

4.2 Error Power Ratio

As outlined in the introduction, we use the term error power ratio (EPR) to distinguish our EVM estimation method from the traditional NPR [68, 116]. The principle of the EPR is depicted in Fig. 4.1. In Fig. 4.2, we zoom into the third stopband and illustrate the notation used in the definition of the EPR below.

[2]Under the premise that the inband frequency-response of the DUT and the error is gentle, which is derived and discussed in Section 4.3.1 and 4.5.2.

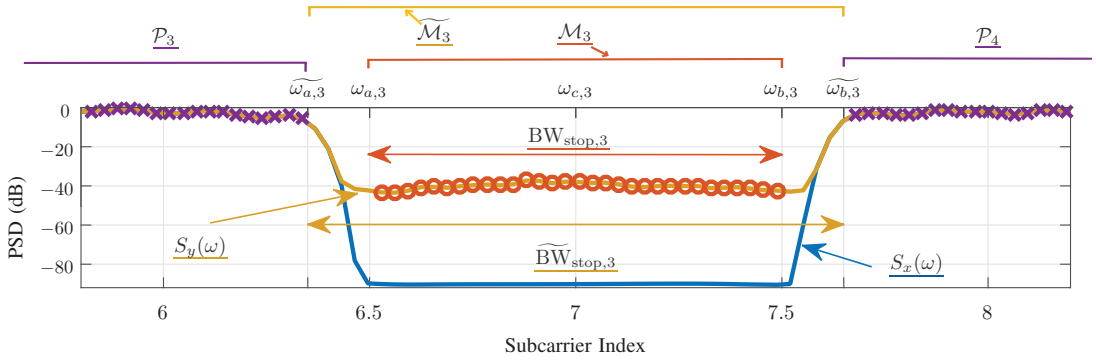

Figure 4.2: Close-up of the third stopband $\mathcal{M}_3$ from Fig. 4.1. The baseband center frequency is at 2.1875 MHz, i.e., $\omega_{c,3} = 7\Delta_f 2\pi$, with the WLAN OFDM subcarrier spacing being $\Delta_f = 312.5$ kHz. We choose the stopband-width for integrating the error power as $\mathrm{BW}_{\mathrm{stop}} = \Delta_f$. The filter stopband $\widetilde{\mathcal{M}_3}$ with bandwidth $\widetilde{\mathrm{BW}}_{\mathrm{stop}} = 1.3\Delta_f$ is chosen to be slightly wider to account for the practically limited filter slope steepness.

4.2.1 Definition

We define the EPR of a signal $x(t)$ as a ratio of the PSD of $x(t)$ averaged over different frequency sets $\mathcal{M}$ and $\mathcal{P}$ as

$$\mathrm{EPR}\{x(t)\} = \frac{\bar{S}_x(\mathcal{M})}{\bar{S}_x(\mathcal{P})} \tag{4.1}$$

where $\mathcal{M}$ is the set of stopband frequencies

$$\mathcal{M} = \bigcup_{m=1}^{N_M} \mathcal{M}_m \tag{4.2}$$

i.e., the union of $N_M \in \mathbb{N} : N_M \geq 1$ individual stopbands $\mathcal{M}_m$. The m-th stopband $\mathcal{M}_m$ is a set of angular frequencies satisfying

$$\mathcal{M}_m = \{\omega \in \mathbb{R} : \omega_{a,m} \leq \omega < \omega_{b,m}\} \tag{4.3}$$

where $\omega_{a,m}$ and $\omega_{b,m}$ are the start and stop frequency of the m-th stopband with center frequency $\omega_{c,m}$ and stopband bandwidth $\mathrm{BW}_{\mathrm{stop},m}$, respectively, as illustrated in Fig. 4.2. The relation to the m-th stopband's center frequency $\omega_{c,m}$ is

$$\omega_{a,m} = \omega_{c,m} - \mathrm{BW}_{\mathrm{stop},m}/2 \tag{4.4a}$$

$$\omega_{b,m} = \omega_{c,m} + \mathrm{BW}_{\mathrm{stop},m}/2 \tag{4.4b}$$

Analogously to (4.3), the set of present bands is denoted as $\mathcal{P} = \bigcup_{p=1}^{N_P} \mathcal{P}_p$, with $\mathcal{P}_p = \{\omega \in \mathbb{R} : \omega_{a,p} \leq \omega < \omega_{b,p}\}$. To compare the EPR of individual stopbands with the subcarrier-dependent EVM defined in (2.71), we define

$$\mathrm{EPR}(k_m) = \frac{\bar{S}_x(\mathcal{M}_m)}{\bar{S}_x(\mathcal{P})} \tag{4.5}$$

where $\mathcal{M}_m$ has a center frequency of $\omega_{c,m} = k_m 2\pi\Delta_f$, with k_m being the OFDM subcarrier index belonging to the mth stopband center, and Δ_f is the subcarrier spacing in hertz. With equal stopband bandwidth $\mathrm{BW}_{\mathrm{stop},m} = 2\pi\Delta_f$, the overall EPR as in (4.1) is the mean over the subcarrier-dependent EPRs, i.e.,

$$\mathrm{EPR} = \frac{1}{N_M} \sum_{m=1}^{N_M} \mathrm{EPR}(k_m)\,. \tag{4.6}$$

Our goal is to use the EPR of the DUT response $y(t)$, i.e., $\mathrm{EPR}\{y(t)\}$ for estimating the EVM. To this end, two constraints are required in addition to the definition in (4.1):

1) Sufficient test signal stopband rejection: The EPR of the test signal $x(t)$ used to excite the DUT must be smaller than the expected error vector power (EVP) to estimate. The EVP is the square of the EVM as defined on page 42. A stopband rejection of $R_{\mathcal{M}} = -10\log_{10}(\epsilon)$ dB is achieved if

$$\bar{S}_x(\mathcal{M}) = \epsilon \bar{S}_x(\mathcal{P})\,. \tag{4.7}$$

As depicted in Fig. 4.2 we achieve approximately 90 dB stopband rejection, which is well below the expected EVM of typical transceiver components. As further explained in Section 4.2.3, not only the signal generation but also the PSD analysis is a crucial factor to be able to observe such a high stopband rejection.

2) Reasonable selection of $\mathcal{P}$ and $\mathcal{M}$: To achieve requirement 1), i.e., a small value of $\mathrm{EPR}\{x(t)\}$, and to provide maximum averaging over frequency, $\mathcal{P}$ should cover the whole signal bandwidth with exclusion of the stopband and transition-band frequencies $\widetilde{\mathcal{M}}$, as indicated in Fig. 4.2. As discussed in Sec. 4.3, a good choice for the individual stopband-widths is the OFDM subcarrier-spacing, i.e., $\mathrm{BW}_{\mathrm{stop,m}} = \Delta_f$. The optimum number and location of the center frequencies of the stopbands $\mathcal{M}_m$ is problem-dependent. There is the following trade-off: Setting N_m too high, i.e., using too many stopbands, increases the likelihood of altering the signal statistics significantly. By using a single stopband $N_m = 1$, on the other hand, frequency-dependent errors cannot be resolved with a single measurement and there is only little averaging of stopband power, which increases the variance of the estimate.

A convenient choice for $\omega_{c,m}$ is to use the pilot-tone locations of the OFDM signal standard, e.g., subcarriers $[-21, -7, 7, 21]$ for the 20–MHz WLAN signal in Fig. 4.1. This way, smooth frequency-dependent errors can be resolved, and an increase in bandwidth increases the number of stopbands. Furthermore, the EPR can be readily compared with the EVM averaged only over the pilots which is provided by typical EVM analyzers. However, one has to be aware that by using the symmetric pilot locations as stopband centers, IQ mismatch is excluded from the EPR, as shown in Sec. 4.3. We further discuss the placement of the stopbands in Section 4.3 and Section 4.5.2.

4.2.2 Signal Generation

We use a digital approach to generate a test signal $x[n]$. In a measurement scenario where an analog signal $x(t)$ is required, we copy the signal vector $\mathtt{vX} = \{x[n]\}$ to the memory of a signal generator which performs the required digital to analog conversion. Similar to Reveyrand *et al.* [115, 116], we generate our test signal vector `vX` by means of an IFFT. However, instead of using constant amplitudes and random phases, we obtain the frequency-domain vector `vXf` via an FFT of the communication signal vector `vS`, and set those bins `vIndexNull` that correspond to stopband frequencies $\omega \in \widetilde{\mathcal{M}} \supset \mathcal{M}$ to zero before the IFFT. This procedure is precised in Listing 4.1.

Above, $\widetilde{\mathcal{M}} \supset \mathcal{M}$ indicates that we set broader bands to zero than the actual integration range $\mathcal{M}$ used to compute the EPR in (4.1). $\widetilde{\mathcal{M}}$ features the same center frequencies $\omega_{c,m}$ as $\mathcal{M}$ in (4.3). The only difference is that we use $\widetilde{\mathrm{BW}}_{\mathrm{stop},m} = K_{\mathrm{stop}}\,\mathrm{BW}_{\mathrm{stop},m}$, $K_{\mathrm{stop}} \in \mathbb{R} : K_{\mathrm{stop}} \geq 1$ to form $\widetilde{\mathcal{M}}$, as shown in Fig. 4.2. If not stated otherwise, we use $K_{\mathrm{stop}} = 1.3$. This way, we accommodate for the limited steepness of the PSD analysis window, as discussed below on page 83. Furthermore, using broader stopbands increases the robustness against clock frequency offset.

Listing 4.1: Pseudo Matlab code for EPR test signal generation

```
1 vXf = fft(vS);         % transform the baseband WLAN signal to freq. domain
2 vXf(vIndexNull) = 0; % null the bins described by vector vIndexNull
3 vX = ifft(vXf);        % transform back to get the EPR test signal
```

The proposed multiplication in the frequency domain with zero at the bins to be nulled, and one otherwise, corresponds to a circular (cyclic) convolution in the time domain. This is welcome in measurement applications, because a typical signal generator repeats the signal vector continuously, i.e., it is periodically extended. Quoting Teyssier et. al [144] "99% of active component tests are performed using waveform files replayed repetitively"; In contrast to repeating a linearly-filtered signal vector, no discontinuities occur due to the repetition of the circularly-filtered signal vector. Consequently, we do not require synchronization when analyzing the signal.

The procedure in Listing 4.1 is the simple and effective. The following, more complicated procedures did not show any advantage in practice:

- Using a stop-band window other than rectangular, i.e., a smooth fade-out instead of the hard nulling to decrease ringing in the time-domain.
- Implementing the desired multi-stopband-filter using a lowpass filter prototype modulated to the desired stopband-center frequencies. Additional processing is required to avoid discontinuities due to the transient behavior when the signal is repeated.

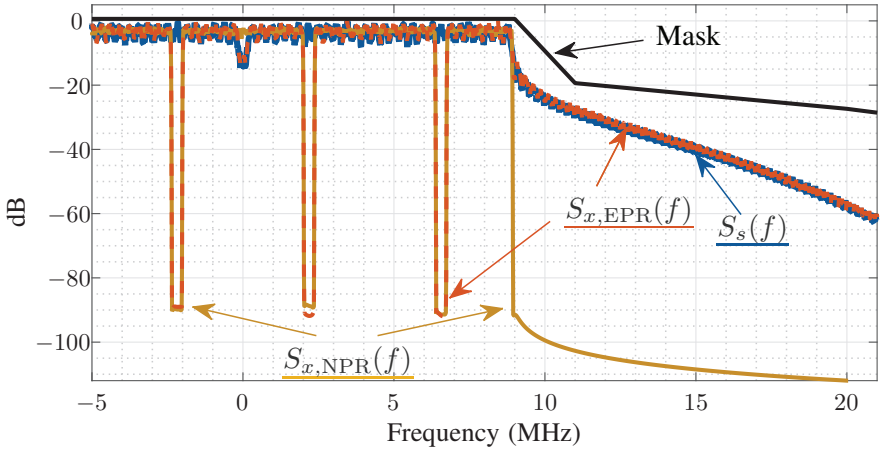

Figure 4.3: PSDs of three different test signals generated and analyzed on a PC (not measured). $S_s(f)$ is the PSD estimate of a 320-symbol WLAN signal with 20 MHz bandwidth oversampled in the IFFT to 60 MHz. In contrast to the traditional NPR signal generation resulting in a strictly band-limited $S_{x,\mathrm{NPR}}(f)$, our EPR test signal $S_{x,\mathrm{EPR}}[n]$ features the same out-of-band behavior as the original communication signal $S_s(f)$.

In Section 1.2, we have already highlighted the importance of using a test signal matching the statistics of the communication signal and that OFDM signals are CSCN distributed. A test signal $x_{\mathrm{NPR}}[n]$ generated with the method in [116] approaches a CSCN distribution, because the phases are independent random variables. Since a CSCN signal is invariant to linear filtering [129], also our method delivers a CSCN signal. We denote the test signal generated with our method with $x_{\mathrm{EPR}}[n]$. However, even if the distributions of the individual samples of two signals are the same, the PSDs can be quite different. A signal $x_{\mathrm{NPR}}[n]$ generated with i.i.d random phases does not include possible correlations due to cyclic prefix, windowed overlap and oversampling via IFFT zero padding. Consequently, the PSD $S_{x,\mathrm{NPR}}(f)$ is strictly band-limited, as shown in Fig. 4.3. In contrast, the PSD of our EPR test signal $S_{x,\mathrm{EPR}}(f)$ resembles the PSD $S_s(f)$ of the communication signal $s(t)$. Consequently, out-of-band measurements using an EPR test signal generated with our approach lead to results well comparable with those made with the actual communication signal $s(t)$. Summing up, our signal generation approach allows for measurements of out-of-band metrics, e.g., spectral mask [62] or ACLR [122], with the same signal that is used for measuring the inband error.

4.2.3 Signal Analysis

The following section describes two EPR signal analysis methods: The first method uses Welch's method for PSD estimation based on the baseband time-domain (TD) DUT output, whereas the second method uses a swept-tuned (ST) spectrum analyzer

to measure the DUT output power in different bands. An advantage of the TD method is that the same analyzer code can be used in measurements and simulations. Furthermore, the measurement chain can be exactly the same as for EVM measurements, which is beneficial when comparing both methods with each other.

The ST method features the advantages outlined in Section 2.1.3. It does not require demodulation of the baseband IQ samples and for a low noise floor at high bandwidths. Welch's method and swept-tuned measurements are outlined in Section 2.1.3.

Time Domain (TD) Approach

The TD approach is based on analyzing N samples of $\tilde{y}[n]$, the digitized baseband-equivalent of the DUT output $y(t)$. Using Welch's method we obtain $S_y(\omega_k)$, i.e., a DUT ouput PSD estimate on a discrete frequency grid $\omega_k = \omega_0 + \frac{k2\pi f_s}{K}$, $K \in \mathbb{N}$, $k \in \mathbb{Z} : \lceil -K/2 \rceil \leq k \leq \lceil K/2 \rceil - 1$, where K is the FFT length. Given $S_y(\omega_k)$, the EPR can be computed as suggested in (4.1); however, due to discrete-frequency grid, the integrals turn into sums.

For the considered WLAN application, the following PSD estimation settings deliver good results: a resolution of $f_s/K = 10$ kHz, a four-term minimum sidelobe Nuttall window [101], and 50% overlap, i.e., $K_{\text{olap}} = \lceil 0.5K \rceil$. If not stated otherwise, this is also the setting we use in all PSD plots, e.g., in Fig. 4.3. Note that if the resolution was too high, e.g., 50 kHz instead of 10 kHz, we would not be able to resolve the steep stopband notches anymore. For the same reason, a window with good side-lobe behavior is crucial for the analysis. Given the PSD estimate, we just need to implement (4.1) by averaging over the respective PSD frequency bins to obtain the EPR.

As shown in Fig. 4.3, we resolve EPRs down to -90 dB, which is enough for typical transceiver building blocks. With a rectangular analysis window-length exactly matching the IFFT-length of the signal generation, there is theoretically no lower limit on the EPR, i.e., the bins set to zero remain zero if there is no error. The lack of averaging when using a single long window is also not a problem. Since the power is integrated in (4.1), the lack of averaging when using a single long window is also not a problem. However, a slight mismatch of synthesis and analysis window-length, e.g., due to a mismatch of the DAC and ADC clock, drastically deteriorates the achievable floor. In contrast, the proposed windowed PSD estimation is insensitive to window-length mismatch.

Swept-Tuned (ST) Approach

We discussed measurements with a swept-tuned spectrum analyzer in Section 2.1.3. To obtain the EPR according to (4.1), we have to measure the power in the stopbands $\bar{S}_y(\mathcal{M})$ and the present signal power $\bar{S}_y(\mathcal{P})$. We could achieve this similar to the TD method discussed above by first getting a PSD estimate via sweeping the whole

bandwidth of the signal with a narrow RBW. The RBW must be narrow, e.g., 10 kHz, because otherwise, the steep stopband edges are not resolved adequately and signal power leaks into the stopband. However, using a narrow RBW when sweeping over a wide bandwidth results in a long measurement duration, as shown in (2.18) and discussed on page 27.

By tuning into each stopband separately, we can achieve faster measurements: To obtain the average stopband PSD $\bar{S}_y(\mathcal{M})$ in the numerator of (4.1), we make N_M separate sweeps and set the m-th sweep's start and stop frequency to the m-th stopband's start and stop frequencies, i.e., $\frac{\omega_{a,m}}{2\pi}$ and $\frac{\omega_{b,m}}{2\pi}$, respectively. The RBW must be small enough to prevent that power from neighboring present-bands is included when measuring the stopband power. In our WLAN application we use an RBW = 10 kHz, $C = 10$, and $f_{\text{span}} = 312.5$ kHz. According to (2.18), this allows for quick measurements because not only the RBW but also the span is small.

To obtain the average present-band PSD $\bar{S}_y(\mathcal{P})$, we could proceed similarly as for $\bar{S}_y(\mathcal{M})$ above and make N_P separate measurements. However, there is again a possibility to decrease the measurement time: It is typically sufficient to make a single sweep over the whole bandwidth of the signal, since the contribution of the stopbands $\bar{S}_y(\mathcal{M})$ to the present power $\bar{S}_y(\mathcal{P})$ is negligible for typical inband error values of interest. For instance, if the true inband error is ≤ -20 dB, we obtain -20.04 dB $= 10\lg(0.01/(1+0.01))$. Since the stopbands do not have to be resolved here, the RBW can be relatively high. We use $(f_{\text{span}}/\,\text{RBW}) = 200$, yielding RBW = 200 kHz for a signal with a bandwidth of $f_{\text{span}} = 40$ MHz. With $C = 100$ we still get T_{sw} in the order of 100 ms. Though the power is integrated over the full signal bandwidth f_{span} when computing $\bar{S}_y(\mathcal{P})$, it is important to normalize the integration by the present-bandwidth $\lambda(\mathcal{P})$.

4.3 Transceiver Impairments and Their Influence on the EPR

In the following, we discuss the influence of the transceiver impairments reviewed in Section 2.2 on the EPR and EVM.

4.3.1 LTI Filter with Additive Noise

As we already know from the discussion on the best linear approximation (BLA) of a nonlinear system introduced on page 31, an LTI system model with additive uncorrelated noise is able to represent a wide range of impairments. Below, we derive the EVM and EPR considering an LTI filter and two scenarios: Noise at the input and noise at the output. We try to use a compact notation that allows for simple comparison of EVM and EPR. In particular, we use the definition

$$\operatorname*{avg}_{k\in\mathcal{K}} H_k = \frac{1}{|\mathcal{K}|}\sum_{k\in\mathcal{K}} H_k \tag{4.8}$$

We start our discussion with the simpler case without a filter, i.e., additive noise only.

Additive Noise

We consider the signal model

$$y(t) = x(t) + v(t) \tag{4.9}$$

Assuming the noise $v(t)$ to be orthogonal to the EPR test signal $x(t)$, the PSD of the noisy signal $y(t)$ is

$$S_y(\omega) = S_x(\omega) + S_v(\omega)\ . \tag{4.10}$$

as presented in (2.24). Inserting (4.10) in the definition of the EPR in (4.1) yields

$$\mathrm{EPR}\{y(t)\} = \frac{\bar{S}_y(\mathcal{M})}{\bar{S}_y(\mathcal{P})} \tag{4.11}$$

$$= \frac{\bar{S}_x(\mathcal{M}) + \bar{S}_v(\mathcal{M})}{\bar{S}_x(\mathcal{P}) + \bar{S}_v(\mathcal{P})}\ . \tag{4.12}$$

Assuming an EPR test signal $x(t)$, (4.7) holds, i.e., $\bar{S}_x(\mathcal{M}) = \epsilon \bar{S}_x(\mathcal{P})$. If we furthermore assume $\bar{S}_v(\mathcal{M}) = \bar{S}_v(\mathcal{P})$, i.e., the noise power averaged over the stopband is representative for the noise at the present bands, (4.12) becomes

$$\mathrm{EPR}\{y(t)\} = \frac{\epsilon \bar{S}_x(\mathcal{P}) + \bar{S}_v(\mathcal{P})}{\bar{S}_x(\mathcal{P}) + \bar{S}_v(\mathcal{P})} = \frac{\epsilon\xi + 1}{\xi + 1} \approx \frac{1}{\xi}\,, \tag{4.13}$$

where

$$\xi = \frac{\bar{S}_x(\mathcal{P})}{\bar{S}_v(\mathcal{P})}\,. \tag{4.14}$$

If we assume that the EPR filter does not change the signal power in the present band, i.e., $\bar{S}_x(\mathcal{P}) = \bar{S}_s(\mathcal{P})$, ξ is the signal to noise ratio averaged over the present band. The approximation in (4.13) holds for $\epsilon \ll \xi$ and $\xi \gg 1$, i.e., if the stopband rejection is significantly higher than the SNR and the SNR is significantly higher than 0 dB. To obtain 0.25 dB estimation error, "significantly higher" amounts to 13 dB [71]. With $\mathrm{SNR}\,(\mathrm{dB}) = 10\log_{10}(\xi)$, $R_{\mathcal{M}} = -10\log_{10}(\epsilon)$, and $\mathrm{EVM} = -\mathrm{SNR}$, we obtain the result depicted in Fig. 4.4.

Note that the fixed, systematic bias at high EVM values results from the definition of the EPR as an error to signal plus error ratio and could be easily removed, whereas the bias at low EVM values could be decreased by increasing the stopband rejection $R_{\mathcal{M}}$. In most practically relevant cases, however, covering the range between -70 dB and -10 dB EVM is sufficient and bias correction is not necessary.

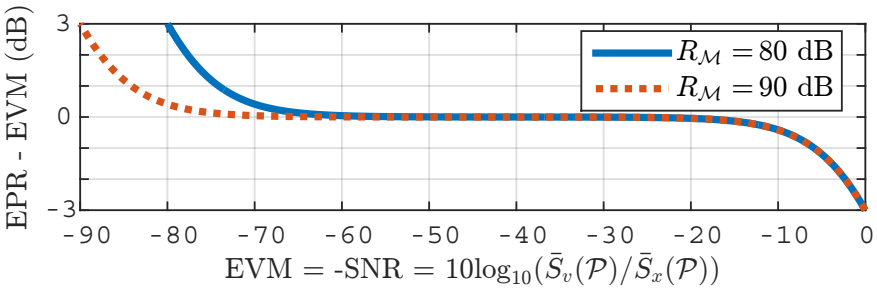

Figure 4.4: Theoretical EPR estimation error in case of additive noise for two different stopband rejection factors $R_{\mathcal{M}}$. At high SNR (−90 dB EVM), the EPR overestimates the EVM, because of the bias due to the limited stopband rejection. At low SNR (0 dB EVM) the EPR underestimates the EVM because we defined the EPR as an error to signal plus error ratio.

LTI Filter with Additive Output Noise

In the following, we investigate a linear system H with noise V at the input. To investigate the EVM, we consider the model

$$Y[k,l] = H_k X[k,l] + V[k,l] \tag{4.15}$$

where k is the subcarrier index and l is the OFDM symbol index. Assuming an equalizer $C_{\mathrm{EQ}_k} = H_k^{-1}$, the error is

$$E[k,l] = X[k,l] - (H_k X[k,l] + V[k,l]) C_{\mathrm{EQ}_k} = V[k,l] H_k^{-1} \tag{4.16}$$

For comparison with the EPR, it is advantageous to use the EVP, i.e., the square of the EVM. According to (2.70), the subcarrier-dependent EVP is given as the ratio of the error power averaged over all symbols l to the clean signal power averaged over both all data subcarriers $k \in \mathcal{D}$ and symbols l. We already computed the EVM for the noisy channel model when analyzing the SLIC-EVM in (3.39). By defining $S_x = \underset{k\in\mathcal{D}}{\mathrm{avg}} \boldsymbol{X}_k^{\mathrm{H}} \boldsymbol{X}_k$ and writing $S_v[k]$ instead of $\frac{1}{L}\boldsymbol{V}_k^{\mathrm{H}}\boldsymbol{V}_k$, the square of (3.39) becomes

$$\mathrm{EVP}[k] = \frac{S_v[k]}{|H_k|^2 \, S_x} \,. \tag{4.17}$$

The EPR evaluated at subcarriers k_m is obtained by inserting the PSD

$$S_y(\omega) = |H(j\omega)|^2 \, S_x(\omega) + S_v(\omega) \,. \tag{4.18}$$

instead of $S_x(\omega)$ in (4.5). Furthermore, we use the notation $S_y[k] = \bar{S}_y[\mathcal{W}_k]$, i.e., we assume that the PSD averaged over a band $\mathcal{W}_k$ centered at subcarrier k with bandwidth equal to the OFDM subcarrier spacing is equal to a PSD estimate obtained from averaging over OFDM symbols $S_x[k] = \frac{1}{L}\boldsymbol{X}_k^{\mathrm{H}}\boldsymbol{X}_k$. This allows to write the EPR in a

form that allows for direct comparison with the EVP above.

$$\mathrm{EPR}[k_m] = \frac{S_v[k_m]}{\underset{k\in\mathcal{P}_\mathcal{K}}{\mathrm{avg}} \left(|H_k|^2 \, S_x[k] + S_v[k] \right)} \tag{4.19a}$$

$$\approx \frac{S_v[m]}{S_x \underset{k\in\mathcal{P}_\mathcal{K}}{\mathrm{avg}} \, |H_k|^2} \tag{4.19b}$$

The approximation leading to (4.19b) is based on two assumptions:

1. The inband PSD is constant, i.e., $S_x[k] = S_x$, which is very reasonable assumption for OFDM communication signals.

2. The SNR is reasonably good, e.g., higher than 10 dB as discussed above in Section 4.3.1.

While in the denominator of the EVP in (4.17) we have the squared filter magnitude at the bin k, in the EPR in (4.19b) there is the mean squared filter magnitude, averaged over the present band. For equivalence of $\mathrm{EPR}[k_m]$ and $\mathrm{EVP}[k_m]$, we require

$$|H_m|^2 \overset{!}{=} \underset{k\in\mathcal{P}_\mathcal{K}}{\mathrm{avg}} \, |H_k|^2 \tag{4.20}$$

which is fulfilled for a flat channel response $H_k = \text{const}$. The overall (average) EVP and EPR are

$$\mathrm{EVP} = \underset{k\in\mathcal{D}}{\mathrm{avg}} \frac{S_v[k]}{|H_k|^2} \frac{1}{S_x} \tag{4.21}$$

and

$$\mathrm{EPR} = \frac{\underset{k\in\mathcal{M}_\mathcal{K}}{\mathrm{avg}} \, S_v[k]}{\underset{k\in\mathcal{P}_\mathcal{K}}{\mathrm{avg}} \, |H_k|^2} \frac{1}{S_x} \, . \tag{4.22}$$

Note that the condition for equivalence of the average EVP and the average EPR is not the same as the condition in (4.20).

We are free to define an alternative EPR, i.e., compute the EPR in a different way. By using an estimate of the channel magnitude and applying it to the measured PSD, i.e., $S_{y,\mathrm{EQ}}[k] = S_y[k]H[k]$ before computing the EPR, we obtain

$$\mathrm{EPR}_\mathrm{EQ}[k_m] = \frac{S_v[k_m] \, |H_{k_m}|^{-2}}{\underset{k\in\mathcal{P}_\mathcal{K}}{\mathrm{avg}} \left(|H_k|^2 \, S_x[k] \, |H_k|^{-2} + S_v[k] \, |H_k|^{-2} \right)} \tag{4.23a}$$

$$\approx \frac{S_v[k_m]}{|H_{k_m}|^2 \, S_x} = \mathrm{EVP}[k_m] \, . \tag{4.23b}$$

LTI Filter with Additive Input Noise

The signal model for a linear system H with noise at the input is

$$Y[k,l] = (V[k,l] + X[k,l])\, H_k. \tag{4.24}$$

The error with equalizer C_{EQ_k} is

$$E[k,l] = X[k,l] - (V[k,l] + X[k,l]) H_k C_{\mathrm{EQ}_k} \approx V[k,l] \tag{4.25}$$

if the channel estimation bias is negligible and we have $C_{\mathrm{EQ}_k} \approx H_k^{-1}$. The EVP is

$$\mathrm{EVP}[k] \approx \frac{S_v[k]}{\underset{k\in\mathcal{D}}{\mathrm{avg}} S_x[k]} \tag{4.26}$$

The PSD of the output signal is

$$S_y[k] = (S_v[k] + S_x[k])\, |H_k|^2 \ . \tag{4.27}$$

Assuming perfect stopband rejection, i.e., $S_x[k_m] = 0\ \forall k_m \in \mathcal{M}_\mathcal{K}$, the EPR is

$$\mathrm{EPR}[k_m] = \frac{S_v[k_m]\, |H_{k_m}|^2}{\underset{k\in\mathcal{P}_\mathcal{K}}{\mathrm{avg}} \left(|H_k|^2 S_x[k] + |H_k|^2 S_v[k] \right)} \tag{4.28}$$

$$\approx \frac{S_v[k_m]\, |H_{k_m}|^2}{S_x \underset{k\in\mathcal{P}_\mathcal{K}}{\mathrm{avg}} |H_k|^2} \tag{4.29}$$

where the approximation requires the same two assumptions, as required for (4.19b). For equivalence of $\mathrm{EPR}[k_m]$ and $\mathrm{EVP}[k_m]$ in (4.29) and (4.26), we have the same requirement as for the case of output noise, i.e.,

$$\frac{|H_{k_m}|^2}{\underset{k\in\mathcal{P}_\mathcal{K}}{\mathrm{avg}} |H_k|^2} \overset{!}{=} 1\,. \tag{4.30}$$

The overall (average) EVP and EPR are

$$\mathrm{EVP} = \frac{\underset{k\in\mathcal{D}}{\mathrm{avg}}\, S_v[k]}{S_x} \tag{4.31}$$

and

$$\mathrm{EPR} = \frac{\underset{k\in\mathcal{M}_\mathcal{K}}{\mathrm{avg}}\ S_v[k]\, |H_k|^2}{S_x \underset{k\in\mathcal{P}_\mathcal{K}}{\mathrm{avg}} |H_k|^2}\,. \tag{4.32}$$

Again, it is possible to get rid of the mismatch between the EVP and the EPR by equalizing the magnitude response, i.e., analyze the EPR of $S_y[k]\,|H_k|^{-2}$ instead of $S_y[k]$ in (4.27). This yields

$$\mathrm{EPR}_{\mathrm{EQ}}[k_m] = \frac{S_v[k_m]}{\underset{k\in\mathcal{P}_\mathcal{K}}{\mathrm{avg}}\ (S_x[k] + S_v[k])} \tag{4.33a}$$

$$\approx \frac{S_v[k_m]}{S_x} = \mathrm{EVP}[k_m]\,. \tag{4.33b}$$

Discussion

If we have a flat filter magnitude response, the EPR is able to accurately estimate the EVM at the stopband bins, i.e., $\mathrm{EPR}[k_m] = \mathrm{EVP}[k_m]$, both for input noise and for output noise. Otherwise, there is a deviation $\mathrm{EPR}[k_m](\mathrm{dB}) - \mathrm{EVM}[k_m](\mathrm{dB})$ given by the left hand side of (4.30) converted to decibel. In the derivations above, we assumed the EVM analyzer's equalizers is able to invert the linear filter. With OFDM, this is typically the case if the channel impulse response is shorter than the cyclic prefix.

Typically, components of communication systems are designed to feature a flat inband magnitude response. If, however, we have a DUT with a strong inband frequency-dependence, we must equalize the magnitude response of the DUT output PSD prior to EVM analysis to avoid bias as shown in (4.23) and (4.33). The identification of this equalizer is simple. We only need to invert the deviation from the average power as displayed on the spectrum analyzer display, which can be easily automatized. However, in all practical measurements conducted, and also in all simulations reported in [A4, A5], the regular EPR worked well and there is no need for the additional equalization.

Above, we discussed the frequency-dependence H_k of the DUT system. A different issue is the frequency-dependence of the error, i.e., the shape of the noise PSD $S_v[k]$ above. To observe the EVM at all inband subcarriers, we would have to notch out the entire signal, which would certainly affect errors that depend on the signal. A single EPR measurement is therefore not able estimate the EVM at all $k \in \mathcal{D}$. Rather, we can only estimate the EVM at a few stopband bins k_m. Therefore, a highly subcarrier-dependent EVM may lead to a significant bias when estimating the overall EVM based on averaging the EPR only over a few subcarriers k_m.

In practice, most transceiver DUTs feature an error that is well-behaved, i.e., not changing abruptly over the inband frequencies. If, however, there is reason to expect highly frequency-dependent error, e.g., when a dynamic element matching DAC [40] is part of the DUT, there is the possibility of making several measurements with different stopband frequencies. In the case of a 160-MHz WLAN signal, using only a single stopband, and stepping the stopband center frequency trough all data subcarrier frequencies, this would require $N_D = 468$ measurements, according to Tab. 2.1. A quicker approach to measure highly frequency-dependent errors and systems is to use the SWEEPR method proposed in Section 5.

4.3.2 Nonlinearity

In case of nonlinear DUT, e.g., a power amplifier, the distorted DUT output $y(t)$ can be decomposed into two components: a component correlated with the input $x(t)$ and an additive uncorrelated distortion noise component $v(t)$, as described in Section 2.2.3.

$$S_y(\omega) = |H_\mathrm{B}(\omega)|^2 \, S_x(\omega) + S_e(\omega) \tag{4.34}$$

where $H_\mathrm{B}(\omega)$ is the BLA to the nonlinear system as defined in (2.30). For the static third-order nonlinearity discussed in Section 2.2.3, we had the frequency-independent factor $H_\mathrm{B} = c_1 + 3c_3\sigma_x^2$.

In an OFDM receiver, new equalizer coefficients are estimated from the preamble in each frame. With the reasonable assumption that the source signal is wide-sense stationary within the OFDM frame, the signal power σ_x^2 is constant within that frame. It is also reasonable to assume that the PA is time-invariant within one frame, so also the PA model coefficients are constant. With these assumptions, an equalizer that inverts a linear channel estimate, will be able to equalize $H_\mathrm{B}(\omega)$, and we have a very similar case as with the LTI filter with additive output noise, discussed above. The main difference to the additive noise scenario above is that the "distortion noise" with PSD $S_e(\omega)$ is not independent from the excitation signal $x(t)$, i.e., the excitation signal affects the error, in general.

Fig. 4.5 illustrates the EPR for a Wiener PA model consisting of a 3-tap FIR filter followed by the Saleh quasi-memoryless model in (3.27). In the simulation belonging to Fig. 4.5, the EVM without equalizer is -16.2 dB, whereas it is -32.7 dB with equalizer. The EPR is also -32.7 dB, i.e., the EPR equals the EVM with equalizer. In addition to the curves already presented in [A4, Fig. 5], the top plot in Fig. 4.5 also depicts the EVM considering fractional delay compensation. Although fractional delay compensation lowers the EVM without equalizer to -25.9 dB, the conclusion that can be made from Fig. 4.5 is the same made in [A4, Fig. 5]: The EPR samples the EVM with EQ, whereas the EVM without EQ (or only a scalar complex gain EQ) is higher, in general. This result does not contradict Pedro and Carvalho's result [108] that the NPR underestimates the co-channel distortion, since they have a different objective. The reference they compare the NPR to includes correlated co-channel distortion, i.e., the reference does not consider an equalizer.

As illustrated in Fig. 4.5, the individual stopband EPRs resemble the EVM at these frequencies. The overall EPR is the mean over the individual stopband EPRs as defined in (4.5). The overall EVM is the mean over the EVM at all data subcarriers. If the mean over the EVM at the stopband subcarriers differs from the overall EVM, the single-measurement multi-stopband EPR will also differ from the overall EVM. To estimate the overall EVM correctly, the error observed in the EPR stopbands must be representative for the error of the whole inband, which we also required for (4.13).

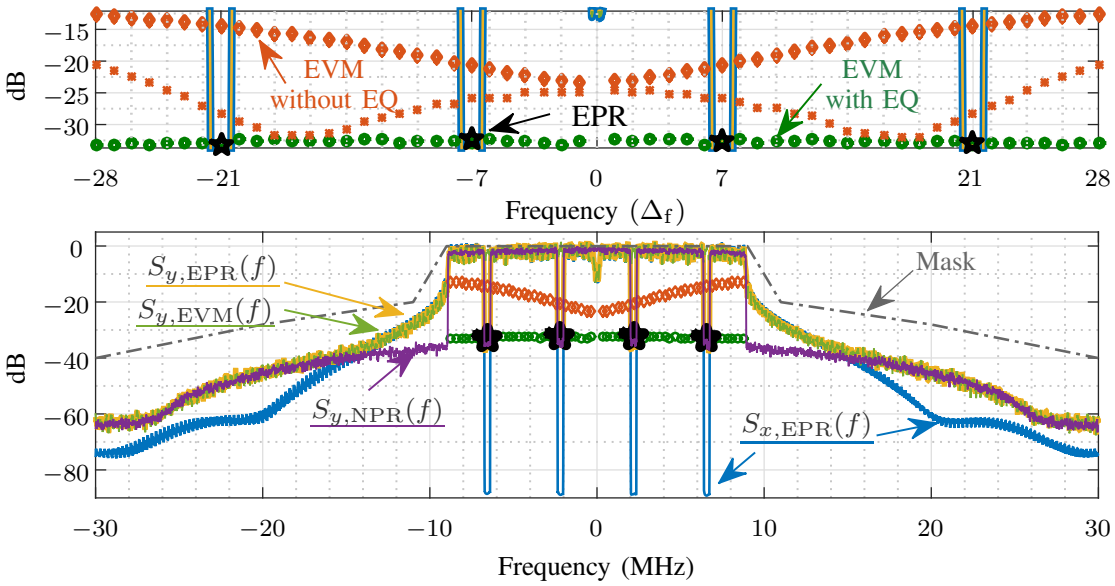

Figure 4.5: Wiener PA model simulation. Top plot: zoomed version of bottom plot with abscissa in multiples of the OFDM tonespacing Δ_f. At the stopband center frequencies $\boldsymbol{\omega}_{c,M} = \{-21, -7, 7, 21\} \cdot 2\pi\Delta_f$, the EPR resembles the EVM with equalizer (EQ) at these tones. The top plot includes two curves for the EVM without EQ. The upper one is obtained without fraction delay compensation, whereas the lower one is based on a compensated fractional delay.

4.3.3 Phase Noise

As presented in Section 2.2.2 a phase noise PSD $S_\phi(\omega)$ results in an impaired PSD

$$S_y(\omega) \approx S_x(\omega) + (S_x * S_\phi)(\omega) \tag{4.35}$$

where $S_x(\omega)$ is the clean signal's PSD. With the EPR, the convolution in (4.35) spills power from neighboring present bands into the stopband. Since the CPE can be removed in EVM analyzers, it is desirable to also exclude CPE contributions from our stopband so that they do not contribute to the error power in the numerator of the EPR defined in (4.1). Similarly, we want ICI to contribute to the stopband power because it is also included in the EVM. Since what is considered ICI and what is CPE depends solely on Δ_f for a given phase noise bandwidth, it is clear that also our stopband width $\mathrm{BW}_{\mathrm{stop}}$ must be related to Δ_f. As can be seen in Fig. 4.6, using $\mathrm{BW}_{\mathrm{stop}} = \Delta_f$ works fine for estimating the EVM with activated phase tracking. For Fig. 4.6, we used rather narrow-band phase-noise with $B_{\mathrm{PLL}} = 10\,\mathrm{kHz}$, $f_{\mathrm{corner}} = 0.5$ kHz, $L_{\mathrm{floor}} = -150$ dB, and $L_0 = -90$ dB in order to clearly see the differences between EVM with and without phase tracking and the influence of different stopband widths. As shown in the measurement chapter 4.4, $\mathrm{BW}_{\mathrm{stop}} = \Delta_f$ is however also appropriate for higher phase noise bandwidths, e.g., $B_{\mathrm{PLL}} = 160$ kHz.

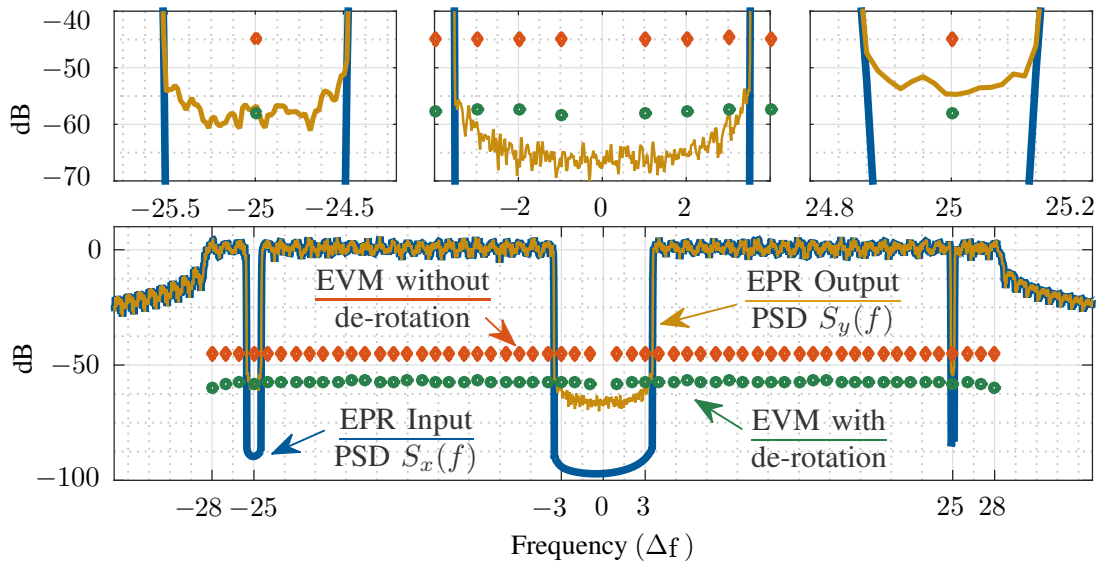

Figure 4.6: Phase noise simulation illustrating the importance of the stopband-width $\mathrm{BW}_{\mathrm{stop}}$ for EVM estimation. Bottom: EPR test signal PSD, DUT output PSD, and EVM per subcarrier. Top: Zoomed stopbands. Left: With $\mathrm{BW}_{\mathrm{stop}} = \Delta_{\mathrm{f}}$, i.e., the stopband-width equals the OFDM tonespacing, good estimates of EVM with de-rotation (phase tracking) can be expected. Middle: With $\mathrm{BW}_{\mathrm{stop}} = 6\Delta_{\mathrm{f}}$, the EPR underestimates the EVM. Right: With $\mathrm{BW}_{\mathrm{stop}} = 0.1\Delta_{\mathrm{f}}$, the EPR overestimates the EVM with de-rotation.

4.3.4 IQ Mismatch

As presented in Section 2.2.4, IQ mismatch results in an error component at frequencies mirrored to the excitation frequencies. The PSD due to IQ mismatch is

$$S_y(\omega) = |A(j\omega)|^2 \, S_x(\omega) + |B(j\omega)|^2 \, S_x(-\omega) \; , \tag{4.36}$$

where $A(j\omega)$ and $B(j\omega)$ are the Fourier transforms of $\alpha(t)$ and $\beta(t)$, respectively. These are given as

$$\alpha(t) = (h_I(t) + g e^{j\varphi} h_Q(t))/2 \tag{4.37a}$$
$$\beta(t) = (h_Q(t) - g e^{j\varphi} h_Q(t))/2 \tag{4.37b}$$

where g is the mixer amplitude imbalance factor, φ is the phase imbalance, and $\tilde{h}_I(t)$ and $\tilde{h}_Q(t)$ are the IRs of the the in-phase and quadrature path of the D/A converter, respectively. If $B(j\omega) \neq 0$, there is IQ mismatch, and an excitation at ω_0 causes interference at the mirrored frequency $-\omega_0$.

With EPR, we can choose where to place the stopbands. Placing them symmetrically around $\omega = 0$, excludes IQ mismatch, because then there is no excitation at mirrored frequencies where we observe the error. If, however, the stopbands are chosen to be

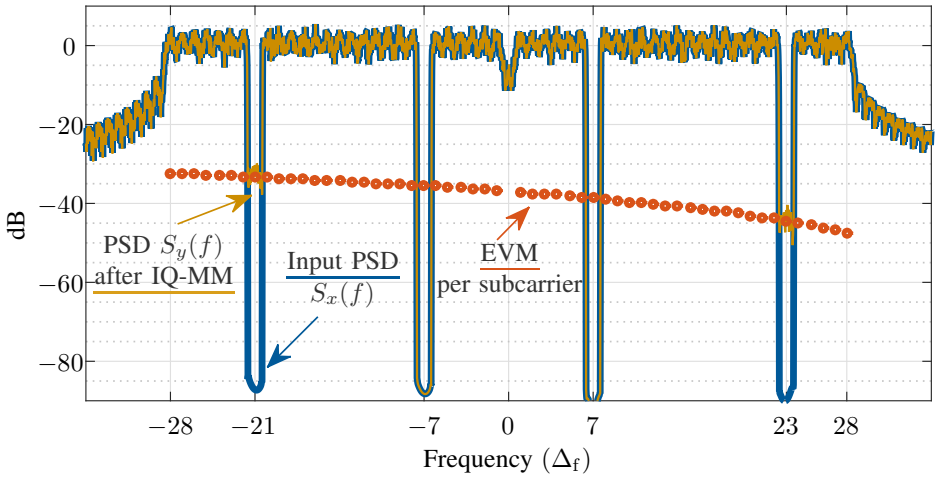

Figure 4.7: IQ mismatch simulation result illustrating the importance of the stopband locations $\omega_{c,m}$. With symmetric tones at $\pm 7\Delta_f$, IQ mismatch is excluded. With asymmetric locations $(-21, +23)\Delta_f$, IQ mismatch is included.

asymmetric, the effect of IQ mismatch is included in the EPR result. In practice this can be very helpful when trying to sort out whether IQ imbalance is the limiting factor that determines the inband-error. The method proposed in Section 3.1, uses the same principle of a mirrored null-excitation to exclude IQ mismatch for EVM. The standard EVM however does not allow for excluding IQ mismatch.

In Fig. 4.7, we illustrate the EVM and EPR for an IQ mismatch simulation using the model in (2.51). The EPR test signal $S_x(f)$ features four stopbands. Two of these stopbands ($\pm 7\Delta_f$) are symmetric around zero, whereas the other two are at $(-21, +23)\Delta_f$, i.e., they are asymmetric and do not have an equivalent mirrored around zero. The simulation confirms our analysis above: The symmetric stopbands are blind to IQ mismatch, i.e., the output PSD resembles the input PSD at these bands. If we only use symmetric bands to compute the EPR, we get nearly -90 dB, i.e., the best our analysis window can achieve, although there is strong IQ mismatch. The asymmetric bands $(-21, +23)\Delta_f$, on the other hand, accurately sample the frequency-dependent error, depicted as EVM per subcarrier. Analyzing only asymmetric stopbands allows to estimate the EVM if IQ mismatch is considered to be a part of the DUT. Using both symmetric and asymmetric locations at the same time as in Fig. 4.7, allows for checking whether the error is dominated by IQ mismatch by just looking at the PSD.

As already discussed in Section 4.3.2 for the case of nonlinearity with memory, for frequency-dependent inband error, the mean over the error at the stopbands must approach the overall error. If this is fulfilled the configuration of the asymmetric stopband is not crucial as long as there is no attenuation of the test signal PSD at mirror-frequencies of the EPR integration range. In Fig. 4.7, we used $(-21, 23)\Delta_f$, i.e. a stopband offset of $2\Delta_f$ to achieve asymmetry. Using only $1\Delta_f$ would not suffice, because the stopband transition would constitute an attenuation at a mirror frequency.

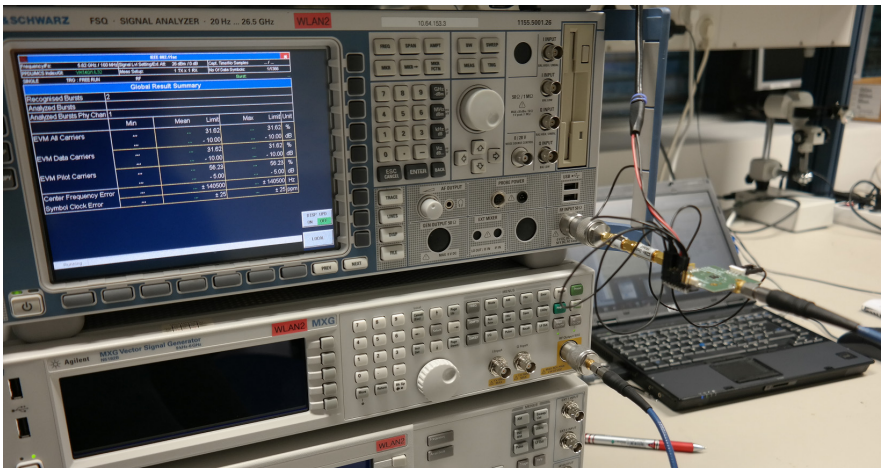

Figure 4.8: Measurement setup including a PC with MATLAB, Agilent MXG signal generator, and R&S FSQ analyzer. As nonlinear DUT we use an RFMD RFPA5522 power amplifier (PA) with a 10 dB attenuator at its output.

4.4 Measurements

To verify the proposed EPR measurement method experimentally, we made measurements comparing the EVM with the EPR. Our measurement setup is depicted in Fig. 4.8. We use a PC connected to the Agilent MXG signal generator and an R&S FSQ Analyzer via LAN. The FSQ's 10 MHz sync output is connected to the MXG's 10 MHz sync input.

4.4.1 Setup

Signal Generation

We generate the 802.11ac source signal $\tilde{s}[n]$ using a PC running MATLAB and the VHT waveform generator tool cited in Annex S of [62]. Unless otherwise stated, we use a single burst with 320 data symbols, 40 MHz bandwidth, and modulation coding scheme (MCS) 1, i.e., QPSK subcarrier modulation. Upsampling to a sample rate of 160 MHz is achieved by zero-padding in the IFFT. For generating EPR excitation signals, we filter $\tilde{s}[n]$ according to Section 4.2.2. We use the standard pilot tone locations $\{-53, -25, -11, +11, +25, +53\}$ for our center frequencies $\omega_{c,m}$ to obtain symmetric stopbands. For asymmetric locations, we offset the positive tones by -2, i.e., we use $\{-53, -25, -11, +9, +23, +51\}$. After downloading the signal $\tilde{x}[n]$ to the MXG, the MXG converts the digital baseband signal to an analog RF signal, centered at 5.6 GHz.

Device Under Test

As a nonlinear DUT, we use an RFMD RFPA 5522, a commercially available, three stage power amplifier (PA) for 802.11a/n/ac applications. To operate the PA in a wide range, from a linear regime to deep saturation, we sweep through the following 15 MXG analog output gain values:

$$\{-30, -25, -20, -15, -12.5, -10, -9, \ldots, -1\}\,\mathrm{dB}\,. \tag{4.38}$$

To test the effect of IQ mismatch and phase noise on EVM and EPR, we add IQ-mismatch and phase noise to the baseband signal in MATLAB, using the models discussed in Section 4.3. The used IQ-mismatch model is given in (2.51). To model phase noise we use (2.25) with the parameters $B_{\mathrm{PLL}} = 160$ kHz, $f_{\mathrm{corner}} = 2$ kHz, $L_{\mathrm{floor}} = -170$ dB, and $L_0 = -93$ dB.

To get the lowest measurable inband error for reference, we made measurements connecting the MXG's RF output directly to the FSQ's RF input via an RF cable. However, we were able to measure the lowest inband error by including the PA and the 10-dB attenuator in the measurement chain and drive it at a low level (around 2 dBm), because the PA is linear at low levels. The resulting reference (best) RF chain results are summarized in Table 4.1 and correspond to the leftmost data points of the PA power sweep depicted in Fig. 4.9.

EVM and EPR Analysis Methods

We use the FSQ analyzer in three different measurement modes, depending on the EVM or EPR measurement approach, as described in the following. To have a reference to compare our own EVM analyzer code implemented in MATLAB, we used the K91ac EVM analyzer firmware running on the FSQ. We use phase tracking, and make channel estimation on the preamble and data. We refer to the resulting average EVM over all data subcarriers as $\mathrm{EVM}_{\mathrm{FSQ}}$. Furthermore, we are interested in the EVM at the pilot tones $\mathrm{EVM}_{\mathrm{FSQ,pilots}}$, since our EPR stopbands are also at the pilot locations, and we expect the FSQ's phase-tracking algorithm to achieve the lowest EVM at the pilot-tones.

Our own, data-aided EVM analyzer implemented in MATLAB analyzes time-domain (TD) baseband data, hence we refer to it as $\mathrm{EVM}_{\mathrm{TD}}$. In contrast to the FSQ's proprietary analyzer, we can use our EVM analyzer in simulations, and have full understanding of the processing. In measurements, we obtain the baseband data via the FSQ's I/Q mode data transfer functionality, i.e., the FSQ downconverts the signal from 5.6 GHz to baseband and performs analog to digital conversion.

For $\mathrm{EPR}_{\mathrm{TD}}$, i.e., the EPR based on PSD estimation using TD data, the measurement chain is exactly the same as for $\mathrm{EVM}_{\mathrm{TD}}$, only the excitation signal and the analysis is different. Having the same measurement chain for $\mathrm{EPR}_{\mathrm{TD}}$ and $\mathrm{EVM}_{\mathrm{TD}}$ is beneficial when directly comparing the results.

Calibration

The FSQ's input attenuator (ATT) and vertical reference (VREF) settings are crucial for obtaining good (low) and comparable results. Particularly at EVMs below −30 dB, we observed that the FSQ's automatic ATT and VREF selection delivers results several dB worse than those obtained with manually optimized settings. Furthermore, the best settings are not necessarily the same in the different modes (WLAN, TD-IQ, swept-tuned channel power measurement). Accordingly, for each tested power level, we optimized the ATT and VREF setting to achieve the lowest EVM or EPR, for each method. Since the signal path is exactly the same for $\mathrm{EPR}_{\mathrm{TD}}$ and $\mathrm{EVM}_{\mathrm{TD}}$, also the optimal ATT and VREF settings are the same.

The generator and the analyzer we used are annually calibrated by the manufacturer. Apart from the selection of the ATT and VREF setting as described above, user calibration is not very critical, because we are using a signal analyzer and not a network analyzer. Furthermore, we are only interested in comparing different methods (EVM, EPR) and not so much in the absolute accuracy, e.g., regarding the power measurement. The different analysis methods (EVM, EPR) themselves do not need absolute power, but power ratios. Consequently, systematic errors in the absolute power level are excluded from the result in the ordinate of Fig. 4.9 by design. The absolute power measurement results varied up to 0.3 dB between the different analysis methods. We removed this variation from our results by using the same data (the power measured with the $\mathrm{EVM}_{\mathrm{TD}}$) for the abscissa of all the different methods in Fig. 4.9. This is valid, because of the following: All excitation signals are digitally scaled to have exactly the same power. The measurement chain (generator, cables, PA) is always the same and differences in output power due to (slightly) different signal statistics (e.g., PAPR) are negligible. Consequently, it is reasonable that the power at the output of the DUT is the same for all analysis methods.

4.4.2 Results

The results of the PA power sweep are depicted in Fig. 4.9. The wide range of tested EVM conditions can be seen from Fig. 4.9 (a). At the highest level (around 30 dBm), the PA is in saturation and the distortion leads to −15 dB of inband error. At low levels, the PA behaves very linear, achieving EVMs down to −53 dB. In essence, the results of all methods agree over the whole power range. To see differences in more detail, the deviation from $\mathrm{EVM}_{\mathrm{FSQ}}$ is plotted in Fig. 4.9 (b). $\mathrm{EPR}_{\mathrm{TD}}$ and $\mathrm{EVM}_{\mathrm{TD}}$ have an absolute difference less than 0.35 dB over the whole test range. Since the EPR obtained via swept-tuned (ST) RF power measurements allows for a lower measurement floor, the deviation defined $\mathrm{EPR}_{\mathrm{ST,deviation}} = \mathrm{EPR}_{\mathrm{ST}} - \mathrm{EVM}_{\mathrm{FSQ}}$ is negative for low PA output powers. In Fig. 4.9 (c), we present results of the same PA power sweep as in (a) but with IQ mismatch added to the test signal $x[n]$. With symmetric stopbands, the EPR does not capture IQ mismatch. Therefore, $\mathrm{EPR}_{\mathrm{symm}}$ in Fig. 4.9 (c) agrees with the

Table 4.1: RF Chain: Measured Inband Error (dB)

EVM_{FSQ}	EPR_{ST}	EVM_{TD}	EPR_{TD}
-51.5	-56.3	-47.2	-47.2

Table 4.2: Phase Noise: Measured Inband Error (dB)

Method	EVM	EPR
FSQ/ST	-38.4	-38.9
TD	-38.1	-38.5
SIM	-38.9	-39.0
FSQ, pilots	-39.0	

Table 4.3: IQ Mismatch: Measured Inband Error (dB)

Method	EVM	EPR_{asymm}	EPR_{symm}
FSQ/ST	-35.8	-35.9	-56.3
TD	-35.8	-35.6	-46.8
SIM	-35.8	-35.7	-88.6

result without added IQ mismatch in subplot (a). With asymmetric rejection bands, IQ mismatch is included and hence EPR_{asymm} resembles the EVM in Fig. 4.9 (c).

Table 4.1 presents inband error results of the RF chain presented in Section 4.4.1, i.e., at low PA output power (2 dBm). The values of EVM_{TD} and EPR_{TD} equal, which indicates that if the measurement chain is the same, the EPR is able to estimate the EVM very well. While the achieved noise floor with the TD measurement chain is around -47 dB, the swept-tuned method EPR_{ST} allows for a lower noise-floor of -56 dB.

EVM and EPR results for the case of phase noise are shown in Table 4.2. As already explained on page 95, the phase noise impairment was simulated and added to the source signal. Then, a measurement with that noisy signal was made. As a reference, we also show the simulated EVM (SIM). EPR_{ST} resembles EVM_{SIM} and $EVM_{FSQ,pilots}$. As expected, the EVM result at the data tones is slightly (0.6 dB) worse. EVM_{TD} and EPR_{TD} are slightly biased to higher values by the higher floor of the TD RF signal path.

The results in Table 4.3 confirm our findings in Sec. 4.3 regarding IQ mismatch. With asymmetric stopbands, the EPR results resemble the EVM results for IQ mismatch. Symmetric stopbands, however, lead to EPR results resembling the case without added impairments. The symmetric EPR results $EPR_{ST,symm} = -56.3$ is perfectly in line with the respective result in Table 4.1.

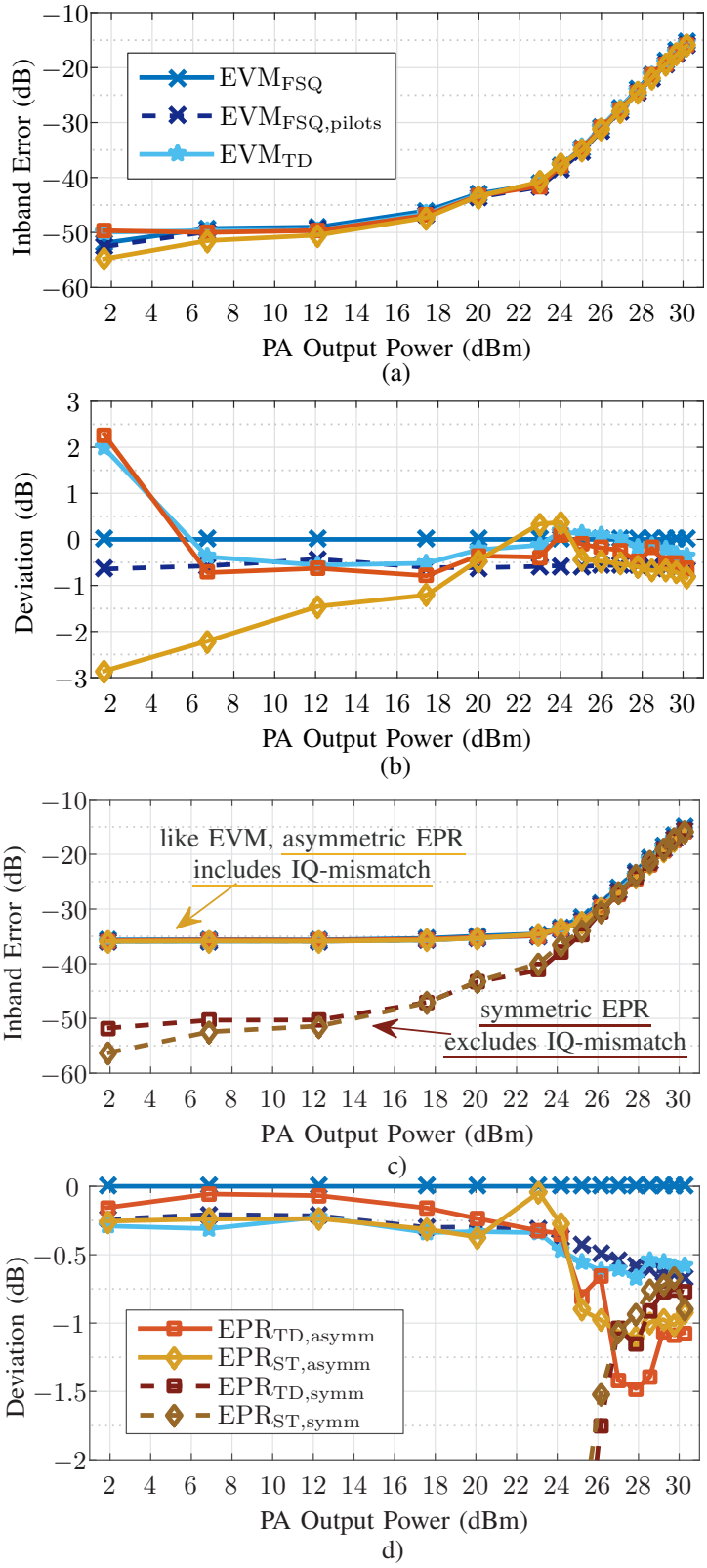

Figure 4.9: Inband error measurement results comparing several methods/settings for EVM and EPR. The DUT is a WLAN power amplifier (PA). The signal generator's output gain is swept. (a) PA measurement. (b) Same data as (a), but deviation from EVM_{FSQ} is shown. (c) PA measurement with IQ mismatch added to the test signal $x[n]$. (d) Same data as c), but deviation from EVM_{FSQ} is shown.

4.5 Uncertainty and Bias

4.5.1 Measurement Uncertainty

In the following, we discuss the uncertainty involved in EPR measurements. Uncertainty is the doubt about the measurement result [117], i.e., a measure of the variation to expect when making repeated measurements affected by random errors. Uncertainty analysis of EVM measurements is discussed in [20, 114], and references [20-29] in [114]. We discuss systematic errors and bias, i.e., the expected deviation from the true value, separately in Sec. 4.5.2. We define three classes depending on the source of uncertainty. These are

1. Randomness of the excitation signal.
2. Randomness of the DUT.
3. Randomness of the remaining measurement chain.

All three types of uncertainty can affect the repeatability of the measurement. If we use a fixed test signal, which we did in the measurements described above in Section 4.4, there is no uncertainty of the first type. However, there can be bias, as discussed in Section 4.5.2.

Uncertainty of the second type arises due to limited observation time and bandwidth of random DUT errors, e.g., thermal noise of a PA. The EPR has more of that type-2 uncertainty than EVM, because the EPR observes the error only in a fraction

$$\alpha_{BW} = \frac{\lambda(\mathcal{M})}{BW} < 1 \tag{4.39}$$

of the bandwidth BW used for averaging the error in EVM. If there is only type-2 uncertainty, the variance of EPR is hence $1/\alpha_{BW} > 1$ times the variance of EVM, if the measurement duration is the same. For deterministic errors, e.g., a nonlinear DUT and negligible type-1 and type-3 uncertainties, repeated measurements have the same result, so both EPR and EVM have zero variance.

The type-3 uncertainties of $\mathrm{EVM}_{\mathrm{TD}}$ and $\mathrm{EPR}_{\mathrm{TD}}$ are the same, because the measurement chain is the same. Although we do not know the internals of the FSQ and its EVM analyzer software, we expect $\mathrm{EVM}_{\mathrm{FSQ}}$ to have similar uncertainty as $\mathrm{EVM}_{\mathrm{TD}}$. For $\mathrm{EPR}_{\mathrm{ST}}$, a different detector (RMS instead of sample) is used and random errors in the RX IQ path are excluded. Still, informal experiments indicate that the difference in uncertainty of $\mathrm{EPR}_{\mathrm{ST}}$ compared to $\mathrm{EPR}_{\mathrm{TD}}$ is small, in practice. This is also supported by the experiment described below. Apart from excluding synchronization errors potentially biasing the result, the swept-tuned principle allows for EPR measurements with a lower measurement floor at high bandwidths.

To get more insight for the amount of type-3 uncertainties and the repeatability of our measurements, we made ten successive trials of the power sweeps in Fig. 4.9 with fixed

excitation signals. The deviation from the mean (in dB) was low for all methods, over the whole power range. For the EPR methods the deviation was within ±0.17 dB over the whole range. For EVM it was in the same range (±0.12 dB) apart for an outlier deviating up to −0.32 dB for higher levels. At lower levels, the uncertainty of EPR was slightly higher compared to EVM. This is reasonable because at low levels, the influence of additive noise is stronger and hence we have type-2 uncertainty, leading to an increased variance of EPR compared to EVM.

4.5.2 Bias and Stopband Selection

In the following, we discuss the bias of the EPR, i.e., the systematic deviation of the EPR from the true EVM value. Since, in general, the bias depends on the DUT, it is difficult to remove. However, bias can often be avoided by setting up the EPR measurement right. Below, we discuss both sides of the following tradeoff. Using only few stopbands is beneficial in order to have the same error *occur* in response to the EPR test signal as in response to the EVM test signal. However, for heavily frequency-dependent error it is important that we *observe* the error at many different frequency-locations, i.e., use many stopbands.

Using multiple stopbands, each being one subcarrier spacing broad, with an overall stopband width of 3 to 10% of the original signal bandwidth seems to be a good compromise, in practice (six stopbands at 40-MHz WLAN correspond to about 5%). Choosing the width of each stopband to be the OFDM subcarrier spacing is important to avoid bias in case of phase noise. Placing the stopband-centers at OFDM subcarrier-frequencies is convenient for comparison with subcarrier-dependent EVM values. Then, the individual EPRs at each stopband resemble the EVMs at these subcarriers, i.e., $\mathrm{EPR}(k_m) \approx \mathrm{EVM}(k_m)$. For nonlinear DUTs this is, however, only true if the EPR test signal statistics are sufficiently similar to the EVM test signal statics.

While for static nonlinearities preserving the amplitude statistics (the PDF) is sufficient, for nonlinearities with memory it can be important to also preserve the correlation and higher order moments of the test signal. However, retaining the PDF, e.g., a CSCN distribution, does not mean that the EPR test signal has the same PSD as the source signal (and consequently also not the same autocorrelation). Quite the contrary, it cannot have the same PSD, since we need a PSD with stopbands for EPR, whereas the EVM test signal features no stopbands. The more bandwidth we null for EPR, the less will the PSDs resemble, and the more we are risking to produce a different amount of distortion at the output compared to the EVM signal which may lead to a biased EPR. However, many experiments with measured and simulated systems suggest that this issue is not very critical in practice when nulling, e.g., 10% of the bandwidth. This experience is also supported by the Monte-Carlo simulation results presented in the next section. Another important issue is that the test signal should not be too short in order to excite the DUT in the same way as a standard EVM test signal. Therefore, we used 320 symbols according to the EVM test WLAN standard, i.e., 1.28 ms.

Now we discuss the issue of observing the error adequately, i.e., the observed error must be representative for the overall error. When the frequency-dependence of the error and the DUT is mild, which seems to be the case for many practical systems, the above presented stopband placement works well for estimating the EVM. Then, the exact number (between three and 10% of the number of OFDM subcarriers) and absolute location of the stopbands is also not critical. We used the pilot locations as stopband-centers, because they are easy to remember and the result can be directly compared to EVM averaged at the pilots, which is provided by most commercial EVM analyzers. Sometimes, the error increases or decreases at the band-edges or around DC, so it can be useful to also include the outermost and innermost modulated subcarriers. Having a look on the individual EPR results at the different stopband-subcarriers is always advisable. If the EPR varies a lot between the individual stopbands, it is sensible to make a second measurement with different stopband locations. If the result differs from the first one, it makes sense to make several measurements, sweeping the stopband locations over the whole inband.

4.6 Monte Carlo Simulations

Although we have discussed the effectiveness and limitations of EPR above at length, a proof of approximate equivalence with EVM was only possible for additive noise. Hence, the question may remain whether the EPR can be trusted as a replacement for EVM in complex scenarios with compound IQ mismatch, phase noise, and nonlinearity. In the following, we address this question by investigating the bias and uncertainty we can expect when measuring many different DUTs. Instead of showing measurement results for another few hardware DUTs, we can address many more cases by randomly mixing up parameters of impairment models in Monte-Carlo simulations. We evaluate what deviations from the EVM we can expect from the EPR, when we have an unknown system with IQ-mismatch, phase noise, nonlinearity, or the combination of these typical transceiver impairments. As discussed above, the overall EPR cannot be expected to resemble the overall EVM in case of highly frequency-dependent errors. Hence the frequency-dependence of the error must be kept within certain bounds, which we achieve by carefully selecting the distributions of the randomly varied impairment parameters.

4.6.1 Impairment Models

IQ Mismatch and Phase Noise

For modeling frequency-dependent IQ mismatch, we use the model described in (24) of [A4]. In discrete time n, the output of our IQ-mismatch model is

$$y[n] = \boldsymbol{x}^{\mathrm{T}}[n]\left(\boldsymbol{h}_{\mathrm{I}} + \gamma \boldsymbol{h}_{\mathrm{Q}}\right)/2 + \boldsymbol{x}^{\mathrm{H}}[n]\left(\boldsymbol{h}_{\mathrm{I}} - \gamma \boldsymbol{h}_{\mathrm{Q}}\right))/2 \tag{4.40}$$

where $\boldsymbol{x}[n] = \Big(x[n], x[n-1], \ldots, x[n-N+1]\Big)^{\mathrm{T}}$ is the vector of baseband input samples, and $(\cdot)^{\mathrm{H}}$ denotes combined transposition $(\cdot)^{\mathrm{T}}$ and conjugation. The real-valued column vectors $\boldsymbol{h}_{\mathrm{I}}$ and $\boldsymbol{h}_{\mathrm{Q}}$ represent N samples of the discretized impulse responses $h_{\mathrm{I}}[n]$ and $h_{\mathrm{Q}}[n]$ that model the I- and the Q-path, respectively, and $\gamma = g e^{j\varphi}$ includes the amplitude mismatch factor g and phase mismatch φ.

To simulate phase noise, we use the PLL phase noise model in (4.35).

Nonlinearity with Memory

Although we want to model a wide range of nonlinearities with memory, it is desirable to have a small number of model parameters that are easy to control and comprehend. Therefore, a Volterra series or memory polynomial structure is probably not the best choice. A Wiener Hammerstein model seems to be better suited. It consists of a cascade of an LTI filter $H_{\mathrm{pre}}(z)$, a static nonlinearity $\mathrm{NL}_{\mathrm{stat}}$, and a post-filter

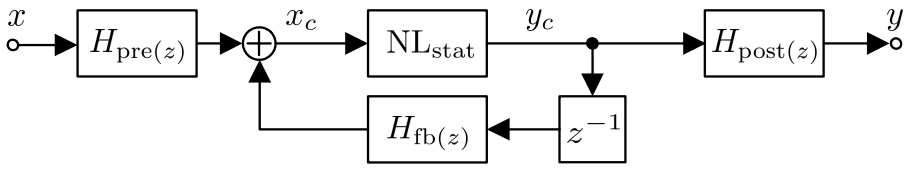

Figure 4.10: Wiener-Hammerstein model with feedback. This model allows to cover a wide class of nonlinear systems with memory, with relatively few, easy-to-interpret parameters.

$H_{\mathrm{post}}(z)$. Each of them can be specified with few parameters. To introduce additional modeling capability, we add a feedback filter $H_{\mathrm{fb}}(z)$, as depicted in Fig. 4.10. Although the amplitude-dependent phase modulation (AM/PM) inherent to baseband quasi-memoryless models [31] is already able to model continuous time band-pass systems with feedback [110], the proposed feedback in our baseband model allows for more complex nonlinear memory effects with just a few additional parameters. As the static nonlinearity in Fig. 4.10, we use an extension of Rapp's PA model to also include AM/PM effects [48]. With x_c being the baseband input sample of the static nonlinearity $\mathrm{NL}_{\mathrm{stat}}$, the output y_c is given as

$$y_c = A(|x_c|)e^{j\left(\angle x_c + \Delta_\phi(|x_c|)\right)} \tag{4.41}$$

with the AM/AM $A(|x_c|)$ and AM/PM $\Delta_\phi(|x_c|)$ given as

$$\begin{aligned} A(|x_c|) &= g_0\,|x_c|\,G^{-\frac{1}{2p}} \\ \Delta_\phi(|x_c|) &= \big(\,(a-b)\,|x_c| + c - d\big)G^{-\left(\frac{1}{2p}+1\right)} + b\,|x_c| + d \end{aligned}$$

where $G = 1 + \left(\frac{g_0|x_c|}{y_{\mathrm{c,max}}}\right)^{2p}$ and $g_0 > 0$ is a simple input gain factor. The transition factor p allows to account for soft-clipping (small p, e.g. $p = 2$) and hard-clipping (large p) above the output saturation point $y_{\mathrm{c,max}}$. The AM/PM parameters a, b, c, d are described in detail in [48].

A nonlinear system with arbitrary feedback can easily become unstable. Neglecting the static nonlinearity, the feedback loop constitutes a linear all-pole filter if we limit $H_{\mathrm{fb}}(z)$ to be an FIR filter. The resulting IIR filter is stable if all zeros of $H_{\mathrm{fb}}(z)$ are within the unit circle. With the nonlinearity present, the same stability condition holds if $|y_c| \leq |x_c|$, i.e., the static nonlinearity does not expand the signal, which we ensure by setting $y_{\mathrm{c,max}} \leq 1$.

4.6.2 Monte Carlo Simulation Setup

We test the EVM and EPR caused by the above-described parametric impairment models with random parameters. The distributions we used for nonlinearity and phase noise are summarized in Table 4.4 and Table 4.5, respectively, with

Table 4.4: Phase Noise Model - Parameter Distributions

Parameter	Distribution	Unit
B_{PLL}	$\mathcal{U}(10,50)$ $\mathcal{U}(3,300)$ 1/3 2/3	kHz
f_{corner}	$\mathcal{U}(0.3,30)$	kHz
L_0	$\mathcal{U}(-75,-150)$	dBc/Hz
L_{floor}	$\mathcal{U}(-200,-120)$	dBc/Hz

Table 4.5: Wiener-Hammerstein Model with Feedback - Parameter Distributions

Parameter	Distribution
$N_{z_{0,pre}}, N_{z_{0,post}}, N_{z_{0,fb}}$	$\mathcal{U}\{1,4\}$
$N_{z_{\infty,pre}},, N_{z_{\infty,post}}$	$\mathcal{U}\{1,4\}$
$\angle \boldsymbol{z}_{0,pre}, \angle \boldsymbol{z}_{0,post}, \angle \boldsymbol{z}_{0,fb}$	$\mathcal{U}(0,2\pi)$
$\angle \boldsymbol{z}_{\infty,pre}, \angle \boldsymbol{z}_{\infty,post}$	$\mathcal{U}(0,2\pi)$
$\lvert\boldsymbol{z}_{0,pre}\rvert, \lvert\boldsymbol{z}_{0,post}\rvert$	$\mathcal{U}(0,0.1)$ $\mathcal{U}(10,20)$ 2/3 1/3
$\lvert\boldsymbol{z}_{\infty,pre}\rvert, \lvert\boldsymbol{z}_{\infty,post}\rvert, \lvert\boldsymbol{z}_{0,fb}\rvert$	$\mathcal{U}(0,0.1)$
p	$\mathcal{U}(1,3)$ $\mathcal{U}(3,5)$ 1/3 2/3
$y_{c,max}$	$\mathcal{U}(0.2,0.8)$ $\mathcal{U}(0.6,0.9)$ $\mathcal{U}(0.9,1)$ 1/3 1/3 1/3
g_0 (dB)	$\mathcal{U}(-4,4)$ $\mathcal{N}(0,0.1)$ $\mathcal{N}(-3,1)$ 1/3 1/3 1/3
a (deg)	$\mathcal{U}(0,100)$ $\mathcal{N}(0,5)$
b (deg)	$\mathcal{U}(-100,0)$ $\mathcal{N}(0,10)$
c (deg)	$\mathcal{U}(50,0.1)$ $\mathcal{N}(0,5)$
d (deg)	$\mathcal{U}(0,100)$ $\mathcal{U}(0,5)$ 1/2 1/2

- $\mathcal{N}(\mu,\sigma)$, the normal distribution with expected value μ and standard deviation σ
- $\mathcal{U}(a,b)$, the uniform distribution between a and b
- $\mathcal{U}\{a,b\}$, the discrete uniform distribution between a and b.

Choosing appropriate distributions for the parameter values is not trivial, because the inband-error is typically dominated by the worst block parameter setting. Consequently, when assigning independent random numbers to several impairment parameters, ending up with many similar, rather bad (high) EVM values is very likely. To ensure that we have enough trials were all parameters have "good values", resulting in a low overall EVM, we use heuristic rules to draw realizations from different distributions with a certain probability. For instance, as indicated in Table 4.4, B_{PLL} is drawn uniformly either between 10-50 kHz or 3-300 kHz, with a probability of 1/3 or 2/3, respectively. Consequently, in more than one third of the cases we can expect to have little influence of phase-noise on the EVM, because we employ phase de-rotation correcting the effect of phase-noise having low bandwidth compared to our WLAN-OFDM subcarrier spacing of 312.5 kHz. We use a 320-symbol, 40-MHz bandwidth, 200-MHz sample rate WLAN-OFDM test signal with a maximum value of around 0.8 and an RMS value of 0.22.

The AM/PM parameters a, b, c, d of $\mathrm{NL}_{\mathrm{stat}}$ are linked together, i.e., they are all based on the same decision probability. Hence, with $\geq 50\%$ chance we have rather low AM/PM distortion. The unity-norm filters are defined based on a random number N_{z_∞} and N_{z_0} of poles z_∞ and zeros z_0, respectively. By avoiding pole and zero locations close to the unit circle, we avoid non-smooth frequency-dependence of the error. This is crucial for EPR and also practically justified, because non-smooth inband frequency-dependence is also avoided in practical PA designs.

We generate the impulse responses for our IQ mismatch model by randomly disturbing a unit impulse $\delta[n]$.

$$h_{\mathrm{I}}[n] = \delta[n] + \left(\frac{B_5}{10} v_1[n] + \frac{B_{40}}{100} v_2[n] + \frac{B_{40}}{1000} v_3[n]\right) r_{N_I}[n] \tag{4.42}$$

The Q-path $h_{\mathrm{Q}}[n]$ is independent and identically distributed (i.i.d) as $h_{\mathrm{I}}[n]$. Above, $v_k[n] \sim \mathcal{N}(0,1)$,

$$B_K = \begin{cases} 1, & \text{if} \quad \mathcal{U}(0,100) < K \\ 0, & \text{else} \end{cases} \tag{4.43}$$

and

$$r_{N_I}[n] = (1 - n/N_I)\,(u[n] - u[n - N_I]) \tag{4.44}$$

where $u[n]$ is the step sequence, i.e., $r_{N_I}[n]$ is a linearly decaying ramp of length $N_I \sim \mathcal{U}\{1, 10\}$, i.e. the IRs have a maximum length of 10 samples. The gain mismatch is

$$\begin{aligned} g = 1 &+ \gamma\mathcal{N}(0, 10^{-5}) + (1-\gamma)\mathcal{N}(0, 10^{-3}) \\ &+ B_{20}\mathcal{U}(-0.005, 0.005) + B_{10}\mathcal{U}(-0.05, 0.05) \end{aligned} \tag{4.45}$$

with $\gamma = B_{50}$. The phase mismatch in degree is

$$\varphi(\mathrm{deg}) = \mathcal{N}(0, 10^{-3}) + \xi_{=1}\mathcal{N}(0, 10^{-2}) + B_{10}\mathcal{U}(-5, 5) + \xi_{=2}\mathcal{U}(-1, 1) \tag{4.46}$$

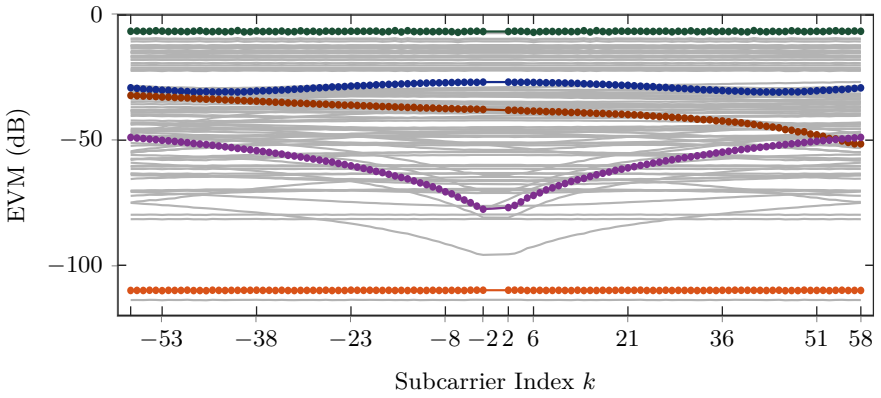

Figure 4.11: Frequency-dependent EVM for 100 trials of our IQ-mismatch model. Five results are highlighted, exemplifying the wide range of error levels and different frequency-shapes of the IQ-mismatch error.

with $\xi \sim \mathcal{U}\{1, 4\}$ and

$$\xi_{=K} = \begin{cases} 1, & \text{if} \quad \xi = K \\ 0, & \text{else} \end{cases} \tag{4.47}$$

To simplify the notation, $\mathcal{U}$ and $\mathcal{N}$ in (4.46) and (4.46) describe random variables drawn from the respective distributions. As shown in Fig. 4.11, the model in (4.42) generates a wide range of IQ-mismatch scenarios featuring the desired smooth frequency-dependence. Besides the outer- and innermost modulated subcarriers ± 58 and ± 2, the subcarrier ticks indicate the eight stopband-centers we used in all EPR simulations.

4.6.3 Results

Fig. 4.12 summarizes the results of all four (impairment types) times 3000 (trials) simulations in a single box-and-whisker plot of the estimation error. For each of the tested systems, the EPR is a good estimate of the EVM. This is a much stronger result than showing a low error for a single system, especially if we consider the modeling capabilities of the used models and the wide range of random parameter variations. The tested EVM-range is depicted in Fig. 4.13. There is no lower floor on the EPR at -90 dB as discussed above in Section 4.2.2, because we use a coherent analysis, i.e., a rectangular window.

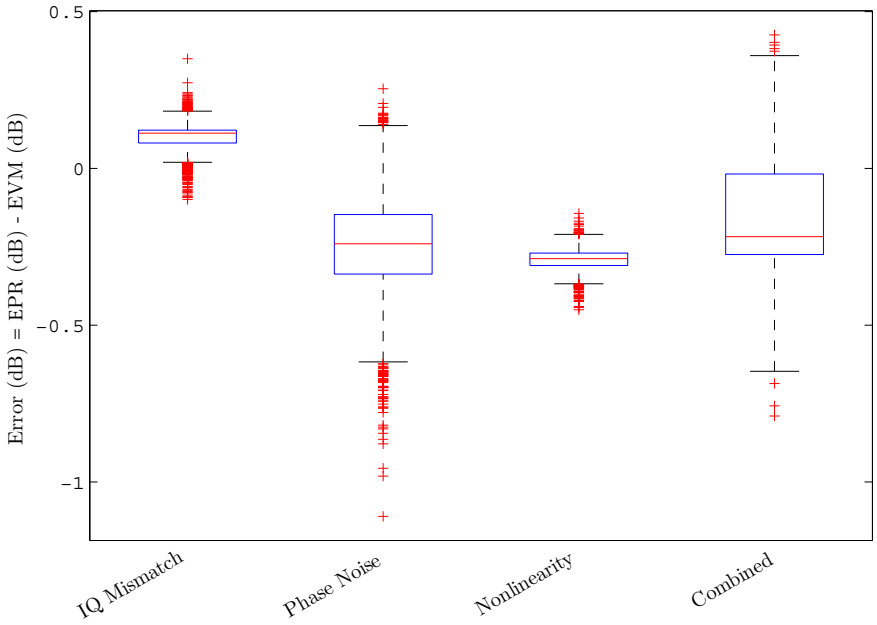

Figure 4.12: Box-and-whisker plot of the estimation error $\text{Error(dB)} = \text{EPR(dB)} - \text{EVM(dB)}$ for all three presented impairment models and their combination (serial connection) for 3000 trials for each scenario. The whiskers indicate $p_{75} + w_{max}(p_{75} - p_{25})$ and $p_{25} - w_{max}(p_{75} - p_{25})$, where $w_{max} = 1.5$ is the maximum whisker length and p_{75} and p_{25} are the 75th and 25th percentile, respectively. The blue boxes indicate p_{25} p_{75}, the red line is the median, the red pluses are outliers. The absolute bias in estimating the EVM for each system is less than 0.3 dB. Furthermore, there are no extreme outliers, which indicates the reliability and robustness of the method.

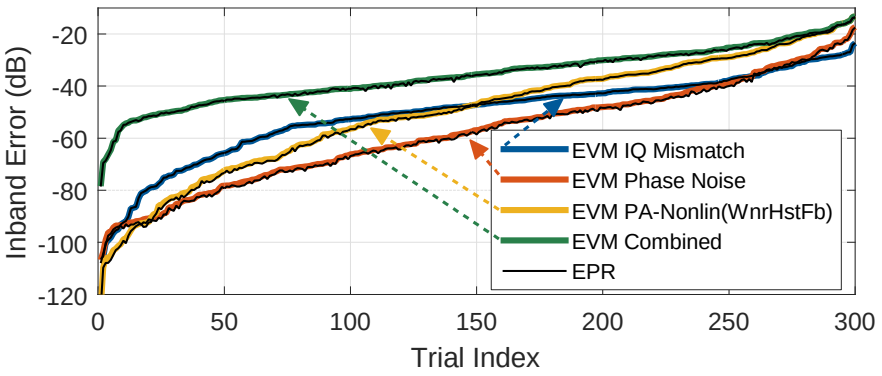

Figure 4.13: First 300 individual trial results, sorted by EVM. This plot indicates the wide EVM range of the tested trials. The individual impairment scenarios are independent. For the combined system test, the indiviual impairments are connected in series in the following order: IQ-mismatch, phase noise, nonlinearity. Consequently, the curve showing the added EVM is higher than the individual impairment curves, because the EVM adds up and gets worse.

4.7 Conclusions

This chapter presented an NPR measurement method with the goal of estimating the EVM. To discern the proposed method from the traditional approach with a single, broad notch in the center of the spectrum, and to account for the fact that the NPR is inversely defined, we introduced the term error power ratio (EPR) for the proposed NPR-based EVM estimation method. The EPR is an attractive alternative to the EVM because, in contrast to the EVM, the EPR does not need high-accuracy demodulation and digitization of the whole signal bandwidth. Rather, a standard swept-tuned spectrum analyzer is all that is needed to make high accuracy, low-floor measurements more or less independent of the bandwidth.

The EPR can be a good estimate of the EVM (with equalizer and phase de-rotation employed) in case of additive noise, nonlinearity, phase noise, and IQ mismatch. We were able to explain this by analytical considerations illustrated with exemplary simulation results, and verified it by measurements. Besides estimating the EVM by using asymmetric stopbands, the EPR provides the possibility to exclude IQ mismatch by using symmetric stopbands. This can be handy when tracking the source of limited EVM performance or when measuring EVM of DUTs with very low EVM, without biasing the result with non-ideal IQ-modulation and/or -demodulation.

Although we focused on WLAN signals, our method should be readily applicable to other OFDM-based communication standards. However, for signals that are not circularly symmetric normal (CSCN), some further work is necessary. Straightforward linear filtering changes the statistics of a non-CSCN signal, in general. Hence, a key issue when trying to use the EPR to estimate the EVM for non-CSCN signals is how to generate a signal retaining the communication signal statistics but featuring the required stopbands.

In contrast to model-based EVM estimation methods reviewed in Section 1.2.1, our NPR-approach does not rely on a certain DUT model assumption. We only use DUT models to test and understand the characteristics of our method. Our only assumption required for estimating the EVM with a single measurement run is that the frequency-dependence of the EVM is "well-behaved", i.e., smooth. More precisely, the mean over a few EVM estimates at stopband subcarriers must resemble the EVM averaged over all subcarriers.

To sample the EVM at a few distinct subcarriers, the EPR uses N_m distinct stopbands. While that is already possible with commercial NPR measurement tools [43], only traditional NPR results, where a notch in the center of the bandwidth is used, are presented in the literature. Using only a single notch in the center does not capture the effect of IQ mismatch on the EVM, as discussed in Section 4.3.4.

As outlined above, the validity of the result of a single EPR measurement is limited in case of heavily frequency-dependent EVM. This limitation is resolved with the swept EPR (SWEEPR) method presented in Section 5.

5

SWEEPR - Swept Error Power Ratio

This chapter presents a new swept error power ratio (SWEEPR) method that is based on the same principle as the EPR, but overcomes its main drawback: The EPR observes the inband error solely at certain stopband locations, which limits its applicability in case of heavily frequency-dependent error. The key idea of SWEEPR is to use a test signal featuring a linearly swept stopband center frequency. To this end, we propose a straightforward digital baseband structure to filter the communication signal. To measure the frequency-dependent EPR, we use a swept-tuned analyzer triggered in sync with the stopband sweep. Measurement results confirm that SWEEPR is able to estimate a heavily frequency-dependent EVM. Besides the content submitted as a letter [A6], this chapter includes additional contributions, in particular in Section 5.3.

5.1 Introduction

A fundamental limitation of the NPR and EPR is that the error is only observed within the stopband, which can only be a fraction of the signal bandwidth. It is therefore impossible to observe the error over the entire inband with a single EPR measurement. Making several measurements at different stopband locations increases the measurement time significantly. By contrast, SLIC-EVM and other methods that measure the error by removing a linear approximation of the DUT output from the DUT output are able to estimate a heavily frequency-dependent EVM with a single measurement. However, either a synchronized VSA measurement chain similar to EVM measurements [A2, 120, 138] or an accurately calibrated vector network analyzer [149] is required. By contrast, SWEEPR measurements can be performed with a swept-tuned spectrum analyzer, which brings all the advantages already discussed in the introduction and the chapter on the EPR (cheap, simple, no errors due to synchronization and demodulation, high bandwidth). Swept-sine methods are either designed only for linear systems [90] or rely on the analysis of harmonic distortion, which requires high capture sampling rates and limits the use to Hammerstein nonlinearities [100].

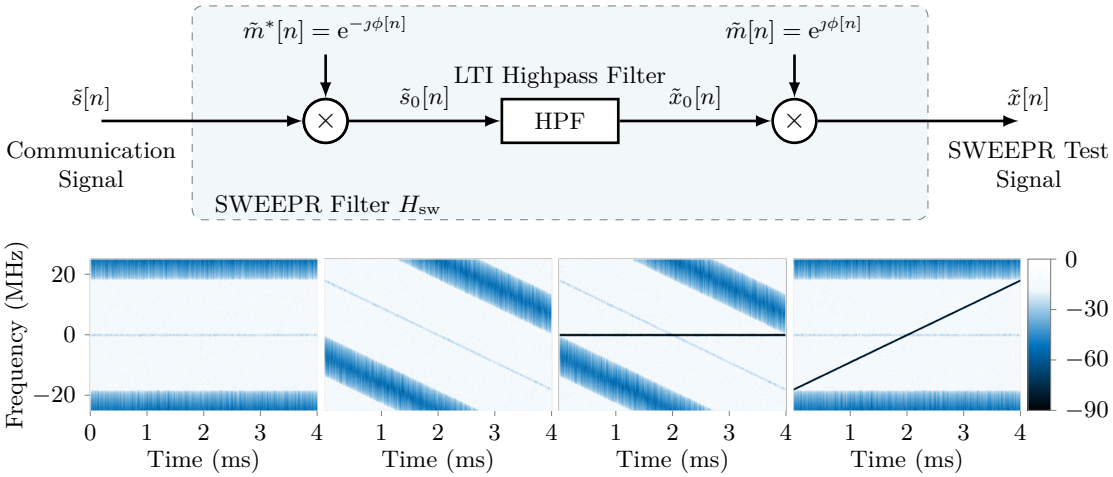

Figure 5.1: Principle of SWEEPR test signal generation with a swept-stopband filter. This filter is implemented by modulating a source signal $\tilde{s}[n]$ with $\tilde{m}^*[n] = e^{-j\phi[n]}$, filtering with a linear time-invariant (LTI) highpass filter, and modulating back with $\tilde{m}[n] = e^{j\phi[n]}$. By sweeping the instantaneous phase $\phi[n]$ appropriately, the desired swept-stopband filter characteristic is obtained.

5.2 Single-Stopband SWEEPR

In this section, we introduce the concept of SWEEPR with the simplest case: We show how to filter a complex-valued baseband signal to obtain a single time-varying stopband, and how to analyze such a signal. Furthermore, we derive that the proposed SWEEPR metric estimates the EVM even in case of heavily frequency-dependent errors and DUT frequency responses, whereas the EPR is biased in that case as shown in 4.3.1.

5.2.1 Signal Generation

The approach to generate the SWEEPR test signal is the same as for the EPR described Section 4.2.2: We filter the digital baseband source signal $\tilde{s}[n]$. However, the filter stopband center location is not constant but should change over time. We want to linearly sweep the center frequency of the stopband from a start frequency $f_0 = f(t = 0)$ to a stop frequency $f_1 = f(t = T_1)$, where t denotes time and T_1 is the duration of the stopband sweep. A reasonable choice for the start and stop frequency is to cover the whole inband, e.g., from -20 to 20 MHz for a 40 MHz bandwidth communication signal.

To implement the swept stopband filter, we propose the structure shown in Fig. 5.1, consisting of two chirp modulators and a linear time-invariant highpass filter that can be implemented in the same straightforward way as the EPR filter in Listing 4.1. The source spectrum is (circularly) shifted to the 'right' (to DC), the band around DC is suppressed by the highpass filter, and shifted back to the 'left'.

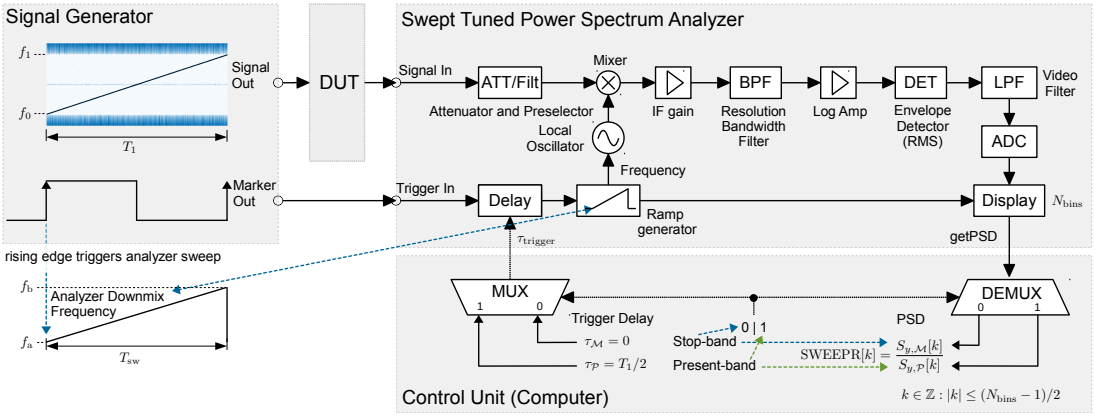

Figure 5.2: Principle of SWEEPR measurements with a swept-tuned spectrum analyzer. The analyzer's sweep is synchronized to the test signal's stopband sweep by externally triggering the analyzer with a marker signal. Depending on the trigger delay, the error (stopband) PSD or the signal (present band) PSD is obtained. The ratio of the error PSD to the signal PSD is a frequency-dependent EVM estimate.

For the chirp modulation, consider the complex exponential $\tilde{m}(t) = e^{j\phi(t)}$, with an instantaneous phase

$$\phi(t) = 2\pi\,(f_0 + \kappa t/2)\,t \tag{5.1}$$

where $\kappa = \frac{f_1 - f_0}{T_1}$ is the chirp rate. The corresponding instantaneous frequency is

$$f(t) = \frac{1}{2\pi}\frac{\mathrm{d}\phi(t)}{\mathrm{d}t} = f_0 + \kappa t \tag{5.2}$$

i.e., we have the desired linear chirp sweeping from f_0 to f_1 during T_1. The modulation theorem of the Fourier transform is $s(t)e^{j\nu t} \overset{\mathscr{F}}{\longleftrightarrow} S(\omega - \nu)$, i.e., by modulating with $e^{j\nu t}$, we shift the spectrum to the 'right' if $\nu > 0$. To shift $f_0 = -20$ MHz to DC, we must set $\nu = -f_0 = 20$ MHz. Therefore, $\tilde{s}[n]$ is first modulated with the inverse sweep $\tilde{m}^*(t) = e^{-j\phi(t)}$ having an instantaneous frequency $-f_0$ at $t = 0$ and $-f_1$ at $t = T_1$. The shift back after the highpass is achieved by modulating with $\tilde{m}(t)$. The discrete time modulator signal is given as $\tilde{m}[n] = \tilde{m}(nT_s)$, where the sampling interval is $T_s = 1/f_s$ and the sampling rate is $f_s = 50$ MHz in our examples.

5.2.2 Swept-Tuned SWEEPR Analysis

Swept-tuned spectrum analyzers tune into different analysis frequencies by sweeping the local oscillator frequency of the down-mixer, from a start frequency f_a to a stop frequency f_b during a sweep time T_sw. This sweep is used to mix the input signal down to an intermediate frequency (IF). After downmixing to IF, the signal is filtered with a band-pass filter (BPF) centered at IF. This BPF determines the resolution bandwidth (RBW) of the spectral analysis. The power of the BPF output is measured using

an envelope detector, whose output can further be smoothed by the video bandwidth (VBW) filter.

Because the start of the analyzer sweep can typically be triggered from an external input, swept-tuned analyzers are perfectly suited to analyze SWEEPR signals. We only have to make the start and the stop frequency, and the sweep time of the analysis equal to the respective parameters of the SWEEPR signal and coarsely compensate for a potential delay between the trigger and the signal path. This can be done by cyclically shifting the marker signal used for triggering, such that the spectrum analyzer displays the stopband PSD for a trigger delay $\tau_{\mathcal{M}} = 0$. By using an appropriate offset, e.g., half the sweep time $\tau_{\mathcal{P}} = T_1/2$ in the single stopband case, we leave the stopband and sample the signal PSD instead.

Fig. 5.2 shows a block diagram visualizing the setup of SWEEPR measurements. Note that the required synchronization, i.e., setting trigger delay, sweep time, start and stop frequency, is much simpler than the sample-wise synchronization needed for EVM measurements.

Setting the number of bins displayed on the spectrum analyzer to $N_{\text{bins}} = 2k_{\max} + 1$, allows for direct translation of the power measured at frequencies f_k in hertz to subcarrier bins by

$$k = \frac{f_k - f_c}{\Delta_f}. \tag{5.3}$$

The ratio of the stopband PSD to the signal PSD is a frequency-dependent EVM estimate:

$$\text{SWEEPR}[k] = \frac{S_{y,\mathcal{M}}[k]}{S_{y,\mathcal{P}}[k]} \tag{5.4}$$

An estimate of the overall EVM is obtained by averaging SWEEPR$[k]$ over the set of subcarriers $\mathcal{D}$ also used for averaging the EVM.

$$\text{SWEEPR} = \frac{1}{|D|} \sum_{k \in \mathcal{D}} \text{SWEEPR}[k]. \tag{5.5}$$

SWEEPR does neither experience the EPR's bias in case of frequency-dependence of the error, nor in case of a highly frequency-dependent related best linear approximation of the DUT, that we investigated in Section 4.3.1. This is shown in the following. We start with the case of an LTI filter with additive noise at its output. The EVP (the squared EVM) and the EPR for that case are given in (4.17), and (4.19b), respectively. If we assume an ideal stopband attenuation, i.e., $S_{x,\mathcal{M}}[k] = 0$ and insert $S_y[k] = |H_k|^2 S_x[k] + S_v[k]$ from (4.18) in (5.4), we obtain

$$\text{SWEEPR}[k] = \frac{S_v[k]}{|H_k|^2 S_x[k] + S_v[k]} \approx \frac{S_v[k]}{|H_k|^2 S_x[k]} = \text{EVP}[k]\,. \tag{5.6}$$

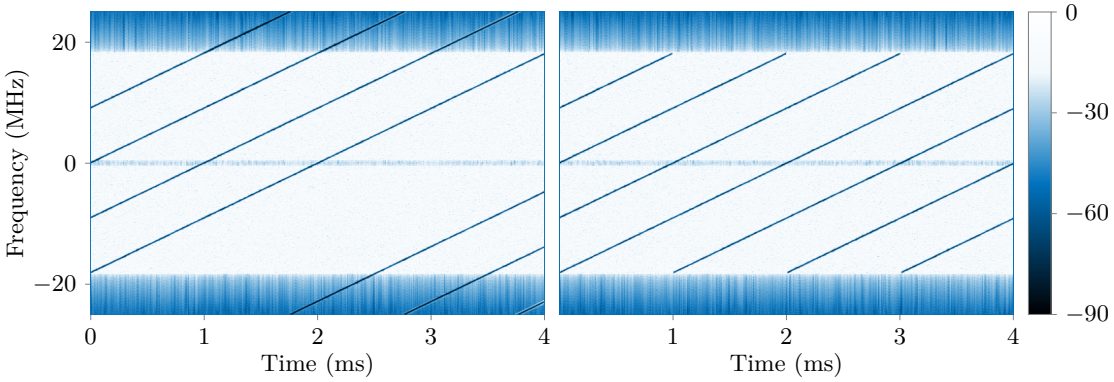

Figure 5.3: Spectrograms of SWEEPR signals with multiple ($N_{\text{sw}} = 4$) stopbands. (a) By using the same structure as in the single stopband case in Fig. 5.1 but replacing the highpass filter with a multi-stopband (EPR) filter, we obtain stopband sweeps that cover the whole bandwidth. This is not desired, since time is wasted by sweeping through the out-of-band region, e.g., 18.5 to 20 MHz. This can be avoided by using a cascade of N_{sw} filters, each applying a different single stopband, as shown in Fig. 5.4. The resulting spectrogram is shown in (b).

For the case of noise at the input, we obtained the EVP in (4.26), and the EPR in (4.29). By inserting $S_y[k] = H_k(S_x[k] + S_v[k])$ from (4.27) into (5.4), we obtain

$$\text{SWEEPR}[k] = \frac{|H_k|^2 S_v[k]}{|H_k|^2 S_x[k] + |H_k|^2 S_v[k]} \approx \frac{S_v[k]}{S_x[k]} = \text{EVP}[k]\,. \tag{5.7}$$

The requirements for the theoretical equivalence of the SWEEPR result and the EVP for both cases above are only that the stopband rejection and the SNR are reasonably good, e.g. > 80 and $> 10dB$, as shown in Fig. 4.4. These requirements are the same as required for the EPR in the case of additive white Gaussian noise.

5.3 Multi-Stopband SWEEPR

5.3.1 Signal Generation

With the EPR discussed in Section 4, we used not only a single stopband, but several stopbands. The reason was twofold:

1. To observe the error at several, distinct center frequencies.

2. To observe more bandwidth of the error to increase the precision of the measurement.

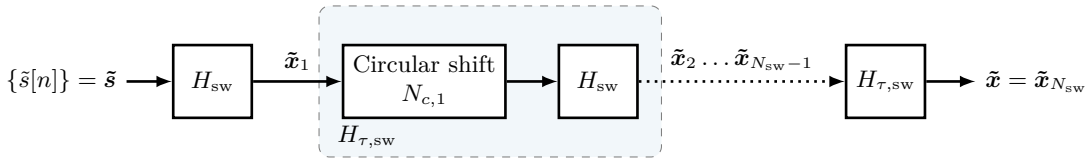

Figure 5.4: Proposed filter structure to generate a SWEEPR test signal with multiple concurrent stopband sweeps, as shown in Fig. 5.3 (b). The N_{sw} stopbands are generated using N_{sw} consecutive filter operations. The first filter is the single stopband filter H_{sw} shown in Fig. 5.1. The following $N_{\mathrm{sw}}-1$ stopbands are generated by applying $N_{\mathrm{sw}}-1$ times the filter $H_{\tau,\mathrm{sw}}$ that shifts the signal vector circularly in time before applying H_{sw}. The signal vector notation, e.g., $\tilde{\boldsymbol{x}} = (\tilde{x}[0], \tilde{x}[1], \ldots, \tilde{x}[N_1 - 1])$, is used to emphasize that the circular shift must be done "offline" with the entire signal of length N_1 samples.

Since SWEEPR is designed to observe the error at all inband frequencies, the first point is not relevant for SWEEPR. However, the second point suggests to use several concurrent stopbands also with SWEEPR.

Fig. 5.3 shows SWEEPR signals with $N_{\mathrm{sw}} = 4$ concurrent sweeps, with an equidistant center frequency spacing of $(f_1 - f_0)/N_{\mathrm{sw}}$ Hz. The first signal, (a), is generated by using the structure in Fig. 5.1 but replacing the the highpass filter (having a stopband at DC) with a multi-stopband filter. This approach results in stopband sweeps that extend over the whole bandwidth, i.e., from $-f_s/2$ to $f_s/2$. Consequently, time is wasted sweeping through the out-of-band region, e.g., from 18.5 to 25 MHz, in Fig. 5.3 (a). Fig. 5.3 (b) shows the desired spectrogram of a SWEEPR signal with multiple stopbands. This signal is obtained by applying the filter from Fig. 5.1 N_{sw} times, i.e., we simply cascade N_{sw} filters. To obtain the different stopband locations, we shift the input signal to all individual filters but the first circularly in time, i.e. a sample shifted out at the end appears at the beginning of the signal. The applied delay is

$$\tau_{N_{\mathrm{sw}}} = \frac{T_1}{N_{\mathrm{sw}}}\,. \tag{5.8}$$

The corresponding filter structure is depicted in Fig. 5.4.

5.3.2 Symmetric Stopband Signal Generation

As shown in Fig. 4.7, the error observed in asymmetric stopbands includes the effect of IQ mismatch whereas in symmetric stopbands the IQ mismatch does not show up. When measuring RF devices it can be desirable to exclude IQ mismatch completely, as discussed in Section 3.1. Consequently, it is desirable to be able to generate SWEEPR test signals featuring symmetric stopbands. The spectrogram of a SWEEPR signal with symmetric stopbands is shown in Fig. 5.5. Such a symmetric-stopband SWEEPR signal can be generated by applying an additional downward-sweeping stopband filter on the

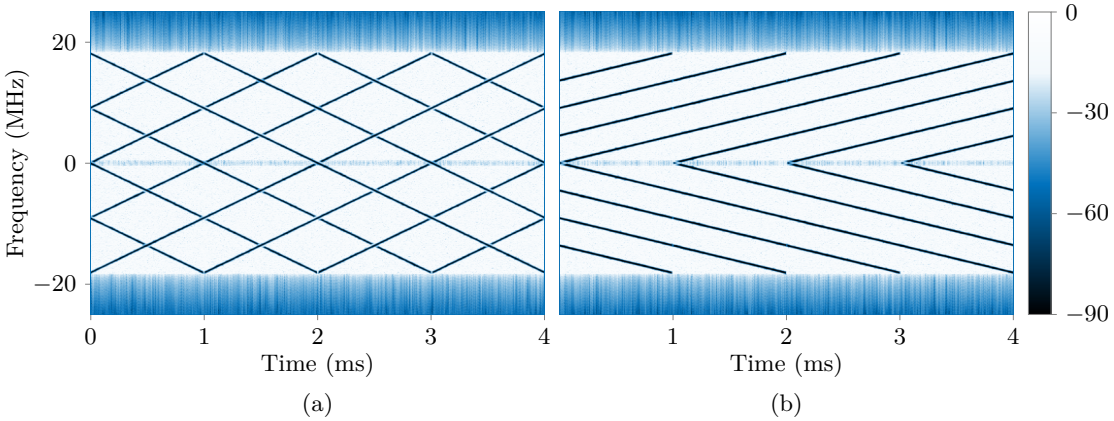

Figure 5.5: (a) Signal with four *symmetric* stopbands by taking the signal from Fig. 5.1 (b) and applying another four stopband filters that sweep downwards, by exchanging f_0 and f_1 from the upward sweep filters. (b) Spectrogram of a real-valued SWEEPR signal, generated with the structure shown in Fig. 5.6. While (a) is useful for analysis of RF signals, the signal in (b) lends itself to analysis of baseband or audio circuits. The stopbands of the signal in (b) can be analyzed with a sweep starting at $f_a = 0$, whereas (a) requires negative analysis frequencies, meaning that an additional modulation to a carrier frequency larger than half the bandwidth is required.

upward-sweeping stopband signal shown in Fig. 5.3, i.e. after applying a first (multi-stopband) filter using chirp modulation based on (5.1) sweeping from $f_{0,1} = -k_{\max}\Delta_f$ to $f_{1,1} = k_{\max}\Delta_f$, we apply a second filter that is identical with exception of the chirp modulator frequency setting. The second filter sweeps downwards from $f_{0,2} = -k_{\max}\Delta_f$ $f_{1,2} = k_{\max}\Delta_f$.

The signal in Fig. 5.3 (b) features asymmetric stopbands most of the time. At $t = 0$ there is, however, a symmetric stopband at about ± 10 MHz. More precisely, there are symmetrical stopbands around DC ($f = 0$) at times

$$t_{\text{sym,i}} = \frac{iT_1}{2N_{\text{sw}}},\ \forall\, i = \{0, 1, \cdots, 2N_{\text{sw}}\}\,. \tag{5.9}$$

5.3.3 Real-Valued Signal Generation

Simply taking the real part of a complex-valued SWEEPR signal as generated with Fig. 5.1 does not work. The signal is of course real, but the stopband is lost. Taking the real-value of the symmetric-stopband signal in Fig. 5.5 (a) yields a real-valued signal with swept stopbands. The spectrogram looks basically the same as in Fig. 5.5 (a). However, to analyze all the stopbands, we would either have to start the analyzer sweep at negative frequencies or be able to sweep downwards, which is both not possible with a swept-tuned analyzer like the PSA. Fig. 5.5 (b) shows a signal with the desired

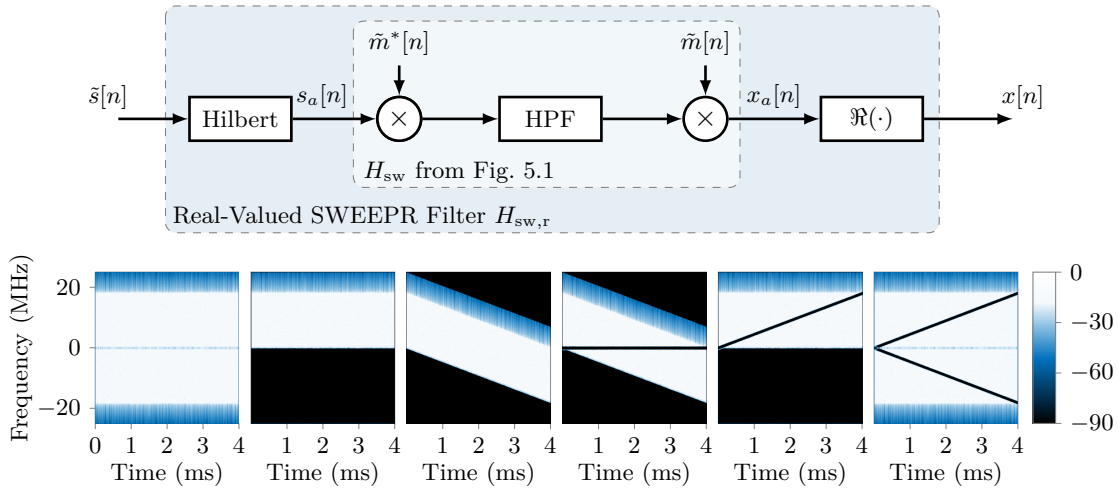

Figure 5.6: A real-valued SWEEPR signal can be generated by sending an analytic signal trough the filter from Fig. 5.1, and taking the real-part of the result. The analytic signal is $s_a[n] = \Re(\tilde{s}[n]) + j\mathcal{H}\{\Re(\tilde{s}[n])\}$, where $\mathcal{H}\{\cdot\}$ is the Hilbert Transform and $\tilde{s}[n]$ is the source signal.

characteristic. It is real-valued and hence symmetric around $f = 0$. The important difference to (a) is that it can be analyzed with a swept-tuned analyzer without additional modulation to a carrier frequency $f_c > f_0$.

While the output $x[n]$ in Fig. 5.6 is real-valued, the processing and the intermediate signals within the filter are complex-valued. To generate a real-valued signal with multiple stopbands as in Fig. 5.5 (b), the same approach can be used as for generating multiple stopbands in the complex-valued case. The only difference compared to Fig. 5.4 is to use $H_{\mathrm{sw,r}}$ instead of H_{sw}.

5.4 Measurements

To verify the performance of our method, we compare SWEEPR measurement results with subcarrier-dependent EVM results. We use a 40-MHz WLAN source signal $\tilde{s}[n]$ of length $T_1 = 4$ ms at a samplerate $f_s = 50$ MHz. To obtain the SWEEPR signal $\tilde{x}[n]$, we use a sweep start frequency of $f_0 = -k_{\max}\Delta_f$ and sweep stop frequency of $f_1 = k_{\max}\Delta_f$, respectively, where $\Delta_f = 312.5$ kHz is the subcarrier spacing of WLAN. With $k_{\max} = 60$ we cover all modulated subcarriers ($|k| \leq 58$) of 40-MHz WLAN. We generate an error sequence $\tilde{e}[n]$ consisting of colored Gaussian noise and two additional single-tone interferers. We add $\tilde{e}[n]$ to $\tilde{s}[n]$ and compute the EVM directly in Matlab to obtain a reference EVM[k]. We also add $\tilde{e}[n]$ to the SWEEPR test signal $\tilde{x}[n]$, yielding an impaired signal $\tilde{y}[n]$. We download $\tilde{y}[n]$ to an Agilent PSG E8267C, which mixes the signal to a center frequency of $f_c = 5.6$ GHz. The PSG's RF output is directly

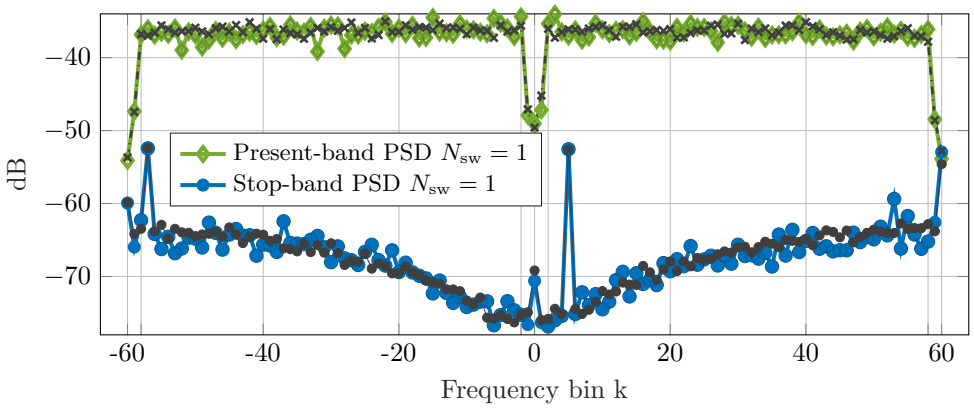

Figure 5.7: Measured present band PSD $S_{y,\mathcal{P}}[k]$ and stopband PSD $S_{y,\mathcal{M}}[k]$, obtained from the power spectrum analyzer (PSA). The results for a single stopband $N_{\text{sw}} = 1$ are shown in color, whereas the result for $N_{\text{sw}} = 4$ stopbands are shown in gray. The resulting SWEEPR results are shown in Fig. 5.8.

connected to the RF input of an Agilent PSA E3330A Analyzer. The sweep of the PSA is synchronized to the stopband sweep as shown in Fig. 5.2.

5.4.1 Results

To compute the SWEEPR in (5.4), we require the stopband and the inband PSD. Fig. 5.7 shows the measured PSDs. Our EVM estimate is the difference of the measured PSDs in dB, i.e.,

$$\text{SWEEPR}[k]\,(\text{dB}) = S_{y,\mathcal{M}}[k]\,(\text{dB}) - S_{y,\mathcal{P}}[k]\,(\text{dB})\,. \tag{5.10}$$

Fig. 5.8 compares the SWEEPR measurement result with the true EVM. The interference at the bins $k = -57$ and $k = 5$ is clearly identified. Since SWEEPR observes less bandwidth per time, its variance is higher than the variance of the EVM for a given length of the measurement.

The variance of SWEEPR can be reduced by increasing T_1 or using more than one stopband sweep, as shown in Fig. 5.9. The sample standard deviation (averaged over k) of $D_{\text{sweepr}}[k]$ using a single stopband $N_{\text{sw},1} = 1$ is $\sigma_1 \approx 1.66$, whereas with $N_{\text{sw},2} = 4$ stopbands it is $\sigma_2 \approx 0.84$ dB. This result is perfectly in line with theory: By increasing the observed bandwidth by factor of four, the variance decreases by the factor four. The standard deviations are related by

$$\sigma_2 = \sigma_1 \sqrt{N_{\text{sw},1}/N_{\text{sw},2}}\,. \tag{5.11}$$

Fig. 5.10 shows results of a measurement dominated by IQ mismatch. Using the proposed symmetric SWEEPR signal, we can exclude the IQ mismatch like with the proposed

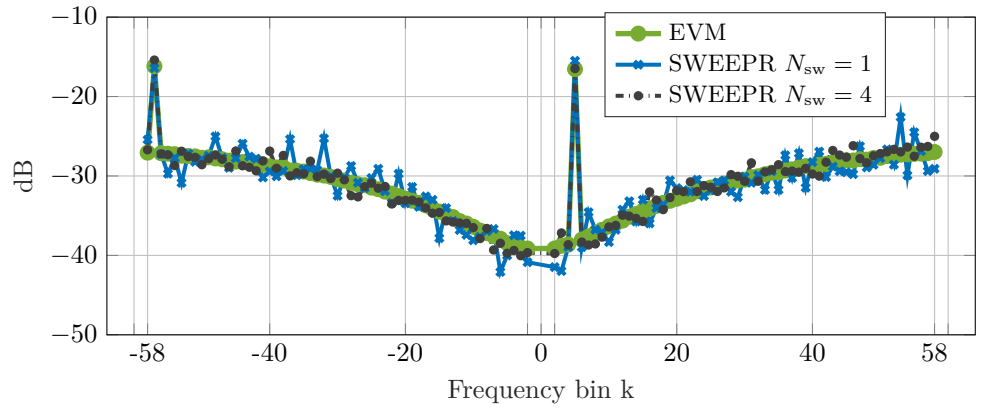

Figure 5.8: Subcarrier-dependent SWEEPR measurement result SWEEPR[k] compared with the true EVM[k]. With a single stopband $N_{sw} = 1$ the variance is quite high, since we observe only a fraction of the bandwidth per time than with the EVM. Using $N_{sw} = 4$ concurrent stopbands reduces the variance. Rounded to the first decimal, the average data EVM is −28.7 dB, whereas the average SWEEPR is −28.3 dB in both cases, i.e., for $N_{sw} = 1$ and $N_{sw} = 4$.

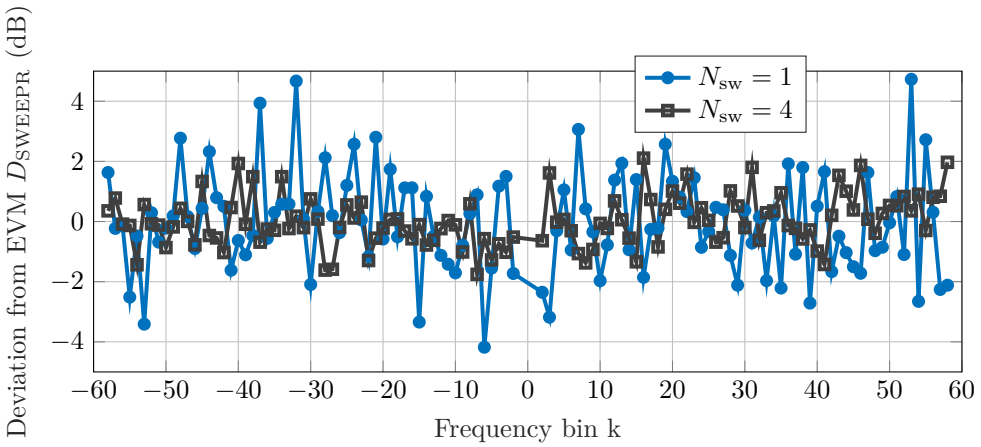

Figure 5.9: Deviation $D_{\mathrm{SWEEPR}}[k] = \mathrm{SWEEPR}[k](\mathrm{dB}) - \mathrm{EVM}[k](\mathrm{dB})$ of the results from 5.8.

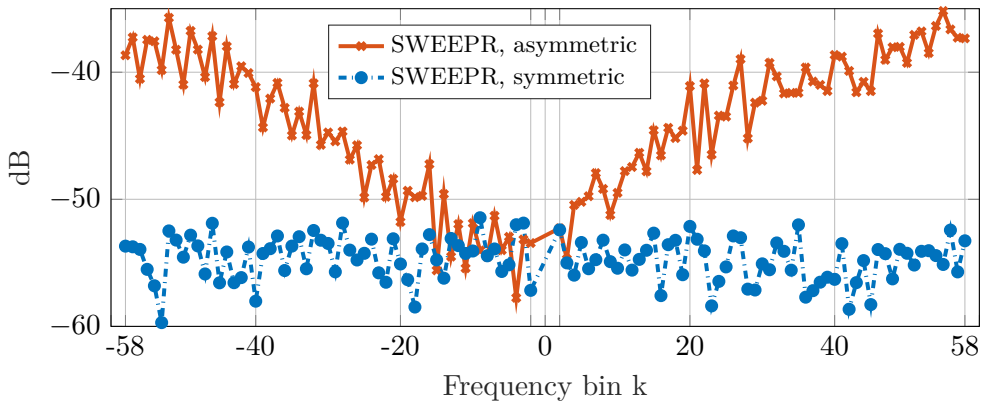

Figure 5.10: SWEEPR measurement at 5.6 GHz obtained by directly connecting the PSG signal generator to the PSA analyzer. Using the SWEEPR signal with a single, asymmetric stopband, we include the frequency-dependent IQ mismatch of the PSG. By using a test signal with a symmetric stopband, IQ mismatch is excluded. We can measure down to around −55 dB over the entire frequency range, without an additional calibration.

methods with symmetric stopbands for the EPR and symmetrically-nulled subcarriers for the EVM. The asymmetric SWEEPR, and also the regular EVM, are biased by our generator's IQ mismatch. By using SWEEPR with symmetric stopbands, we are able to measure RF-DUTs with an EVM down to<-50 dB with our simple measurement setup.

5.4.2 Discussion

A signal cannot be narrow in time and bandwidth at the same time, i.e., the time-bandwidth product is lower-bounded [141, Sec. 2.8.5]. This fundamental principle is known as the uncertainty principle. We already encountered a practical implication of it in the formula on the sweep duration given a certain RBW with a swept-tuned analyzer (2.18). With SWEEPR, this translates to the following issue: We cannot make the sweep time arbitrary short when we want to resolve narrow stopband-widths. Using long sweep times is also beneficial to increase the precision (decrease the variance) of SWEEPR measurements.

Like EPR, SWEEPR observes the error power only within the stopband(s). However, with SWEEPR also the observation time is localized, since the stopband location is continuously varied over time. Assuming an analysis sweep over N_{bins} bins and using a single stopband with a width of Δ_f HZ, the time during which we observe the error power with SWEEPR is

$$T_{\text{avg,SWEEPR}} = \frac{T_{\text{avg,EPR}}}{N_{\text{bins}}} = \frac{T_{\text{avg,EVM}}}{N_{\text{bins}} N_D} \tag{5.12}$$

where N_D is the number of OFDM data subcarriers. For 40-MHz WLAN, $N_D = 108$ and $N_{\text{bins}} = 121$ when sweeping from $k = -60$ to $k = 60$. Clearly, there are two things we can do decrease the variance: use a longer signal T_1, or increase the observed stopband-width B_{stop}. The variance decreases linearly with increasing T_1 and B_{stop}.

To increase the error observation bandwidth, we may increase the stopband width. However, as explained in Section 4.3.3, the stopband-width should resemble the subcarrier-spacing for EVM estimation of phase noise error with de-rotation. The stopband-width may however be broader than the subcarrier spacing in case of a nonlinear DUT or IQ mismatch. For IQ mismatch, only the symmetry of the stopband around the carrier is important. For nonlinearity, the error provoked by the communication signal should not be altered too much by introducing the stopband to the signal. While a general quantitative statement is hard to formulate, a practical guideline may be stated: Using a stopband-width of $2\Delta_f$ to $6\Delta_f$ does not seem to significantly affect the EPR in case of the PA nonlinearities, simulated and measured in this thesis. In case of doubt, two EPR measurements, one with a narrow stopband-width (e.g., Δ_f) and another one with a wide stopband-width (e.g., $6\Delta_f$), may be compared.

Besides using a broader stopband, we can use several concurrent stopbands instead of a single stopband to increase the error observation bandwidth. As as shown in the measurement results in Fig. 5.8, this also leads to a decreased variance.

5.5 Conclusions

This chapter proposed a new measurement method called the swept error power ratio (SWEEPR), that is based on continuously sweeping the stopband center frequency of a noise power ratio (NPR) measurement. SWEEPR measurements can be performed with standard RF lab gear, i.e., an arbitrary waveform generator and a swept-tuned spectrum analyzer. With the EPR, many measurements with different excitation signals are required to observe the EVM at all subcarriers. With SWEEPR, on the other hand, the subcarrier-dependent EVM can be estimated using only a single test signal and two measurements to capture the stopband and present-band PSD. The SWEEPR method can do this much quicker, with a single excitation signal and two measurements to capture the stopband and present-band PSD, respectively. In contrast to the EVM, SWEEPR measurements do neither require accurate synchronization nor standard-dependent receiver capabilities, which makes SWEEPR measurements readily adaptable to new signal standards and higher bandwidths.

6
Summary and Conclusions

6.1 Summary

In this thesis we have investigated new methods for measuring the EVM of OFDM signals impaired by non-ideal transceiver hardware.

Chapter 1 introduced the EVM as the primary method to measure the inband error due to transceiver impairments like nonlinearity, phase noise, and IQ-mismatch. The NPR was introduced as a traditional, alternative method to measure noise and distortion that allows for straightforward measurements with a swept-tuned analyzer. Besides being simple and cheap, swept-tuned measurements allow for a low noise floor at high signal bandwidths.

Chapter 2 subsumed important preliminaries required in the later chapters. We reviewed PSD estimation and measurement, transceiver impairments like IQ mismatch, phase noise and nonlinearity, and the EVM of OFDM signals with focus on WLAN.

In Chapter 3, we had three distinct sections related to the EVM. First, Section 3.1 presented an extension of the regular EVM to exclude IQ mismatch from EVM measurement. To be able to do so, we required a special test signal obtained by modifying the standard OFDM signal. For every OFDM symbol we nulled different pairs of subcarriers nulled symmetrically around DC. The measurement was the same as with regular EVM, the only difference was that the EVM of the nulled bins was analyzed separately. We have shown analytically and in simulations that using the proposed method, a single measurement can provide us the regular EVM and a second, IQ mismatch-free EVM result at the same time.

Section 3.2 presented SLIC-EVM, a method to estimate the EVM without demodulating the data symbols. SLIC-EVM subtracts a linear approximation of the DUT output from the DUT output and performs a PSD analysis. We implemented SLIC-EVM by means of digital baseband signal processing and -analysis, requiring the same measurement setup as EVM measurements. The test signal was the original communication signal. By subtracting the correlated parts (linear approximation) we reproduced the effect of using an equalizer in EVM analysis. Furthermore, we were able to implement de-rotation in SLIC-EVM to reduce the effect of common phase error in the same way as in regular EVM analysis. The presented simulation and measurement results agreed

very well with regular EVM results. The main advantage of SLIC-EVM is that due to the lack of data symbol demodulation it is simple to implement and can be easily adapted to new standards.

Section 3.3 presented an application of the EVM. We have optimized the EVM of a signal impaired by a power amplifier nonlinearity by identifying digital predistorter coefficients via differential evolution, i.e., a stochastic optimizer. To fulfill the WLAN standard we had to consider a second objective, the distance of the out-of-band PSD to the spectrum mask. The proposed multi-objective optimization approach lead to a set of Pareto-optimal solutions, indicating a trade-off between minimizing the EVM and the mask distance. We stressed that stochastic optimization for DPD identification allows for a very low feedback sample rate. However, EVM measurements require accurate ADCs at the high rate. We pointed out that using a measurement based on the NPR may avoid this principal problem.

In Chapter 4, we had a close look on the capability of NPR-based measurements to estimate the EVM in OFDM systems and introduced the term error power ratio (EPR) for the proposed method. Using the same principle as in Chapter 3, i.e., stopbands that are symmetric around the carrier (DC in baseband), we were able to exclude IQ mismatch. By using asymmetric stopbands, on the other hand, we were able to estimate the EVM in case of IQ mismatch. We found the stopband-width to be crucial in case of phase noise. To estimate the EVM with de-rotation the width of each stopband should equal the subcarrier spacing. We derived and discussed that a single EPR measurement is not well suited for systems featuring a heavy inband magnitude frequency dependency or highly-frequency-dependent EVMs. The main problem is that the stopband location is fixed and can only cover a fraction of the inband.

In Chapter 5, we introduced the swept EPR (SWEEPR) that overcomes the problem of the static stopband location in EPR measurements. We discussed how to generate test signals with a stopband center frequency that is swept linearly over time. A swept tuned power spectrum analyzer (PSA) is the perfect tool to analyze such signals. By setting the analyzer sweep parameters equal to the test signal sweep parameters and using the PSA's external trigger and trigger delay functionality, we were able to measure the stopband and the inband PSD. The ratio of these PSDs estimates the EVM. The variance of SWEEPR is higher than for EPR and EVM, due to the decreased observation time and bandwidth. To decrease the variance, we have investigated a filter structure to generate SWEEPR test signals with multiple stopbands. Furthermore, we have shown how to generate a real-valued SWEEPR signal for testing baseband devices. Similar to the symmetric EPR and the EVM with nulled subcarriers proposed in Section 3.1, we were able to exclude IQ mismatch by using a symmetric stopband sweep. Measurement results corroborated the capability of the proposed SWEEPR measurement to estimate highly frequency-dependent EVM.

6.2 Conclusions

Both research questions stated on page 14 can be answered with *yes*. First, the proposed SLIC-EVM method allows to measure the subcarrier-dependent EVM without demodulating the communication signal's data symbols and without restricting to certain, assumed models of the DUT. Second, the EPR allows to estimate the EVM with a swept-tuned power spectrum analyzer, without the need for accurate wideband ADCs and synchronization. There is however a severe restriction: the inband frequency-dependence of the EVM and of the DUT must be gentle. The novel SWEEPR measurement removes this restriction and allows for estimating heavily subcarrier-dependent EVMs without bias, but at the cost of a higher variance.

At the same time while we were working on SLIC-EVM, other researcher have proposed related EVM estimation methods [120, 138]. In contrast to [120, 138], however, we compared the standard EVM side by side with our estimate, showing an excellent agreement both in simulations and measurements. Furthermore, we did not restrict to nonlinearities but also covered phase noise and IQ mismatch. SLIC-EVM and the proposed method to exclude IQ mismatch by nulling data symbols require a standard EVM measurement chain that includes high-bandwidth ADCs, IQ demodulation. Furthermore, accurate synchronization is required to achieve a low measurement floor.

The NPR is an established measurement method to quantify the signal to distortion and noise power that does not require high-bandwidth ADCs, IQ demodulation and synchronization. There is not much literature dealing with the relation of the EVM and the NPR. The discussion on the formal identity of NPR and EVM in [137] is built on a simple definition of both quantities as functions of the carrier (signal) to noise ratio. This thesis had a much closer look on EVM-estimation based on NPR and revealed several restrictions on the "formal identy" of the NPR and EVM: We discussed that equalization and phase de-rotation must be considered in the EVM analysis. We have shown the importance of the location of the stopband in case of IQ mismatch and the width of the stopband in case of phase noise. Furthermore, we analytically derived the estimation bias that can arise if the DUT system or the EVM are frequency-dependent. With SWEEPR, Section 5 presented an innovative twist to the NPR that is well-suited for measuring unknown, heavily frequency-dependent DUTs and EVMs with a power spectrum analyzer.

The measurement methods discussed in this thesis helped us to solve practical problems when measuring the performance of DPD systems or verifying the performance of WLAN transmitters. We started using EPR measurements out of necessity, since in our lab we did not have the required measurement devices and software licenses for EVM analysis. Our industry partner, on the other hand, acclaimed the EPR due to its low measurement noise floor that is crucial when measuring high quality chips featuring a low SNR at high bandwidths. The EPR also excelled for measurement of transmitter chips that do not have a 10 MHz connector for synchronization. Furthermore, consider a prototype transmitter that does not feature the final IQ mismatch performance

because the calibration is not yet working. In that case we can simply use symmetric stopbands with the EPR and are free from IQ mismatch.

Summing up, the following guidelines relate the proposed measurement methods with some hands-on, practical problems:

The EPR and the SWEEPR are good alternatives to the EVM if –

- the EVM should be measured but only a VSG and a spectrum analyzer, but no VSA, are available.
- the DUT is a transmitter chip without a 10 MHz connector for synchronization.
- the results obtained from a regular EVM measurement are worse than expected, e.g., due to a limited noise floor.

The SWEEPR is preferred to the EPR if –

- the EVM should be measured over all subcarriers, which is required if the EVM of the DUT varies a lot over frequency.
- the DUT magnitude response is heavily frequency-dependent.

The EPR is preferred to the SWEEPR if –

- the DUT and its EVM are feature only a gentle frequency-dependence
- there is need for using shorter test signals or a simpler measurement, without sweep synchronization.

The SLIC-EVM is useful if –

- The time-domain baseband DUT output data is available but the software to analyze the EVM of a certain signal standard is missing.

If IQ mismatch is suspected to be the reason for limited EVM performance, or if IQ mismatch should be excluded when measuring an RF DUT, there are the following options:

- In case that an EVM measurement setup is available, the EVM with nulled subcarriers as proposed in Section 3.1 is a good choice for troubleshooting. A single measurement provides an EVM result with IQ mismatch and a result without IQ mismatch.
- In case that the above EVM with nulled subcarriers is no option, the EPR or SWEEPR can be used. To estimate the EVM with IQ mismatch, asymmetric stopbands must be used. To exclude IQ mismatch, symmetric stopbands are required.

Besides presenting new measurement methods to estimate the EVM, we highlighted the capability of using the EVM, or its estimate, as an objective for DPD identification. A DPD adapted based on the SLIC-EVM error signal has the potential to reduce only the uncorrelated error, instead of wasting modeling power for the reduction of correlated errors, which are irrelevant for the EVM. Furthermore, by filtering the error signal to suppress either the inband or out-of-band, a trade-off between the inband and out-of-band error may be achieved with standard time-domain adaption based on regression. The direct DPD optimization approach described in Section 3.3 has the capability for low-cost DPD adaption using a very low feedback rate. However, that approach suffers from slow convergence since the variables interact and must be optimized jointly. This issue has been tackled very recently by means of an orthogonal scalar feedback DPD [118]. The linearization performance is confirmed by measurement results of a Doherty amplifier using a DPD that minimizes an out-of-band cost function (the ACPR). However, minimizing only the ACPR does not guarantee an optimal EVM that fulfills the standard requirements. To obtain an optimal EVM, the EVM must (also) be used as an objective in the optimization. This would, however, counteract the advantage of a low-rate, scalar feedback DPD, since EVM measurements require synchronization and high-rate feedback. Therefore, the proposed EPR measurement might be a key enabler for scalar feedback predistortion that optimizes the EVM.

A

Appendix

A.1 Linear Least Squares Based on Wirtinger Calculus

In the following, we review the derivation of the solution to a complex-valued linear least squares problem. We assume a model that is linear in its parameters $\boldsymbol{c}$, written as

$$\boldsymbol{y}[n] = \boldsymbol{X}[n]\boldsymbol{c} \tag{A.1}$$

where $\boldsymbol{X}[n]$ is the basis matrix belonging to the input signal $\{x[n]\}$, and $\boldsymbol{y}[n]$ is the vector of output samples. An example for such a model is the following memoryless baseband polynomial:

$$\begin{aligned}
y[n] &= \sum_{p=1}^{P} c_p x[n]\,|x[n]|^{p-1} && \text{(A.2)}\\
\boldsymbol{c} &= \Big[c_1, \ldots, c_P\Big]^T && \text{(A.3)}\\
\boldsymbol{p}[n] &= \Big[x[n]\,|x[n]|^0, \ldots, x[n]\,|x[n]|^{P-1}\Big]^T && \text{(A.4)}\\
\boldsymbol{y}[n] &= \Big[y[n], \ldots, y[n-N+1]\Big]^T && \text{(A.5)}\\
\boldsymbol{d}[n] &= \Big[d[n], \ldots, d[n-N+1]\Big]^T && \text{(A.6)}\\
\boldsymbol{X}[n] &= \Big[\boldsymbol{p}[n], \ldots, \boldsymbol{p}[n-N+1]\Big]^T && \text{(A.7)}
\end{aligned}$$

The error is defined as the difference of the desired signal $d[n]$ and the output $y[n]$.

$$\boldsymbol{e}[n] = \boldsymbol{d}[n] - \boldsymbol{y}[n] \tag{A.8}$$

The least squares cost function is

$$\begin{aligned}
J(\boldsymbol{c}) &= \sum_{m=0}^{N-1} |e[n-m]|^2 = \boldsymbol{e}^H[n]\boldsymbol{e}[n] && \text{(A.9)}\\
&= (\boldsymbol{d}[n] - \boldsymbol{X}[n]\boldsymbol{c})^H (\boldsymbol{d}[n] - \boldsymbol{X}[n]\boldsymbol{c})\,. && \text{(A.10)}
\end{aligned}$$

The solution $\boldsymbol{c}_{opt}$ can be derived by means of Wirtinger calculus [38], as follows. The dependence on n is dropped for the sake of brevity.

$$\begin{aligned} J(\boldsymbol{c}) &= (\boldsymbol{d}-\boldsymbol{X}\boldsymbol{c})^H(\boldsymbol{d}-\boldsymbol{X}\boldsymbol{c}) && \text{(A.11)}\\ &= \boldsymbol{d}^H\boldsymbol{d}-(\boldsymbol{X}\boldsymbol{c})^H\boldsymbol{d}-\boldsymbol{d}^H\boldsymbol{X}\boldsymbol{c}+(\boldsymbol{X}\boldsymbol{c})^H\boldsymbol{X}\boldsymbol{c} && \text{(A.12)}\\ &= \boldsymbol{d}^H\boldsymbol{d}-\boldsymbol{c}^H\boldsymbol{X}^H\boldsymbol{d}-\boldsymbol{d}^H\boldsymbol{X}\boldsymbol{c}+\boldsymbol{c}^H\boldsymbol{X}^H\boldsymbol{X}\boldsymbol{c} && \text{(A.13)}\\ \frac{\partial J(\boldsymbol{c})}{\partial \boldsymbol{c}^*} &= -\boldsymbol{X}^H\boldsymbol{d}+\boldsymbol{X}^H\boldsymbol{X}\boldsymbol{c} && \text{(A.14)}\\ \frac{\partial J(\boldsymbol{c})}{\partial \boldsymbol{c}^*} &\stackrel{!}{=} 0 \quad \Rightarrow \quad \boldsymbol{X}^H\boldsymbol{d}=\boldsymbol{X}^H\boldsymbol{X}\boldsymbol{c}_{opt} && \text{(A.15)}\\ \boldsymbol{c}_{opt} &= \left(\boldsymbol{X}^H\boldsymbol{X}\right)^{-1}\boldsymbol{X}^H\boldsymbol{d}=\boldsymbol{X}^\dagger\boldsymbol{d} && \text{(A.16)} \end{aligned}$$

Equation (A.16) is the well known least squares solution with the pseudo-inverse $\boldsymbol{X}^\dagger$. It is of the same form as for real-valued coefficients.

A.2 OFDM Demodulation

According to (2.58), the demodulated data symbols $Y[l,k]\in\mathbb{C}$ can be obtained from the received time domain baseband OFDM signal $y(t)$ by[1]

$$Y[l_0,k_0]=\frac{1}{T_K}\int_{t=l_0T}^{l_0T+T_K} y(t)e^{-j\frac{2\pi k_0}{T_K}(t-l_0T)}\,\mathrm{d}t\,. \tag{A.17}$$

In the following, we assume the symbol start time l_0T to be known. In practice, frame start detection and time delay compensation is required for estimating l_0T prior to the actual demodulation. If there is no signal impairment, we have $y(t)=s(t)$ and hence:

$$\begin{aligned} Y[l_0,k_0] &= \frac{1}{T_K}\int_{t=l_0T}^{l_0T+T_K}\left(\sum_{l\in\mathcal{L}} w(t-lT)\sum_{k\in\mathcal{K}} S[l,k]e^{j\frac{2\pi k}{T_K}(t-lT)}\right)e^{-j\frac{2\pi k_0}{T_K}(t-l_0T)}\,\mathrm{d}t && \text{(A.18)}\\ &= \frac{1}{T_K}\int_{t=l_0T}^{l_0T+T_K}\sum_{k\in\mathcal{K}} S[l_0,k]e^{j\frac{2\pi k}{T_K}(t-l_0T)}e^{-j\frac{2\pi k_0}{T_K}(t-l_0T)}\,\mathrm{d}t && \text{(A.19)}\\ &= \frac{1}{T_K}\sum_{k\in\mathcal{K}}\int_{u=0}^{T_K} S[l_0,k]e^{j\frac{2\pi}{T_K}(k-k_0)u}\,\mathrm{d}u && \text{(A.20)}\\ &= S[l_0,k_0] && \text{(A.21)} \end{aligned}$$

(A.19) follows from (A.18) because of the integration bounds and the support of $w(t)$, (A.20) from (A.19) because of the substitution $u=t-l_0T$, and (A.21) from (A.20) because of the orthogonality of the complex exponentials, i.e. the integral is 0 for all $k\neq k_0$.

[1] We use l_0 and k_0 instead of l and k to not get confused when inserting $S[l,k]$ in (A.18).

Publications Covered in this Thesis

[A1] K. Freiberger, H. Enzinger, and C. Vogel, "A method to exclude IQ mismatch from multicarrier EVM measurements", *IEEE Transactions on Microwave Theory and Techniques*, pp. 1–6, 2017, planned submission (cit. on pp. 16, 18, 43).

[A2] K. Freiberger, H. Enzinger, and C. Vogel, "SLIC EVM – Error vector magnitude without demodulation", in *89th ARFTG Microwave Measurement Conference*, Honolulu, HI, USA, Jun. 2017, pp. 1–4 (cit. on pp. 16, 18, 21, 43, 44, 57, 109).

[A3] K. Freiberger, M. Wolkerstorfer, H. Enzinger, and C. Vogel, "Digital predistorter identification based on constrained multi-objective optimization of WLAN standard performance metrics", in *IEEE International Symposium on Circuits and Systems (ISCAS)*, Lisbon, Portugal, 2015, pp. 862–865 (cit. on pp. 16, 18, 65, 66, 70).

[A4] K. Freiberger, H. Enzinger, and C. Vogel, "A noise power ratio measurement method for accurate estimation of the error vector magnitude", *IEEE Transactions on Microwave Theory and Techniques*, vol. 65, no. 5, pp. 1632–1645, 2017 (cit. on pp. 17, 18, 21, 44, 55, 58, 63, 75, 89, 90, 102).

[A5] K. Freiberger, H. Enzinger, and C. Vogel, "The error power ratio estimates EVM for a wide class of impairments: Monte carlo simulations", in *Integrated Nonlinear Microwave and Millimetre-wave Circuits Workshop (INMMiC)*, Graz, Austria, 2017, pp. 1–3 (cit. on pp. 17, 18, 75, 89).

[A6] K. Freiberger, H. Enzinger, and C. Vogel, "SWEEPR – The swept error power ratio for measuring the EVM with a spectrum analyzer", *IEEE Microwave and Wireless Components Letters*, pp. 1–3, Oct. 2017, submitted (cit. on pp. 17, 18, 109).

[A7] K. Freiberger, *Error Measurement Method Using a Time-Variant Stopband Test Signal*, US provisional patent application 62/476405, Intel Corporation, 2200 Mission College Boulevard, Santa Clara, California, 95054 USA, Mar. 2017 (cit. on pp. 17, 18).

Bibliography

[1] A. H. Abdelhafiz, O. Hammi, A. Zerguine, A. T. Al-Awami, and F. M. Ghannouchi, "A PSO based memory polynomial predistorter with embedded dimension estimation", *IEEE Transactions on Broadcasting*, vol. 59, no. 4, pp. 665–673, 2013 (cit. on pp. 65, 66).

[2] E. Acar and S. Ozev, "Low-cost characterization and calibration of RF integrated circuits through I–Q data analysis", *IEEE Transactions on Computer-Aided Design of Integrated Circuits and Systems*, vol. 28, no. 7, pp. 993–1005, 2009 (cit. on p. 11).

[3] L. Angrisani, M. D'Arco, and M. Vadursi, "Error vector-based measurement method for radiofrequency digital transmitter troubleshooting", *IEEE Transactions on Instrumentation and Measurement*, vol. 54, no. 4, pp. 1381–1387, 2005 (cit. on pp. 11, 44).

[4] L. Angrisani, I. Ghidini, and M. Vadursi, "A new method for I/Q impairment detection and evaluation in OFDM transmitters", *IEEE Transactions on Instrumentation and Measurement*, vol. 55, no. 5, pp. 1480–1486, 2006 (cit. on p. 11).

[5] L. Anttila, M. Valkama, and M. Renfors, "Frequency-selective I/Q mismatch calibration of wideband direct-conversion transmitters", *IEEE Transactions on Circuits and Systems II: Express Briefs*, vol. 55, no. 4, pp. 359–363, 2008 (cit. on pp. 5, 35, 45, 63).

[6] L. Anttila, P. Handel, and M. Valkama, "Joint mitigation of power amplifier and I/Q modulator impairments in broadband direct-conversion transmitters", *IEEE Transactions on Microwave Theory and Techniques*, vol. 58, no. 4, pp. 730–739, 2010 (cit. on p. 45).

[7] A. G. Armada, "Understanding the effects of phase noise in orthogonal frequency division multiplexing (OFDM)", *IEEE Transactions on Broadcasting*, vol. 47, no. 2, pp. 153–159, 2001 (cit. on p. 29).

[8] I. J. Bahl, *Fundamentals of RF and Microwave Transistor Amplifiers*. Hoboken, New Jersey: John Wiley & Sons, Inc., 2002, ISBN: 978-0-470-39166-2 (cit. on p. 76).

[9] A. Banerjee, V. Natarajan, S. Sen, A. Chatterjee, G. Srinivasan, and S. Bhattacharya, "Optimized multitone test stimulus driven diagnosis of RF transceivers using model parameter estimation", in *Internatioal Conference on VLSI Design*, 2011, pp. 274–279 (cit. on p. 10).

[10] R. A. Belcher, "ADC standard IEC 60748-4-3: Precision measurement of alternative ENOB without a sine wave", *IEEE Transactions on Instrumentation and Measurement*, vol. 64, no. 12, pp. 3183–3200, 2015 (cit. on p. 76).

[11] M. Bertocco and A. Sona, "On the measurement of power via a superheterodyne spectrum analyzer", *IEEE Transactions on Instrumentation and Measurement*, vol. 55, no. 5, pp. 1494–1501, 2006 (cit. on p. 26).

[12] R. B. Blackman and J. W. Tukey, "The measurement of power spectra from the point of view of communications engineering — part I", *The Bell System Technical Journal*, vol. 37, no. 1, pp. 185–282, 1958 (cit. on p. 25).

[13] R. B. Blackman and J. W. Tukey, "The measurement of power spectra from the point of view of communications engineering — part II", *The Bell System Technical Journal*, vol. 37, no. 2, pp. 485–569, 1958 (cit. on p. 25).

[14] W. Bösch and G. Gatti, "Measurement and simulation of memory effects in predistortion linearizers", *IEEE Transactions on Microwave Theory and Techniques*, vol. 37, no. 12, pp. 1885–1890, 1989 (cit. on p. 9).

[15] S. Boyd and L. Chua, "Fading memory and the problem of approximating nonlinear operators with volterra series", *IEEE Transactions on Circuits and Systems*, vol. 32, no. 11, pp. 1150–1161, 1985 (cit. on p. 31).

[16] J. J. Bussgang, "Crosscorrelation Functions of Amplitude-Distorted Gaussian Signals", Massachusetts Institute of Technology, Cambridge, MA, USA, Technical Report 172, Mar. 1952 (cit. on pp. 5, 31).

[17] N. Carvalho, K. Remley, D. Schreurs, and K. Gard, "Multisine signals for wireless system test and design [application notes]", *IEEE Microwave Magazine*, vol. 9, no. 3, pp. 122–138, 2008 (cit. on p. 77).

[18] N. B. Carvalho and D. Schreurs, *Microwave and Wireless Measurement Techniques*. Cambridge University Press, 2014 (cit. on p. 9).

[19] S. W. Chen, W. Panton, and R. Gilmore, "Effects of nonlinear distortion on CDMA communication systems", *IEEE Transactions on Microwave Theory and Techniques*, vol. 44, no. 12, pp. 2743–2750, 1996 (cit. on p. 76).

[20] C. Cho, J.-G. Lee, J.-H. Kim, and D.-C. Kim, "Uncertainty analysis in EVM measurement using a monte carlo simulation", *IEEE Transactions on Instrumentation and Measurement*, vol. 64, no. 6, pp. 1413–1418, 2015 (cit. on p. 99).

[21] S. Choi, E. R. Jeong, and Y. H. Lee, "Adaptive predistortion with direct learning based on piecewise linear approximation of amplifier nonlinearity", *IEEE Journal of Selected Topics in Signal Processing*, vol. 3, no. 3, pp. 397–404, 2009 (cit. on p. 55).

[22] D. Dardari, V. Tralli, and A. Vaccari, "A theoretical characterization of nonlinear distortion effects in OFDM systems", *IEEE Transactions on Communications*, vol. 48, no. 10, pp. 1755–1764, 2000 (cit. on p. 32).

[23] "Digital Video Broadcasting (DVB); Measurement guidelines for DVB systems", Tech. Rep., 2001, ETSI TR 101 290. [Online]. Available: `http://www.etsi.org/deliver/etsi_tr/101200_101299/101290/01.02.01_60/tr_101290v010201p.pdf` (cit. on pp. 76, 77).

[24] L. Ding, G. T. Zhou, D. R. Morgan, Z. Ma, J. S. Kenney, J. Kim, and C. R. Giardina, "A robust digital baseband predistorter constructed using memory polynomials", *IEEE Transactions on Communications*, vol. 52, no. 1, pp. 159–165, 2004 (cit. on pp. 65, 69).

[25] P. M. Djuric and S. M. Kay, "Spectrum estimation and modeling", in *The Oxford Handbook of Innovation*, V. K. Madisetti and D. B. Williams, Eds., Boca Raton: CRC Press LLC, 1999, ch. 10, pp. 4-1–14-21 (cit. on p. 24).

[26] H. Enzinger, "Behavioral Modeling and Digital Predistortion of Radio Frequency Power Amplifiers", PhD thesis, Graz University of Technology, 2018 (cit. on pp. 9, 17, 39).

[27] H. Enzinger, K. Freiberger, G. Kubin, and C. Vogel, "A survey of delay and gain correction methods for the indirect learning of digital predistorters", in *IEEE International Conference on Electronics, Circuits and Systems (ICECS)*, 2016, pp. 285–288 (cit. on pp. 17, 39, 59).

[28] H. Enzinger, K. Freiberger, G. Kubin, and C. Vogel, "A survey of delay and gain correction methods for the indirect learning of digital predistorters", in *IEEE International Conference on Electronics, Circuits and Systems (ICECS)*, Dec. 2016, pp. 285–288 (cit. on p. 17).

[29] H. Enzinger, K. Freiberger, G. Kubin, and C. Vogel, "Baseband Volterra filters with even-order terms: Theoretical foundation and practical implications", in *Asilomar Conference on Signals, Systems and Computers*, Nov. 2016, pp. 220–224 (cit. on pp. 4, 17).

[30] H. Enzinger, K. Freiberger, G. Kubin, and C. Vogel, "Fast time-domain Volterra filtering", in *Asilomar Conference on Signals, Systems and Computers*, 2016, pp. 225–228 (cit. on pp. 17, 31).

[31] H. Enzinger, K. Freiberger, and C. Vogel, "Analysis of even-order terms in memoryless and quasi-memoryless polynomial baseband models", in *IEEE International Symposium on Circuits and Systems (ISCAS)*, 2015, pp. 1714–1717 (cit. on pp. 9, 17, 27, 55, 103).

[32] H. Enzinger, K. Freiberger, and C. Vogel, "A joint linearity-efficiency model of radio frequency power amplifiers", in *IEEE International Symposium on Circuits and Systems (ISCAS)*, 2016, pp. 281–284 (cit. on p. 17).

[33] H. Enzinger, K. Freiberger, and C. Vogel, "Competitive linearity for envelope tracking: dual-band crest factor reduction and 2D-vector-switched digital predistortion", *IEEE Microwave Magazine*, 2018, accepted for publication (cit. on p. 17).

[34] N. Y. Ermolova and O. Tirkkonen, "Theoretical characterization of memory polynomial models with gaussian inputs", *IEEE Signal Processing Letters*, vol. 16, no. 8, pp. 651–654, 2009 (cit. on p. 32).

[35] C. Eun and E. J. Powers, “A new volterra predistorter based on the indirect learning architecture”, *IEEE Transactions on Signal Processing*, vol. 45, no. 1, pp. 223–227, 1997 (cit. on p. 55).

[36] C. Fager and K. Andersson, “Improvement of oscilloscope based RF measurements by statistical averaging techniques”, in *IEEE MTT-S International Microwave Symposium*, 2006, pp. 1460–1463 (cit. on p. 12).

[37] B. Farhang-Boroujeny, “OFDM versus filter bank multicarrier”, *IEEE Signal Processing Magazine*, vol. 28, no. 3, pp. 92–112, 2011 (cit. on p. 45).

[38] “Precoding and signal shaping for digital transmission”, in, R. F. H. Fischer, Ed. Wiley and Sons, Inc., 2002, ch. Appendix A - Wirtinger Calculus, pp. 405–413 (cit. on p. 128).

[39] A. R. G. Heinzel and R. Schilling, “Spectrum and spectral density estimation by the discrete Fourier transform (DFT), including a comprehensive list of window functions and some new flat-top windows”, Max-Planck-Institut für Gravitations-physik, Hannover, Feb. 2000 (cit. on p. 25).

[40] I. Galton, “Why dynamic-element-matching DACs work”, *IEEE Transactions on Circuits and Systems II: Express Briefs*, vol. 57, no. 2, pp. 69–74, 2010 (cit. on p. 89).

[41] K. G. Gard, H. M. Gutierrez, and M. B. Steer, “Characterization of spectral regrowth in microwave amplifiers based on the nonlinear transformation of a complex gaussian process”, *IEEE Transactions on Microwave Theory and Techniques*, vol. 47, no. 7, pp. 1059–1069, 1999 (cit. on p. 6).

[42] A. Geens, Y. Rolain, W. V. Moer, K. Vanhoenacker, and J. Schoukens, “Discussion on fundamental issues of NPR measurements”, *IEEE Transactions on Instrumentation and Measurement*, vol. 52, no. 1, pp. 197–202, 2003 (cit. on pp. 12, 23, 32, 33, 77).

[43] O. Gerlach and F. Schütze, *NPR - Noise Power Ratio Signal Generation and Measurement*, Rohde & Schwarz Application Note 1MA29, May 2015. [Online]. Available: `http://www.rohde-schwarz.com/appnote/1MA29` (cit. on pp. 76, 108).

[44] F. M. Ghannouchi and O. Hammi, “Behavioral modeling and predistortion”, *IEEE Microwave Magazine*, vol. 10, no. 7, pp. 52–64, 2009 (cit. on p. 31).

[45] K. M. Gharaibeh, K. G. Gard, and M. B. Steer, “Accurate estimation of digital communication system metrics - SNR, EVM and ρ in a nonlinear amplifier environment”, in *Fall ARFTG Microwave Measurements Conference.*, 2004, pp. 41–44 (cit. on p. 12).

[46] K. M. Gharaibeh, K. G. Gard, and M. B. Steer, “In-band distortion of multisines”, *IEEE Transactions on Microwave Theory and Techniques*, vol. 54, no. 8, pp. 3227–3236, 2006 (cit. on pp. 10, 23).

[47] K. Gharaibeh, *Nonlinear Distortion in Wireless Systems - Modeling and Simulation with Matlab*. John Wiley & Sons, 2011 (cit. on pp. 8, 10, 58, 76, 77).

[48] S. Glock, J. Rascher, B. Sogl, T. Ussmueller, J.-E. Mueller, and R. Weigel, "A memoryless semi-physical power amplifier behavioral model based on the correlation between AM-AM and AM-PM distortions", *IEEE Transactions on Microwave Theory and Techniques*, vol. 63, no. 6, pp. 1826–1835, 2015 (cit. on p. 103).

[49] M. Golio, *The RF and Microwave Handbook*. Boca Raton, Florida: CRC Press LLC, 2001, ISBN: 0-8493-8592-X (cit. on p. 76).

[50] Q. Gu, *RF System Design of Transceivers for Wireless Communications*. Springer, 2005 (cit. on p. 4).

[51] L. Guan and A. Zhu, "Green communications: Digital predistortion for wideband RF power amplifiers", *IEEE Microwave Magazine*, vol. 15, no. 7, pp. 84–99, 2014 (cit. on p. 31).

[52] A. Halder and A. Chatterjee, "Low-cost alternate EVM test for wireless receiver systems", in *IEEE VLSI Test Symposium*, 2005, pp. 255–260 (cit. on p. 44).

[53] A. Halder, "Efficient Alternate Test Generation for RF Transceiver Architectures", PhD thesis, Georgia Institute of Technology, Aug. 2006 (cit. on p. 10).

[54] A. Halder, S. Bhattacharya, and A. Chatterjee, "System-level specification testing of wireless transceivers", *IEEE Transactions on Very Large Scale Integration (VLSI) Systems*, vol. 16, no. 3, pp. 263–276, 2008 (cit. on p. 10).

[55] N. Hammler, Y. C. Eldar, and B. Murmann, "Low-rate identification of memory polynomials", in *IEEE International Symposium on Circuits and Systems (ISCAS)*, 2014, pp. 1034–1037 (cit. on p. 73).

[56] M. Helfenstein, E. Baykal, K. Muller, and A. Lampe, "Error vector magnitude (EVM) measurements for GSM/EDGE applications revised under production conditions", in *IEEE International Symposium on Circuits and Systems*, 2005, 5003–5006 Vol. 5 (cit. on p. 76).

[57] B. D. Holbrook and J. T. Dixon, "Load rating theory for multi-channel amplifiers", *The Bell System Technical Journal*, vol. 18, no. 4, pp. 624–644, 1939 (cit. on p. 76).

[58] M. Hotz and C. Vogel, "Linearization of time-varying nonlinear systems using A modified linear iterative method", *IEEE Transactions on Signal Processing*, vol. 62, no. 10, pp. 2566–2579, 2014 (cit. on p. 65).

[59] H. Huang, P. Mitran, and S. Boumaiza, "Digital predistortion function synthesis using undersampled feedback signal", *IEEE Microwave and Wireless Components Letters*, vol. 26, no. 10, pp. 855–857, 2016 (cit. on p. 73).

[60] M. A. Hussein, V. A. Bohara, and O. Venard, "On the system level convergence of ILA and DLA for digital predistortion", in *International Symposium on Wireless Communication Systems (ISWCS)*, 2012, pp. 870–874 (cit. on pp. 65, 68, 70).

[61] "IEEE standard for terminology and test methods for analog-to-digital converters", *IEEE Std 1241-2010 (Revision of IEEE Std 1241-2000)*, pp. 1–139, Jan. 2011. DOI: 10.1109/IEEESTD.2011.5692956 (cit. on p. 76).

[62] IEEE Std 802.11ac-2013, *Wireless LAN Medium Access Control (MAC) and Physical Layer (PHY) Specifications–Amendment 4: Enhancements for Very High Throughput for Operation in Bands below 6 GHz.* IEEE Std 802.11ac-2013 (cit. on pp. 1, 13, 30, 37, 39, 41, 52, 67, 76, 78, 82, 94).

[63] F. H. Irons, K. J. Riley, D. M. Hummels, and G. A. Friel, "The noise power ratio-theory and ADC testing", *IEEE Transactions on Instrumentation and Measurement*, vol. 49, no. 3, pp. 659–665, 2000 (cit. on p. 76).

[64] T. Jensen and T. Larsen, "Robust computation of error vector magnitude for wireless standards", *IEEE Transactions on Communications*, vol. 61, no. 2, pp. 648–657, 2013 (cit. on p. 41).

[65] J. W. Jeong, "Low-Overhead Built-In Self-Test for Advanced RF Transceiver Architectures", PhD thesis, Arizona State University, Dec. 2015 (cit. on p. 10).

[66] A. Katz and R. Gray, *Noise power ratio measurement tutorial*, Jan. 2012. [Online]. Available: http://www.lintech.com/PDF/npr_wp.pdf (cit. on p. 76).

[67] S. M. Kay, *Modern Spectral Estimation: Theory and Applications*. Englewood Cliffs, NJ, USA: Prentice-Hall, 1988 (cit. on p. 24).

[68] W. Kester, *Noise Power Ratio (NPR) - A 65-year old telephone system specification finds new life in modern wireless applications*, Analog Devices Inc. Tutorial MT-005, 2008 (cit. on pp. 8, 76–78).

[69] Keysight Technologies, *8 Hints for Making and Interpreting EVM Measurements*, Application Note 5989-3144EN (cit. on p. 7).

[70] Keysight Technologies, *Creating and Optimizing 802.11ac Signals and Measurements*, Application Note 5991-0574EN. [Online]. Available: http://literature.cdn.keysight.com/litweb/pdf/5991-0574EN.pdf (cit. on p. 41).

[71] Keysight Technologies, *Improved Methods for Measuring Distortion in Broadband Devices*, Application Note 5989-9880EN. [Online]. Available: http://literature.cdn.keysight.com/litweb/pdf/5989-9880EN.pdf (cit. on pp. 76, 85).

[72] Keysight Technologies, *Isolating Problems and Optimizing Wireless Designs with Digital Demodulation and EVM*, Application Brief 5992-1514EN (cit. on p. 13).

[73] Keysight Technologies, *Spectrum Analysis Basics - AN 150*, Application Note 5952-0292 (cit. on pp. 24, 25, 27).

[74] J. Kim and K. Konstantinou, "Digital predistortion of wideband signals based on power amplifier model with memory", *Electronics Letters*, vol. 37, no. 23, pp. 1417–1418, 2001 (cit. on p. 10).

[75] H. Ku, M. D. McKinley, and J. S. Kenney, "Quantifying memory effects in RF power amplifiers", *IEEE Transactions on Microwave Theory and Techniques*, vol. 50, no. 12, pp. 2843–2849, 2002 (cit. on p. 31).

[76] S. Kukkonen and J. Lampinen, "GDE3: the third evolution step of generalized differential evolution", in *IEEE Congress on Evolutionary Computation*, 2005, 443–450 Vol.1 (cit. on pp. 66, 68).

[77] B. D. Laki and C. J. Kikkert, "Adaptive digital predistortion for wideband high crest factor applications based on the WACP optimization objective: A conceptual overview", *IEEE Transactions on Broadcasting*, vol. 58, no. 4, pp. 609–618, 2012 (cit. on p. 72).

[78] B. D. Laki and C. J. Kikkert, "Adaptive digital predistortion for wideband high crest factor applications based on the WACP optimization objective: An extended analysis", *IEEE Transactions on Broadcasting*, vol. 59, no. 1, pp. 136–145, 2013 (cit. on pp. 65, 66, 72).

[79] S. Laurent, J. P. Teyssier, R. Quere, J. Sombrin, and M. Prigent, "Linearity characterization of RF circuits through an unequally spaced multi-tone signal", in *ARFTG Microwave Measurement Conference (ARFTG)*, 2016, pp. 1–4 (cit. on p. 12).

[80] P. M. Lavrador, N. B. Carvalho, and J. C. Pedro, "Evaluation of signal-to-noise and distortion ratio degradation in nonlinear systems", *IEEE Transactions on Microwave Theory and Techniques*, vol. 52, no. 3, pp. 813–822, 2004 (cit. on pp. 12, 23, 32, 33, 35).

[81] Z. Li, Y. Xia, W. Pei, K. Wang, Y. Huang, and D. P. Mandic, "Noncircular measurement and mitigation of I/Q imbalance for OFDM-based WLAN transmitters", *IEEE Transactions on Instrumentation and Measurement*, vol. 66, no. 3, pp. 383–393, 2017 (cit. on p. 44).

[82] D. Liebl, *Measuring with Modern Spectrum Analyzers*, Rohde & Schwarz Educational Note 1MA201_09e, Feb. 2013. [Online]. Available: `http://www.rohde-schwarz.com/appnote/1MA201` (cit. on p. 27).

[83] L. Ljung, *System Identification: Theory for the User*. Prentice-Hall, 1987, ISBN: 0-13-881640-9 (cit. on p. 32).

[84] S. Luke, *Essentials of Metaheuristics*, second. Lulu, 2013, Available for free at https://cs.gmu.edu/ sean/book/metaheuristics/ (cit. on pp. 66, 72).

[85] H. Mahmoud and H. Arslan, "Error vector magnitude to SNR conversion for nondata-aided receivers", *IEEE Transactions on Wireless Communications*, vol. 8, no. 5, pp. 2694–2704, 2009 (cit. on pp. 6, 41, 58).

[86] D. Marco and D. L. Neuhoff, "The validity of the additive noise model for uniform scalar quantizers", *IEEE Transactions on Information Theory*, vol. 51, no. 5, pp. 1739–1755, 2005 (cit. on p. 28).

[87] P. Medrel, T. Reveyrand, A. Martin, P. Bouysse, J.-M. Nebus, and J. Sombrin, "Time domain envelope characterization of power amplifiers for linear and high efficiency design solutions", in *IEEE Annual Wireless and Microwave Technology Conference (WAMICON)*, 2013, pp. 1–6 (cit. on pp. 76, 77).

[88] W. V. Moer and L. Gomme, "NVNA versus LSNA: enemies or friends?", *IEEE Microwave Magazine*, vol. 11, no. 1, pp. 97–103, 2010 (cit. on p. 12).

[89] D. R. Morgan, Z. Ma, J. Kim, M. G. Zierdt, and J. Pastalan, "A generalized memory polynomial model for digital predistortion of RF power amplifiers", *IEEE Transactions on Signal Processing*, vol. 54, no. 10, pp. 3852–3860, 2006 (cit. on p. 31).

[90] S. Müller and P. Massarani, "Transfer-function measurement with sweeps", *J. Audio Eng. Soc*, vol. 49, no. 6, pp. 443–471, 2001 (cit. on p. 109).

[91] B. Murmann, C. Vogel, and H. Koeppl, "Digitally enhanced analog circuits: System aspects", in *IEEE International Symposium on Circuits and Systems, ISCAS*, 2008, pp. 560–563 (cit. on p. 65).

[92] C. Nader, P. N. Landin, W. V. Moer, N. Bjorsell, P. Handel, and D. Ronnow, "Peak-power controlling technique for enhancing digital pre-distortion of RF power amplifiers", *IEEE Transactions on Microwave Theory and Techniques*, vol. 60, no. 11, pp. 3571–3581, 2012 (cit. on pp. 67, 70).

[93] A. Nassery, S. Byregowda, S. Ozev, M. Verhelst, and M. Slamani, "Built-in self-test of transmitter I/Q mismatch and nonlinearity using self-mixing envelope detector", *IEEE Transactions on Very Large Scale Integration (VLSI) Systems*, vol. 23, no. 2, pp. 331–341, 2015 (cit. on p. 11).

[94] A. Nassery, "Low Cost Analytical Techniques for Transceiver Characterization", PhD thesis, Arizona State University, 2013 (cit. on p. 10).

[95] A. Nassery, S. Ozev, and M. Slamani, "Analytical modeling for EVM in OFDM transmitters including the effects of IIP3, I/Q imbalance, noise, AM/AM and AM/PM distortion", in *IEEE European Test Symposium (ETS)*, 2013, pp. 1–6 (cit. on p. 10).

[96] A. Nassery, S. Ozev, M. Verhelst, and M. Slamani, "Extraction of EVM from transmitter system parameters", in *Sixteenth IEEE European Test Symposium*, 2011, pp. 75–80 (cit. on p. 11).

[97] V. Natarajan, H. W. Choi, A. Banerjee, S. Sen, A. Chatterjee, G. Srinivasan, F. Taenzler, and S. Bhattacharya, "Low cost EVM testing of wireless RF SoC front-ends using multitones", *IEEE Transactions on Computer-Aided Design of Integrated Circuits and Systems*, vol. 31, no. 7, pp. 1088–1101, 2012 (cit. on p. 10).

[98] V. Natarajan, "Self-healing RF SoCs: Low cost built-in test and control driven simultaneous tuning of multiple performance metrics", PhD thesis, Georgia Institute of Technology, 2010 (cit. on p. 10).

[99] L. Noel and P. Brousse, "Low-cost EVM test methodology for wireless transmitters applied to W-CDMA", *IEEE Transactions on Instrumentation and Measurement*, vol. 60, no. 1, pp. 170–175, 2011 (cit. on pp. 11, 76).

[100] A. Novak, L. Simon, F. Kadlec, and P. Lotton, "Nonlinear system identification using exponential swept-sine signal", *IEEE Transactions on Instrumentation and Measurement*, vol. 59, no. 8, pp. 2220–2229, 2010 (cit. on p. 109).

[101] A. Nuttall, "Some windows with very good sidelobe behavior", *IEEE Transactions on Acoustics, Speech, and Signal Processing*, vol. 29, no. 1, pp. 84–91, 1981 (cit. on p. 83).

[102] A. H. Nuttall, "Theory and Application of the Separable Class of Random Processes", PhD thesis, Massachusetts Institute Of Technology, May 1958 (cit. on p. 32).

[103] A. V. Oppenheim and R. W. Schafer, *Discrete Time Signal Processing*, 3rd. Pearson, 2013 (cit. on pp. 27, 37).

[104] A. Papoulis, *The Fourier Integral and its Applications*. New York: McGraw-Hill Book Company, Inc., 1962, ISBN: 978-0070484474 (cit. on p. 34).

[105] A. Papoulis and U. S. Pillai, *Probability, Random Variables, and Stochastic Processes*, 4th ed. New York: McGraw-Hill Higher Education, 2002, ISBN: 978-0073660110 (cit. on pp. 22, 23, 34).

[106] J. Pedro and N. Carvalho, "On the use of multitone techniques for assessing RF components' intermodulation distortion", *IEEE Transactions on Microwave Theory and Techniques*, vol. 47, no. 12, pp. 2393–2402, 1999 (cit. on p. 45).

[107] J. Pedro and N. Carvalho, "A novel nonlinear distortion characterisation standard for RF and microwave communication systems", *Engineering Science and Education Journal*, vol. 10, no. 3, pp. 113–119, 2001 (cit. on p. 12).

[108] J. Pedro and N. Carvalho, "Characterizing nonlinear RF circuits for their in-band signal distortion", *IEEE Transactions on Instrumentation and Measurement*, vol. 51, no. 3, pp. 420–426, 2002 (cit. on pp. 8, 12, 23, 33, 57, 58, 76, 77, 90).

[109] J. Pedro and N. Carvalho, "Designing multisine excitations for nonlinear model testing", *IEEE Transactions on Microwave Theory and Techniques*, vol. 53, no. 1, pp. 45–54, 2005 (cit. on pp. 31, 77).

[110] J. Pedro, N. Carvalho, and P. Lavrador, "Modeling nonlinear behavior of band-pass memoryless and dynamic systems", in *IEEE MTT-S International Microwave Symposium*, 2003, 2133–2136 vol.3 (cit. on pp. 9, 12, 77, 103).

[111] J. C. Pedro and N. B. Carvalho, *Intermodulation distortion in microwave and wireless circuits*. Artech House, 2002 (cit. on p. 31).

[112] R. Pintelon and J. Schoukens, *System Identification: A Frequency Domain Approach*. IEEE Press, 2001, ISBN: 0-7803-6000-1 (cit. on p. 32).

[113] C. Rapp, "Effects of HPA-nonlinearity on a 4-DPSK/OFDM-signal for a digital sound broadcasting system", in *In ECSC-2, Proceedings of the Second European Conference on Satellite Communications, Liege, Belgium*, Oct. 1991 (cit. on pp. 31, 69).

[114] K. A. Remley, D. F. Williams, P. D. Hale, C. M. Wang, J. Jargon, and Y. Park, "Millimeter-wave modulated-signal and error-vector-magnitude measurement with uncertainty", *IEEE Transactions on Microwave Theory and Techniques*, vol. 63, no. 5, pp. 1710–1720, 2015 (cit. on pp. 13, 99).

[115] T. Reveyrand, D. Barataud, J. Lajoinie, M. Campovecchio, J.-M. Nebus, E. Ngoya, J. Sombrin, and D. Roques, "A novel experimental noise power ratio characterization method for multicarrier microwave power amplifiers", in *ARFTG Conference -Spring*, 2000, pp. 1–5 (cit. on pp. 77, 78, 81).

[116] T. Reveyrand, D. Barataud, J.-M. Nebus, A. Mallet, F. Gizard, L. Lapierre, and J. Sombrin, "Accurate characterization of intermodulation noise in multi carrier wide band power amplifiers based on a digital synthesis of pseudo noise gaussian stimuli", *Annales Des Télécommunications*, vol. 61, no. 5, pp. 627–644, 2006, ISSN: 1958-9395. DOI: 10.1007/BF03219926 (cit. on pp. 78, 81, 82).

[117] N. Ridler, B. Lee, J. Martens, and K. Wong, "Measurement uncertainty, traceavility, and the GUM", *IEEE Microwave Magazine*, vol. 8, no. 4, pp. 44–53, 2007 (cit. on p. 99).

[118] H. D. Rodrigues, T. C. Pimenta, R. A. A. de Souza, and L. L. Mendes, "Orthogonal scalar feedback digital pre-distortion linearization", *IEEE Transactions on Broadcasting*, vol. PP, no. 99, pp. 1–12, 2017 (cit. on p. 125).

[119] Y. Rolain, W. V. Moer, R. Pintelon, and J. Schoukens, "Experimental characterization of the nonlinear behavior of RF amplifiers", *IEEE Transactions on Microwave Theory and Techniques*, vol. 54, no. 8, pp. 3209–3218, 2006 (cit. on pp. 11, 12).

[120] Y. Rolain, M. Zyari, E. Van Nechel, and G. Vandersteen, "A measurement-based error-vector-magnitude model to assess non linearity at the system level", in *International Microwave Symposium (IMS)*, Jun. 2017 (cit. on pp. 11, 12, 57, 109, 123).

[121] H. Rosen and A. Owens, "Power amplifier linearity studies for SSB transmissions", *IEEE Transactions on Communications Systems*, vol. 12, no. 2, pp. 150–159, 1964 (cit. on p. 77).

[122] M. Rumney, Ed., *LTE and the Evolution to 4G Wireless: Design and Measurement Challenges*, 2nd. John Wiley & Sons, 2013 (cit. on pp. 1, 2, 37, 76, 78, 82).

[123] A. A. M. Saleh, "Frequency-independent and frequency-dependent nonlinear models of TWT amplifiers", *IEEE Transactions on Communications*, vol. 29, no. 11, pp. 1715–1720, 1981 (cit. on pp. 31, 55).

[124] A. Samelis, E. Whittaker, M. Ball, A. Bruce, J. Nisbet, L. Lam, and W. Vaillancourt, "Front-end modules with versatile dynamic EVM correction for 802.11 applications in the 2GHz band", in *IEEE Topical Conference on Power Amplifiers for Wireless and Radio Applications (PAWR)*, 2014, pp. 10–12 (cit. on p. 15).

[125] M. Schetzen, *The Volterra an Wiener Theories of Nonlinear Systems*, Reprint with additional material, originally published: Wiley, New York, 1980. Malabar, Florida: Krieger Publishing Company, 2006 (cit. on pp. 31, 33).

[126] J. Schoukens, T. Dobrowiecki, and R. Pintelon, "Parametric and nonparametric identification of linear systems in the presence of nonlinear distortions-a frequency domain approach", *IEEE Transactions on Automatic Control*, vol. 43, no. 2, pp. 176–190, 1998 (cit. on p. 11).

[127] J. Schoukens, R. Pintelon, and T. Dobrowiecki, "Linear modeling in the presence of nonlinear distortions", *IEEE Transactions on Instrumentation and Measurement*, vol. 51, no. 4, pp. 786–792, 2002 (cit. on p. 11).

[128] M. Schoukens, "Identification of Parallel Block-Oriented Models starting from the Best Linear Approximation", PhD thesis, Vrije Universiteit Brussel, Mar. 2015 (cit. on p. 32).

[129] P. J. Schreier and L. L. Scharf, *Statistical Signal Processing of Complex-Valued Data*. Cambridge University Press, 2010 (cit. on pp. 45, 77, 82).

[130] D. Schreurs, A. A. Goacher, and M. Gadringer, *RF power amplifier behavioral modeling*. Cambridge University Press, 2009, vol. 269 (cit. on p. 31).

[131] S. Sen, S. Devarakond, and A. Chatterjee, "Phase distortion to amplitude conversion -based low-cost measurement of AM-AM and AM-PM effects in RF power amplifiers", *IEEE Transactions on Very Large Scale Integration (VLSI) Systems*, vol. 20, no. 9, pp. 1602–1614, 2012 (cit. on p. 10).

[132] R. Senguttuvan, S. Bhattacharya, and A. Chatterjee, "Efficient EVM testing of wireless OFDM transceivers using null carriers", *IEEE Transactions on Very Large Scale Integration (VLSI) Systems*, vol. 17, no. 6, pp. 803–814, 2009 (cit. on p. 10).

[133] C. E. Shannon, "The mathematical theory of communication", *Bell System Technical Journal*, vol. 27, no. 3, pp. 379–423, Jul. 1948 (cit. on p. 2).

[134] P. Singerl and G. Kubin, "Constructing memory-polynomial models from frequency - dependent AM/AM and AM/PM measurements", in *Midwest Symposium on Circuits and Systems*, 2007, pp. 321–324 (cit. on p. 10).

[135] L. Smaini, *RF Analog Impairments Modeling for Communication Systems Simulation: Application to OFDM-based Transceivers*. John Wiley & Sons, 2012 (cit. on pp. 3, 27–30, 37).

[136] Society of Cable Technology Engineers, *Measurement Procedure for Noise Power Ratio*, ANSI/SCTE 119 2011 Standard, 2011. [Online]. Available: `http://www.scte.org/documents/pdf/standards/SCTE_119_2011.pdf` (cit. on p. 77).

[137] J. B. Sombrin, "On the formal identity of EVM and NPR measurement methods: Conditions for identity of error vector magnitude and noise power ratio", in *European Microwave Conference (EuMC)*, 2011, pp. 337–340 (cit. on pp. 76, 123).

[138] J. Sombrin and P. Medrel, "Cross-correlation method measurement of error vector magnitude and application to power amplifier non-linearity performances", in *ARFTG Microwave Measurement Conference (ARFTG)*, 2016, pp. 1–4 (cit. on pp. 57, 109, 123).

[139] R. Sperlich, J. A. Sills, and J. S. Kenney, "Power amplifier linearization with memory effects using digital pre-distortion and genetic algorithms", in *No. IEEE Radio and Wireless Conference (IEEE*, 2004, pp. 355–358 (cit. on pp. 65, 66).

[140] G. P. Srinivasan, "Efficient Production Testing of High-Performance RF Moduleas and Systems Using Low-Cost ATE", PhD thesis, Georgia Institute of Technology, Dec. 2006 (cit. on p. 10).

[141] P. Stoica and R. Moses, *Spectral Analysis of Signals*. Upper Saddle River, NJ, USA: Prentice-Hall, 2005 (cit. on pp. 23, 119).

[142] M. Tanahashi and K. Yamaguchi, "Uncertainty of out-of-band distortion measurement with a spectrum analyzer", *IEEE Transactions on Broadcasting*, vol. 61, no. 3, pp. 532–540, 2015 (cit. on p. 26).

[143] A. S. Tehrani, H. Cao, S. Afsardoost, T. Eriksson, M. Isaksson, and C. Fager, "A comparative analysis of the complexity/accuracy tradeoff in power amplifier behavioral models", *IEEE Transactions on Microwave Theory and Techniques*, vol. 58, no. 6, pp. 1510–1520, 2010 (cit. on p. 12).

[144] J.-P. Teyssier, J. Dunsmore, J. Verspecht, and J. Kerr, "Coherent multi-tone stimulus-response measurements with a VNA", in *89th ARFTG Microwave Measurement Conference*, Jun. 2017 (cit. on pp. 14, 15, 81).

[145] H. T. Than, G. W. Sun, G. S. Cuellar, J. Zeng, N. T. Schultz, M. E. Moya, Y. Chung, B. C. Deckman, and M. P. DeLisio, "Design and performance of a 600-W C-band amplifier using spatially combined GaAs FETs for satellite communications", *IEEE Journal of Solid-State Circuits*, vol. 47, no. 10, pp. 2309–2315, 2012 (cit. on p. 76).

[146] M. J. Trezise, "Understanding the measures of signal quality in DVB systems", in *International Broadcasting Convention IBS*, 1997, pp. 488–492 (cit. on p. 76).

[147] W. G. Vaillancourt and S. E. Yates, "High speed noise power ratio measurement techniques on RF power amplifiers", in *IEEE MTT-S International Microwave Symposium*, 1997, 1451–1454 vol.3 (cit. on p. 76).

[148] M. Valkama, M. Renfors, and V. Koivunen, "Advanced methods for I/Q imbalance compensation in communication receivers", *IEEE Transactions on Signal Processing*, vol. 49, no. 10, pp. 2335–2344, 2001 (cit. on pp. 44, 45).

[149] W. Van Moer, L. Lauwers, and K. Barbé, "Measuring and characterizing nonlinear radio-frequency systems", in *Microwave De-Embedding*, G. Crupi and D. Schreurs, Eds., Elsevier Ltd., 2014, pp. 225–1280 (cit. on pp. 11, 57, 109).

[150] Z. Wang, W. Chen, G. Su, F. M. Ghannouchi, Z. Feng, and Y. Liu, "Low feedback sampling rate digital predistortion for wideband wireless transmitters", *IEEE Transactions on Microwave Theory and Techniques*, vol. 64, no. 11, pp. 3528–3539, 2016 (cit. on p. 73).

[151] L. Ward, *802.11ac Technology Introduction*, Rohde & Schwarz White Paper 1MA192, Mar. 2012. [Online]. Available: `http://www.rohde-schwarz.com/appnote/1MA192` (cit. on p. 41).

[152] D. Webster, R. Hudgens, and D. Lie, "Replacing error vector magnitude test with RF and analog BISTs", *IEEE Design & Test of Computers*, vol. 28, no. 6, pp. 66–75, 2011 (cit. on p. 11).

[153] P. Welch, "The use of fast fourier transform for the estimation of power spectra: A method based on time averaging over short, modified periodograms", *IEEE Transactions on Audio and Electroacoustics*, vol. 15, no. 2, pp. 70–73, 1967 (cit. on pp. 24, 60).

[154] J. R. Wilkerson, K. G. Gard, and M. B. Steer, "Automated broadband high-dynamic-range nonlinear distortion measurement system", *IEEE Transactions on Microwave Theory and Techniques*, vol. 58, no. 5, pp. 1273–1282, 2010 (cit. on p. 12).

[155] K. Witrisal, "OFDM air-interface design for multimedia communications", Ph.D. Thesis, Delft Univ. of Technology, 2002. [Online]. Available: `https://theses.eurasip.org/theses/339/ofdm-air-interface-design-for-multimedia` (cit. on pp. 38, 77).

[156] M. Wolkerstorfer and S. Trautmann, "Sequential multiobjective optimization for large-scale passive filter synthesis", in *European Conference on Circuit Theory and Design (ECCTD)*, 2013, pp. 1–4 (cit. on p. 66).

[157] E. Yilmaz, "Efficient Test Strategies for Analog RF Circuits", PhD thesis, Arizona State University, Dec. 2012 (cit. on p. 10).

[158] E. Yilmaz, A. Nassery, and S. Ozev, "Built-in EVM measurement with negligible hardware overhead", *IEEE Design & Test*, vol. 31, no. 1, pp. 75–82, 2014 (cit. on p. 10).

[159] S.-W. Yoon, "Static and dynamic error vector magnitude behavior of 2.4-GHz power amplifier", *IEEE Transactions on Microwave Theory and Techniques*, vol. 55, no. 4, pp. 643–647, 2007 (cit. on p. 15).

[160] L. Zhang and Y. Feng, "An improved digital predistortion in wideband wireless transmitters using an under-sampled feedback loop", *IEEE Communications Letters*, vol. 20, no. 5, pp. 910–913, 2016 (cit. on p. 73).

[161] D. Zhou and V. E. DeBrunner, “Novel adaptive nonlinear predistorters based on the direct learning algorithm”, *IEEE Transactions on Signal Processing*, vol. 55, no. 1, pp. 120–133, 2007 (cit. on pp. 55, 65, 67).